Nonlinear analysis of masonry and concrete structures under monotonic and cyclic loading: a regularized multidirectional d^+/d^- damage model

By

Claudia Tesei

****

Supervisors:
Prof. Giulio Ventura
Prof. Miguel Cervera

Declaration

I hereby declare that the contents and organization of this dissertation constitute my own original work and does not compromise in any way the rights of third parties, including those relating to the security of personal data.

Claudia Tesei

2018

* This dissertation is presented in partial fulfillment of the requirements for **Ph.D. degree** in the Graduate School of Politecnico di Torino (ScuDo).

Abstract

A rigorous structural analysis is fundamental in the safety assessment of the built heritage and in its efficient conservation and rehabilitation. In line with the necessity of refined techniques, the objective of the present thesis is to develop and validate, in a displacement-based finite element framework, a nonlinear model apt for the study of masonry and concrete structures under monotonic and cyclic loading.

The proposed constitutive law adopts two independent scalar damage variables, d^+ and d^-, in combination with the spectral decomposition of the elastic strain tensor, to simulate the pronounced dissimilar response under tension and compression, typical of these materials. The assumption of energy-equivalence between the damaged solid and the effective (undamaged) one is considered for representing the orthotropy induced in the material by the degradation process, with the consequence that a thermodynamically consistent constitutive operator, positive definite, symmetric and strain-driven, is derived.

The formulation is integrated with a multidirectional damage procedure, addressed to extend the microcrack closure-reopening (MCR) capabilities to generic cyclic conditions, especially shear cyclic conditions, making the model suitable for dealing with seismic actions. Maintaining unaltered the dependence of the constitutive law from d^+ and d^-, this approach activates or deactivates a tensile (compressive) damage value on the base of the current maximum (minimum) principal strain direction. In correspondence with damage activation (crack opening) or deactivation (crack closure), a smooth transition is introduced, in order to avoid abrupt changes in stiffness and enhance the numerical performance and robustness of the multidirectional procedure.

Moreover, the mesh-objectivity of the numerical solutions is ensured by resorting to a nonlocal regularization technique, based on the adoption of damage variables driven by an averaged elastic strain tensor. To perform the averaging of the strain tensor, an internal length l_{RG} is considered in the continuum. The strategy chosen to define the parameters affecting the softening behaviour consists in the

modification of the local softening law on the base of the internal length, with the intent of ensuring the proper evaluation of the correct fracture energy G_f.

The adequacy of the proposed constitutive model in reproducing experimental results is proven for both monotonic and cyclic loading conditions. Under monotonic loads, unreinforced concrete notched elements subjected to pure tension, pure bending and mixed-mode bending are studied. The two examples of application involving cyclic loads, a masonry and a reinforced concrete wall under in-plane cyclic shear, constitute a validation of the multidirectional damage approach, showing how the suitable representation of unilateral effects and permanent deformations is essential to model the observed structural response in terms of maximum resistance and dissipation capacity.

The effectiveness of the regularized damage formulation is proven by successfully studying a masonry arch and reinforced and unreinforced concrete elements. Besides the validation of the numerical results with experimental or analytical data, each application is exploited to highlight one or more features of the formulation: the mesh-size and mesh-bias independence of the results, the effect of the choice of the variable to be averaged, the possibility to reproduce structural size effects, the influence of the internal length l_{RG}. On this latter aspect, the almost null dependence of the regularized solutions on the internal length in terms of force-displacement curves, achieved thanks to the calibration strategy adopted to define the energy dissipation, suggests the interpretation of the internal length as a regularization parameter. On the one hand, this implies an analogy between the role played by the nonlocal internal length in a nonlocal model and the one's of the mesh size in the crack band approach (Bažant and Oh, 1983). On the other hand, this translates in the versatility of the regularized damage model, which requires only the identification of the standard material properties (elastic constants, fracture energies and strengths).

Finally, the d^+/d^- damage model is successfully applied to the study of a three-span masonry arch bridge subjected to a concentrated vertical load, in order to evaluate its carrying capacity and its failure mechanism. Numerical issues, usually neglected in large-scale applications, are also addressed proving the reliability of the regularized approach to provide mesh-independent results and its applicability.

Contents

List of Figures

List of Tables

Chapter 1

Introduction

1.1 Motivation

The engineering modelling of traditional building materials, such as masonry and concrete, and its implementation in computer-based structural analysis tools, has undergone a raised interest in the last decades. The necessity of an accurate structural analysis for the assessment and conservation of the built heritage is nowadays present, as it was in the past. By means of it, the determination of the structural safety as well as the design of the intervention measures is possible with respect to a variety of actions (gravity, soil settlements, earthquakes and also actions of anthropogenic nature such as architectural modifications or effects related to the construction stages).

Such a need becomes stronger over time because the built heritage suffers an ageing process whose consequences on the structural state are not completely understood. On the one hand, the built heritage is composed of masonry structures, the majority of which were erected centuries ago and can be classified as historical constructions. If their longevity reassures, their vulnerability against seismic actions can not be neglected. In addition, these structures are nowadays subjected to service loads which are usually heavier than the ones foreseen in the original design. In this respect, the most significant example is represented by the masonry arch bridges, which constitute a relevant part of the current Italian and European railway and road infrastructures.

On the other hand, there are reinforced concrete structures, whose advent in the construction sector dates back to the beginning of the twentieth century and whose great expansion in Italy, both in the residential buildings and in the infrastructures, is associated to the sixties. These structures can be considered only relatively recent and their durability over time is somehow uncertain.

Considering the Italian case, the age of the built heritage can be quantified taking into account a survey performed in 2001 on masonry and reinforced concrete residential buildings by the National Institute of Statistics (ISTAT). On a total of 11 226 595 buildings, it resulted that more than 60% were erected before the 1971 (Pasca, 2012). These data suggest another important reflection, which is the meager adequacy of the Italian built heritage in terms of the modern anti-seismic requirements. The last time this fact was dramatically evidenced is very recent and refers to the seismic sequence which hit the centre of Italy in 2016, causing almost 300 deaths, the destruction of several villages and the ruin of a vast cultural heritage.

Figure 1.1: Effects of the earthquake in the centre of Italy in 2016: (a) Pescara del Tronto completely destroyed; (b) shear cracks in a masonry building at Amatrice; (c) plastic hinge and overturning of a masonry wall in a reinforced concrete building at Pescara del Tronto. (b) and (c) are images from (Celano et *al*., 2016).

Some images, attesting the severity of this event, are plotted in Figure 1.1. Together with the wider picture of a village totally leveled by the earthquake, some details on the typical damages induced by earthquakes on masonry and reinforced concrete structures are also provided.

On the basis of these considerations, reliable analysis techniques are indispensable in the hands of structural engineers to predict the behaviour of a construction and hold the potentialities of saving human lifes and economic resources. Therefore, the development of methods able to suitably simulate the response of masonry and concrete elements represents nowadays a stimulating and open challenge in the structural engineering field.

Firstly, the difficulties related to such a task derive from the constitutive behaviour of these materials, which is far from the one of an isotropic linear elastic homogeneous material. Indeed, masonry is a composite material that consists of units (bricks, ashlars, blocks, stones) and joints (mortar, clay, bitumen, glue), whose mechanical properties and geometrical rearrangement can be very different. Hence, it is characterized by marked anisotropy and inhomogeneity. Concrete, as well, is composed of different constituents (cement, water and aggregates), although the directionality of the mechanical performance and the lack of homogeneity are much less accentuated. Moreover, some distinctive aspects that can be identified both in the different masonry tipologies and in the concrete are the pronounced asymmetry between tension and compression and the occurrence of cracking even for low stress levels, due to the scarse tensile strength. In terms of fracture behaviour, concrete and masonry can be both classified as *quasi-brittle materials*, i.e. materials characterized by a stress reduction after the attainment of the maximum strength (softening). Differently from a pure brittle response, a quasi-brittle material shows a measurable deformation prior to failure, which is not associated to a dislocation motion, as in plasticity, but is related to the nucleation and stable growth of defects. In terms of failure criterion, both concrete and masonry can be defined as *frictional-cohesive materials*.

Secondly, a further complication derives from the need of modelling the above described complex constitutive behaviour with reference to real-scale structures. The advances perfomed in the last decades in the use of computer methods for the prediction of mechanical phenomena encourage to replace simplified structural analysis techniques with more refined tools. Despite the great variety of proposed approaches, the numerical structural analysis of masonry and concrete structures still represents an active research field, since in the engineering practice the use of simplified techniques is usually preferred. The simplification can regard the

material behaviour, for instance with the recourse to linear elastic analysis, or the schematization of the resisting structure, which can be intended as the composition of linear (beam) members. It is worth noting that these simplifications are drastic especially for masonry structures but can be misleading even for reinforced concrete structures, when the study regards, for instance, slabs loaded in their own plane, deep beams or, alternatively, massive concrete structures, without reinforcement, as gravity dams and retaining walls.

In line with the necessity of refined structural analysis techniques, the objective of the present thesis is to develop and validate, in a displacement-based finite element framework, a continuum nonlinear model apt for the study of masonry and concrete structures under monotonic and cyclic loading. Specifically, the interest for the cyclic material behaviour is addressed in order to make the proposed constitutive model suitable for seismic analysis.

1.2 State of the art

Among the several approaches proposed for the structural analysis of masonry and concrete structures, it is possible to cite finite element or discrete element methods and limit analysis (Roca et *al.*, 2010).

A complete review of each one of these techniques is far beyond the scope of the present section, which is, instead, more specifically addressed to provide an overview of the existing formulations to model quasi-brittle materials in the finite element method (FEM).

For what regards the modelling of masonry structures according to FEM based approaches, a distinction between micro- and macro-modelling can be recalled: the former considers separately units, joints and mortar/unit interfaces while the latter regards masonry as a fictitious homogeneous continuum. On the one hand, due to the huge computational effort required and the huge number of necessary consitutive parameters, micro-modelling approaches are adopted for the study of small elements or structural details, when the stress distribution in the different masonry components is of interest (Rots, 1991; Lotfi and Shing, 1994; Gambarotta and Lagomarsino, 1997; Lourenço and Rots, 1997). On the other hand, for real-scale structures, the main target of the present thesis, macro-modelling appears the most suitable choice since it implies advantages related to calculation demand and meshing procedure, while ensuring acceptable accuracy (Addessi et *al.*, 2014).

In the framework of macro-modelling, some proposals taking into account the orthotropy of the material in the initial state exist, both in the framework of damage

mechanics (Papa, 1996; Berto et *al.* 2002; Pelà et *al.*, 2011; Pelà et *al.*, 2013) and plasticity (Lourenço et *al.*, 1998). However, the majority of them renounce to describe the intrinsic anisotropy of masonry in favour of an isotropic formulation (Clemente et *al.*, 2006; Mallardo et *al.*, 2008; Pelà et *al.*, 2009; Roca et *al.*, 2012; Toti et *al.*, 2015; Saloustros et *al.*, 2017c).

In the follow up, masonry is represented by means of a macro-modelling approach, in order to make the application of the proposed model versatile and apt for the analysis of brick and stone masonry and also concrete and cementitious materials in general. Therefore, masonry and concrete indistinctly are considered as quasi-brittle materials and are studied under the simplyfing assumptions of initial isotropy and homogeneity.

As mentioned earlier, quasi-brittle materials exhibit a strongly nonlinear behaviour even for low stress levels, because of tensile cracking. The main modelling strategies to deal with cracking proposed in the past decades by the computational solid mechanics' community can be classified into two main groups, discontinuous and continuous approaches. For an exhaustive discussion about this very broad topic, the dissertation presented in (Hofstetter and Meschke, 2011) is recommended.

At a continuum level, this distinction is explained by means of Figure 1.2. A crack can be considered as a discontinuity of the displacement field; specifically, the displacement jump w is the crack opening normal to the fracture line S (2D problems) or the fracture surface (3D problems). The strains associated to this displacement field are unbounded and represented by a Dirac's delta function, as shown in Figure 1.2.a. The stress tensor can be computed by means of a softening stress σ - separation w law. This approach can be defined with the name of *continuum strong discontinuity*. Alternatively, it is possible to smear the jump w on a localization band h, in order to have a continuous displacement field and a bounded strain field, resulting from the gradient of the regularized displacement. The strain field presents two weak discontinuity at the surfaces S^- and S^+, which delimit the localization band. The stress tensor can be computed by means of a softening stress σ – strain ε law. This procedure, displayed in Figure 1.2.b, can be referred to as *continuum weak discontinuities*.

At a discrete level, i.e. in a finite-element framework, the explicit representation of separation proper of the continuum strong discontinuity (Figure 1.2.a) is interpreted in several different procedures named *discrete strong discontinuity* approaches.
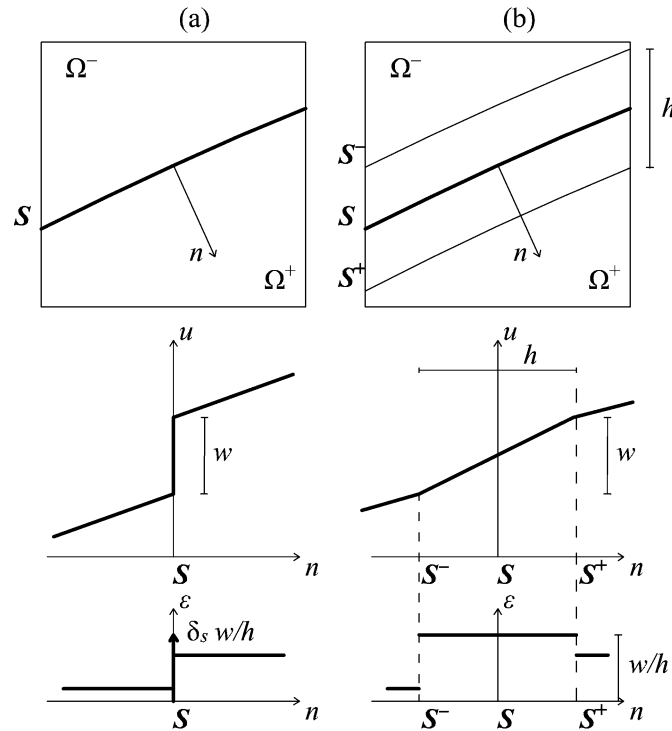
Figure 1.2: Crack modelling at a continuum level: (a) continuum strong discontinuity and (b) continuum localization band and weak discontinuities.

All these procedures are characterized by the necessity of a method to take into account the kinematics of the cracks and some criteria to establish the length and the direction of the propagated defect, usually based on fracture mechanics.

Among the first discrete strong discontinuity approaches, it is worth mentioning the interelement separation methods, which model cracks by separating mesh nodes initially occupying the same position (Ngo and Scordelis, 1967; Nilson, 1968; Camacho and Ortiz, 1996; Pandolfi et al., 1999). Such strategies can describe defects only along the boundaries of the finite elements; hence they are intrinsically mesh-dependent. To reduce the mesh-objectivity issue, remeshing is proposed with the aim of including new elements with the boundaries along the progressive crack directions. The increase in the objectivity of the results is however accompanied by a non-negligible increase in the complexity and the computational effort, required by the remeshing procedure.

A progress with respect to the interelement-separation methods is represented by the embedded finite element methods (EFEM), which allow dealing with strong discontinuities within the finite elements, withouth the necessity of remeshing. To do this, the displacement field of the standard displacement-based finite element

method is enhanced with a discontinuous displacement function in correspondence with the crack and the additional enriching variables are condensed at the element level. In such a form, the method was presented for the first time in (Dvorkin et al., 1990) but precursor works of this approach can be considered also the ones by Ortiz and Belytschko (Ortiz et al., 1987; Belytschko et al., 1988). Several formulations exploiting the embedded finite element methods have been proposed (Oliver et al., 1999; Jirásek, 2001), for studying concrete (Sancho et al., 2007) and also masonry (Reyes et al., 2009).

A more recent numerical method which includes the strong discontinuity within the finite element is the extended finite element method (XFEM), proposed in 1999 by Belytschko and co-workers (Belytschko and Black, 1999; Möes et al., 1999; Sukumar et al., 2000). This approach allows for crack propagation withouth remeshing, by tracking the crack progression through the discretization, and simultaneously enriching the nodal degrees of freedom with new ones, which represent either the displacement jumps across the crack or the singular stress field at the crack tip. The method implies the partition of unity concept and the additional nodal unknowns in the elements cut by the crack are not condensed at the element level but solved through the global stiffness matrix. Differently from the EFEM, the XFEM ensures the crack path continuity, which can be represented either explicitly, with piecewise straight/planar segments or, in a more elegant way, by means of level sets. However, crucial features of this method regard the integration schemes to be adopted in the enriched elements (Ventura, 2006; Gracie et al., 2008; Ventura and Benvenuti, 2015) and the treatment of the so-called blending elements, i.e. those elements adjacent to the enriched ones (Chessa, 2003; Fries, 2008). The accuracy of the results and the robustness of the procedure depend drastically on these aspects.

The computational strategies just described represent the most popular techniques to deal with strong discontinuitites in a finite element environment, but they are not the only ones. For more details about the procedures just mentioned and for other approaches, as meshless and particle methods, the following reviews are suggested (Dias-da-Costa, 2010; Rabczuk, 2013; Belytschko et al., 2009). These discontinuous approaches for modelling cracking in quasi-brittle materials are characterized by a high degree of complexity and a high number of variables, which make them not computationally efficient and not practical for large-scale analyses. In addition, almost all of them require the adoption of local or global crack tracking schemes (Areias and Belytschko, 2005; Riccardi et al., 2017; Zhang et al., 2015), in order to describe the advance of the defects avoiding spurious mesh

dependence. Withouth tracking, the remeshing in the interface-separation elements, as well as the progressive element enriching in EFEM and XFEM, performed on the base of not sufficiently accurate information provided by standard displacement based formulations, would be strongly mesh dependence. This adds complexity to the finite element method implementation and requires further computational resources.

The discrete counterpart of the continuum weak discontinuities (Figure 1.2.b) is represented by continuous approaches for modelling cracking, which can be named, according to the previous notation, as *discrete weak discontinuities* procedures or, as more commonly known, *smeared crack approaches*. Such a formulation was first proposed in the late sixties by Rashid (Rashid, 1968) and, thanks to its intrinsic simplicity of implementation, computational efficiency, possibility to be adopted in combination with other phenomena (viscosity, thermal problems, plasticity) has become the one favoured by commercial finite element codes and practitioners, especially for studying large-scale engineering problems. Indeed, the smeared crack approaches consider the cracked material as a continuum and model the deterioration at a constitutive level, reducing the stiffness and the strength. Consequently, the failure zones are not characterized by a jump in the displacement field but by the localization of the deformations, which remain however bounded. Several advantages derive from such a representation of cracking: the material behaviour can be described in terms of stress-strain constitutive laws, the failure criteria which identify the formation and the propagation of the defects can be established in terms of stress and strains, i.e. on the base of the continuum mechanics theory and the discretization can be used as it is, withouth the inclusion of discontinuity or remeshing.

In the framework of smeared crack approaches, a lot of constitutive models were developed in the 1980's (Bažant and Cedolin, 1983; Rots et *al.*, 1985; Bažant and Pfeiffer, 1986; Rots and De Borst, 1987; Cervera et *al.*, 1990). They are based on the decomposition of the strain tensor in an elastic and inelastic contribution: while the former is related to the stress tensor by means of linear elasticity, the latter is defined as work-conjugate to the traction vector normal to the crack. After the achievement of the peak strength, the material is treated as orthotropic, with different behaviours along the different principal stress directions.

Initially, *fixed crack models* were formulated, characterized by a frozen crack direction and by the use of a coefficient, named the retention factor, to deal with the shear transfers across the crack (Suidan and Schnobrich, 1973). Then, *rotating crack models* were proposed, which allow the crack direction to rotate and to be

always aligned with the current maximum principal strain direction (Cope et *al.*, 1980; Gupta and Akbar, 1984). Moreover, also the possibility of considering multiple non-orthogonal fixed cracks was taken into account in the so-called *multidirectional fixed crack models* (De Borst and Nauta, 1985).

One of the main drawbacks exhibited by the smeared crack approaches is represented by the stress locking, which is basically due to the poor kinematic representation of the discontinuous displacement field across the crack and is particularly evident when the mesh is misaligned with respect to the macroscopic crack orientation. Such an issue is more emphasized in fixed crack models with non null retention factor, because of the presence of shear stresses across the crack (Rots, 1988). Conversely, in rotating crack models, shear stresses are not produced across the crack, which is aligned with the maximum principal strain direction; therefore, such a problem is more limited. A remedy provided to the problem of stress locking is for instance described in (Jirásek and Zimmermann, 1998) and consists in the transition from a rotating crack model to a damage one. Although the damage model is based on a single scalar degradation variable *d*, the resulting constitutive matrix is not the one of an isotropic material but preserves the orthotropy of the smeared crack approach initially adopted.

In view of the above considerations, damage and plasticity models, incorporating strain softening, can be interpreted as a necessary evolution with respect to smeared crack procedures, in order to reduce stress locking. An insight on continuum damage mechanics and on the existing damage formulations, combined also with plasticity, is provided in Section 1.2.1. Such a deepening is necessary to understand the framework in which the damage model proposed in the present thesis for concrete and masonry structures fits in.

Another serious drawback of smeared crack approaches, emerged immediately after the first applications, is their pathological dependence on the size of the elements composing the discretization and on their alignement.

For what regards the objectivity of the results with respect to the mesh-size, in the 1970's it was noted that the energy dissipated during the cracking process is inversely proportional to the size of the finite elements: higher is the mesh refinement, lower is the dissipated energy, more brittle is the behaviour of the material. The limit case is represented by infinitesimally small elements, which do not dissipate energy at all as they crack.

Hillerborg and co-workers for the first time faced this problem in 1976, in a discrete strong discontinuity framework, formulating the fictitious crack model,

which ensures an objective representation of the dissipated energy by relating the loss of cohesion in the crack opening to the experimentally measurable fracture energy G_f (Hillerborg et *al.*, 1976). Then, the same concept was introduced in a smeared crack approach by Bažant and Oh (Bažant and Oh, 1983), who understood that, by rescaling the post-localization part of the local softening law on the base of the discretization length *h* (related to the size and orientation of the finite elements), the correct fracture energy G_f can be caught, independently of the mesh refinement. Hence, according to this formulation, named crack band model, the strain softening in a discrete environment should not be considered as a material feature only, because it has to be defined by means of the fracture energy, which is a material property, and the size of one-element band crossed by the smeared crack. Nowadays such an approach is well accepted in the research community and is also adopted in the commercial finite element softwares.

However, a still open issue regards the objectivity of the results with respect to the mesh-bias. Indeed, the crack band model is not able to prevent the dependence of the numerical failure pattern on the alignement of the discretization. A short review of the possible solutions for such a problem is provided in Section 1.2.2 and 1.2.3, which is functional to contextualize the proposed regularitazion technique adopted in the present thesis in conjunction with the continuum damage model.

1.2.1 Damage models for quasi-brittle materials

Continuum damage models, as smeared crack approaches, are characterized by their simplicity of implementation, versatility, computational efficiency, compatibilities with other theories (such as plasticity) and consistency in the framework of the thermodynamics of irreversible processes. All these features make their application to the structural analysis of masonry and concrete structures particularly adequate.

Continuum damage mechanics is based on the introduction of suitable internal variables in the constitutive law with the aim of simulating the elastic stiffness degradation and the strength decrease associated with the growth of microvoids and microcracks in the material. Starting from the precursor work of Kachanov (Kachanov, 1958), the study of the structural response of the nominal, real, cracked solid (*nominal configuration*) is possible by taking into account the behaviour of a fictitious one (*effective configuration*), which represents the intact material between defects. Such an undamaged solid has an effective resisting section reduced by the factor $(1 - d)$ with respect to the section of the real solid, with the damage variable *d* varying from 0 (undamaged state) to 1 (completely damaged state). Different

hypotheses exist to relate the nominal and the effective configurations and, depending on them, the form of the constitutive operator ruling the damage model changes. Simó and Ju, Mazars and Lemaitre, Caboche, Wu and Li, Faria and coworkers (Simó and Ju, 1987; Mazars and Lemaitre, 1985; Caboche, 1988a; Caboche, 1988b; Faria et *al*., 1998; Wu and Li, 2008) assume the strain equivalence between the effective and the nominal configurations; in (Simó and Ju, 1987) a stress-equivalent alternative is proposed. Finally, in (Cordebois and Sidoroff, 1982; Carol et *al*., 2001), both the strain and the stress tensors are different between the nominal and the effective configurations and the equivalence is established in terms of strain energy.

The essential mechanical features which need to be captured in the modelling of quasi-brittle materials are the following:

(i) degradation of the elastic stiffness and softening response in the post-peak regime, with reduction of the peak strength for increasing deformation levels;

(ii) accumulation of permanent deformations associated to intergranular displacement at a microscopic level;

(iii) non-symmetrical material behaviour between tension and compression due to different strengths and different fracture energies;

(iv) anisotropy induced in the material by the damage process, due to nucleation and evolution of planar microvoids "in the planar direction perpendicular to the maximum tensile strain" (Krajcinovic and Fonseka, 1981). Hence, except for the case of hydrostatic stress or strain conditions, isotropic models are incomplete in the description of damage, which is intrinsically an anisotropic phenomenon (Wu and Li, 2008), and drastically neglects the possibility of a strut action in the assessment of the structural capacity (De Borst, 2002). In (De Borst, 2002) it is noticed that, only with the recourse to orthotropic damage models, the original smeared crack approaches can be considered in the unified context of damage mechanics;

(v) microcrack closure-reopening (MCR) effects, i.e. partial or total stiffness recovery in the transition from tension to compression, crucial in cyclic conditions, experimentally documented for concrete in (Reinhardt, 1984; Reinhardt and Cornelissen, 1984).

Property (i) is satisfied by any damage model, because stiffness degradation and strain-softening represent the basis of damage mechanics.

Regarding the fulfillment of property (ii), several formulations combine damage with plasticity, as the ones proposed in (Simó and Ju, 1987; Lubliner et *al*.,

1989; Ju, 1989; Wu et *al*., 2006; Addessi et *al*., 2002; Contraffatto and Cuomo, 2006; Voyiadjis et *al*., 2008).

However, also damage models which do not take into account permanent deformations, or which define them in a simplified way, are able to provide a reliable mechanical response for a great variety of loading conditions, as observed in (Comi and Perego, 2001a), requiring also a reduced number of constitutive parameters. Among the others, some relevant contributions to the field of pure damage mechanics are presented in (Ortiz, 1985; Mazars and Pijaudier-Cabot, 1989; Faria et *al*., 1998; Comi and Perego, 2001a; Papa and Taliercio, 1996; He et *al*., 2015).

A general methodology to deal with property (iii) consists in considering different damage variables in tension and compression and in adopting an interface for distinguishing the response into tensile and compressive regimes.

Several authors have chosen as separating interface the trace of the strain tensor $I_1(\varepsilon)$ and their proposal results in tensile (d^+) and compressive (d^-) isotropic damage models, depending on the positive or negative sign of $I_1(\varepsilon)$ (Comi and Perego, 2001a; Contraffatto and Cuomo, 2006; Toti et *al*., 2015; He et *al*., 2015). These procedures take inspiration from the work presented in (Curnier et *al*., 1995), addressed to the formulation of constitutive elastic laws for bimodular materials, i.e. materials, as the cracked concrete or masonry, which have an asymmetric stiffness if loaded in tension or compression. In that work, the conditions to be fulfilled in correspondence with the separating interface (chosen as $I_1(\varepsilon) = 0$) are established; they regard the continuity of both the strain energy and the constitutive law. Specifically, it is observed that, to satisfy these conditions, only the volumetric part of the stiffness constitutive operator can vary across the interface while the shear component has to be maintained constant.

These necessary conditions are ensured by the damage models proposed by Comi and Perego, by Contraffatto and Cuomo and by He and collegues, while they seem to be neglected by Toti and co-workers. This is shown considering, on the one hand, the constitutive law proposed in (Comi and Perego, 2001a)

$$\sigma = \begin{cases} \sigma^+ = 2G \cdot (1-d^+) \cdot (1-d^-)\boldsymbol{e} + K \cdot (1-d^+) \cdot (1-d^-)I_1(\varepsilon)\boldsymbol{I} & I_1(\varepsilon) \geq 0 \\ \sigma^- = 2G \cdot (1-d^+) \cdot (1-d^-)\boldsymbol{e} + K \cdot (1-d^-)I_1(\varepsilon)\boldsymbol{I} & I_1(\varepsilon) \leq 0 \end{cases} \quad (1.1)$$

and, on the other hand, the constitutive law proposed in (Toti et *al*., 2015):

$$
\sigma = \begin{cases} \sigma^+ = \left(1-d^+\right)\left(2Ge + K \cdot I_1(\varepsilon)\mathbf{I}\right) & I_1(\varepsilon) \geq 0 \\ \sigma^+ = \left(1-d^-\right)\left(2Ge + K \cdot I_1(\varepsilon)\mathbf{I}\right) & I_1(\varepsilon) \leq 0 \end{cases} \tag{1.2}
$$

where G and K are the shear and bulk moduli of the undamaged material, e is the deviatoric elastic strain, $\mathbf{I}$ is the identity second order tensor and, withouth any loss of generality, irreversible deformations are considered null. While in the constitutive law expressed in Eq. (1.1), for $I_1(\varepsilon) = 0$, σ^- and σ^+ always coincide, the same does not hold in Eq.(1.2) for any stress-strain state, but only in the case of $\varepsilon = \mathbf{0}$.

However, it is worth noting that the respect of the conditions set in (Curnier et al., 1995) induce some non-negligible limitations in the modelling of the microcrack closure-reopening capabilities; indeed, in the transition from tension to compression in a uniaxial cyclic load history, only a partial stiffness recovery can be obtained, because of the necessity of maintaining unaltered the shear part of the constitutive operator. Moreover, this implies also that unilateral effects in shear cyclic conditions can not be modelled at all. Being the latter consideration true for all the d^+/d^- damage formulations based on the use of $I_1(\varepsilon) = 0$ as separating interface, it is possible to conclude that such a procedure is not adequate to model quasi-brittle materials accurately. Firstly, any form of damage-induced anisotropy can not be simulated (feature iv); secondly, microcrack closure reopening effects in generic cyclic conditions, especially in shear, are absent (feature v).

Conversely, as pointed out by Wu and Xu (Wu and Xu, 2013), those formulations based on the spectral decomposition of a specific second order tensor (the stress or the strain one) are able to reproduce contemporarily damage-induced anisotropy (feature iv) and unilateral effects (feature v). The separating interface, in such models, is actually represented by the eigenvalues of the second order tensor. This approach, used for the first time in the pioneering work of Ortiz (Ortiz, 1985), introduces in the constitutive law two fourth-order projection operators, which extract the positive and negative tensor counterparts. A classification of these damage formulations can be performed depending on the nature of the damage variables used in conjunction with the spectral decomposition: one or more scalar damage variables are adopted in (Cervera et al., 1995; Cervera et al., 1996; Faria et al., 1998; Mazars et al., 1990; Wu et al., 2006) whereas models based on second- or fourth-order tensors are presented in (Ortiz, 1985; Simo and Ju, 1987; Ju, 1989; Yazdani and Schreyer, 1990; Carol and Willam, 1996; Papa and Taliercio, 1996; Cicekli et al., 2007; Voyiadjis et al., 2008).

The use of the second set of damage models is avoided in practical applications, because they need the monitoring of more variables, due to the anisotropy of damage itself, requiring a high number of input parameters and significant computational resources. Consequently, the first set of damage models are usually preferred in large-scale analysis. However, some limitations derive from the adoption of scalar damage variables combined with the spectral decomposition approach and they are highlighted in the following paragraph.

Regarding the topic of damage-induced anisotropy, a restricted form of orthotropy is described using scalar degradation quantities, since only the projection operators performing the spectral decomposition are responsible for the directionality of the stiffness reduction. Moreover, it is worth noting that the orthotropic constitutive operators proposed in (Cervera et $al.$, 1995; Cervera et $al.$, 1996; Faria et $al.$, 1998; Wu et $al.$, 2006) are not endowed with both major and minor symmetries, and this represents a lack of thermodynamic consistency as well as a shortcoming in computational terms. Very recently, such an issue has been addressed also in (Wu and Cervera, 2017); there, to achieve the major and minor symmetries of the constitutive operator, a new projection fourth-order tensor, defined in energy-norm, is proposed.

Regarding the description of MCR effects, the spectral decomposition approach combined with the adoption of scalar damage variables is effective only in specific cyclic conditions, characterized by alternating tensile and compressive regimes. This can be shown with reference to the illustrative case of a bar cyclically loaded first in tension and then in compression (Figure 1.3.a). The unilateral effects, visible in the stress-strain response in Figure 1.3.d, are modelled thanks to the spectral decomposition which allows one to consider the axial stiffness first affected by d^+ in tension and then unaffected in compression, upon loading reversal.

Although the unilateral behaviour is adequately taken into account in a 1D tension-compression cyclic history or in bending-dominated cyclic problems (as shown in (Faria et $al.$, 2004)), the stiffness recovery in presence of cyclic shear can not be captured. This is not due to the necessity of maintaining unaltered the shear stiffness component across the separating interface, condition which holds only for the isotropic damage formulations based on the use of $I_1(\varepsilon) = 0$. The motivation is different and is explained by considering the problem shown in Figure 1.4.a, involving shear cyclic conditions. During the loading stage (Figure 1.4.b), the internal variable d^+, related to the opening of microcracks perpendicularly to the current maximum tensile direction $\boldsymbol{p_{max}}$, grows up to the value d_I^+. After the loading reversal, at the beginning of the reloading stage (Figure 1.4.c), the value d_I^+ is

assigned once again to the current p_{max}, which is actually an intact direction, and, consequently, no stiffness recovery is exhibited in the structural response (Figure 1.4.d).
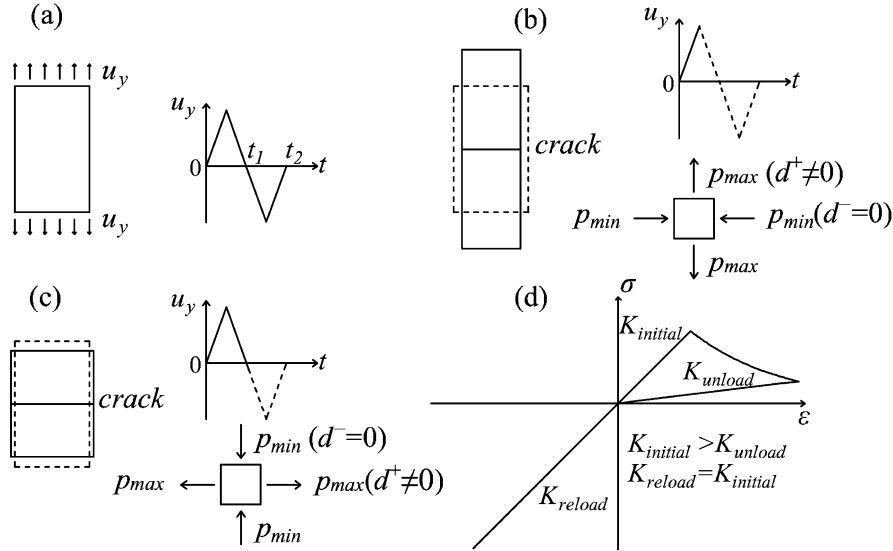
Figure 1.3: Successful modelling of unilateral effects in a 1D cyclic history resulting from the adoption of scalar damage models combined with spectral decomposition.
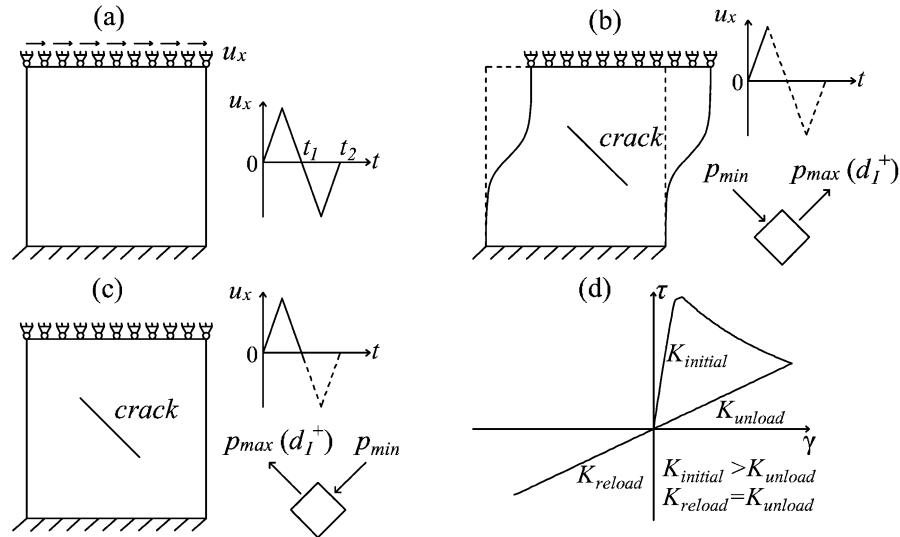
Figure 1.4: Unsuccessful modelling of unilateral effects in presence of cyclic shear resulting from the adoption of scalar damage models combined with spectral decomposition.

In other words, due to the scalar nature of the damage variables, the formulation is not able to associate a damage value to a physical direction and this translates in

the incapability of dealing with closure and reopening of orthogonal (or however intersecting) cracks, typical of shear cyclic conditions.

The majority of the existing models tend to neglect the problem of reproducing MCR effects in generic cyclic conditions, focusing only on the stiffness recovery capabilities exhibited by the damage models in cyclic uniaxial conditions. Among the few works aware of such an issue, it is worth mentioning the ones presented in (Silva et *al*., 2012; Saloustros et *al*., 2017a). In the former, the underestimation of the dissipation capacity and the non-realistic description of the unloading stiffness deriving from the use of a d^+/d^- damage model are underlined with reference to masonry panels under cyclic in-plane shear. In the latter, a procedure to capture the orthogonal cracks typical of cyclic shear loading by means of enhanced tracking algorithms is proposed.

1.2.2 Regularized techniques to ensure mesh objectivity

In a displacement-based finite element framework, the use of regularization techniques in the modelling of quasi-brittle materials with a smeared crack approach has been proposed to ensure the mesh-objectivity of the results. Specifically, as mentioned in Section 1.2, the crack band approach is able to guarantee only mesh-size independence but not mesh-bias independence, hence alternative (or additional) techniques have been proposed in the last three decades to solve such an issue.

One of the first developed regularization scheme is represented by the nonlocal integral procedure, proposed in its initial version for damage formulations in (Pijaudier-Cabot and Bažant, 1987) and later assimilated also in (Bažant and Lin, 1988; Bažant and Pijaudier-Cabot, 1988). Only subsequently, the nonlocal procedure has been extended to plasticity, for instance in (Tveergard and Needleman, 1995; Jirásek and Rolshoven, 2003).

Such an approach consists in replacing inside the mechanical model a variable evaluated at a given point x with its spatial averaging on a certain neighbourhood of x, considering the size of the interaction domain defined by means of an internal length l_{RG}. The variables subjected to the nonlocal averaging can be either scalars, such as the damage energy release rates or the damage variables themselves, or, less frequently, tensors, such as the elastic strain tensor or the inelastic strain associated to cracking. An exhaustive review of nonlocal damage models is proposed in (Bažant and Jirásek, 2002).

Contemporarily to the nonlocal integral approach, another procedure, named gradient-enhanced approach, was identified in the eighties to perform a regularization of the strain localization, first applied in plasticity (Aifantis, 1984; De Borst and Muhlhaus, 1992) and then extended to damage (Peerlings et *al.*, 1996; Geers et *al.*, 1998; Comi, 1999). These gradient-enhanced formulations are based on the idea of considering the constitutive law affected by higher-order deformation gradients, which can enter the equilibrium equations explicitely (explicit gradient enhanced models) or in an implicit way, by means of an additional partial differential equation (implicit gradient enhanced models).

More recently, phase field models have been introduced (Miehe et *al.*, 2010; Kuhn and Müller, 2010; Vignollet et *al.*, 2014); they depart from a strong discontinuity description of fracture and regularize it by replacing, in a mathematically consistent way, the zero-width discontinuity with a small finite zone with sharp gradients.

In all these approaches (nonlocal, gradient-enhanced, phase field formulations) a length scale is embedded in the continuum, in order to act as "strain localization limiter" and to avoid an energy dissipation which tends to zero with the progressive mesh refinement. Besides the correct representation of the dissipated energy, this implies also the objectivity of the results independently of the mesh-alignement. It is worth noting that the nonlocal integral approach appears the simplest way to introduce the localization limiter concept. The other two regularized formulations introduce the length scale in a less transparent way and they have in common the solution of an additional partial differential equation due to the inclusion of spatial derivatives in the energy functional (De Borst and Verhoosel, 2016). The higher mathematical complexity of these formulations with respect to the nonlocal integral ones does not correspond to clear advantages. On the one hand, as observed in (Peerlings et *al.*, 2001), the solutions obtained with implicit gradient-enhanced schemes and nonlocal ones are almost equivalent and this can be explained by the fact that the former formulation can be rewritten in the integral format proper of the latter. On the other hand, the use of a phase-field approach is difficult in the case of generic constitutive laws, characterized by anisotropy, microcrack closure-reopening effects and distinct degradation variables in tension and compression.

A clear interpretation of the internal length introduced by all these regularization techniques is not provided by consulting the existing literature. As stressed in (Bažant and Jirásek, 2002), the majority of the formulations relates it to the heterogeneity maximum size of the material. However, such a physical interpretation of the nonlocal length can be argued.

Firstly, this interpretation could compromise the monitoring of the progressive loss of cohesion on the bases of the fracture energy. The use of fracture energy as a material parameter represents one of the foundation of crack modelling (Hillerborg et *al.*, 1976; Bažant and Oh, 1983) and is a standpoint shared by both fracture mechanics and continuum mechanics. Secondly, it could limit the application of the regularized damage models to other materials than concrete. Indeed, if for concrete a large number of studies have been performed, for instance in (Bažant and Pijaudier-Cabot, 1989), and a value of approximately 3 times the aggregate size has been found to be the characteristic one for the internal length, for other materials, as masonry, likewise data are not available. Moreover, cracking in homogeneous materials can not be studied in this way, due to the impossibility of finding a physical definition of the internal length.

Only very recently, the consideration of the nonlocal length as a pure regularization parameter has been proposed in (Wu, 2017). According to this reinterpretation, the different formulations (nonlocal, enhanced gradients, phase fields models) can be seen as regularized versions of the smeared approach, in which the internal length plays the role of localization limiter acting as a regularization parameter. This is sketched in Figure 1.5, where the strong discontinuity of Figure 1.2.a or the localization band of Figure 1.2.b are substituted by a regularized localization band.
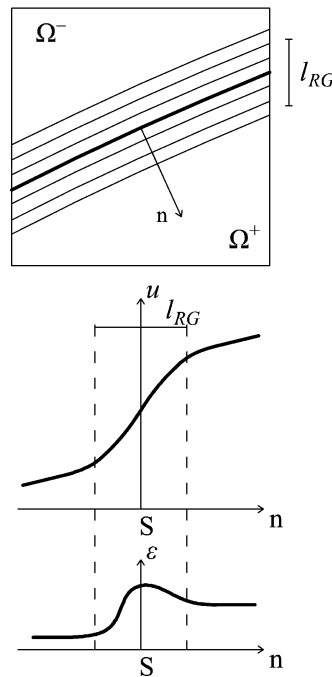
Figure 1.5: Continuum regularized localization band and localization limiter.

Note that the regularization procedure eliminates both the strong discontinuity of the displacement field in $\mathbf{S}$ and the two weak discontinuities of the strain field in $\mathbf{S^-}$ and $\mathbf{S^+}$. Note also that the regularization length l_{RG} is not equal to the width of the localization band, as there is not a clear cut band in the regularized approach, but they are related. The link between the discontinuous (Figure 1.2.a), the smeared (Figure 1.2.b) and the regularized (Figure 1.5) approaches should be the dissipation of the fracture energy.

1.2.3 Alternatives to ensure mesh objectivity

An alternative to these regularization techniques consists in the use of tracking algorithms. These procedures are able to circumvent the problem of mesh-bias dependence of the numerical strain localizations not only in a strong discontinuity approach, but also in a weak discontinuities (smeared) one (Cervera and Chiumenti, 2006; Slobbe et al., 2014). Indeed, in a smeared setting, the automatic application of the crack criteria to define also the direction of propagation leads to unacceptable errors, due to the fact that the strain and stress fields, in correspondence with the discontinuity, are far from being exact in a displacement-based finite element environment. The recourse to tracking algorithms reduces such local errors, while providing also a realistic representation of cracking, with damage that localizes in a narrow band of the discretization. A recent application of smeared crack approaches enriched with tracking algorithms for the structural analysis of masonry structures is presented in (Saloustros et al., 2017a; Saloustros et al., 2017c), where 2D problems are analyzed. In fact, the main limitation of tracking algorithms lies in the difficult extension to 3D problems, and this discourages their use in most engineering problems.

Finally, a completely novel approach to deal with strain localization both using plasticity and damage constitutive laws has been developed in the recent years by Cervera and co-workers (Cervera et al., 2010a; Cervera et al., 2010b; Cervera et al., 2015; Cervera et al., 2017; Barbat et al., 2018). They propose to replace the displacement-based finite element framework with a mixed displacement-strain finite element one, where strains are computed independently of the displacement field in each finite element. The enhancement in the kinematics of standard finite elements provides more accurate stress and strain fields, and consequently this results in a reliable prediction of the failure patterns, almost mesh-independent. To ensure the correct energy dissipation, mesh-size adjusted softening moduli are adopted, in accordance with the crack band approach. It is noted that a mixed displacement-strain approach which uses continuous interpolations both for

displacements and strains derives the local calculation of strains at a point from an nodal set which is enlarged with respect to the standard approach. In some way, it is a smeared approach with enhanced continuity, where the localization limiter is related to the element size.

1.3 Objective of the thesis

On the basis of the State-of-the-Art review proposed in Section 1.2, the present thesis is addressed to develop a new damage model for the structural analysis of masonry and concrete structures with a twofold objective: (a) to improve the modelling of damage-induced orthotropy and microcrack closure-reopening effects in the framework of scalar damage mechanics and (b) to provide a regularization technique independent of the definition of a physical internal length.

The starting point of the new formulation is represented by the d^+/d^- model first introduced in (Faria and Oliver, 1993; Cervera et *al*., 1995; Cervera et *al*., 1996), described in depth in (Faria et *al*., 1998) and then extended to plasticity in (Wu et *al*., 2006), hereafter termed the "original" d^+/d^- model. It is based on the split of a second order tensor, specifically the effective stress one, and on the use of two scalar damage quantities, d^+ and d^-, in order to distinguish tension from compression.

The interest for this model derives from the fact that it combines an adequate nonlinear structural response and algorithmic efficiency, its implementation and use in standard finite element codes being relatively easy. Confirmation of its effectiveness can be found in the several structural applications in which it has been satisfactorily adopted: for the seismic analysis of concrete dams (Faria et *al*., 1998), in the assessment of reinforced concrete structures subjected to cyclic loading (Faria et *al*., 2004), for the characterization of the in-plane (Silva et *al*., 2017) and out-of-plane (Petracca et *al*., 2017) behaviour of masonry panels, in the evaluation of historical masonry structures (Roca et *al*., 2012) and in the macro-modelling of masonry, combined with a tensor mapping procedure (Pelà et *al*., 2011; Pelà et *al*., 2013) or with tracking algorithms (Saloustros et *al*., 2017a; Saloustros et *al*., 2017c).

On the one hand, despite the abundant research work delving into the topic of continuum damage mechanics, some specific aspects related to its application to quasi-brittle materials require further investigation. In fact, as commented in Section 1.2.1, at a *constitutive* level, the original damage model could be improved

both in terms of damage-induced orthotropy and in terms of microcrack-closure reopening effects.

Regarding the former aspect, thermodynamic and practical reasons require the constitutive stiffness operator to be positive definite and endowed with both major and minor symmetries. The fullfilment of these features leads to the formulation of a new d^+/d^- damage model based on the energy equivalence assumption. Such a choice ensures full thermodynamic consistency, reflects in the formulation of a stable orthotropic damaged material and allows to adopt a symmetric global stiffness matrix to solve the algebraic system of equilibrium equations.

Regarding the latter, the lack of information about damage orientation, resulting in the absence of unilateral effects under cyclic shear conditions (as shown in Figure 1.4), is comparable to the inability of the rotating crack models (Cope et al., 1980) to take into account the orientation of previous defects, as observed by Bažant (1983). To improve the MCR capabilities of the d^+/d^- damage formulation, the local constitutive behaviour of the material needs to incorporate some aspects which are instead proper of fixed crack models (Rots et al., 1985). To this end, a "multidirectional" damage procedure is proposed in the present thesis, which preserves memory regarding degradation directionality while maintaining unaltered the dependence of the stress tensor from only the scalars d^+ and d^-. This procedure ensures the represententation of the microcrack closure reopening effects in generic cyclic conditions; hence it is suitable also for seismic analysis.

On the other hand, the smeared crack formulation needs to be combined with a regularization technique to have mesh-independent results at a *structural* level, in a standard finite-element framework. Such results have been previously obtained with the original d^+/d^- damage model by adopting tracking algorithms (Pelà et al., 2014; Saloustros et al., 2015; Saloustros et al., 2017b).

Another alternative is here examined, with potential wider application also to 3D structures, which is the nonlocal intergral approach, characterized by its simplicity of formulation and implementation. The elastic strain tensor is identified as the variable to be averaged, in order to provide a smoothing of the kinematic field similar to the one performed by the mixed displacement-strain finite elements formulations. In this way, damage is driven by the regularized elastic strains and the dependence of the strain localization on the discretization is circumvented.

Moreover, the thorny issue of the definition of the internal length, discussed in Section 1.2.2, is faced, in order to show how the evaluation of the correct fracture energy is possible, independently of l_{RG}. This suggests that the obtained solution

can be released from the choice of the nonlocal internal length, which can be interpreted as a regularization parameter more than as a physical constant.

The validation of the proposed formulation is a necessary step in order to assess its predictive capabilities in terms of ultimate loads, failure patterns, energy dissipation capacity and also its mesh objectivity. Therefore, experimental tests on masonry, concrete and reinforced concrete structures subjected to both monotonic and cyclic loading conditions are numerically reproduced with the adoption of the new damage model, for establishing its reliability.

1.4 Outline of the thesis

The present thesis is outlined as follows.

In Chapter 2 the salient aspects of the original d^+/d^- model are briefly recalled and different possible definitions for a new consistent constitutive operator in a strain equivalence framework are explored. Then, the new d^+/d^- formulation is presented in detail and its thermodynamic consistency discussed. The main novelties of the damage model are put in evidence: the assumption of energy-equivalence between nominal and effective configuration for the derivation of a consistent fourth-order constitutive operator, the use of a coupled dissipative approach to describe the evolution of the internal variables and the proposal of new evolution laws for both damage and irreversible deformations.

Chapter 3 is devoted to the description of the multidirectional damage procedure, to be applied in presence of cyclic loadings, providing some parallels between this new approach and the fixed/rotating smeared crack concepts. Reflections on how to extend the formulation to the 3D case are however added. The section is enriched with the introduction of a smoothing function, addressed to increase the numerical robustness of the multidirectional procedure in the transition from an open to a close microcrack state (or viceversa). The enhanced microcrack closure reopening capabilities are highlighted by solving at a finite element level the problem of a panel subjected to in-plane cyclic shear, with and without the multidirectional approach.

In Chapter 4, the nonlocal regularization technique adopted in conjunction with the new constitutive model is described. Firstly, the choice of the elastic strain tensor as variable to be averaged is justified and the regularized extension of the proposed damage model is developed, underling the unaltered thermo-dynamic consistency of the formulation. Secondly, the issue of identifying the input parameters of the regularized model is addressed, with the intent of correctly

estimate the dissipated energy. In this context, particular attention is directed towards the nature of the internal length l_{RG}, which can be interpreted either as a regularization parameter or as a physical property.

The algorithmic implementation of the new constitutive law is proposed in Chapter 5, with the purpose of showing how the new energy-equivalent d^+/d^- formulation, combined with the inclusion of permanent deformations, with a multidirectional treatment of damage and with a regularized approach, allows following an efficient full strain-driven formalism. In the same chapter, details about the method chosen to solve the algebraic system of equations, that is the secant (Picard) one, are provided.

The damage formulation is validated in Chapter 6 and Chapter 7. To assess separately the enhancements deriving from the new constitutive law and the regularization technique, in Chapter 6 the new energy-equivalent damage model is adopted in its local version. Structural problems involving both monotonic and cyclic loading conditions are considered. Firstly, unreinforced concrete notched samples are solved under monotonic loading conditions to show the adequacy of the new damage formulation in fitting experimental results under pure tension, pure bending and mixed-mode bending. Secondly, a masonry wall and a reinforced concrete panel, both subjected to in-plane cyclic shear, are analyzed in order to highlight the enhanced dissipative behaviour ensured by the multidirectional damage approach in conjunction with permanent deformations. Some quantitative considerations regarding the numerical robustness of the model are also included.

In Chapter 7, the versatility of the regularized d^+/d^- damage model is exhibited by successfully studying a masonry arch and reinforced and unreinforced concrete elements. Besides the validation of the numerical results with experimental or analytical data, each example is exploited to highlight one or more features of the formulation: the mesh-size and mesh-bias independence of the results, the influence of the internal length l_{RG}, the effect of the choice of the variable to be averaged and the possibility to reproduce structural size effects.

Chapter 8 is addressed to investigate the adequacy of the regularized d^+/d^- damage model to assess the structural behaviour of a multi-span masonry arch bridge. The reference solution is represented by the laboratory tests carried out on a 1:5 scale model of a three-span arch bridge, subjected to a concentrated vertical load. After a short historical perspective on the structural analysis of masonry arch bridges, the numerical results are compared with the experimental ones in terms of load carrying capacity, post-peak response and failure mechanism. Moreover, the objectivity of the response with respect to the discretization is also verified, in order

to guarantee the reliability of the regularization technique even in large-scale applications.

Finally, in Chapter 9, the main contributions of the present thesis and some suggestions about how to extend the present work are briefly summarised.

Chapter 2

Energy-equivalent d^+/d^- damage model for quasi-brittle materials

In the present Chapter, the new continuum mechanical model formulated for describing the behaviour of quasi-brittle materials, including both the stiffness and strength degradation due to damage and the presence of irreversible deformations proper of plasticity, is presented. In order to represent these non-linear features in a consistent way, the framework of the irreversible thermo-dynamics with internal variables (Horstemeyer and Bammann, 2010) is taken into account. The internal scalar variables related to damage, d^+ and d^-, together with the spectral decomposition of a second order strain tensor, allow to simulate the asymmetrical behaviour typical of quasi-brittle materials under tension and compression, while the tensor internal variable ε_p represents the permanent strain accumulated during the loading history.

As underlined in the Introduction, the formulation of a "new" constitutive law is addressed to provide an enhancement of the "original" d^+/d^- damage formulation presented in (Faria et al., 1998). Therefore, the first section of this Chapter is devoted to briefly outline the salient aspects of the original formulation. Then, in the following sections, the new formulation is described in detail focusing on the main novelties of the damage model, which regard the assumption of energy-equivalence between the nominal and effective configurations for the derivation of a thermo-dynamic consistent fourth-order constitutive operator, the use of a coupled dissipative approach to describe the evolution of the internal variables d^+, d^- and ε_p

and the proposal of new evolution laws for both damage and irreversible deformations. Part of the work presented in this Chapter is included in (Cervera and Tesei, 2017) and in (Cervera et *al.*, 2018).

2.1 Original d^+/d^- damage formulation

2.1.1 Strain equivalence and constitutive law

The original d^+/d^- damage model is based on the notion of effective stress and on the hypothesis of strain equivalence. The effective stress $\bar{\sigma}$ and the effective strain $\bar{\varepsilon}$ are the stress and strain to which the undamaged material between microcracks is subjected; they are related by the fourth-order elastic tensor $\boldsymbol{D_0}$:

$$\bar{\sigma} = \boldsymbol{D_0} : \bar{\varepsilon} \qquad (2.1)$$

The nominal quantities $\boldsymbol{\sigma}$ and ε_e ($\varepsilon_e = \varepsilon - \varepsilon_p$) refer to an average of the corresponding effective quantities on the total surface of the material (including also microcracks); for instance, the nominal stress tensor is related to the effective one by means of a fourth-order tensor $\boldsymbol{A}$ dependent on damage:

$$\boldsymbol{\sigma} = \boldsymbol{A} : \bar{\sigma} \qquad (2.2)$$

The strain equivalence assumption, as formulated in (Simó and Ju, 1987; Lemaitre and Chaboche, 1978) asserts that: "the strain associated with a damage state under the applied stress $\boldsymbol{\sigma}$ is equivalent to the strain associated with its undamaged state under the effective stress $\bar{\sigma}$". In other words, it is considered by hypothesis that the nominal elastic strain and the effective one are equal ($\varepsilon_e = \bar{\varepsilon}$) and that only the nominal and the effective stress are different. Consequently, the effective stress of Eq. (2.1) can be rewritten as:

$$\bar{\sigma} = \boldsymbol{D_0} : \varepsilon_e \qquad (2.3)$$

The basic features of concrete that the original model reproduces are the following ones: (i) the development of irreversible deformations; (ii) the strongly asymmetrical behaviour under tension and compression; (iii) the microcrack closure-reopening (MCR) effects visible in the case of uniaxial cyclic actions, i.e., the stiffness recovery when passing from tension to compression and vice versa; and (iv) the anisotropy induced by the damage process in the material.

In order to represent the differences between the stress-strain envelops under tension and under compression, two independent scalar variables, one for tension

d^+ and one for compression d^-, are introduced. Moreover, to deal with points (ii), (iii) and (iv), a spectral decomposition of the effective stress tensor (Eq. (2.3)) into a positive and a negative part is carried out:

$$\bar{\sigma}^+ = \sum_{i=1}^{3} \langle \bar{\sigma}_i \rangle \boldsymbol{p_i} \otimes \boldsymbol{p_i} = \boldsymbol{Q} : \bar{\sigma}$$

$$\bar{\sigma}^- = \bar{\sigma} - \bar{\sigma}^+ = (\boldsymbol{I} - \boldsymbol{Q}) : \bar{\sigma} \tag{2.4}$$

where $\boldsymbol{p_i}$ is the eigenvector identifying the principal direction *i-th* of the effective stress tensor while the Macaulay brackets act on the *i-th* principal value of the effective stress tensor $\bar{\sigma}_i$ in such a way that: if $\bar{\sigma}_i$ is positive (tensile principal stress), $\langle \bar{\sigma}_i \rangle = \bar{\sigma}_i$; else (compressive principal stress) $\langle \bar{\sigma}_i \rangle = 0$. The fourth-order projection operator $\boldsymbol{Q}$, which extracts from the effective stress tensor its positive part, is:

$$\boldsymbol{Q} = \sum_{i=1}^{3} H(\bar{\sigma}_i) \boldsymbol{p_i} \otimes \boldsymbol{p_i} \otimes \boldsymbol{p_i} \otimes \boldsymbol{p_i} \tag{2.5}$$

and its explicit expression is given in (Faria et *al.*, 2000). $H(\bar{\sigma}_i)$ is the Heaviside function, such that, if $\bar{\sigma}_i$ is positive, $H(\bar{\sigma}_i) = 1$; else, $H(\bar{\sigma}_i) = 0$.

The constitutive law of the original model is written in terms of the spectral decomposition of the effective stress tensor (2.4) and has the following expression:

$$\sigma = \boldsymbol{D_S} : \varepsilon_e = \left(1 - d^+\right)\bar{\sigma}^+ + \left(1 - d^-\right)\bar{\sigma}^- \tag{2.6}$$

where $\boldsymbol{D_S}$ is the fourth-order secant stiffness operator (subscript "s" stands for strain equivalence), introduced in order to relate the nominal stress tensor σ to the nominal elastic strain tensor ε_e.

The versatility of the model in treating the damage-induced anisotropy is intrinsic in Eq. (2.6). In fact, depending on the sign of the principal effective stresses, two different cases can be distinguished:

- $\bar{\sigma}_i$ with concordant sign ($\bar{\sigma} = \bar{\sigma}^+$ or $\bar{\sigma} = \bar{\sigma}^-$): isotropy is preserved after damage, and an isotropic (tensile or compressive, respectively) damage model is recovered.

- $\bar{\sigma}_i$ with discordant sign: the damaged material is anisotropic, and the directions of maximum and minimum axial stiffness are coincident with the principal directions of the effective stress tensor.

As observed in (Cowin, 1994; Pedersen, 1989), the coaxiality between the reference system of the anisotropic material and the principal directions of the nominal strain ε_e is a particular condition in anisotropic elasticity, which corresponds to the extremization of the strain energy density. In addition, the maximization or minimization of the strain energy density implies the coaxiality between the nominal strain tensor ε_e and the nominal stress tensor σ. These observations lead to assert that the d^+/d^- formulation can be interpreted within the rotating smeared crack concept, due to the co-rotation of the axes of material anisotropy with the principal axes of the strain ε_e, which consequently coincide also with the principal axes of the stress σ.

2.1.2 Discussion on different constitutive operators based on strain equivalence

In (Faria et al., 1998), the constitutive law (2.6) is provided, but not the definition of the fourth-order secant stiffness tensor D_S relating the nominal stress σ and the nominal strain ε_e. In this section, this issue is addressed evaluating two different expressions for the secant stiffness D_S, both derived in the hypothesis of strain equivalence, i.e., considering the effective stress definition shown in Eq. (2.3). In order to guarantee thermo-dynamic consistency, two properties have to be fulfilled by the secant operator: major symmetry (in addition to the minor ones), as stated in (Faria et al., 1998) with reference to the Schwartz theorem about the equality of the mixed partial of the potential; positive definiteness, a major requirement in order to have a damaged orthotropic material with stable behaviour.

The first expression to be considered for the secant stiffness tensor, D_{S1}, is obtained by replacing in the constitutive law (2.6) the positive and negative parts of the effective stress tensor (2.4), expressed in terms of the positive projection operator Q (2.5):

$$\sigma = \left(1-d^+\right)\bar{\sigma}^+ + \left(1-d^-\right)\bar{\sigma}^- = \left(1-d^+\right)Q : D_0 : \varepsilon_e + \left(1-d^-\right)(I-Q) : D_0 : \varepsilon_e \quad (2.7)$$

From Equation (2.7), exploiting the distributive rule, the expression for D_{S1} is:

$$D_{S1} = \left(1-d^+\right)Q : D_0 + \left(1-d^-\right)(I-Q) : D_0 \quad (2.8)$$

Considering the constitutive law written in terms of $\boldsymbol{D_{S1}}$ (Eq. (2.8)) and referring to the relationships (2.2) and (2.3) for the nominal and effective stress tensors, respectively, the definition of the fourth-order operator $\boldsymbol{A}$ appearing in Eq. (2.2) is:

$$A = \left(1 - d^+\right)\boldsymbol{Q} + \left(1 - d^-\right)(\boldsymbol{I} - \boldsymbol{Q}) \tag{2.9}$$

Although both the projection operator $\boldsymbol{Q}$ (Eq. (2.5)) and the elastic fourth-order tensor $\boldsymbol{D_0}$ have major symmetry, this does not imply that the fourth-order tensor $\boldsymbol{D_{S1}}$ (2.8) resulting from their double contraction is necessarily endowed with major symmetry. Specifically, besides the undamaged situation ($\boldsymbol{D_{S1}} = \boldsymbol{D_0}$), the symmetry of the secant operator is guaranteed only when the Poisson's ratio is null or when an isotropic damage model is recovered, i.e., in the cases of purely tensile regimes or purely compressive regimes previously discussed.

Since the quadratic form associated with a non-symmetric matrix is equal to the quadratic form associated with its symmetric part only, the second expression to be evaluated for the constitutive operator, $\boldsymbol{D_{S2}}$, is the symmetric part of the non-symmetric operator $\boldsymbol{D_{S1}}$ (2.8):

$$\begin{aligned}
\boldsymbol{D_{S2}} &= \frac{1}{2}\left(\boldsymbol{D_{S1}} + \boldsymbol{D_{S1}^T}\right) = \\
&\frac{1}{2}\left(1 - d^+\right)\left[\boldsymbol{Q} : \boldsymbol{D_0} + \boldsymbol{D_0} : \boldsymbol{Q}\right] + \frac{1}{2}\left(1 - d^-\right)\left[(\boldsymbol{I} - \boldsymbol{Q}) : \boldsymbol{D_0} + \boldsymbol{D_0} : (\boldsymbol{I} - \boldsymbol{Q})\right]
\end{aligned} \tag{2.10}$$

However, for this second proposal, the positive definiteness cannot be proven. This is shown by resorting to Eq. (2.11), where the matrix form of $\boldsymbol{D_{S2}}$ is given in the principal reference system of orthotropy of the damaged material, in terms of the Lamé constants and the damage variables; a 3D stress state composed of two tensile directions and a compressive one is considered in such a way that two eigenvectors contribute in defining $\boldsymbol{Q}$ (Eq. (2.5)).

$$\begin{bmatrix}
(1-d^+)(2G+\lambda) & \left[(1-d^+)\lambda + (1-d^-)\lambda\right]/2 & (1-d^+)\lambda & 0 & 0 & 0 \\
\left[(1-d^+)\lambda + (1-d^-)\lambda\right]/2 & (1-d^-)(2G+\lambda) & \left[(1-d^+)\lambda + (1-d^-)\lambda\right]/2 & 0 & 0 & 0 \\
(1-d^+)\lambda & \left[(1-d^+)\lambda + (1-d^-)\lambda\right]/2 & (1-d^+)(2G+\lambda) & 0 & 0 & 0 \\
0 & 0 & 0 & (1-d^-)G & 0 & 0 \\
0 & 0 & 0 & 0 & (1-d^-)G & 0 \\
0 & 0 & 0 & 0 & 0 & (1-d^-)G
\end{bmatrix}$$

$$\tag{2.11}$$

Despite the evident symmetry of the matrix (2.11), it is easy to demonstrate its lack of positive definiteness by adopting Sylvester's criterion. In fact, analyzing the first principal minor of order two, equal to:

$$\Delta_2 = \left(1-d^+\right)\cdot\left(1-d^-\right)\left(2G+\lambda\right)^2 - \left[\left(1-d^+\right)+\left(1-d^-\right)\right]^2 \lambda^2/4 \qquad (2.12)$$

and considering $d^+= 1$ and $d^-= 0$, it follows that the quantity (2.12) is negative.

Therefore, the necessity of formulating a new version of the original d^+/d^- model derives mainly from the just described difficulties found in the definition of a consistent secant stiffness operator in a strain-equivalence framework. Consequently, in accordance with the discussion provided in (Carol et al., 2001) for a general anisotropic damage model, in the new d^+/d^- formulation presented henceforth, the strain equivalence assumption is abandoned in favor of assuming energy equivalence.

2.2 "New" d^+/d^- damage model based on energy equivalence

2.2.1 Symmetric constitutive operator

The hypothesis of energy equivalence (Cordebois and Sidoroff, 1982; Carol et al., 2001) consists in considering the coincidence between the energy stored in terms of the nominal quantities and secant stiffness and the elastic energy stored in terms of the effective quantities and undamaged linear elastic stiffness. This means that neither the nominal stress, nor the nominal elastic strain are equal to their effective counterparts; therefore, in addition to the relation (2.2) between the nominal and the effective stress, a relation between the effective and the nominal elastic strain is needed. Following the procedure described in (Carol et al., 2001), this relation is governed by the fourth-order tensor A introduced in Eq. (2.2) and is written as:

$$\bar{\varepsilon} = A : \varepsilon_e \qquad (2.13)$$

From the mechanical point of view, this lack of coincidence between the effective and the nominal strain tensor is essential in representing a fundamental feature of orthotropic damage models, i.e., the fact that the nominal Poisson's ratio does not remain constant throughout the damage process. Due to the adoption of the strain equivalence assumption, this feature is not taken into account by the original model.

Exploiting Eqs. (2.1) and (2.13), the effective stress tensor, expressed as a function of the nominal elastic strain ε_e, is:

$$\bar{\boldsymbol{\sigma}} = \boldsymbol{D_0} : \bar{\boldsymbol{\varepsilon}} = \boldsymbol{D_0} : A : \boldsymbol{\varepsilon_e} \tag{2.14}$$

For the damage model described in (Faria et al., 1998), the operator A relating the nominal and the effective stress is the one expressed in Eq. (2.9). Herein, some minor modifications with respect to Eq. (2.9) are introduced for the definition of this fourth-order tensor, even though its fundamental dependence on the damage variables and on a spectral projection operator is maintained. Firstly, the integrity quantities in tension and in compression $(1 - d^+)$ and $(1 - d^-)$ are replaced by their square roots, in order to keep comparable the amount of stiffness degradation between the original model and the new one. Secondly, the quantity on which the decomposition is performed is no longer the effective stress, as done in Eqs. (2.4) and (2.5): the reason lies in the dependence of $\bar{\sigma}$ obtained in an energy-equivalence framework (see Eq. (2.14)) on the fourth-order tensor A (hence, on the projection operator and on the damage variables), which would make the procedure of the definition of the projection operator iterative. Consequently, the nominal strain tensor ε_e is chosen as the variable object of the spectral decomposition, similarly to what is done in (Ortiz, 1985); in this way, the algorithmic efficiency related to a strain-based formulation, one of the attractiveness of the original model, is kept unchanged. In addition, a definition for the projection operator slightly different from Eq. (2.5) is here preferred. Specifically, a tensor first introduced in (Carol and Willam, 1996) and then presented again in (Wu and Xu, 2013) is adopted; its expression is:

$$\boldsymbol{Q} = \sum_{i=1}^{3} H\left(\varepsilon_{ei}\right)\boldsymbol{p_i} \otimes \boldsymbol{p_i} \otimes \boldsymbol{p_i} \otimes \boldsymbol{p_i} + \sum_{\substack{i,j=1 \\ j>i}}^{3} \left(H\left(\varepsilon_{ei}\right) + H\left(\varepsilon_{ej}\right)\right)\boldsymbol{P^{ij}} \otimes \boldsymbol{P^{ij}} \tag{2.15}$$

$$\boldsymbol{P^{ij}} = \boldsymbol{P^{ji}} = \frac{1}{2}\left(\boldsymbol{p_i} \otimes \boldsymbol{p_j} + \boldsymbol{p_j} \otimes \boldsymbol{p_i}\right) \tag{2.16}$$

where ε_{ei} and $\boldsymbol{p_i}$ are the i-th principal value and the eigenvector associated with the i-th principal direction of the nominal elastic strain tensor $\boldsymbol{\varepsilon_e}$. $H(\varepsilon_{ei})$ is the Heaviside function, such that, if ε_{ei} is positive, $H(\varepsilon_{ei}) = 1$; else, $H(\varepsilon_{ei}) = 0$.

This projection operator does not alter the positive and negative components extracted from the strain tensor, which are exactly the same obtained adopting the conventional $\boldsymbol{Q}$ (2.5). The advantage of using it lies in the fact that, when all the

strain eigenvalues ε_i are of the same sign, Q (2.15) satisfies the so-called natural property. For a generic fourth-order projection operator P that performs a spectral decomposition on a second-order tensor a, this property can be written in the following way:

$$\begin{cases} P^+ = I & \text{iff } a_i \geq 0 & (\forall i = 1,2,3) \\ P^- = I & \text{iff } a_i < 0 & (\forall i = 1,2,3) \end{cases} \tag{2.17}$$

The satisfaction of property (2.17) is discussed in (Ju, 1989; Carol and Willam, 1996).

Referring to Eq. (2.9) and applying the mentioned minor modifications, the proposal A^* for the fourth-order tensor A, appearing in Eqs. (2.13) and (2.14), is:

$$A^* = \sqrt{1 - d^+}\, Q + \sqrt{1 - d^-}\, (I - Q) \tag{2.18}$$

where Q is the one expressed in Eq. (2.15). In view of this definition, the relations (2.2), (2.13) and (2.14) between the nominal and the effective quantities in an energy-equivalent framework can be re-written as:

$$\sigma = A^* : \bar{\sigma} \tag{2.19}$$

$$\bar{\varepsilon} = A^* : \varepsilon_e \tag{2.20}$$

$$\bar{\sigma} = D_0 : \bar{\varepsilon} = D_0 : A^* : \varepsilon_e \tag{2.21}$$

Making use of relations (2.20) and (2.21), the equality between the strain energy in the effective and in the real configuration is:

$$\frac{1}{2}\bar{\sigma} : \bar{\varepsilon} = \frac{1}{2}\varepsilon_e : A^* : D_0 : A^* : \varepsilon_e = \frac{1}{2}\varepsilon_e : D_E : \varepsilon_e \tag{2.22}$$

From Eq. (2.22), the form of the secant stiffness fourth-order tensor D_E (subscript "$_E$" stands for energy equivalence) is derived:

$$D_E = A^* : D_0 : A^* \tag{2.23}$$

By replacing the definition of A^* in Eq. (2.23), the complete expression for the secant matrix D_E is:

$$D_E = \left[\sqrt{1-d^+}\,Q + \sqrt{1-d^-}\,(I-Q) \right] : D_0 : \left[\sqrt{1-d^+}\,Q + \sqrt{1-d^-}\,(I-Q) \right] \qquad (2.24)$$

A similar secant stiffness operator, obtained under the same assumption of energy equivalence, can be found in (Voyiadjis et al., 2008): there, the projection operator is adopted in its classical form (analogously to Eq. (2.5)), and the split is performed on the nominal stress tensor σ, which, as mentioned earlier, makes the definition of the projection operator iterative.

From Equation (2.24), some immediate considerations can be done. Firstly, in the absence of damage, the linear elastic stiffness tensor D_0 is recovered. Secondly, Eq. (2.23) shows how, due to the major symmetry of the tensor A^*, the hypothesis of energy equivalence (2.22) induces automatically major symmetry in the secant stiffness tensor D_E.

In addition, the versatility of the original model in treating the damage-induced anisotropy is preserved in the new formulation. As a matter of fact, in the case of ε_{ei} with concordant sign ($\varepsilon_e = \varepsilon_e^+$ or $\varepsilon_e = \varepsilon_e^-$), an isotropic damage model is regained, while in the case of ε_{ei} with discordant sign, the damaged material is orthotropic, and the coaxiality between the directions of induced orthotropy and the principal directions of the strain and stress tensors is assured. The differences between the decomposition performed by the original formulation and the new one are sketched in Figure 2.1, where the isotropic model is distinguished by the orthotropic one in the principal reference system of the elastic stress tensor σ_e:

$$\sigma_e = D_0 : \varepsilon_e \qquad (2.25)$$
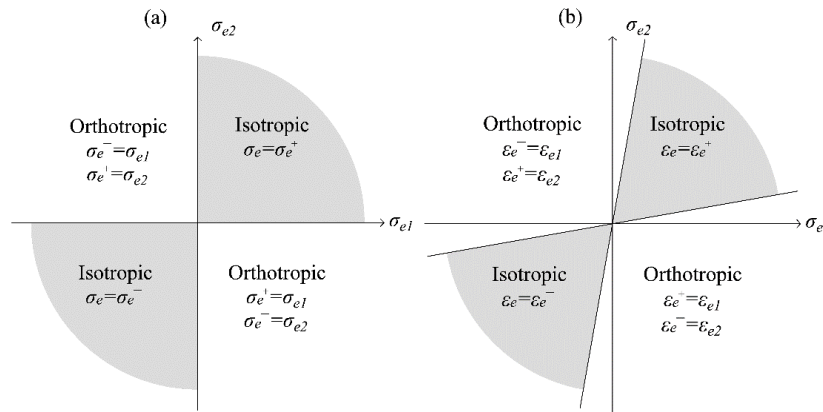
Figure 2.1: Spectral decompositions (a) of the original damage formulation (Faria et al., 1998) and (b) of the new one, in plane stress conditions.

Such a stress quantity coincides with the effective stress tensor only for the original formulation by (Faria et *al.*, 1998), as confirmed by Eq. (2.3). Contrariwise, for the new formulation, due to the energy-equivalence assumption, the effective stress tensor has a different expression (see Eq. (2.21)). Analyzing Figure 2.1, it is clear that the spectral decomposition on the elastic strain tensor (Figure 2.1.b) allows to describe the problem of uniaxial loading by means of an orthotropic formulation, instead of an isotropic one. This fact, combined with the use of the new orthotropic constitutive operator (2.24), implies that the variation of the nominal Poisson's ratio, related to microcracking, can be modelled. This fact is discussed in detail in Section 2.2.3.

The matrix form of the secant stiffness operator $\boldsymbol{D_E}$ is given in Eq. (2.26) in the principal reference system of orthotropy of the damaged material. As done for the expression of the matrix form of $\boldsymbol{D_{S2}}$ (2.11), a 3D strain state composed of two elongation directions and a contraction one is considered:

$$
\begin{bmatrix}
(1-d^+)(2G+\lambda) & \left(1-d^-\right)^{0.5}\left(1-d^+\right)^{0.5}\lambda & \left(1-d^+\right)\lambda & 0 & 0 & 0 \\
\left(1-d^-\right)^{0.5}\left(1-d^+\right)^{0.5}\lambda & (1-d^-)(2G+\lambda) & \left(1-d^-\right)^{0.5}\left(1-d^+\right)^{0.5}\lambda & 0 & 0 & 0 \\
\left(1-d^+\right)\lambda & \left(1-d^-\right)^{0.5}\left(1-d^+\right)^{0.5}\lambda & (1-d^+)(2G+\lambda) & 0 & 0 & 0 \\
0 & 0 & 0 & \left[\left(1-d^-\right)^{0.5}+\left(1-d^+\right)^{0.5}\right]^2 G/4 & 0 & 0 \\
0 & 0 & 0 & 0 & \left[\left(1-d^-\right)^{0.5}+\left(1-d^+\right)^{0.5}\right]^2 G/4 & 0 \\
0 & 0 & 0 & 0 & 0 & \left(1-d^+\right)G
\end{bmatrix}
$$

(2.26)

First of all, it is interesting to note how the stiffness matrix associated with the operator $\boldsymbol{D_E}$ here derived fits perfectly within the framework described in (Carol et *al.*, 2001), based on the hypotheses of energy equivalence and sum-type symmetrization. Differently from a generic orthotropic material, which is characterized by nine independent material properties, the secant stiffness matrix defined in Eq. (2.26) depends on four variables (the two elastic constants G and λ of the initial isotropic material and the two damage variables d^+ and d^-). This aspect is strictly related to one of the particularities of this formulation, i.e., the coaxiality between directions of induced orthotropy and principal directions of nominal elastic strain and stress tensors.

Moreover, considering the shear stiffness terms in matrix (2.26), it is possible to see that the shear modulus G is reduced by the square of the average of both

$\left(1 - d^+\right)^{0.5}$ and $\left(1 - d^-\right)^{0.5}$. This constitutes a modification with respect to the secant operators $\boldsymbol{D}_{S1}$ and $\boldsymbol{D}_{S2}$ (see Eq. (2.11)), due to the adoption of the projection operator $\boldsymbol{Q}$ (2.15) instead of $\boldsymbol{Q}$ (2.5); the main positive implication deriving from this choice is the recovery not only of the constitutive law, but also of the secant stiffness matrix of an isotropic damage model, when $\varepsilon_e = \varepsilon_e^+$ or $\varepsilon_e = \varepsilon_e^-$.

Besides an evident symmetry visible in Eq. (2.26), the stiffness operator $\boldsymbol{D}_E$ (2.24) is also positive definite, and this can be checked, without loss of generality, by applying Sylvester's criterion to its matrix form (2.26). In fact, as demonstrated by the relations (2.27), all of the minors of (2.26) are always positive, provided that the damage variables range from zero (virgin material) to one (completely damaged material):

$$\Delta_1 = D_{E11} = \left(1 - d^+\right)\left(2G + \lambda\right) \geq 0$$

$$\Delta_2 = D_{E11}D_{E22} - D_{E12}^2 = \left(1 - d^+\right)\left(1 - d^-\right)\left(2G + \lambda\right)^2 - \left(1 - d^+\right)\left(1 - d^-\right)\lambda^2 \geq 0$$

$$\Delta_3 = \left(D_{E11}D_{E22} - D_{E12}^2\right)D_{E33} - D_{E23}^2 D_{E11} + 2D_{E23}D_{E12}D_{E13} - D_{E13}^2 D_{E22}$$

$$= \left(1 - d^+\right)^2\left(1 - d^-\right)\left(2G + \lambda\right)^3 - \left(1 - d^+\right)^2\left(1 - d^-\right)\left(2G + \lambda\right)\lambda^2 - \left(1 - d^+\right)^2\left(1 - d^-\right)\left(2G + \lambda\right)\lambda^2 +$$

$$+ 2\left(1 - d^+\right)^2\left(1 - d^-\right)\lambda^3 - \left(1 - d^+\right)^2\left(1 - d^-\right)\left(2G + \lambda\right)\lambda^2 \geq 0$$

$$\Delta_4 = \Delta_3 D_{E44} = \Delta_3 G\left(0.5\left(1 - d^+\right) + 0.5\left(1 - d^-\right)\right)^2 \Big/ 4 \geq 0$$

$$\Delta_5 = \Delta_3 D_{E44}D_{E55} = \Delta_3 G^2\left(0.5\left(1 - d^+\right) + 0.5\left(1 - d^-\right)\right)^4 \Big/ 16 \geq 0$$

$$\Delta_6 = \Delta_3 D_{E44}D_{E55}D_{E66} = \Delta_3 G^3\left(1 - d^+\right)\left(0.5\left(1 - d^+\right) + 0.5\left(1 - d^-\right)\right)^4 \Big/ 16 \geq 0$$

$$(2.27)$$

Therefore, the new d^+/d^- damage model, based on the hypothesis of energy equivalence, is governed by the secant stiffness operator $\boldsymbol{D}_E$ (2.24), which is symmetric and positive definite; consequently, it provides an adequate representation of the damage-induced orthotropy.

To sum up, the relationships between the effective and the nominal configuration deriving from the energy equivalence assumption, together with the constitutive laws proper of each space, are summarized in Figure 2.2.

$$\sigma = A^* : \bar{\sigma}$$

$$\sigma \quad\quad \bar{\sigma}$$

Nominal orthotropic stress space   Effective isotropic stress space

$$\sigma = D_E : \varepsilon_e \quad\quad\quad\quad \bar{\sigma} = D_0 : \bar{\varepsilon}$$

Nominal orthotropic strain space   Effective isotropic strain space

$$\varepsilon_e \quad\quad \bar{\varepsilon}$$

$$\bar{\varepsilon} = A^* : \varepsilon_e$$
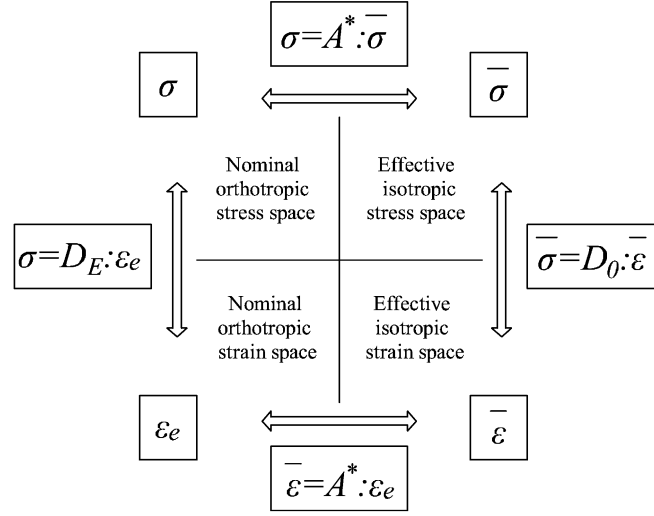
Figure 2.2: Energy equivalence hypothesis: relationships between effective and nominal spaces.

A further confirmation of the adequacy of the new constitutive operator (2.24) can be found in an interesting parallelism between the relationships shown in Figure 2.2, adopted to derive an orthotropic d^+/d^- damage model, and the mapping procedure presented in (Pelà et al., 2014) to define a damage model for orthotropic materials. In (Pelà et al., 2014), the stress σ and strain ε_e tensors of the orthotropic real space are related by means of suitable fourth-order symmetric transformation tensors to those (σ^* and ε^*, respectively) of an equivalent isotropic solid:

$$\sigma = \left(A^\sigma\right)^{-1} : \sigma^* \tag{2.28}$$

$$\varepsilon^* = A^\varepsilon : \varepsilon_e \tag{2.29}$$

Considering the equivalence between the orthotropic real space and the real damaged material (nominal σ and nominal ε_e) and between the mapped isotropic space and the effective undamaged configuration ($\bar{\sigma}$ and $\bar{\varepsilon}$), the similarity of Eqs. (2.28) and (2.29) with Eqs. (2.19) and (2.20) is evident. Specifically, in accordance with (Carol et al., 2001), in the present orthotropic damage model, the tensor $(A^\sigma)^{-1}$ and A^ε are coincident and equal to the mapping operator A^* (2.18). All the features required for the mapping operators $(A^\sigma)^{-1}$ and A^ε (fourth-order tensors, minor and major symmetry, positive definiteness in order to be invertible) are satisfied by A^*.

2.2.2 Thermo-dynamic consistency

In accordance with the energy equivalence assumption (2.22), the free energy potential of the orthotropic damage model here presented is the following:

$$\psi\left(\varepsilon_e, d^+, d^-\right) = \frac{1}{2}\varepsilon_e : \boldsymbol{D}_E : \varepsilon_e \qquad (2.30)$$

where the positive definiteness of the constitutive fourth-order tensor $\boldsymbol{D}_E$ (2.24) has been proven in Section 2.2.1.

In order to assess the thermo-dynamic consistency of the proposed model, the satisfaction of both the first and the second law of thermo-dynamics needs to be investigated.

On the one hand, the first law of thermo-dynamics for elastic-degrading materials demands considering the conservation of energy in the unloading-reloading regime, for a fixed state of degradation. As pointed out in (Carol and Willam, 1996; Wu and Xu, 2013), under those conditions and when non-proportional loadings are applied, damage models including micro-crack closure reopening (MCR) effects may suffer the problem of energy generation/dissipation under closed-load cycles. Specifically, only in the presence of anisotropic degradation, a lack of energy dissipation occurs. The here-formulated damage model is orthotropic in the sense that a directional degradation in stiffness is induced in the material after surpassing the linear threshold. From the definition of $\boldsymbol{A}^*$ (2.18), which is the fourth-order operator performing the mapping between the isotropic and the orthotropic spaces, it is asserted that the projection operator $\boldsymbol{Q}$ is responsible for the damage-induced orthotropy, since the damage variables are scalars. Both in (Carol and Willam, 1996) and in (Wu and Xu, 2013), the term "anisotropic degradation" is adopted for describing those damage models that include an anisotropic (or orthotropic) stiffness reduction, beyond the application of the projection operator $\boldsymbol{Q}$. Therefore, the here-presented damage model cannot be classified as anisotropic according to these references, even if an orthotropic behaviour is induced by the damage process; consequently, it observes the first law of thermo-dynamics.

On the other hand, the second law of thermo-dynamics states that the total entropy of an isolated system tends to increase over time, taking into account the irreversibility of the natural processes. This condition can be expressed by the Clausius–Duheim inequality (Lubliner, 1972):

$$\dot{\gamma} = -\dot{\psi} + \boldsymbol{\sigma} : \dot{\boldsymbol{\varepsilon}} \geq 0 \tag{2.31}$$

Replacing the total derivative of the energy potential (2.30) with its partial derivatives with respect to the strain ε and the internal variables d^+, d^- and ε_p, the positiveness of the energy damage dissipation can be rewritten in this way:

$$\dot{\gamma} = \left(\boldsymbol{\sigma} - \frac{\partial \psi}{\partial \boldsymbol{\varepsilon}}\right) : \dot{\boldsymbol{\varepsilon}} - \frac{\partial \psi}{\partial d^+} \cdot \dot{d}^+ - \frac{\partial \psi}{\partial d^-} \cdot \dot{d}^- - \frac{\partial \psi}{\partial \boldsymbol{\varepsilon_p}} : \dot{\boldsymbol{\varepsilon}}_p \geq 0 \tag{2.32}$$

Since ε is a free variable, in order to have the non-negativeness of the dissipated energy satisfied in the general case, the quantity between round brackets in Eq. (2.32) has to be null; this results in one of the Coleman's relations (Coleman and Gurtin, 1967) and leads to the establishment of the constitutive law:

$$\boldsymbol{\sigma} = \frac{\partial \psi}{\partial \boldsymbol{\varepsilon}} = \boldsymbol{D_E} : \boldsymbol{\varepsilon_e} \tag{2.33}$$

Hence, the Clausius-Duheim inequality (2.32) reduces to:

$$\dot{\gamma} = -\frac{\partial \psi}{\partial d^+} \cdot \dot{d}^+ - \frac{\partial \psi}{\partial d^-} \cdot \dot{d}^- - \frac{\partial \psi}{\partial \boldsymbol{\varepsilon_p}} : \dot{\boldsymbol{\varepsilon}}_p \geq 0 \tag{2.34}$$

From Eq. (2.34), it is evident that the dissipative behaviour of the material is due to both damage evolution and generation of permanent strains. On the one hand, the partial derivatives of the potential with respect to d^+ and d^-, with signs reversed, represent the elastic strain energy release rates produced by a unit growth of the corresponding damage variables; they play the role of thermo-dynamic forces conjugated to the damage variables. On the other hand, the derivative of the free energy with respect to ε_p, with sign reversed, coincides with the nominal stress $\boldsymbol{\sigma}$ and plays the role of a thermo-dynamic force associated to the permanent strain. Whilst the non-negativeness of the energy dissipated by permanent strains is treated in Section 2.4, where two definitions of the permanent strain rate $\dot{\boldsymbol{\varepsilon}}_p$ are provided, the discussion on the non-negativeness of the energy dissipated due to damage evolution is here faced. The positiveness of all the terms present in Eq. (2.34) will allow concluding on the consistency of the proposed damage model for what regards the second principle of thermo-dynamics.

Since the rates $\dot{d}^+$ and $\dot{d}^-$ of the damage variables are positive (due to the choice of the monotonically-increasing damage evolution laws; see Section 2.5),

the non-negativeness of the work done by the generalized thermo-dynamic forces associated to damage is satisfied as long as the damage energy release rates are positive. The definition for these quantities, referring to the potential ψ expressed in Eq. (2.30), is:

$$-\frac{\partial \psi}{\partial d^+} = -\frac{1}{2} \boldsymbol{\varepsilon}_e : \frac{\partial \boldsymbol{D}_E}{\partial d^+} : \boldsymbol{\varepsilon}_e \qquad (2.35)$$

$$-\frac{\partial \psi}{\partial d^-} = -\frac{1}{2} \boldsymbol{\varepsilon}_e : \frac{\partial \boldsymbol{D}_E}{\partial d^-} : \boldsymbol{\varepsilon}_e \qquad (2.36)$$

Accounting for Eqs. (2.18) and (2.23), the derivatives of the constitutive operator with respect to the damage variables are:

$$\frac{\partial \boldsymbol{D}_E}{\partial d^+} = 2 \frac{\partial \boldsymbol{A}^*}{\partial d^+} : \boldsymbol{D}_0 : \boldsymbol{A}^* =$$
$$-\frac{1}{\sqrt{1-d^+}} \left[\sqrt{1-d^+} \boldsymbol{Q} : \boldsymbol{D}_0 : \boldsymbol{Q} + \sqrt{1-d^-} \boldsymbol{Q} : \boldsymbol{D}_0 : (\boldsymbol{I} - \boldsymbol{Q}) \right] \qquad (2.37)$$

$$\frac{\partial \boldsymbol{D}_E}{\partial d^-} = 2 \frac{\partial \boldsymbol{A}^*}{\partial d^-} : \boldsymbol{D}_0 : \boldsymbol{A}^* =$$
$$-\frac{1}{\sqrt{1-d^-}} \left[\sqrt{1-d^-} (\boldsymbol{I} - \boldsymbol{Q}) : \boldsymbol{D}_0 : (\boldsymbol{I} - \boldsymbol{Q}) + \sqrt{1-d^+} (\boldsymbol{I} - \boldsymbol{Q}) : \boldsymbol{D}_0 : \boldsymbol{Q} \right] \qquad (2.38)$$

Replacing these definitions in Eqs. (2.35) and (2.36) and recalling that $\varepsilon_e^+ = \boldsymbol{Q} : \varepsilon_e$ and $\varepsilon_e^- = (\boldsymbol{I} - \boldsymbol{Q}) : \varepsilon_e$, clearer expressions for the damage energy release rates are provided:

$$-\frac{\partial \psi}{\partial d^+} = \frac{1}{2} \left[\boldsymbol{\varepsilon}_e^+ : \boldsymbol{D}_0 : \boldsymbol{\varepsilon}_e^+ + \frac{\sqrt{1-d^-}}{\sqrt{1-d^+}} \boldsymbol{\varepsilon}_e^+ : \boldsymbol{D}_0 : \boldsymbol{\varepsilon}_e^- \right] =$$
$$\frac{1}{2} \left[\left(\lambda \left(tr\varepsilon_e^+ \right)^2 + 2G\varepsilon_e^+ : \varepsilon_e^+ \right) + \frac{\sqrt{1-d^-}}{\sqrt{1-d^+}} \lambda tr\varepsilon_e^+ tr\varepsilon_e^- \right] \qquad (2.39)$$

$$-\frac{\partial \psi}{\partial d^-} = \frac{1}{2}\left[\varepsilon_e^- : \boldsymbol{D_0} : \varepsilon_e^- + \frac{\sqrt{1-d^+}}{\sqrt{1-d^-}}\varepsilon_e^- : \boldsymbol{D_0} : \varepsilon_e^+\right] =$$
$$\frac{1}{2}\left[\left(\lambda\left(tr\varepsilon_e^-\right)^2 + 2G\varepsilon_e^- : \varepsilon_e^-\right) + \frac{\sqrt{1-d^+}}{\sqrt{1-d^-}}\lambda tr\varepsilon_e^+ tr\varepsilon_e^-\right] \qquad (2.40)$$

The quantities inside round brackets in Eqs. (2.39) and (2.40) are always positive while $\lambda tr\varepsilon_e^+ tr\varepsilon_e^-$ is zero in the cases of the full tensile regime ($\varepsilon_e^- = 0$) or full compressive regime ($\varepsilon_e^+ = 0$) and negative otherwise. Consequently, the positiveness of Eqs. (2.39) and (2.40) is assured for the situations of full tensile regime ($\varepsilon_e^- = 0$) and full compressive regime ($\varepsilon_e^+ = 0$), while having to be proven in the other cases. In order to do this, three strain states are identified as the most critical ones for the satisfaction of the second principle of thermo-dynamics; the non-negativeness of the damage strain energy release rates (2.39) and (2.40) for these situations allows asserting the consistency of the present model with respect to the second principle.

- In pure shear conditions ($tr\varepsilon_e^+ = -tr\varepsilon_e^-$, $\varepsilon_e^+ : \varepsilon_e^+ = (tr\varepsilon^+)^2 = \varepsilon_e^- : \varepsilon_e^- = (tr\varepsilon^-)^2$, $d^+ \neq 0$, $d^- \neq 0$), the positiveness of the quantities (2.39) and (2.40) translates in the following inequalities, respectively:

$$\sqrt{1-d^+} \geq \frac{v}{1-v}\sqrt{1-d^-} \qquad (2.41)$$

$$\sqrt{1-d^+} \leq \frac{1-v}{v}\sqrt{1-d^-} \qquad (2.42)$$

Considering the typical mechanical parameters of a quasi-brittle material, such as concrete or masonry, these relations among the damage variables, strictly related to the fracture energies in tension and compression (see Section 2.5), are satisfied.

- In case of uniaxial tensile load in direction 1 ($tr\varepsilon_e^+ = \varepsilon_1$ and $tr\varepsilon_e^- = -2v\varepsilon_1\sqrt{1-d^+}$, $d^+ \neq 0$, $d^- = 0$), the quantity contained in Eq. (2.39) is always positive and can be expressed in the following way:

$$\frac{1}{2}\left(\lambda\varepsilon_1^2\left(1-2v\right)+2G\varepsilon_1^2\right) \geq 0 \qquad (2.43)$$

The same results can be obtained for the case of uniaxial compressive load ($d^+ = 0$ and $d^- \neq 0$).

- Although the quantity $\sqrt{1-d^+}$ is at the denominator in Eq. (2.39), in the case of d^+ close to one, the work done by $-\partial\psi/\partial d^+$ in the Clausius-Duheim inequality (2.34) remains bounded, specifically tends to be null, because in that situation, $\dot{d}^+$ tends to zero. An analogous consideration holds for the work performed by $-\partial\psi/\partial d^-$ when d^- is close to one.

2.2.3 Enhanced representation of the damage-induced orthotropy

The proposed energy-equivalent damage model, based on the consistent secant operator $\boldsymbol{D_E}$ (2.24), represents a step forward with respect to the original formulation thanks to an adequate consideration of the Poisson effect on the representation of the damage-induced orthotropy. The implications deriving from this fact are shown with reference to the plane stress problem of a bar loaded in tension along the x-axis, with initial Poisson's ratio equal to 0.2.

Comparing the normalized $\sigma_x - \varepsilon_x$ curves obtained with the original model and with the new energy-equivalent one, no significant differences can be found in the softening response (see Figure 2.3.a). The substantial improvement of the proposed damage model is instead visible looking at the strain behaviour in the transversal direction y (see Figure 2.3.b). By plotting in abscissa the longitudinal strain ε_x and in ordinate the absolute value of $\varepsilon_y/\varepsilon_x$, i.e., the nominal Poisson's ratio predicted by the models, completely different trends result. On the one hand, with the original damage model, the nominal Poisson's ratio maintains constant throughout the loading history, meaning that the transversal contractions ε_y increase unrealistically throughout the whole loading history, together with the growing of the axial elongations ε_x. On the other hand, the adoption of the proposed orthotropic symmetric damage model allows one to take into account a progressive reduction of the nominal Poisson's ratio with the development of tensile damage. This is related to both the strain decomposition adopted, which considers an orthotropic model associated to the uniaxial loading conditions (see Figure 2.1), and the new constitutive symmetric operator proposed (2.24). Specifically, by deriving this constitutive matrix for a uniaxial tensile plane stress problem and by equating to zero the transversal normal stress σ_y, it is easy to find the expression of the nominal Poisson's ratio predicted by the model, which is $\bar{v} = -\varepsilon_y/\varepsilon_x = \sqrt{1-d^+}\,v$.
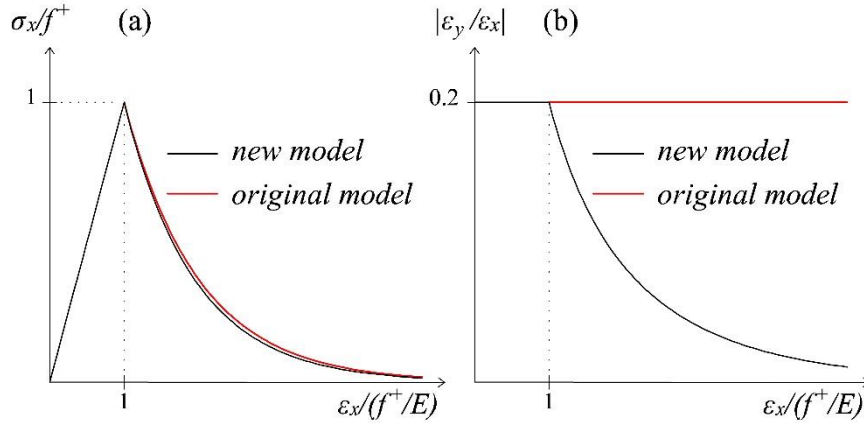
Figure 2.3: Comparison between the original formulation and the new energy-equivalent model for the problem of a bar uniaxially loaded in tension: (a) σ_x-ε_x curves and (b) nominal Poisson's ratio trends.

As noticed in (De Borst, 2002), the feature of a constant Poisson's ratio is usually typical of isotropic damage models, and it is not coherent within the framework of the classical smeared crack models (Rashid, 1968; Rots et *al.*, 1985). In fact, from a mechanical point of view, a crack generation under uniaxial tension is accompanied by a release of the transversal strains, due to the progressive loss of coupling between longitudinal and transversal directions induced by the degradation process.

2.3 Damage criterion for quasi-brittle materials

In accordance with the original d^+/d^- damage model (Faria et *al.*, 1998), the degradation process in tension and in compression is treated separately by means of independent damage criteria and independent damage evolution laws.

In analogy with (Petracca et *al.*, 2017; Saloustros et *al.*, 2017b), two damage surfaces, one in tension and one in compression, are defined, taking inspiration from the failure criterion proposed for concrete in (Lubliner et *al.*, 1989). Their expressions are the following ones, where $\tau\pm$ represent the equivalent stress quantities, monitoring the strain-stress state under tension and under compression while $r\pm$ are the internal state variables identifying the tensile and compressive damage thresholds:

$$g^{\pm} = \tau^{\pm} - r^{\pm} = 0 \tag{2.44}$$

The definitions for the equivalent stress variables $\tau\pm$ are the following:

$$\tau^+ = H(\sigma_{emax})\frac{1}{1-\alpha}\frac{f_e^+}{f^-}\left(\sqrt{3J_2} + \alpha I_1 + \beta\langle\sigma_{emax}\rangle\right) \tag{2.45}$$

$$\tau^- = H(-\sigma_{emin})\frac{1}{1-\alpha}\left(\sqrt{3J_2} + \alpha I_1 + \beta \cdot k \cdot \langle\sigma_{emax}\rangle\right) \tag{2.46}$$

where the material strength parameters α and β, defined accordingly to (Lubliner et al., 1989), are:

$$\alpha = \frac{(f_b^-/f^-)-1}{2(f_b^-/f^-)-1} \tag{2.47}$$

$$\beta = (1-\alpha)\frac{f^-}{f_e^+} - (1+\alpha) \tag{2.48}$$

In expressions (2.45) and (2.46), I_1, J_2, σ_{emax} and σ_{emin} are the first invariant, the deviatoric second invariant, the maximum and minimum principal values referred to the elastic stress tensor $\boldsymbol{\sigma_e}$ defined in Eq. (2.25). The choice of $\boldsymbol{\sigma_e}$, as the quantity determining the equivalent variables, is addressed to avoid an iterative procedure for the computation of d^+ and d^-, which would be otherwise necessary opting for the effective stress $\bar{\sigma}$ defined in Eq. (2.21). In fact, the computation of $\boldsymbol{\sigma_e}$ is straightforward and follows directly from the computation of the nominal elastic strain tensor $\boldsymbol{\varepsilon_e}$.

The other parameters necessary for the definition of the damage criterion, related to the frictional-cohesive behaviour of the material are the uniaxial tensile and compressive peak strengths of the material f^+ and f^-, the biaxial compressive strength f_b^-, the parameter k (k between 0 and 1) which fixes the size of the compressive surface in the shear quadrants (see Figure 2.4) and the values f_e^+ and f_e^-. These quantities identify the onset of damage in uniaxial tension and compression respectively, by means of the proportional parameters γ_e^+ and γ_e^- $(0 < \gamma_e \pm \leq 1)$:

$$f_e^\pm = \gamma_e^\pm f^\pm \tag{2.49}$$

The initial values of the damage thresholds $r\pm$ coincide with $f_e^\pm$ and consequently, according to Eq. (2.44), they define the size of the damage surfaces in the initial undamaged state, i.e. the size of the initial elastic domain:

$$r_0^{\pm} = f_e^{\pm} \tag{2.50}$$

In Figure 2.4, the limit tensile and compressive surfaces for the activation of damage in the initial elastic stage, derived by equating τ^+ and τ^- (Eqs. (2.45) and (2.46)) to r_0^+ and r_0^- (Eq. (2.50)), are plotted in the elastic stress principal space, for the plane stress case. In the first and third quadrants, thanks to the presence of the Heaviside functions in the definitions of $\tau\pm$, the limit surfaces are ruled by τ^+ and τ^-, separately, meaning that only tensile damage can be activated in the first quadrant and only compressive damage in the third one. Specifically, in biaxial compression, the Drucker–Prager criterion is recovered.

In the second and fourth quadrants, two damage surfaces are present, one for the activation of d^+ and one for the activation of d^-. In particular, the shape of the compressive damage surface is here affected by the parameter k. For values of k close to 1, the compressive damage surface tends to overlap with the tensile one and is close to the failure surface proposed in (Lubliner et al., 1989). For low values of k, the compressive damage surface broadens, going to coincide with the Drucker–Prager criterion for $k = 0$. Such a modelling of the failure conditions in the second and fourth quadrants is a betterment with respect to the damage limit surface considered in the original model. As a matter of fact, in (Faria et al., 1998), the behaviour of the material in these quadrants is not represented directly, but is only considered as the intersection of the two distinct failure criteria in pure tension (first quadrant) and pure compression (third quadrant).

(a)
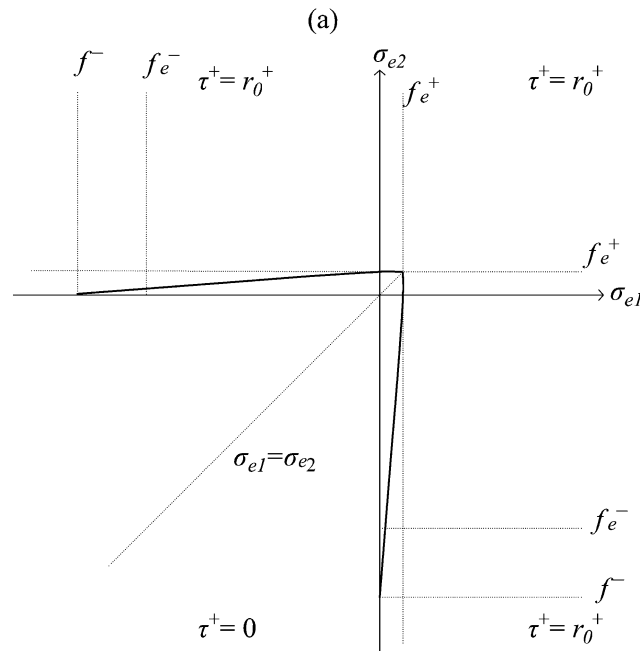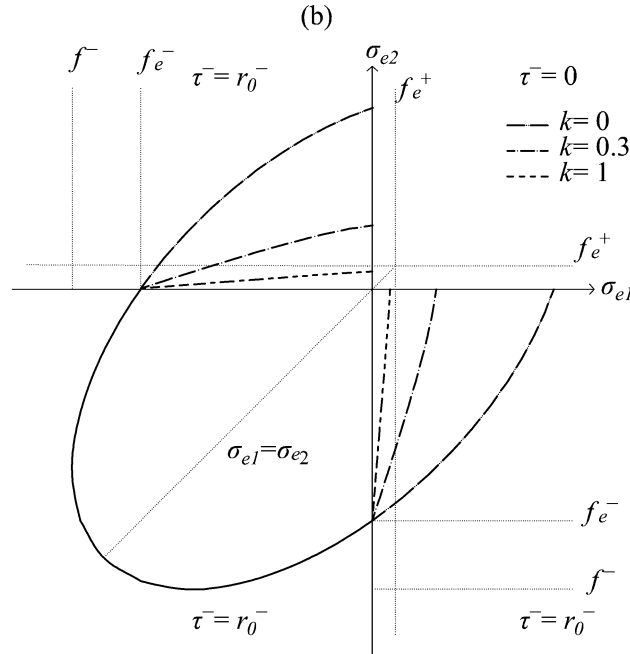
Figure 2.4: Initial damage surface in plane stress conditions, for $\alpha = 0.121$, $\beta = 7.667$ and for different values of k.

2.4 Simplified definitions of the permanent strain tensor

The modeling of permanent strains is necessary in the prediction of the structural behaviour of concrete and quasi-brittle materials in general, since during a loading history irreversible strains accumulate, affecting in a non-negligible way both strength and stiffness. Moreover, it is essential, in presence of cyclic actions, to match experimental and numerical results.

Although a plastic-damage theory represents the most accurate way to develop a constitutive model for quasi-brittle materials, the formulation of "simplified" evolution laws for permanent deformations can be successfully considered in conjunction with damage models. This is the procedure adopted for the simulation of irreversible strains in the follow up. Specifically, the simplification deals with the consideration of a unique failure criterion to describe the inelastic behaviour of quasi-brittle materials (Wu and Cervera, 2016), characterized by both damage and permanent deformations. Assuming the formation of microcracks and microvoids as the dominant inelastic mechanism, the damage failure criterion is identified as the governing one. Consequently, the modelling of permanent deformations becomes possible without the introduction of a plasticity surface and a flow rule. In

the present section, two different definitions of the permanent strain rate tensor, based on this simplification, are proposed.

2.4.1 Fundamental kinematic decompositions

First of all, two fundamental decompositions of the total strain tensor are here recalled, in order to highlight the deformation mechanisms characterizing a quasi-brittle material. The first is expressed in Eq. (2.51) and is based on the split of the strain tensor in a reversible (elastic ε_e) and irreversible (permanent ε_p) part:

$$\varepsilon = \varepsilon_e + \varepsilon_p \tag{2.51}$$

The second, shown in Eq. (2.52), deals with the decomposition performed in the classical smeared crack models (Rots and Blaauwendraad, J., 1989; Armero and Oller, 2000), according to which the total strain tensor is divided in a contribution related to the initial elastic compliance matrix C_0 and an inelastic contribution ε_{in}:

$$\varepsilon = C_0 : \sigma + \varepsilon_{in} = C_0 : \sigma + \varepsilon_d + \varepsilon_p = C_0 : \sigma + C_d : \sigma + \varepsilon_p \tag{2.52}$$

From Eq. (2.52), it is clear that the inelastic strain ε_{in} is produced by two dissipative mechanisms, acting in series, which are the development of damage (ε_d), responsible for the increase of the constitutive compliance matrix C with respect to the initial undamaged one C_0 ($C_d = C - C_0$) and the evolution of irreversible deformations (ε_p). Moreover, comparing Eqs. (2.51) and (2.52), the reversible elastic strain results equal to:

$$\varepsilon_e = C_0 : \sigma + \varepsilon_d \tag{2.53}$$

According to Eqs. (2.51) and (2.52), the rate of the total strains can be expressed in the two following ways:

$$\dot{\varepsilon} = \dot{\varepsilon}_e + \dot{\varepsilon}_p \tag{2.54}$$

$$\dot{\varepsilon} = C_0 : \dot{\sigma} + \dot{\varepsilon}_{in} = C_0 : \dot{\sigma} + \dot{\varepsilon}_d + \dot{\varepsilon}_p = C_0 : \dot{\sigma} + C_d : \dot{\sigma} + \dot{C}_d : \sigma + \dot{\varepsilon}_p = C : \dot{\sigma} + \dot{\varepsilon}_{dis} \tag{2.55}$$

In Eq. (2.55), the dissipative strain rate $\dot{\varepsilon}_{dis}$ is introduced, whose definition is:

$$\dot{\varepsilon}_{dis} = \dot{C} : \sigma + \dot{\varepsilon}_p \tag{2.56}$$

The just mentioned strain quantities are shown, both in their total and incremental form, in Figure 2.5, with reference to a 1D softening history.
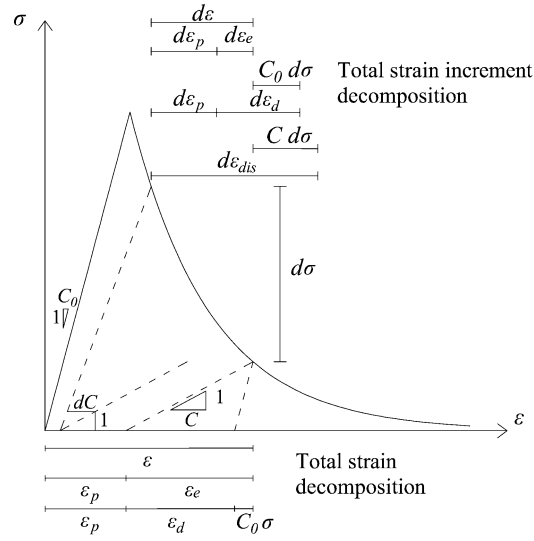
Figure 2.5: Total strain decomposition in total and incremental form in a 1D softening history.

2.4.2 Revisitation of the permanent strain rate proposed in (Faria et *al.*, 1998)

Following (Faria et *al.*, 1998), the permanent strain rate tensor can be defined as:

$$\dot{\varepsilon}_p = \left[b^+ \cdot H\left(\dot{d}^+\right) + b^- \cdot H\left(\dot{d}^-\right) \right] \frac{\langle \sigma_e : \dot{\varepsilon} \rangle}{\sigma_e : \varepsilon_e} \cdot \varepsilon_e \tag{2.57}$$

In Eq. (2.57), b^+ and b^- are two positive material parameters defining the entity of the permanent strains under tensile and compressive regimes, ranging from 0 (only damage) to 1; regarding the tensor quantities, $\dot{\varepsilon}$ is the total strain rate, ε_e is the elastic strain and σ_e is the elastic stress tensor (2.25).The ratio between the elastic power $\sigma_e : \dot{\varepsilon}$ and the double of the elastic strain energy $\sigma_e : \varepsilon_e$ contributes to define the intensity of the plastic strains.

The main simplification of Eq. (2.57) with respect to a plastic theory is that, instead of the adoption of a flow rule, the irreversible strain evolves in the direction of the elastic strain tensor ε_e and of the elastic stress tensor σ_e. This is coherent with the definition of the evolution of damage in terms of the elastic stress values, as discussed in Section 2.3. In addition, in line with the idea of considering a unique failure criterion, the same conditions holding for damage progression are taken into account for the permanent strain evolution and this relation is established by means of the Heaviside functions $H\left(\dot{d}^+\right)$ and $H\left(\dot{d}^-\right)$.

With respect to the proposal made in (Faria et al., 1998), the development of irreversible deformations is not only associated to compressive regimes but the possibility of permanent strain evolution under tensile regimes is also considered. This choice is addressed to catch more realistic results both in pure tension and in case of coexistence of compressive and tensile regimes, i.e. in shear conditions.

Moreover, referring to the definition of $\dot{\varepsilon}_p$ (2.57), the quantity related to the permanent strain tensor appearing in the Clausius–Duhem inequality (2.34) can be expressed in the following way:

$$-\frac{\partial \psi}{\partial \varepsilon_p} : \dot{\varepsilon}_p = \boldsymbol{\sigma} : \dot{\varepsilon}_p = \boldsymbol{D}_E : \varepsilon_e : \left[b^+ \cdot H\left(\dot{d}^+\right) + b^- \cdot H\left(\dot{d}^-\right) \right] \frac{\langle \boldsymbol{\sigma}_e : \dot{\varepsilon} \rangle}{\boldsymbol{\sigma}_e : \varepsilon_e} \cdot \varepsilon_e \qquad (2.58)$$

$$= a \cdot \boldsymbol{D}_E : \varepsilon_e : \varepsilon_e = 2 \cdot a \cdot \psi$$

where the scalar a is:

$$a = \left[b^+ \cdot H\left(\dot{d}^+\right) + b^- \cdot H\left(\dot{d}^-\right) \right] \frac{\langle \boldsymbol{\sigma}_e : \dot{\varepsilon} \rangle}{\boldsymbol{\sigma}_e : \varepsilon_e} \qquad (2.59)$$

Since a (2.59) is non-negative and the free energy potential (2.30) is a quadratic form ruled by the positive definite secant stiffness $\boldsymbol{D}_E$, the energy dissipated due to irreversible deformations is non-negative and this ensures the satisfaction of the Clausius-Duheim inequality (2.34) discussed in Section 2.2.2.

2.4.3 Alternative definition of the permanent strain rate

From the mechanical point of view, the hypothesis of considering the damage criterion as the unique failure criterion for d^+, d^- and ε_p corresponds to consider the development of permanent deformations related to the partial irreversibility of the microcrack opening. This is in accordance with Bažant (Bažant, 1983a) and Ortiz (Ortiz, 1985), who noticed that the microcracking of concrete is not perfectly brittle. On the base of this consideration, the alternative definition of $\dot{\varepsilon}_p$ here proposed aims to link the irreversible deformations to the kinematic quantity responsible for the microcracking, which is the damage strain tensor ε_d (see Eqs. (2.52) and (2.53)). Specifically, in incremental terms, the permanent strain rate is related to $\dot{\varepsilon}_d^*$, which is the damage strain rate tensor computed in the hypothesis of a perfectly brittle material. Such a hypothesis consists in considering the coincidence between the total strain increment and the reversible strain one ($\dot{\varepsilon}_e^* = \dot{\varepsilon}$) and in freezing the evolution of the permanent deformations ($\dot{\varepsilon}_p^* = 0$):

$$\dot{\boldsymbol{\varepsilon}}_d^* = \dot{\boldsymbol{\varepsilon}}_d\big|_{\dot{\boldsymbol{\varepsilon}}_p=0} = \dot{\boldsymbol{\varepsilon}} - \boldsymbol{C}_0 : \dot{\boldsymbol{\sigma}}^* = \boldsymbol{C}_d^* : \dot{\boldsymbol{\sigma}}^* + \dot{\boldsymbol{C}}_d^* : \boldsymbol{\sigma}^* \tag{2.60}$$

In Eq. (2.60), the superscript * is used to identify all those quantities computed in the hypothesis of a pure damage formulation.

Therefore, the simplified evolution law here proposed for the permanent deformations is the following one, where ξ^+ and ξ^- are constitutive parameters, representing the entity of the permanent deformations as a fraction of $\dot{\boldsymbol{\varepsilon}}_d^*$.

$$\dot{\boldsymbol{\varepsilon}}_p = \frac{\left\langle \boldsymbol{\sigma} : \left[\xi^+ \cdot H\left(\dot{d}^{+*}\right) + \xi^- \cdot H\left(\dot{d}^{-*}\right)\right] \dot{\boldsymbol{\varepsilon}}_d^* \right\rangle}{\boldsymbol{\sigma} : \boldsymbol{\varepsilon}_e} \cdot \boldsymbol{\varepsilon}_e \tag{2.61}$$

A discussion on the meaning of ξ and on its limit values ($0 < \xi < \xi_{lim}$ with ξ_{lim} lower than 1) is provided in Section 2.5.1. Moreover, the presence of the Heaviside function H ensures that the evolution of permanent deformations occurs only when the damage variables d^{+*} or d^{-*} increase.

To graphically clarify Eq. (2.60), in Figure 2.6 the strain increments associated to $\dot{\boldsymbol{\varepsilon}}_d^*$ (Eq. (2.60)) and $\dot{\boldsymbol{\varepsilon}}_p$ are shown with reference to a 1D loading history.

Analogously to the definition of the irreversible deformations (2.57), the new definition foresees the coincidence, in terms of directions, between the permanent strain increment and the reversible strain tensor. However, differently from (2.57), a relation between the permanent deformations and the damage strain rate is set in (2.61). This relation is explicit in 1D loading conditions, as visible in Figure 2.6, where:

$$\dot{\boldsymbol{\varepsilon}}_p = \xi \cdot H\left(\dot{d}^*\right) \dot{\boldsymbol{\varepsilon}}_d^* \tag{2.62}$$

In more generic loading conditions, it can be interpreted in energetic terms. In fact, the magnitude of the irreversible strain increment with respect to the one of the reversible strain tensor is defined resorting to a ratio between energetic quantities (see Figure 2.6.b): it is a portion of the energy dissipated by the damage strain rate, quantified by means of ξ^+ and/or ξ^-, over the potential ψ doubled.
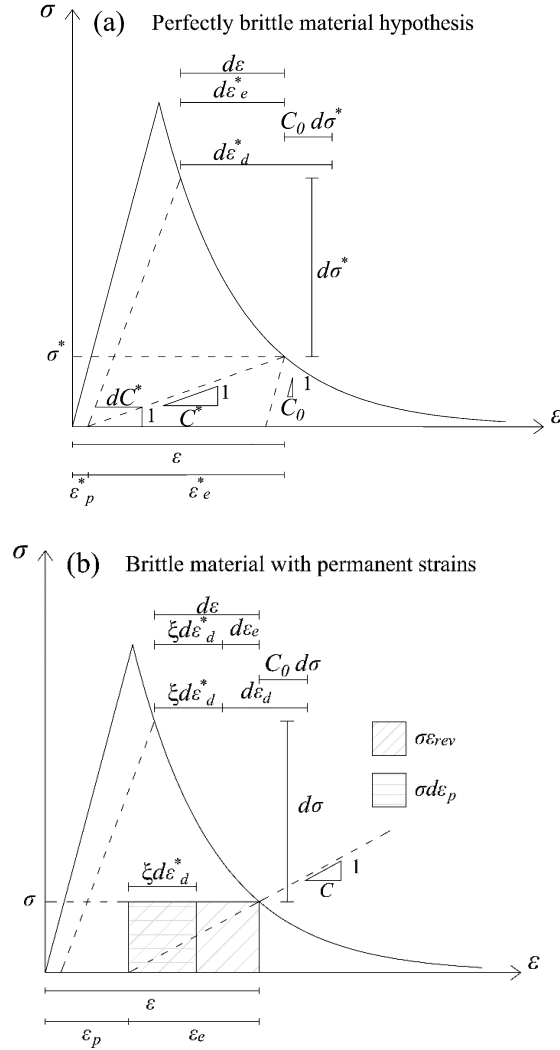
Figure 2.6: Clarification of the evolution law (2.61) for the permanent strain tensor: (a) identification of the quantity (2.60) in the hypothesis of perfectly brittle materials and (b) correction of all the quantities to describe the real situation with damage and $\varepsilon_{p.}$

Repeating the procedure shown in Section 2.4.2, the non negativeness of the energy dissipated by the permanent strain rate (2.61) can be demonstrated:

$$-\frac{\partial \psi}{\partial \varepsilon_p} : \dot{\varepsilon}_p = \sigma : \dot{\varepsilon}_p = D_E : \varepsilon_e : \frac{\left\langle \sigma : \left[\xi^+ \cdot H\left(\dot{d}^{+*}\right) + \xi^- \cdot H\left(\dot{d}^{-*}\right) \right] \dot{\varepsilon}_d^* \right\rangle}{\sigma : \varepsilon_e} \cdot \varepsilon_e \quad (2.63)$$

$$= a \cdot D_E : \varepsilon_e : \varepsilon_e = 2 \cdot a \cdot \psi$$

where the scalar a is:

$$a = \frac{\left\langle \boldsymbol{\sigma} : \left[\xi^+ \cdot H\left(\dot{d}^{+*}\right) + \xi^- \cdot H\left(\dot{d}^{-*}\right) \right] \dot{\boldsymbol{\varepsilon}}_d^* \right\rangle}{2\psi} \qquad (2.64)$$

Thanks to the non-negativeness of the potential (2.30) and of a (2.64), the satisfaction of the Clausius-Duheim inequality (2.34) can be guaranteed with the new definition of the permanent strain rate tensor (2.61).

It is worth doing some additional considerations about the alternative definition proposed for the evolution of the reversible strain tensor (2.61). First of all, the proportionality between $\dot{\boldsymbol{\varepsilon}}_p$ and $\boldsymbol{\varepsilon}_e$ is maintained because other choices for the direction of evolution of the irreversible strains implies non reliable results in presence of some specific loading conditions. This fact is qualitatively shown in Figure 2.7 for the problem of pure cyclic shear, adopting a definition for the permanent strain rate tensor based on the direct proportionality between the tensorial quantities $\dot{\boldsymbol{\varepsilon}}_p$ and $\dot{\boldsymbol{\varepsilon}}_d^*$:

$$\dot{\boldsymbol{\varepsilon}}_p = \left[\xi^+ \cdot H\left(\dot{d}^{+*}\right) + \xi^- \cdot H\left(\dot{d}^{-*}\right) \right] \dot{\boldsymbol{\varepsilon}}_d^* \qquad (2.65)$$
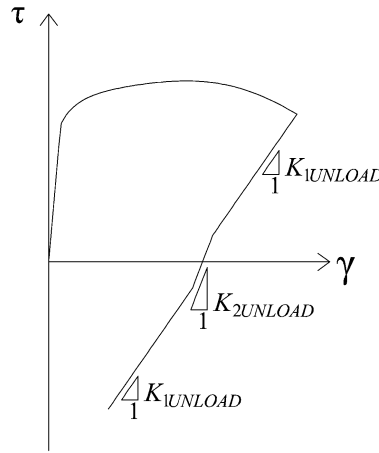
Figure 2.7: Loading and unloading τ-γ curve obtained with the adoption of the orthotropic rotating d^+/d^- damage model in conjunction with the permanent strain rate tensor (2.65).

Looking at Figure 2.7, in the reversal of the loading sign, an unrealistic stiffness modification is visible, attributable to the transition from one positive and one negative principal elastic strains to two negative ones. This shows that generic definitions for $\dot{\boldsymbol{\varepsilon}}_p$ inducing lack of proportionality between the total and the

reversible strain tensors are not adequate in conjunction with rotating orthotropic models, as the one proposed in the present work.

Differently from other simplified evolution laws for the permanent strain tensor (Faria et *al.*, 1998; Saloustros et *al.*, 2017a), also based on the proportionality between $\dot{\varepsilon}_p$ and ε_e, the novelty of the definition (2.61) lies in the relation between permanent and damage deformations. The idea to associate permanent strains to the partial irreversibility of the crack opening is similar to the idea proposed in (Ortiz, 1985; Wu and Cervera, 2016), where $\dot{\varepsilon}_p$ is considered a fraction of the dissipative strain rate $\dot{\varepsilon}_{dis}$, defined in Eq. (2.56). The choice of the damage strain rate with respect to the dissipative strain one for describing the evolution of the irreversible deformations is related to the higher physical meaning held by the former. As a matter of fact, the damage strains are present in the decomposition (2.52) of ε whereas the dissipative strains can be expressed only in a rate form and do not correspond to an actual strain tensor (Armero and Oller, 2000).

2.5 Unified dissipative approach for the evolution of the internal variables

As commented in Section 2.4, only one failure criterion, the one governing the progression of damage and described in Section 2.3, rules the evolution of both damage and permanent deformations. A first implication of this fact is that the Kuhn-Tucker relations and the persistency conditions, which identify the situations of loading, unloading and reloading for the progression of the damage variables, hold also for the evolution of the permanent deformations. As a matter of fact, both the definitions provided for the permanent strain increment (2.57) and (2.61) show a direct dependence on the increment of the damage variables. These relations are expressed in the following, in terms of the equivalent stress variables $\tau^{\pm}$ and of the damage thresholds $r^{\pm}$:

$$\dot{r}^{\pm} \geq 0 \qquad g^{\pm} = \tau^{\pm} - r^{\pm} \leq 0 \qquad \dot{r}^{\pm} \cdot g^{\pm} = 0 \qquad (2.66)$$

$$\dot{r}^{\pm} \cdot \dot{g}^{\pm} = 0 \qquad (2.67)$$

The damage limit surfaces in tension and compression are $g^{\pm} = 0$ (see Eq. (2.44)), increasing in size in case of loading ($g^{\pm} = 0$, $\dot{r}^{\pm} > 0$) and remaining unchanged during the unloading or in the undamaged situation ($g^{\pm} < 0$, $\dot{r}^{\pm} = 0$). The definition for the non-decreasing functions $r^{\pm}$, representing the damage

thresholds, can be inferred by imposing $\dot{g}\pm = 0$, necessary condition for satisfying Eq. (2.67) in the loading case:

$$r^{\pm} = \max\left(r_0^{\pm}; \max_{[0,t]}\left(\tau^{\pm}\right)\right) \quad (2.68)$$

where $r_0\pm$ are defined in Eq. (2.50) and $\max(\tau\pm)$ represent the maximum values of the equivalent quantities in tension and compression until the current instant t.

Besides the necessity of a common criterion for establishing the progression or not of all the internal variables, there is also the necessity of defining the evolution laws of damage and irreversible deformations within a unified approach (Cervera et al., 2018). The combined treatment of the two causes of dissipation (see Eq. (2.34)) derives from the fact that the fracture energy G_f, usually considered as a pure fracture parameter ruling only the evolution of damage, is actually composed of both damage and plastic dissipative contents, as discussed in (Nguyen and Houlsby, 2008; Bažant, 1996).

In analogy with (Oliver, 2000; Cervera, 2003), the evolution of the damage variables $d\pm$ is defined by means of a stress-like function $q(r\pm)$, depending on the damage thresholds $r\pm$:

$$d^{\pm}\left(r^{\pm}\right) = 1 - \frac{q\left(r^{\pm}\right)}{r^{\pm}} \quad (2.69)$$

The parameters affecting the hardening-softening function q are the initial damage thresholds $r_0\pm$ and the hardening-softening moduli $H_d\pm$. Specifically, $H_d\pm$ take into account the fracture properties of the material, which are the uniaxial strengths $f\pm$, the fracture energies $G_f\pm$ and the widths of the localization zone $l\pm$ (Bažant and Oh, 1983).

The coupling between energy dissipated by irreversible strains and damage is modelled in the following way. Given a certain stress-like hardening/softening function $q(r)$, the corresponding modulus H_d ruling the growth of damage is adjusted on the base of the definition of the permanent strain increment, in such a way to guarantee that the total dissipated energy is coherent with the fracture energy of the material.

In order to find proper relationships (with general validity) between the hardening-softening moduli $H_d\pm$ and the fracture energies $G_f\pm$, a 1D monotonic

loading history from an initial unstressed state to a complete damaged one is considered (Cervera, 2003). Since analogous considerations can be done for 1D tension and in 1D compression, hereafter the superindex $\pm$ is omitted.

The energy per unit volume g_f dissipated in this loading history can be expressed as the sum of an initial undamaged contribution g_{fe}, a contribution related to damage g_{fd} and a contribution related to permanent deformations g_{fp}, in accordance with (Wu and Cervera, 2016; Cervera et al., 2018; Nguyen and Houlsby, 2008):

$$g_f = \int_0^\infty \boldsymbol{\sigma} : \dot{\boldsymbol{\varepsilon}} \cdot dt = \int_0^{t_0} \boldsymbol{\sigma} : \dot{\boldsymbol{\varepsilon}}_e \cdot dt + \int_{t_0}^\infty \boldsymbol{\sigma} : \dot{\boldsymbol{\varepsilon}}_e \cdot dt + \int_{t_0}^\infty \boldsymbol{\sigma} : \dot{\boldsymbol{\varepsilon}}_p \cdot dt = g_{fe} + g_{fd} + g_{fp} \quad (2.70)$$

In Eq. (2.70), the instant t_0 is the one for which the appearance of the nonlinear behaviour occurs, i.e. that instant for which the damage threshold r achieves for the first time the value r_0. According to the crack band theory formulated in (Bažant and Oh, 1983), the specific fracture energy is equal to the ratio between the fracture energy per unit surface G_f and the width of the crack band l. Therefore, since G_f is a material property, the dissipation related to damage g_{fd} and to permanent strains g_{fp} have to be coupled.

In order to compute g_{fd} and g_{fp} as a function of H_d, the following relations, holding after the attainment of r_0, are considered:

$$r = E \cdot \varepsilon_e \quad (2.71)$$

$$\sigma = q(r) \quad (2.72)$$

$$\dot{\varepsilon}_p = \frac{b}{1-b} \dot{\varepsilon}_e \quad (2.73)$$

$$\dot{\varepsilon}_p = \xi \cdot \dot{\varepsilon}_d^* \quad (2.74)$$

Eqs. (2.73) and (2.74) represent the 1D counterparts of the permanent strain rate tensors proposed in Eqs. (2.57) and (2.61), respectively. Due to the assumption of monotonic loading conditions, the Heaviside function H is omitted in both the expressions. It is worth noting that, whilst in Eq. (2.73) $\dot{\varepsilon}_p$ is not affected by damage, in Eq. (2.74), the strict dependence of the irreversible strain rate on the damage evolution is intrinsic in the dependence of $\dot{\varepsilon}_p$ on $\dot{\varepsilon}_d^*$. In fact, considering

Eq. (2.72) and the incremental forms of Eq. (2.74) and of Eq. (2.60), the increment of the permanent deformations from step $n-1$ to step n can be rewritten in this way:

$$\Delta\varepsilon_p = \xi \cdot \left[\left({}^{n}d^{*} - {}^{n-1}d \right) \frac{{}^{n-1}r}{E} + {}^{n}d^{*} \cdot \Delta\varepsilon \right] \tag{2.75}$$

Two types of damage evolution laws are analysed and successively adopted in the structural applications presented in Chapter 6, Chapter 7 and Chapter 8. The first is the one proposed in (Cervera, 2003), with a parabolic hardening stage and an exponential softening one:

$$q(r) = r - A_d \cdot f \cdot \left(\frac{r - r_0}{f_p - r_0} \right)^2 \qquad\qquad r_0 \leq r \leq f_p$$

$$q(r) = f \cdot \exp\left(2H_d \cdot \left(\frac{f_p - r}{f} \right) \right) \qquad\qquad r > f_p \tag{2.76}$$

The introduction of two further variables $f_p \pm$, representing the equivalent quantities for which the peak strength is attained, is necessary ($\gamma_p \pm \geq 1$), together with the definition of the parameter A_d (Cervera, 2003):

$$f_p^{\pm} = \gamma_p^{\pm} f^{\pm} \tag{2.77}$$

$$A_d = \frac{f_p - f}{f} \tag{2.78}$$

Taking $r_0 = f_e$ (2.49) $= f_p = f$, this damage evolution law can be expressed in the form:

$$q(r) = r_0 \, \exp\left\{ 2H_d \left(\frac{r_0 - r}{r_0} \right) \right\} \qquad\qquad r \geq r_0 \tag{2.79}$$

which represents the classical softening exponential law (Cervera et al., 1996).

The second one is a new damage evolution law, inspired by the Gaussian function. Details about the proposal of this new stress-like hardening-softening function are presented in Section 2.5.2. Its expression is:

$$q(r) = r_0 \, \exp\left\{ H_d \left(\frac{r - r_0}{r_0} \right) \cdot \left[1 - H_d \left(\frac{r - r_0}{2r_0} \right) \right] \right\} \qquad r \geq r_0 \qquad (2.80)$$

In Eqs. (2.76), (2.79) and (2.80) the modulus H_d is positive.

In Figure 2.8.a, Figure 2.8.b and Figure 2.8.c, the trend of the hardening-softening (2.76), softening exponential (2.79) and hardening-softening Gaussian (2.80) functions, respectively, is displayed in a $(r\text{-}r_0) - q(r)$ diagram, highlighting the meaning of the softening and hardening/softening modulus H_d in the three cases. Moreover, the linear approximations of the three $q(r)$ functions, i.e. the first order Taylor expansions, are plotted in dashed line.
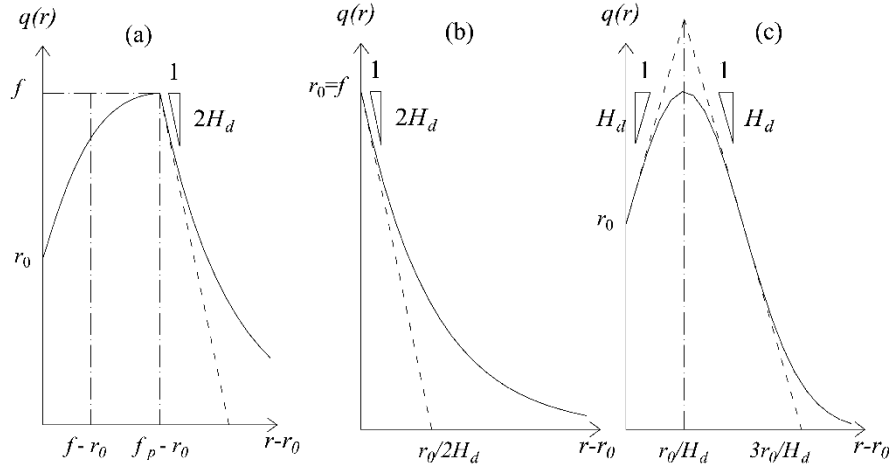
Figure 2.8: (a) Parabolic-exponential hardening-softening function (2.76); (b) exponential softening function (2.79) with its linear approximation; (c) new Gaussian hardening-softening function (2.80) with its bi-linear approximation.

The adjusted moduli H_d are computed in the follow up according to the unified approach. A distinction between the parabolic-exponential softening trend and the Gaussian trend is performed. For the sake of brevity, the expressions of H_d are provided only for those combinations of $q(r)$ functions and definitions of $\dot{\varepsilon}_p$ considered in the structural applications presented in Chapter 6, Chapter 7 and Chapter 8.

2.5.1 Parabolic-exponential damage evolution law

Firstly, the softening modulus of Eq. (2.76) is computed, considering the definition of the permanent strain rate provided in Eq. (2.57) and expressed for the 1D case in Eq. (2.73). In these conditions, the sum of the three contributions present in Eq. (2.70) can be computed as follows:

$$g_f = \frac{f^2}{E}\left(\bar{A}_d + \frac{1}{2H_d} + \frac{1}{2}\frac{f_p}{f} + \frac{b}{1-b}\tilde{A}_d + \frac{b}{1-b}\frac{1}{2H_d}\right) \qquad (2.81)$$

where $\bar{A}_d = A_d\left(f_p^3 - 3f_p \cdot f_e^2 + 2\cdot f_e^3\right)\Big/\left(6f\left(f_p - f_e\right)^2\right)$, $\tilde{A}_d = \left(\frac{f_p^2}{2f^2} - \frac{f_e^2}{2f^2} - \frac{A_d\left(f_p - f_e\right)}{3f}\right)$.

For the single contributions, a detailed computation is provided in (Cervera et al., 2018).

By equating the fracture energy in the form (2.81) to the ratio G_f / l, the expression for the softening modulus is derived:

$$\frac{1}{2H_d} = \left(1-b\right)\left(\frac{EG_f}{f^2}\frac{1}{l} - \frac{1}{2}\frac{f_p}{f} - \bar{A}_d - \frac{b}{1-b}\tilde{A}_d\right) \qquad (2.82)$$

Note that for the limit case of $r_0 = f_e$ (2.49) $= f_p$ (2.77) $= f$, the softening modulus in Eq. (2.82), associated to the exponential softening law (2.79), reduces to:

$$2H_d = \frac{2}{\left(1-b\right)}\left(\frac{\bar{H}\cdot l}{1-\bar{H}\cdot l}\right) \qquad (2.83)$$

where $\bar{H}$ is the material property defined as: $\bar{H} = f^2\big/\left(2E\cdot G_f\right)$. From Eq. (2.83), it is clear that higher is the parameter b, higher is the value of H_d. In addition, for $b = 0$, the softening moduli in (2.82) and (2.83) bring to a well-established result for linear and exponential softening (Cervera et al., 1996; Cervera, 2003):

$$\frac{1}{2H_d} = \frac{EG_f}{f^2}\frac{1}{l} - \frac{1}{2}\frac{f_p}{f} - \bar{A}_d \qquad (2.84a)$$

$$H_d = \left(\frac{\bar{H}\cdot l}{1-\bar{H}\cdot l}\right) \qquad (2.84b)$$

In the structural applications presented in Chapter 6, Chapter 7 and Chapter 8, where this damage evolution law is adopted, a pure exponential softening behaviour ($f_e^+ = f_p^+ = f^+$) is assumed for d^+ and a parabolic hardening followed by an exponential softening is considered for d^- ($f_e^- < f^- < f_p^-$).

Four figures show the qualitative differences between the unified dissipative approach, based on the adoption of the softening moduli (2.82) or (2.83) here computed and the uncoupled one, which independently of the modelling or not of permanent deformations, uses the softening moduli (2.85) or (2.84b).

In each figure, the 1D stress-strain curve in case of $b = 0$ (null irreversible deformations) and $0 < b < 1$ (non-null permanent deformations) are plotted. In Figure 2.9.a and Figure 2.9.b, the case of 1D tension is analysed while in Figure 2.10.a and Figure 2.10.b the case of 1D compression, considering the evolution law for permanent deformations proposed in Eq. (2.57).
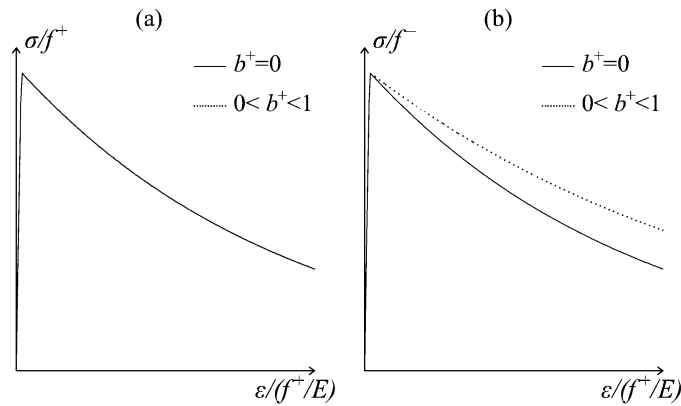
Figure 2.9: 1D tensile behaviour: (a) unified dissipative approach for the computation of the internal variables adopting H_d (2.83) and (b) uncoupled dissipative approach, adopting H_d (2.84b).
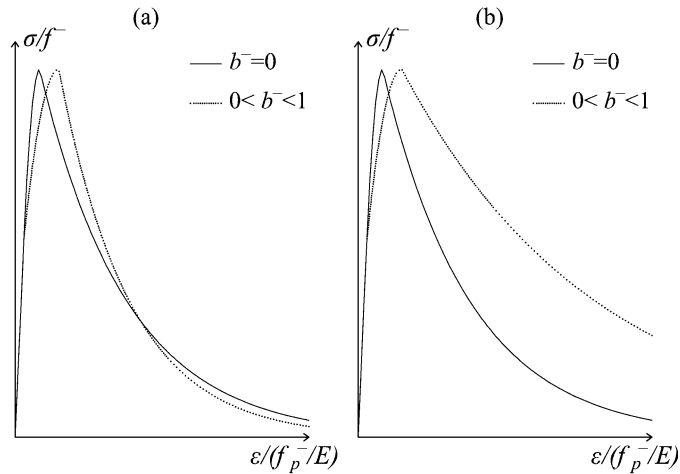
Figure 2.10: 1D compressive behaviour: (a) unified dissipative approach for the computation of the internal variables adopting H_d (2.82) and (b) uncoupled dissipative approach, adopting H_d (2.84b).

As evident from Figure 2.9.a and Figure 2.10.a, the energy released with or without permanent deformations is exactly the same resorting to the coupled approach, whereas a relevant over-dissipation can be noticed with the adoption of the uncoupled one (Figure 2.9.b and Figure 2.10.b), passing from the case of $b = 0$ to the case of $0 < b < 1$.

Secondly, in conjunction with the new definition of the permanent strain rate provided in Eq. (2.61) and expressed for the 1D case in Eq. (2.75), the pure exponential softening function of Eq. (2.79) is considered for computing the adjusted $H_d\,(r_0 = f_e = f_p = f)$. Specifically, to make the following computations easier, the linear approximation of the $q(r)$ function (2.79), identified with a dash line in Figure 2.8.a, is taken into account:

$$q^*(r) = 2H_d\left(r_0 - r\right) + r_0 \qquad r_0 \leq r \leq r_0\left(1 + \frac{1}{2H_d}\right) \qquad (2.85)$$

Substituting in Eq. (2.75) the damage values obtained considering the linear $q^*(r)$ function (2.85) and coming back to a rate form, the expression of the irreversible strain rate results:

$$\dot{\varepsilon}_p = \xi\cdot\left(2H_d + 1\right)\dot{\varepsilon} = \frac{\xi\cdot\left(2H_d + 1\right)}{1 - \xi\cdot\left(2H_d + 1\right)}\dot{\varepsilon}_{rev} \qquad (2.86)$$

The three different contributions identified in Eq. (2.70) are the following ones:

$$g_{fe} = \frac{r_0^2}{2E} \qquad g_{fd} = \frac{r_0^2}{4EH_d} \qquad g_{fp} = \frac{r_0^2}{4EH_d}\frac{\xi\cdot\left(2H_d + 1\right)}{1 - \xi\cdot\left(2H_d + 1\right)} \qquad (2.87)$$

Merging all the contributions and equating the specific fracture energy to the ratio between the fracture energy per unit surface G_f and the width l, a second degree equation in the unknown H_d is found:

$$4\xi H_d^2 - 2H_d\left(1 - \xi\right) + 2H = 0 \qquad (2.88)$$

where $2H$ is the following quantity:

$$2H = \left(\frac{\bar{H}\cdot l}{1 - \bar{H}\cdot l}\right) \qquad (2.89)$$

with the material property $\bar{H} = f^2/(2E \cdot G_f)$. In the generic case of $\xi \neq 0$, between the two possible roots solving Eq. (2.88), the one representing the softening modulus in the post-peak behaviour is:

$$H_d = \frac{(1-\xi) - \sqrt{(1-\xi)^2 - 8\xi H}}{4\xi} \qquad (2.90)$$

In Figure 2.11, the different contributions explicitly defined in Eq. (2.87) are shown, with reference to a linear softening curve. Both the softening modulus driving damage $2H_d$, whose definition is provided in Eq. (2.90), and the constitutive parameter ξ, introduced to identify the portion of $\dot{\varepsilon}_d^*$ associated to permanent deformations, are pointed out. Together with them, the slope of the global softening behaviour (including damage and irreversible deformations) is indicated with $2EH$.
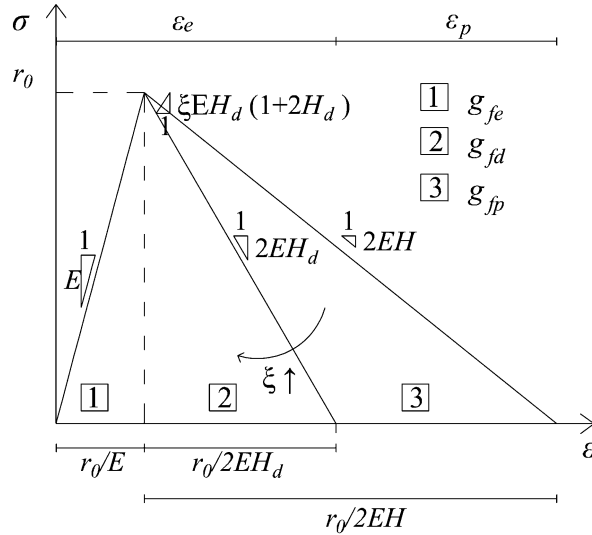
Figure 2.11: Different dissipative contributions highlighted with reference to a 1D history ruled by the linear softening function (2.85) and influence of the parameter ξ.

Such a figure allows understanding the limit cases contemplated by the proposal developed for permanent deformations in Eq. (2.61). For $\xi = 0$, the material behaviour is perfectly reversible, i.e. irreversible strains are absent. In this case, the modulus $2H_d$ is equal to the quantity expressed in (2.89) since the dissipative contribution g_{fp} related to permanent deformations is zero and this is coherent with the linear softening modulus presented in (Cervera et al., 1996; Cervera, 2003). For growing ξ, the dissipation due to permanent deformations g_{fp} increases, while g_{fd}, the dissipation related to damage, decreases. This corresponds

to a growth of the softening modulus H_d and is coherent with the idea of maintaining unaltered the specific energy g_f, being this quantity completely defined starting from a material constant , which is the fracture energy G_f.

From Eq. (2.90), a limit value for ξ, ξ_{lim}, can be found by ensuring the positiveness of the quantity under square root:

$$\xi_{lim} = 1 + 4H - 4\sqrt{H^2 + \frac{H}{2}} \tag{2.91}$$

As shown in the following structural applications (for instance in Section 7.1), this value is sufficiently high to guarantee that the experimental evidence is caught for quasi-brittle materials as concrete and masonry. Moreover, from Eq. (2.91) it derives that ξ_{lim} is lower than 1 and that increases for decreasing H.

2.5.2 Gaussian damage evolution law

Before computing the hardening-softening modulus of the Gaussian stress-like function (2.80) according to the unified dissipative approach, some comments about the derivation of this new $q(r)$ function are provided.

By comparing the new damage evolution law to the exponential one (see Figure 2.8), the former is able to reproduce a more realistic softening behaviour than the latter, especially if compressive loadings are considered. In fact: the linearity is abandoned before the attainment of the material strength f ($r_0 < 1$), and not in correspondence of it; a non- linear hardening trend precedes the softening one; the transition from the linear elastic regime to the softening branch is smooth, and a gradual decrease of the tangent stiffness, from positive to negative values, is simulated.

Moreover, the attractiveness of the new damage evolution law lies in the fact that both the hardening and the softening trends can be modelled by means of only one function, the Gaussian one, and resorting to the same material parameters (G_f, f, E) needed in the case of linear or exponential softening. Other damage evolution laws contemplate both a hardening and a softening part and a smoother passage from the linear elastic range to softening but they generally require more than one function to describe the complete non-linear behaviour and, consequently, more input parameters. For instance, in (Petracca, 2016), for compressive damage, an evolution law including an hardening part, two softening parts and a final constant residual stress part is described. Another case is the one presented in Eqs. (2.76), which consists in a parabolic hardening followed by an exponential softening.

The general way of expressing the Gaussian function is the following:

$$q(r) = a \exp\left\{-\frac{1}{2}\left(\frac{r-b}{c}\right)^2\right\} \tag{2.92}$$

where three parameters (a, b and c) appear. In Figure 2.12, the (r-r_0) − $q(r)$ curve associated to (2.92) is displayed and the parameters a, b and c are identified.
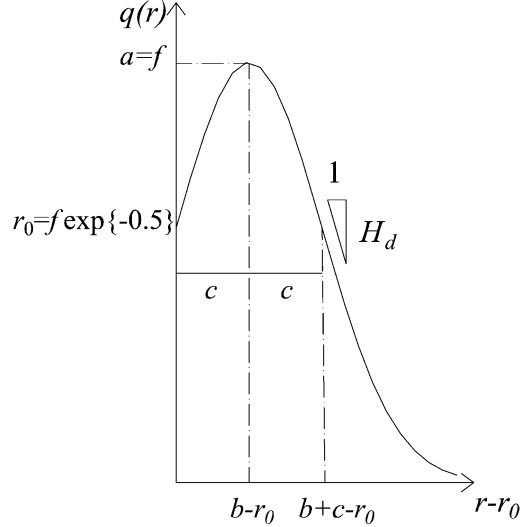
Figure 2.12: Gaussian hardening/softening law with identification of parameters a, b and c in Eq. (2.92) and parameters r_0 and H_d in Eq (2.80).

The choice of these parameters depends on three conditions to be ensured:

(i) the maximum stress σ in a uniaxial test has to be equal to the material strength; consequently, since $\sigma = q(r)$, the maximum value attained by $q(r)$ has to be equal to the peak strength of the material f;

(ii) the energy per unit volume dissipated has to be coincident with the ratio G_f/l;

(iii) damage starts at r_0, so $q(r_0) = r_0 = f \cdot \exp\{-0.5\} = 0.60653\,f$.

Condition (i) can be satisfied considering a, which represents the maximum value attained by $q(r)$, equal to f. Condition (ii) can be guaranteed by varying c, which, as shown in Figure 2.12, controls the width of the bell, i.e. the dissipated energy. It is important to clarify that condition (iii) is an assumption, meaning that other values for r_0 could be considered. The choice here done for r_0 is equivalent to assume:

$$r_0 = b - c = f \cdot \exp\{-0.5\} \tag{2.93}$$

From the relation (2.93) it emerges that b, representing the value of the damage threshold for which the material strength is attained (see Figure 2.12), is not a free

parameter but it depends on c and r_0. Hence, the softening modulus H_d adopted in the definition of the Gaussian hardening-softening function (2.80) can be related to r_0 and c, since it refers to the absolute value of the derivative of $q(r)$ in correspondence of the inflection point $r = b + c$ (see Figure 2.8 and Figure 2.12). With reference to (2.92), this quantity can be expressed in the following way:

$$H_d = \left| \frac{\partial q}{\partial r} \right|_{r=b+c} = r_0 \cdot \frac{1}{c} \tag{2.94}$$

Finally, the Gaussian stress-like function in the form (2.80) is obtained by substituting in (2.92) the parameters a (equal to f), b (Eq. (2.93)) and c (Eq. (2.94)) as functions of H_d and r_0.

The computation of the hardening-softening modulus H_d of the Gaussian damage function is performed only considering the new definition of the permanent strain rate provided in Eq. (2.61) and expressed for the 1D case in Eq. (2.75). To simplify the procedure, the linear approximation of the $q(r)$ function (2.80), identified with a dash line in Figure 2.8.c, is considered:

$$
\begin{aligned}
q_1^*(r) &= H_d \left(r - r_0 \right) + r_0 & r_0 &\leq r \leq r_0 \left(1 + \frac{1}{H_d} \right) \\
q_2^*(r) &= H_d \left(r_0 + \frac{2r_0}{H_d} - r \right) + r_0 & r_0 \left(1 + \frac{1}{H_d} \right) &\leq r \leq r_0 \left(1 + \frac{3}{H_d} \right)
\end{aligned}
\tag{2.95}
$$

Substituting in Eq. (2.75) the damage values obtained considering the bi-linear $q^*(r)$ function (2.95) and coming back to a rate form, the expression of the irreversible strain rate results:

$$
\begin{aligned}
\dot{\varepsilon}_{p1} &= \xi \cdot (1 - H_d) \dot{\varepsilon} = \frac{\xi \cdot (1 - H_d)}{1 - \xi \cdot (1 - H_d)} \dot{r} & r_0 &\leq r \leq r_0 \left(1 + \frac{1}{H_d} \right) \\
\dot{\varepsilon}_{p2} &= \xi \cdot (1 + H_d) \dot{\varepsilon} = \frac{\xi \cdot (1 + H_d)}{1 - \xi \cdot (1 + H_d)} \dot{r} & r_0 \left(1 + \frac{1}{H_d} \right) &\leq r \leq r_0 \left(1 + \frac{3}{H_d} \right)
\end{aligned}
$$

$$\tag{2.96}$$

The three different contributions identified in Eq. (2.70) are the following ones:

$$g_{fe} = \frac{r_0^2}{2E} \qquad g_{fd} = \frac{7r_0^2}{2EH_d}$$

$$g_{fp} = \frac{r_0^2}{EH_d}\left(\frac{3}{2}\frac{\xi\cdot(1-H_d)}{1-\xi\cdot(1-H_d)} + 2\frac{\xi\cdot(1+H_d)}{1-\xi\cdot(1-H_d)}\right) \tag{2.97}$$

Merging all the contributions and equating the specific fracture energy to the ratio between the fracture energy per unit surface G_f/l, a third degree equation in the unknown H_d is found:

$$\xi^2 H_d^3 - H_d\left[(1-\xi)^2 - \xi H_G\right] + (1-\xi)H_G = 0 \tag{2.98}$$

where:

$$H_G = \left(\frac{7\exp\{-1\}\cdot \bar{H}\cdot l}{1 - \exp\{-1\}\cdot \bar{H}\cdot l}\right) \tag{2.99}$$

with the material property $\bar{H} = f^2/(2E\cdot G_f)$.

In the generic case of $\xi \neq 0$, among the three possible roots solving Eq. (2.98), the positive one with value between 0 and 1 must be taken. For ξ growing with respect to the null value, the hardening/softening modulus increases.

Analogously to the case of exponential damage, an upper limit ξ_{lim} exists but its direct expression can not be easily provided; therefore, it has to be found numerically. In case of $\xi = 0$, the material is perfectly reversible and from Eq. (2.98), it is inferable that:

$$H_d = H_G = \frac{2.55\cdot \bar{H}\cdot l}{1 - 0.368\cdot \bar{H}\cdot l} \tag{2.100}$$

The similarity of Eq. (2.100) with the expressions derived for the modulus ruling the exponential softening (Eq. (2.84b)) is evident. However, despite the same formalism, a quantitative comparison between them is not univocal and, only on the base of the width l and of the mechanical properties of the material ($\bar{H}$), the here proposed Gaussian damage function can be defined steepest in the descending branch than the exponential one or viceversa.

In the structural applications of the damage model, the hardening behaviour foreseen by the Gaussian $q(r)$ function is considered only in compression while a

pure softening behaviour is contemplated in tension, through the adoption of the exponential function (2.79).

In Figure 2.13, some curves in 1D tension and 1D compression obtained by considering the new evolution law for the permanent strain tensor (2.61) are displayed with the intent of showing how, by varying ξ and keeping fixed the fracture energy G_f, the softening modulus H_d computed according to the unified procedure changes in order to maintain unaltered the total specific dissipated energy. The material parameters considered are collected in Table 2.1 and, according to Eq. (2.91), the limit value for ξ^+ is equal to 0.7.

Table 2.1: Material parameters.

E [MPa]	ν [-]	f^+ [MPa]	f^- [MPa]	G_f^+ [N/mm]	G_f^- [N/mm]	l [mm]
20000	0.0	2.0	-35	0.1	30.00	20
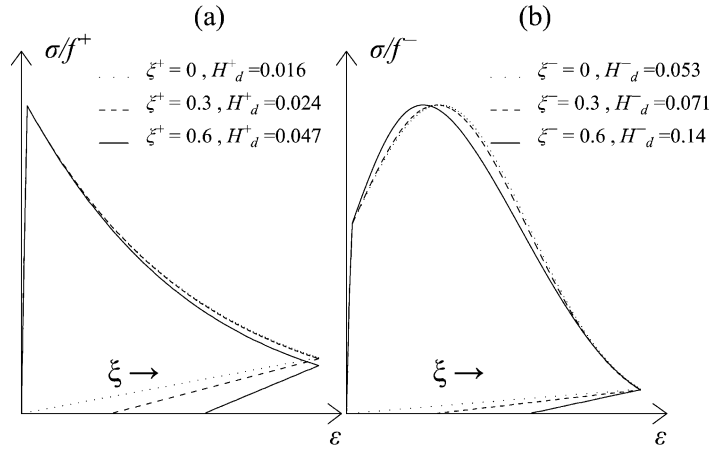
Figure 2.13: 1D σ-ε curves (a) in tension and (b) in compression for different values of the parameter ξ defining ε_p (2.61).

Chapter 3

Multidirectional d^+/d^- damage model for cyclic loading

Together with the damage-induced anisotropy, another essential feature that needs to be taken into account in the constitutive behaviour of quasi-brittle materials as concrete and masonry is the modelling of the microcrack closure-reopening (MCR) effects (Caboche, 1992). These effects consist in the partial or total recovery of the material stiffness upon load reversal from tension to compression, related to the closure of previously generated cracks. The modelling of such a phenomenon is fundamental when the main interest is to perform the analysis of concrete, reinforced concrete or masonry structures under wind and seismic actions (Chang and Mander, 1994; Cervera et al., 1995; Oliveira, 2003; Faria et al., 2004; Xue and Yang, 2014).

As observed in Section 1.2.1, the "original" d^+/d^- damage model by (Faria et al., 1998) is effective in describing the unilateral behaviour of the material only in specific cyclic conditions, characterized by alternating full tensile and full compressive regimes, i.e., for instance, in a 1D tension-compression cyclic history or in bending dominated problems (Faria et al., 2004). In presence of shear cyclic conditions, the stiffness recovery capabilities are instead absent and, as remarked in correspondence with Figure 1.4, this consideration can be generalized to all those damage formulations based on the use of spectral decomposition and scalar damage variables. Therefore, not only the "original" d^+/d^- formulation suffers from this limitation, but also the new energy-equivalent d^+/d^- model presented in Chapter 2.

In order to make the new formulation able to deal with microcrack-closure reopening effects in generic cyclic conditions, and especially in shear, in the present chapter the constitutive model is enriched with a "multidirectional damage procedure" with a twofold goal. On the one hand, memory regarding microcracks orientation has to be preserved. On the other hand, this has to be achieved maintaining only two scalar variables in the constitutive law (2.33).

For the sake of clarity and without loss of generality, first of all, the fundamental aspects of this new approach are described in Section 3.1, referring to plane problems. The interest is specifically addressed to the case of cyclic loading, either considered alone or preceded and/or followed by non-cyclic (permanent or proportionally increasing) loading. Some hints about the possibility of extending the procedure to 3D problems are however included. An interesting interpretation of the multidirectional damage approach is proposed in Section 3.2, by establishing some parallels with the concepts of fixed, multi-directional fixed and rotating crack models (Rots and Blaauwendraad, 1989). In Section 3.3, the numerical performance and robustness of the approach is treated, by proposing a regularization technique able to improve the convergence in correspondence with closure and reopening of cracks. Finally, in Section 3.4, some examples, solved at the local point-wise level, are shown to demonstrate the enhancements which derive from the adoption of the multidirectional damage procedure in terms of histeretic behaviour of the material under shear cyclic conditions.

Part of the work presented in this chapter is already published in (Cervera and Tesei, 2017) and in (Cervera et al., 2018).

3.1 Formulation

At the base of the "multidirectional d^+/d^- damage model", there is the idea of considering two independent damage evolution processes for tension and two independent damage evolution processes for compression, differing for the direction in which they act. This translates in the necessity of monitoring separately two damage values in tension and two damage values in compression and this is performed by means of a plane partition into two regions for d^+ and two regions for d^-. Each region is endowed with its own (tensile or compressive) degradation parameter d and damage threshold r. The assignment of a tensile (compressive) damage value to a certain region occurs on the base of the maximum (minimum) principal strain direction which has caused it; specifically, the reference tensor quantity is the elastic strain ε_e, in order not to alter the strain-driven formalism

followed in the evaluation of the secant matrix and of the internal variables (Section 2.2.1, Section 2.3 and Section 2.4).

The active value of d^+ (d^-), i.e. the one affecting the constitutive law (2.33), is computed starting from the internal variables d^+ and r^+ (d^- and r^-), associated to the damage region in which the current maximum (minimum) principal strain direction falls. In order not to compromise the irreversibility of the damage process, the updating of the active damage values is performed taking into account, within each region, the Kuhn-Tucker and persistency conditions (2.66) and (2.67) and the monotonically increasing evolution laws (2.69). The inactive damage values are however kept in memory with the possibility of being re-activated in correspondence with a principal directions' rotation.

The distinction between two families of cyclic loading conditions is herein considered:

(i) cyclic loading characterized by a fixed principal reference system and by changes of the principal configuration only in presence of load reversal; this is the case in a 1D cyclic history or in pure shear cyclic conditions, when the rotation of the principal directions is represented by a swapping between minimum and maximum principal directions.

(ii) Cyclic loading with continuous rotation of maximum and minimum principal directions; this is the case of cyclic histories preceded by non negligible not-cyclic loading.

To clarify this classification, in Figure 3.1, two problems, one belonging to the category of Load Type (i) (Figure 3.1.a) and the other belonging to the category of Load Type (ii) (Figure 3.1.b) are displayed: the former represents a problem of pure cyclic shear, the latter represents a cyclic shear history preceded by a pre-contraction. The objective is to underline the differences in terms of rotation of the principal maximum (elastic strain) direction with respect to the horizontal axis, quantity which is defined by means of the angle θ^+. While in the case of Load Type (i) the angle θ^+ is fixed except at loading reversal (instant t_1), when a swapping between the maximum and minimum principal directions occurs, in the case of Load Type (ii) this quantity continuously changes during the cyclic history. It is worth noting that, in the case of Load type (ii), the angle θ^+ identifies actually the rotation between the maximum principal current direction and the maximum principal direction in the initial configuration, at time t_0 (which is horizontal, due to the initial vertical pre-contraction).
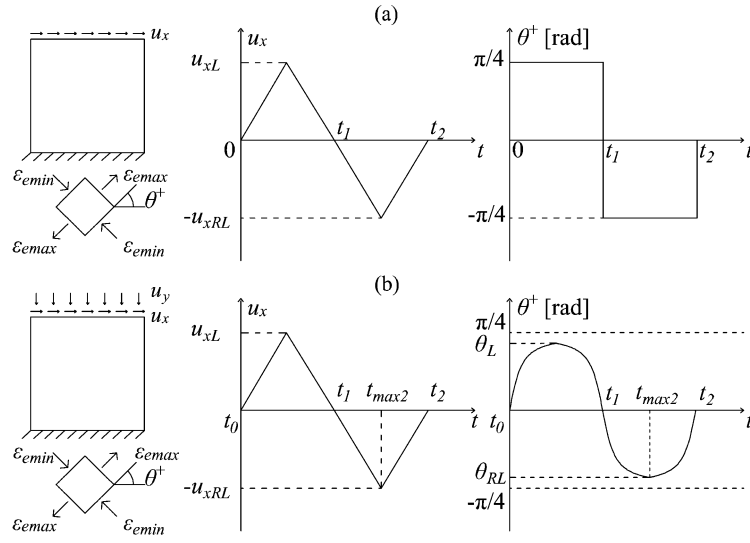
Figure 3.1: Differences between the two types of cyclic loading conditions considered in the multidirectional damage procedure: (a) Load Type (i) and (b) Load Type (ii).

It is important to underline that the multidirectional concepts above described, based on the monitoring of damage depending on its orientation, hold for both the types of loading. As discussed in the follow-up, the differences mainly lie in the way according to which the damage regions are identified during the loading history, related to the differences stressed in Figure 3.1. This will affect also the stiffness recovery capabilities which can be modeled in the two different loading conditions.

3.1.1 Cyclic Load Type (i)

Regarding load Type (i), since, except swappings in correspondence of load reversal, the principal directions are fixed during the loading history, also the damage regions in tension and compression in which the space is divided are considered fixed. Their bisectors are assumed coincident with the principal reference system ($\boldsymbol{p}_{max\_d}$, $\boldsymbol{p}_{min\_d}$) in correspondence of which damage occurs for the first time and their amplitude is equal to $\pi/2$:

$$\boldsymbol{bisector}_1^+ = \boldsymbol{p}_{max\_d} \quad \boldsymbol{bisector}_2^+ = \boldsymbol{p}_{min\_d} \quad amplitude_{1,2}^+ = \pi/2$$
$$\boldsymbol{bisector}_1^- = \boldsymbol{p}_{min\_d} \quad \boldsymbol{bisector}_2^- = \boldsymbol{p}_{max\_d} \quad amplitude_{1,2}^- = \pi/2$$

(3.1)

The orthogonality between the bisectors of the tensile (compressive) damage regions, visible in Eq. (27), allows assuming that the full fracture energy G_f^+ (G_f^-)

is consumed in each tensile (compressive) region, independently from one other. When a change of the principal configuration occurs for the first time after the plane partition, i.e. after appearance of damage, two situations are contemplated. If the rotation is significant, for instance equal to $\pi/2$ in case of swapping between maximum and minimum principal directions, a complete regain of the initial stiffness is assured; if the rotation is not relevant, and lower than $\pi/4$, there is no switching from a region to the other one, and no unilateral effects are visible in the structural response.

The working principles of the multidirectional damage model in case of Load Type (i) are explained, by means of Figure 3.2, considering the problem of a panel subjected to a cyclic horizontal displacement u_x inducing shear, just commented in Figure 3.1.a. It is assumed that $u_{xL} = u_{xRL} = u_{xmax}$.
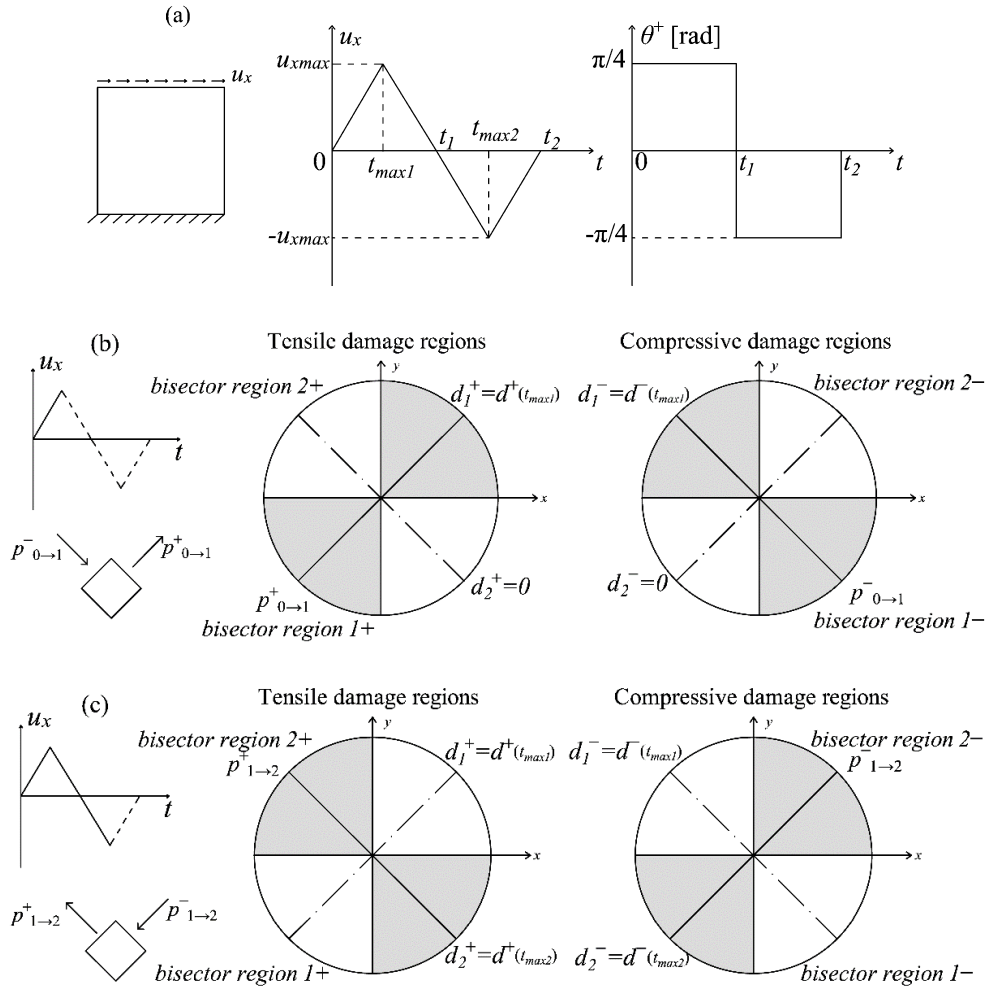
Figure 3.2: (a) Load Type (i) problem: identification of the damage regions and active damage variables (in grey) (b) before and (c) after loading reversal.

In Figure 3.2 it is shown how two damage values for tension and two damage values for compression are kept in memory based on the current principal strain directions (which are $p^+_{0->1}$, $p^-_{0->1}$ in Figure 3.2.b and $p^+_{1->2}$, $p^-_{1->2}$ in Figure 3.2.c). The active damage values in tension and compression are the ones associated to the regions highlighted in gray. It is worth noting how, in correspondence with the instant t_{max1} (Figure 3.2.b), the degradation tensile (compressive) parameter is associated only to the tensile (compressive) damage region 1. The absence of damage in the other tensile (compressive) region allows simulating the recovery of stiffness in correspondence with the instant t_1, i.e., when the swapping between maximum and minimum principal directions occurs.

The problems which can be treated according to this procedure are mainly represented by structural elements in which permanent loads are negligible with respect to the variable loads with cyclic nature, as wind and seismic actions.

3.1.2 Cyclic Load Type (ii)

Regarding load Type (ii), the continuous rotation of the principal directions and the oscillation around the initial configuration requires the adoption of a criterion for defining the activation of a multidirectional damage approach and the consideration of evolving, non-fixed, damage regions. To do this, the introduction of two sets of variables is performed, monitoring the deviation of the principal reference system with respect to the initial conditions; the definition of the first set of variables, the equivalent deviation quantities $\tau_\theta\pm$, is the following:

$$\tau_\theta^\pm = \cos\left(\theta_\tau^\pm\right) \tag{3.2}$$

where θ_τ^+ (θ_τ^-) represents the absolute value of the angle between the current maximum (minimum) principal strain direction and the initial maximum (minimum) principal strain direction, ranging from 0 to $\pi/2$.

The second set of variables is constituted by the threshold deviation quantities $r_\theta\pm$, which can be computed according to the expression:

$$r_\theta^\pm = \cos\left(\theta_r^\pm\right) = \min\left(\cos\left(\theta_{min}\right); \min_{[0,t]}\left(\tau_\theta^\pm\right)\right) \tag{3.3}$$

From Eq. (3.3), it results that θ_r^+ (θ_r^-) represents the maximum value assumed by the equivalent angle θ_τ^+ (θ_τ^-) until the current time t, provided that it is higher than the minimum threshold deviation θ_{min} This parameter assumes the important role

of the minimum deviation angle for which an independent treatment of the damage variable is valid.

The analogy between the definition of the damage threshold $r\pm$ (2.68) and the deviation threshold $r_\theta\pm$ (3.3) is evident: as r^+ (r^-) rules the evolution of the damage variable d^+ (d^-), as $r_\theta{}^+$ $(r_\theta{}^-)$ governs the evolution of the damage regions, in terms of their bisector and their amplitude. Specifically:

$$\begin{aligned}\textbf{\textit{bisector}}_{1,2}^{\pm} &= \pm\theta_r^{\pm} \quad \textit{amplitude}_{1,2}^+ = 2\cdot\theta_r^{\pm} \quad \textit{if } \theta_r^{\pm} \leq \pi/4 \\ \textbf{\textit{bisector}}_{1,2}^{\pm} &= \pi/4 \quad \textit{amplitude}_{1,2}^+ = \pi/2 \quad \textit{if } \theta_r^{\pm} > \pi/4\end{aligned} \tag{3.4}$$

where $\textbf{\textit{bisector}}^+{}_{1,2}$ ($\textbf{\textit{bisector}}^-{}_{1,2}$) refer to the directions evaluated starting from the initial maximum $\boldsymbol{p}_{max\_0}$ (minimum $\boldsymbol{p}_{min\_0}$) principal strain direction. As visible in Eq. (3.4), the amplitude of each region increases with the evolution of the region's bisector: this translates in the fact that two directions initially belonging to the same damage region continue to be affected by the same degradation parameter during the whole loading history. Moreover, due to the orthogonality between the maximum and minimum principal directions, $\tau_\theta{}^+ = \tau_\theta{}^-$ and $r_\theta{}^+ = r_\theta{}^-$; hence, the activation of the multidirectional procedure and the updating of the damage regions in tension and in compression, whose conditions are expressed in Eqs. (3.5), occur simultaneously. For this reason, hereafter, the superindex $\pm$ is dropped.

$$\dot{r}_\theta \leq 0 \qquad g_\theta = \tau_\theta - r_\theta \geq 0 \qquad \dot{r}_\theta \cdot g_\theta = 0 \qquad \dot{r}_\theta \cdot \dot{g}_\theta = 0 \tag{3.5}$$

Once again, a similarity between the conditions (3.5) and the Kuhn-Tucker and persistency conditions (2.66) and (2.67) ruling the updating of the damage variables is present. According to Eqs. (3.5), four different situations can be distinguished:

- $g_\theta > 0$, $\dot{r}_\theta = 0$ and $r_\theta = \cos(\theta_{min})$: the multidirectional procedure is not active since the equivalent deviation angle θ_τ (3.2) has never overcome the minimum deviation θ_{min}. The value of d^+(d^-) is the same in both the tensile (compressive) damage regions. The damage regions are identified according to Eq. (3.4);

- $g_\theta = 0$, $\dot{r}_\theta < 0$ and $\theta_r < \pi/4$ (loading conditions): the multidirectional procedure is active and the bisectors of the damage regions rotate, accompanied by an increase of the regions' amplitude, according to Eq. (3.4);

- $g_\theta = 0$, $\dot{r}_\theta < 0$ and $\theta_r \geq \pi/4$ (loading conditions): the multidirectional procedure is active but the damage regions do not evolve, according to Eq. (3.4), to avoid overlapping;

- $g_\theta > 0$, $\dot{r}_\theta = 0$ and $r_\theta < \cos(\theta_{min})$ (unloading conditions): the multidirectional procedure is active and the damage regions coincide with the ones assumed at the last loading step.

The essentials of the multidirectional damage model in the presence of continuously rotating principal directions (Load Type (ii)) are illustrated by means of Figure 3.3, making reference to the problem of a panel subjected first to pre-contraction and the to cyclic shear, displayed in Figure 3.1.b. It is assumed that $u_{xL} = u_{xRL} = u_{xmax}$.

It is important to note that, except for the positive and negative sign, the θ^+ - t curve shown in Figure 3.3.a represents the trend of the equivalent quantity θ_τ^+ (see Eq. (3.2)), which coincides with the absolute value of the actual deviation angle θ^+. In Figure 3.3.b, no distinction between the values of $d^+(d^-)$ in the two tensile (compressive) damage regions is visible. In fact, this state (instant $t = t_{minL}$) corresponds to the activation of the multidirectional procedure; before it, the deviation has always been lower than θ_{min}, avoiding a directional treatment of damage ($g_\theta > 0$, $\dot{r}_\theta = 0$ and $r_\theta = \cos(\theta_{min})$). The adoption of the grey colour to stress the active damage values is here unuseful, due to the fact that the plane partition in distinct damage regions is not operative yet. Moreover, Figure 3.3.c describes the damage distribution in the unloading conditions after the achievement of the peak displacement in t_{max1}, in the instant t_{minUN}. In this case, the damage values and the damage regions are the ones assumed in correspondence with t_{max1} and the multidirectional procedure is active since, only in the regions including the current principal strain directions (region 1+ and region 1−, the gray ones), the damage variables have evolved with respect to the values in t_{minL} ($g_\theta > 0$, $\dot{r}_\theta = 0$ and $r_\theta < \cos(\theta_{min})$).

Similarly to the case of load Type (i), the description of the microcrack closure-reopening effects is ensured by the transition from a damage region to the other one, occurring in correspondence with the load sign reversal (instant t_1). In fact, from the active tensile damage value d^+_1 (d^-_1) in Figure 3.3.c, there is the passage to the active one d^+_2 (d^-_2) in Figure 3.3.d, corresponding to the maximum reloading instant t_{max2} ($g_\theta = 0$, $\dot{r}_\theta < 0$ and $\theta_r < \pi/4$).
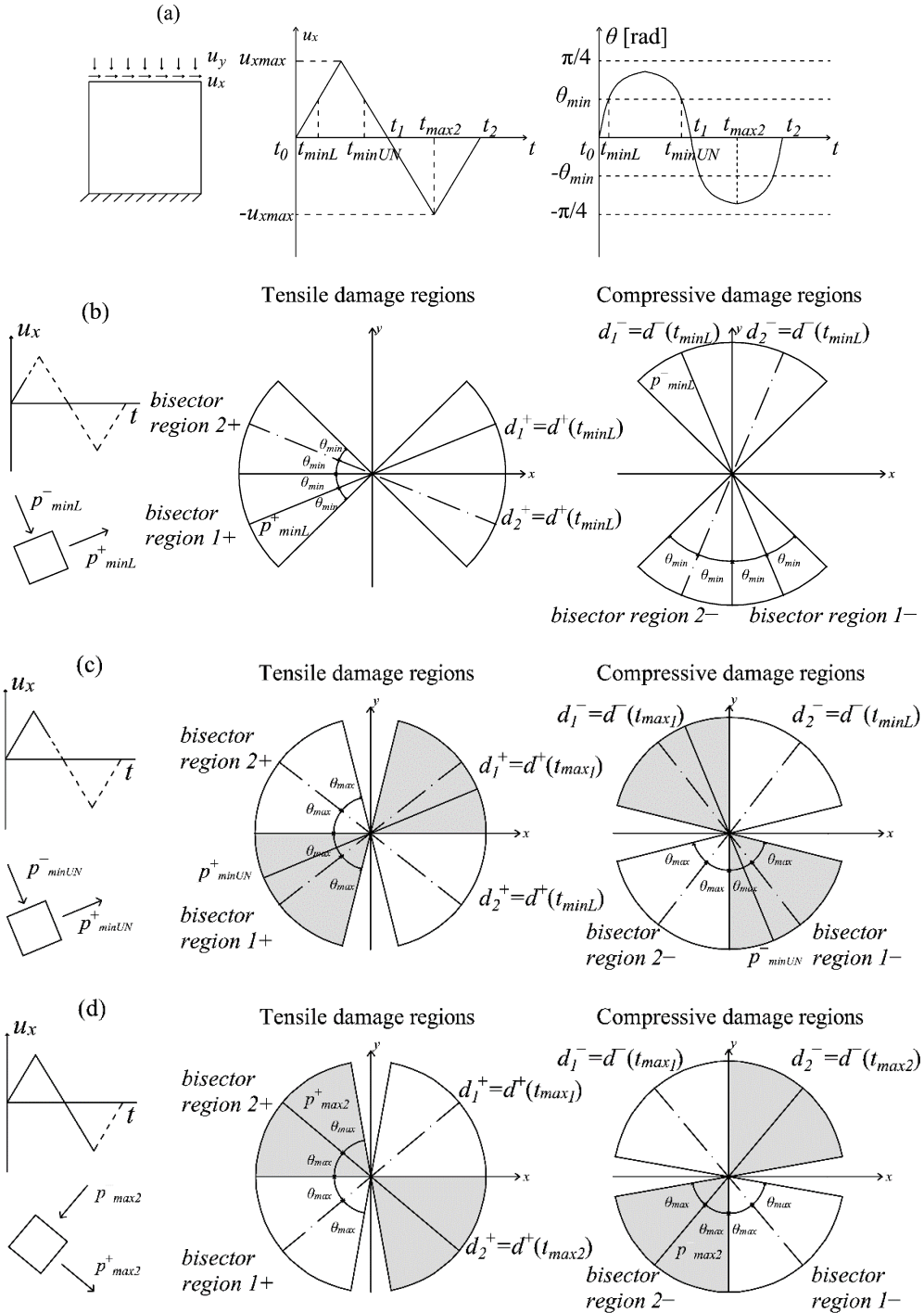
Figure 3.3: (a) Load Type (ii) problem: identification of the damage regions and of the active damage variables (in grey) (b) in correspondence with the activation of the multidirectional procedure, (c) in unloading conditions and (d) at the maximum reloading.

Finally, from Figure 3.3, the evolving nature of the damage regions, foreseen by the multidirectional procedure in case of rotating principal directions, can be observed. In fact, the amplitude of the damage regions is equal to $2\theta_{min}$ in Figure 3.3.b while is equal to $2\theta_{max}$ ($<\pi/4$) in Figure 3.3.c and Figure 3.3.d. Specifically, in Figure 3.3.c, unloading conditions are represented since the bisectors of the damage regions (identified by θ_r) and the principal directions (whose current deviation is θ_τ) do not coincide. Differently, Figure 3.3.d refers to loading conditions: ***bisector*$^+_1$** coincides with the principal direction $\boldsymbol{p}_{max}$ while ***bisector*$^-_1$** coincides with $\boldsymbol{p}_{min}$.

From the above considerations, the introduction of a minimum threshold θ_{min} can be better understood: it has the objective of delaying the activation of a multidirectional damage model, and consequently, it implies the possibility of a partial stiffness recovery in a generic loading history. The modelling of a partial stiffness recovery seems adequate for loading conditions of Type (ii): in fact, a continuous rotation of the principal directions without any brusque variation allows one to transfer a certain amount of damage accumulated in a direction to the closest ones. The two limit cases, characterized by no stiffness recovery and by complete stiffness recovery, are however covered by the present formulation. If the cyclic history does not generate relevant deviations from the principal reference configuration of the permanent load, no stiffness recovery occurs; if no damage is present before the activation of the multidirectional damage procedure, a total stiffness recovery is obtained.

Conversely to load Type (i), this procedure allows to model situations in which permanent loads are non-negligible with respect to variable cyclic actions.

3.1.3 3D extension

The 3D extension of the here-described multidirectional damage model has to be further analyzed, but it seems possible by referring to the same concepts introduced for plane problems and adopting the same distinction in cyclic load Type (i) and cyclic load Type (ii). As in 2D, the partition of the space in regions for tensile and compressive damage is performed, d^+ (d^-) is assigned to all of the regions including an eigenvector associated with a positive (negative) principal strain, and the active value of the tensile damage variable (compressive damage variable) is computed considering the current maximum (minimum) principal elastic strain direction.

As regards load Type (i), the multidirectional procedure is considered active from the beginning of the cyclic loading history, and the space is divided into three regions for tensile damage and into three regions for compressive damage, each

region associated to a principal direction. As in 2D, the bisectors of the damage regions coincide with the principal directions, which are fixed throughout the loading history, and the amplitude of each region is equal to $\pi/2$, meaning that each principal direction that forms an angle θ with the bisector of a region, such that $|\cos(\theta)| \geq \cos(\pi/4)$, belongs to that region.

For load Type (ii), characterized by a continuous rotation of the principal directions, the activation of the multidirectional procedure and the updating of the damage regions are ruled by the same conditions holding in 2D, i.e., the conditions expressed in (3.5). Likewise, the deviation with respect to the initial configuration is evaluated resorting to definition (3.2), and the threshold quantity is provided by (3.3). Since the active damage values are computed based on the maximum and minimum principal directions (not the intermediate principal directions) and the loading conditions foresee a continuous, and not abrupt, rotation of the principal reference system, additional damage regions associated with the rotation of the intermediate principal direction are not necessary. Therefore, as in 2D problems, two regions for tensile damage, related to the rotation of the maximum principal direction, and two regions for compressive damage, related to the rotation of the minimum principal direction, are considered. If the bisector of the tensile damage region 1, coinciding with the current maximum principal direction (loading conditions), is inclined by an angle $+\theta^+_r$ (or $+\pi/4$) with respect to the initial maximum principal strain direction, the bisector of the tensile damage region 2 is automatically defined as the direction inclined of an angle $-\theta^+_r$ (or $-\pi/4$) with respect to the initial maximum principal strain direction and belonging to the plane in which the maximum principal strain direction has rotated in the loading history. A direction is included in a region if it forms an angle θ with the bisector of that region, such that $|\cos(\theta)| \geq |\cos(\theta^\pm_r)|$.

3.2 Parallels among the multidirectional damage model and fixed/rotating smeared crack concepts

The new damage model proposed in Chapter 2 fits within the framework of the rotating smeared crack concept, introduced for the first time in (Cope et. *al*, 1980). In fact, as outlined in Section 2.2.1, the alignment between the axes of orthotropy of the damaged material and the principal strain directions is a feature of the proposed orthotropic damage model. Moreover, the limitations observed in the modelling of MCR effects in presence of shear cyclic loading (Figure 1.4) are comparable to the inability of the rotating crack models to take into account the

orientation of previous defects. The inclusion of the procedure described in Section 3.1 can be interpreted as an enrichment of the constitutive equations with some properties proper of the fixed crack models (Rots et *al*., 1985), specifically the preservation of memory regarding damage orientation. Rather than to a pure fixed crack model, the present proposal can be assimilated to a multidirectional fixed crack model (De Borst and Nauta, 1985; Riggs and Powell, 1986; Rots and Blaauwendraad, 1989).

First of all, a similar use of a threshold angle is present in the multidirectional damage model and in the multidirectional fixed crack model. As in the former, the transition between two different damage values is performed only when a rotation of the principal directions greater than a certain angle occurs, in the latter, a new crack is initiated only when the inclination of the principal directions with respect to existing cracks overcomes a certain threshold. Moreover, some specific hypotheses discussed in (Rots and Blaauwendraad, 1989) for the implementation of a multidirectional model are in good agreement with the choices here done in the modelling of the multidirectional damage. In fact, the assumption to consider the value of the damage variables evolving in a region independently of what happens in the other region is analogous to consider the behaviour of each multidirectional crack as the one of a single crack. In view of this, adequate values for θ_{min}, the minimum threshold deviation appearing in Eq. (3.3), can be chosen in accordance with (Rots and Blaauwendraad, 1989) and range between $\pi/12$ and $\pi/6$. In addition, the choice of considering only one active value of damage in tension and one in compression is in line with the hypothesis done in multidirectional models of adopting the most recently initiated defect as the only currently-active crack. This is supported by experimental evidence: only the most recently initiated crack is active in a system of non-orthogonal defects (Vecchio and Collins, 1986).

A difference between the multidirectional fixed crack concept and the multidirectional damage model lies in the fact that the former deals with a collection of several fixed defects of different orientation while the latter considers only two independent damage regions (2D problems). Finally, differently from the multidirectional fixed damage models, the multidirectional damage formulation maintains during the whole damage process the coaxiality between principal directions of elastic strains and axes of orthotropy. Hence, it keeps the motivating feature of the rotating crack models, coaxiality, which reduces stress locking, while remedying the impossibility of tracking memory of the material defects, the main objection arisen against the rotating crack concept (Bažant, 1983).

3.3 Numerical aspects

In the present section, an implementation detail addressed to improve the numerical robustness of the multidirectional procedure described in Section 3.1 is introduced.

When treating microcrack closure-reopening effects, a further aspect to be taken into account regards the convergence difficulties arising at structural level. As pointed out in (Jefferson and Mihai, 2015), these numerical difficulties are related to the abrupt changes in the secant stiffness going from an open crack state to a closed one, or vice versa.

The passage from a damage region to the other one, performed on the base of the current principal strain directions, implies modifications of the active damage variables d^+ and d^- affecting the secant stiffness (2.24). Therefore, in analogy with the considerations provided in (Jefferson and Mihai, 2015), the multidirectional damage approach described in Section 3.1 may suffer from convergence problems. Hindrance in achieving convergence on the residual nodal forces has been observed especially in case of load Type (ii) (Section 3.1.2); in fact, due to the partition adopted for this kind of loads (see Figure 3.3), at load sign reversal, principal directions tend to oscillate around the boundary between a damage region and the other one.

In order to eliminate these convergence difficulties, the introduction of a transition region, of amplitude $2\theta_t$, is here proposed, with the purpose of making the passage between two different damage regions smoother. The working principles of this smoothing procedure are explained in Figure 3.4, where it is shown how the transition region has, as bisector, the boundary between the damage region 1 and the damage region 2. Superindices + and – for identifying the regions and their corresponding quantities r and d are dropped, since the procedure hereafter described holds for both tensile and compressive regions, provided that the principal current elastic strain direction p refers to p_{max} and p_{min}, respectively.

When the current principal strain direction p belongs to the transition region, the active damage threshold quantity r is evaluated according to Eq. (3.6), resorting to a hyperbolic tangent function:

$$r_t = \frac{1}{2}(r_1 + r_2) + \frac{1}{2}(r_1 - r_2) \cdot \tanh\left(\frac{2\theta_p}{\theta_t}\right) \tag{3.6}$$

where the pedix t stands for transition, r_1 and r_2 are the damage threshold values pertaining to region 1 and 2, respectively, and θ_p is the angle between p and the

boundary. Hence, the active damage value d in the transition region is evaluated starting from the smoothed damage threshold (3.6) and referring to the evolution damage law expressed in Eqs. (2.69).

The trend of the smoothing transition, operated on the damage threshold quantity, is plotted in Figure 3.4.b, where the amplitude of the transition region is also identified. This amplitude, defined by the parameter θ_t, is chosen to be sufficiently small compared to the rotation performed by the principal directions, which can be, at most, $\pi/2$. In case of $\boldsymbol{p}$ falling outside the transition region, the active value of the damage variable is computed referring to r_1 or r_2, according to the procedure declared in Section 3.1.

The impact that such transition has on the numerical robustness of the multidirectional damage approach is studied with reference to a structural application involving cyclic shear conditions in Section 6.3, where convergence histories for different values of the parameter θ_t are compared.
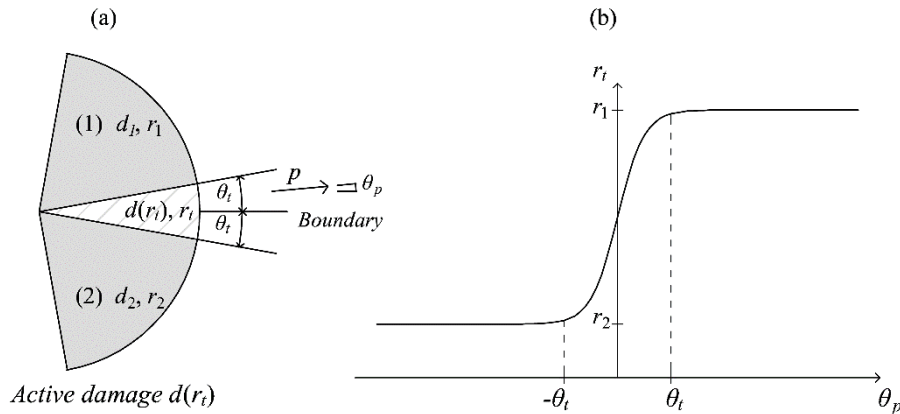
Figure 3.4: Smoothing of the multidirectional procedure: (a) identification of the transition region and (b) hyperbolic tangent function operating the regularization.

3.4 Enhanced microcrack closure-reopening capabilities under cyclic shear

In order to show the enhanced dissipative capabilities of the multidirectional damage model in presence of cyclic load conditions, some problems are solved at a local point-wise level and commented on.

All the numerical analyses are performed considering an exponential damage evolution law in tension (Eq. (2.76) with $r_0{}^+ = f^+ = f_p{}^+$, i.e. $\gamma_e{}^+ = \gamma_p{}^+$) and a parabolic hardening-exponential softening trend in compression (Eq. (2.76) with $r_0{}^- < f^- < f_p{}^-$, $\gamma_e{}^- = 0.5$ and $\gamma_p{}^- = 1.3$).

Initially, the effects of the multidirectional treatment of damage is analyzed in the hypothesis of null permanent deformations. Then, they are included with the intent of showing how the combined adoption of the multidirectional approach and irreversible deformations favorably affects the structural dissipative behaviour under cyclic shear conditions. The definition used for ε_p in this section is the one presented in Eq. (2.57).

The constitutive properties adopted in the numerical analyses are given in Table 3.1. They are representative of masonry, one of the cohesive-frictional materials more of interest in civil structural applications.

Table 3.1: Material parameters used in the numerical analyses.

E [MPa]	ν [-]	f^+ [MPa]	f [MPa]	G_f^+ [N/mm]	G_f^- [N/mm]	f_b^-/f^- [-]	k [-]
1540	0.2	0.13	-3.9	0.1	10	1.15	0.75

First of all, a cyclic uniaxial load history, characterized by alternating 1D tension-1D compression, is considered. Since the constitutive behaviours obtained with or without the adoption of the multidirectional damage procedure are qualitatively the same in terms of unilateral effects, only one σ-ε curve is shown, in Figure 3.5.
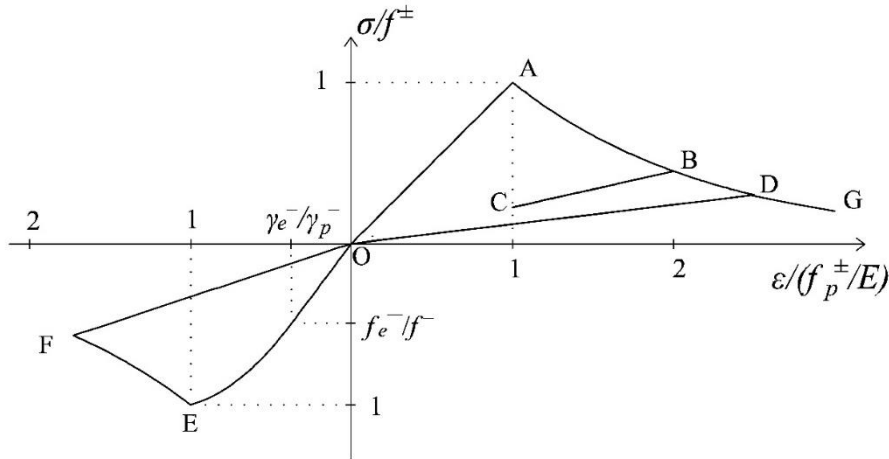
Figure 3.5: 1D cyclic loading history.

It refers to the following loading sequence: a loading in tension with an exceeding of the damage threshold r_0^+ (O-A-B), a partial unloading followed by a reloading

in tension with further progression of damage (B-C-D), an unloading in compression with softening (D-O-E-F) and a reloading in tension (F-O-D-G).

It is evident from Figure 3.5 that the initial stiffness recovery in the transition from tension to compression (D-O-E) is captured. However, as discussed in Section 1.2.1 and at the beginning of this chapter, even the "original" d^+/d^- damage model exhibits such unilateral effects.

Therefore, the advantages of the proposed formulation have to be demonstrated in more generic loading conditions, as the ones previously commented on and represented in Figure 3.1.a (Load Type (i)) and in Figure 3.1.b (Load Type (ii)). Hereafter, it is assumed that the maximum horizontal displacement in the loading stage is lower than the maximum displacement in the reloading one, i.e., $u_{xL} < |u_{xRL}|$.

Regarding the problem of the panel subjected to pure shear cyclic loading conditions (Figure 3.1.a), the normalized τ - γ responses obtained without and with the multidirectional damage procedure are displayed in Figure 3.6.a and Figure 3.6.b, respectively. In this case, the differences in terms of stiffness recovery are clear: in Figure 3.6.a, no stiffness recovery is visible when the inversion of the horizontal displacement occurs in the instant t_1 while in Figure 3.6.b the regain of the initial stiffness is present. As commented on in Section 3.1.1, the total stiffness recovery is justified by the orthogonality of the tensile (compressive) directions between the first loading stage (going from instant 0 to t_1) and the second loading one (going from t_1 to t_2).
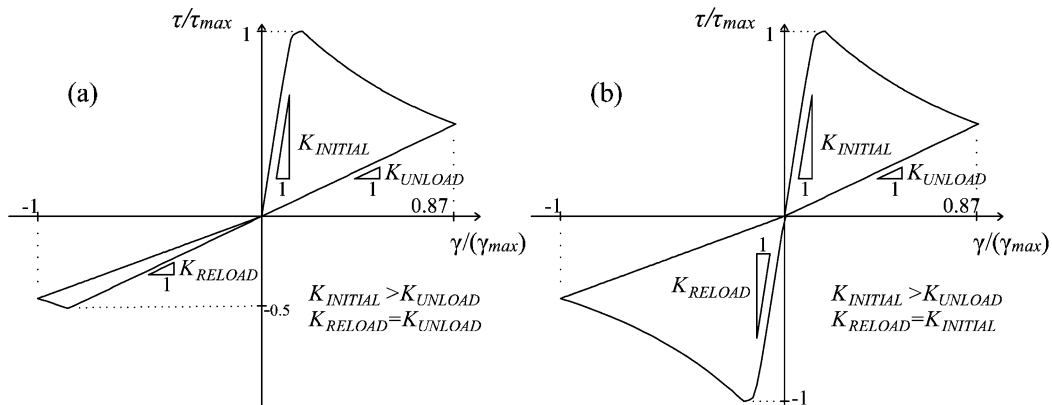
Figure 3.6: Structural response of the problem represented in Figure 3.1.a: (a) without the multidirectional approach and (b) with the multidirectional approach.

As regards the problem of the panel subjected first to a pre-contraction and then to a shear cyclic loading history (Figure 3.1.b), three combinations of horizontal and vertical displacement values are analyzed, differing for the ratio $m = |u_{xmax}/u_y|$

between the maximum u_x attained (u_{xRL}) and the imposed u_y. Different values of this ratio translate into different maximum values assumed in the loading history by the variable $r_\theta\pm$ (Eq. (3.3)). The minimum deviation θ_{min} (Eq. (3.3)) is chosen equal to $\pi/8$.

On the one hand, in Figure 3.7, the value θ^+_τ is lower than θ_{min}, meaning that the multidirectional procedure is never activated ($m = 1$). As a matter of fact, no differences can be found between the τ - γ curves obtained without (Figure 3.7.a) and with the multidirectional approach (Figure 3.7.b), both characterized by the absence of stiffness recovery when the horizontal displacement changes sign. In these conditions, the lack of MCR capabilities is adequate because the maximum and minimum principal strain directions responsible for the damage generation do not deviate significantly from the principal configuration induced by the permanent vertical displacement. On the other hand, in both Figure 3.8 and Figure 3.9, the maximum deviation is greater than θ_{min}, and the ratios between the horizontal and vertical displacements considered are $m = 1.8$ and $m = 8$, respectively. In both these cases, the enhanced microcrack closure-reopening capabilities of the multidirectional damage procedure are evident: the curves resulting from the standard damage formulation (Figure 3.8.a and Figure 3.9.a) do not show any stiffness recovery while the adoption of the multidirectional approach (Figure 3.8.b and Figure 3.9.b) simulates the closure effects satisfactorily.
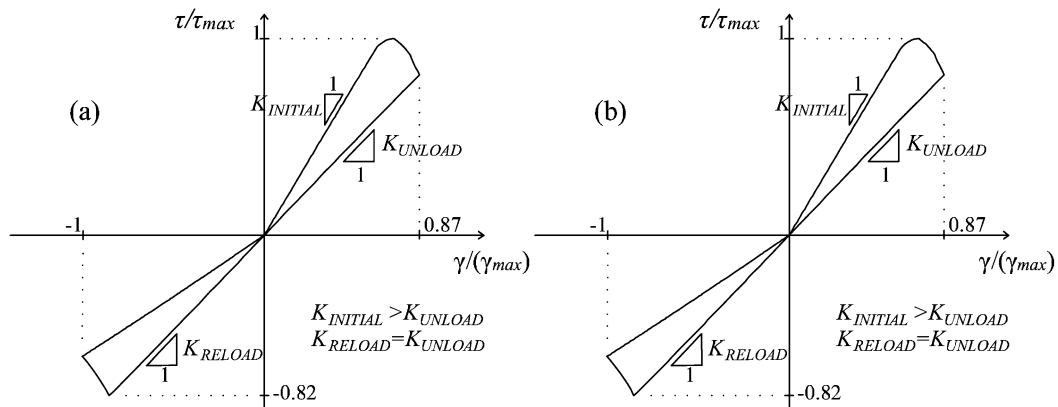
Figure 3.7: Structural response of the problem represented in Figure 3.1.b, ratio m=1: (a) without and (b) with the multidirectional approach.
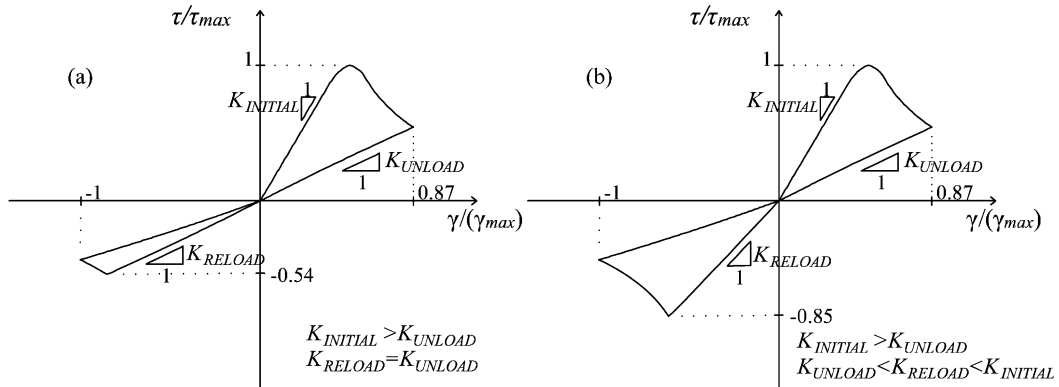
Figure 3.8: Structural response of the problem represented in Figure 3.1.b, ratio m=1.8: (a) without and (b) with the multidirectional approach.
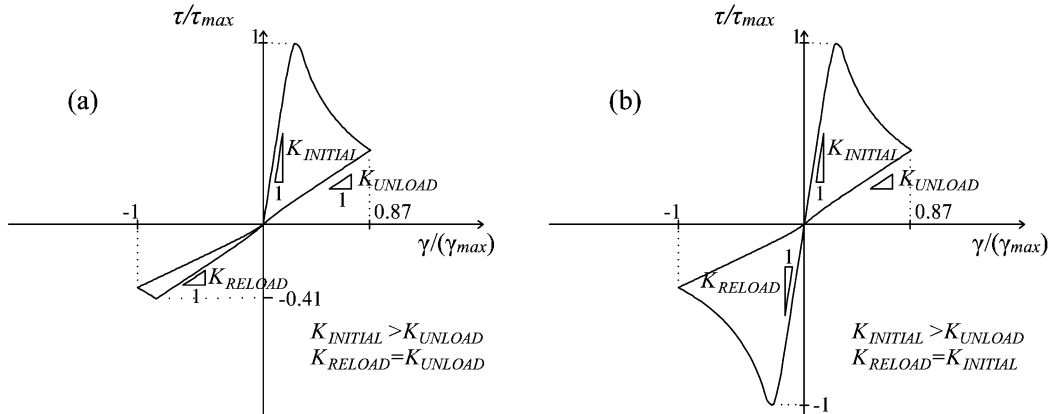
Figure 3.9: Structural response of the problem represented in Figure 3.1.b, ratio m=8: (a) without and (b) with the multidirectional approach.

Specifically, for $m = 1.8$, the stiffness recovery is only partial (Figure 3.8.b), while for $m = 8$ (Figure 3.9.b), it is complete. The response in Figure 3.9.b is analogous to the one in Figure 3.6.b in terms of total recovery of the initial stiffness: this happens because, in \he former case, the vertical displacement is almost negligible compared with the horizontal one, while in the latter case, it is absent. This observation translates in the fact that the multidirectional procedure for Load Type (ii) is able to simulate the same MCR capabilities of the multidirectional procedure in case of Load Type (i), when the maximum rotation performed by the strain principal directions is large enough.

Finally, the in-plane cyclic shear problem illustrated in Figure 3.1.a is studied considering five complete cycles of loading and reloading, with increasing amplitude. For this problem, permanent deformations are included in the analyses,

according to the definition (2.57) and adopting $b^+ = 0.15$ and $b^- = 0.05$. The structural responses obtained without (Figure 3.10.a) and with the multidirectional procedure (Figure 3.10.b) are compared. Once again, the enhanced MCR capabilities of the multidirectional procedure are evident. The absence of unilateral effects in Figure 3.10.a is responsible for a strong asymmetry in the cyclic dissipative behaviour, which is not supported by experimental evidence on shear (masonry or reinforced concrete) panels subjected to cyclic conditions (Magenes and Calvi, 1992; Anthoine and Magonette, 1994; Vecchio, 1999; Silva et *al.*, 2017). Besides the stiffness recovery appreciable in Figure 3.10.b, another effect strictly related to the adoption of the multidirectional procedure is the more adequate representation of the evolution of permanent deformations under cyclic shear. Here, the possibility of differentiating the damage processes depending on the orientation of the principal strain directions reflects in realistically taking into account the energy dissipated in the formation of both the orthogonal cracks.
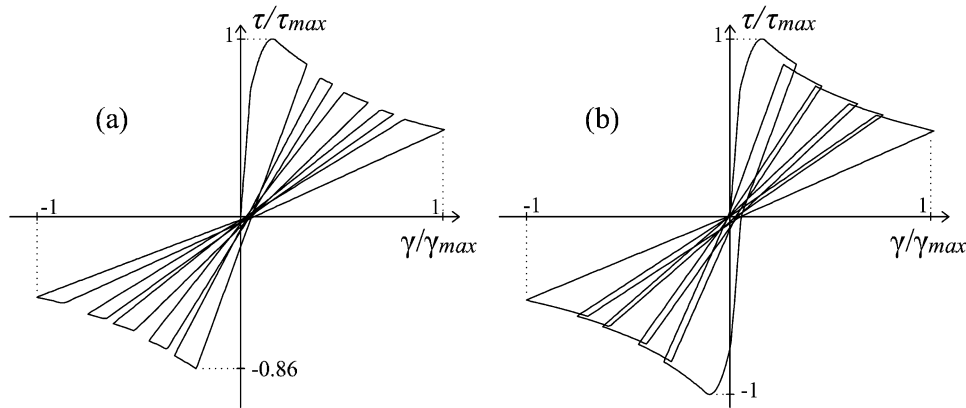
Figure 3.10: Structural response of the problem represented in Figure 3.1.a with multiple cycles: (a) without and (b) with the multidirectional approach.

This translates in considering the active damage values increasing even after loading reversal and has, as consequence, the accumulation both in loading and reloading of the permanent strains (2.57), defined on the base of $\dot{d}^+$ and $\dot{d}^-$ (see Figure 3.10.b). Contrarily, in a pure scalar damage formulation, the lack of unilateral effects in shear conditions implies, due to Eq. (12), an underestimation of the irreversible deformations in the reloading stages (see Figure 3.10.a). These enhanced dissipative capabilities under cyclic conditions ensured by the proposed multidirectional damage model are further underlined in Section 6.3, devoted to structural applications, where the comparison with experimental data is provided.

Chapter 4

Regularized strain tensor damage model

The formulation of the nonlocal integral scheme thought for the regularization of the new d^+/d^- damage model is presented in this chapter. Specifically, the peculiarities of the constitutive model which are, among the others, the differentiation between compressive and tensile regimes and the coincidence between the axes of orthotropy of the damage material and the principal directions of strain and stress, encourage some reflections about the variable or variables to be averaged. A discussion on this topic is presented in Section 4.1.1, in order to reduce the arbitrariness in the choice of the nonlocal quantity by relating it to the particular constitutive model adopted. Then, in Section 4.1.2, the regularized extension of the proposed damage model is developed, underlying the unchanged thermo-dynamic consistency of the formulation. Finally, in Section 4.2, the identification of the input parameters of the regularized damage model is addressed, resorting to the case of a uniaxially loaded bar. In this context, particular attention is directed towards the nature of the nonlocal internal length $l_{RG,}$ which is interpreted either as a regularization parameter or as a material property.

The mesh-size and mesh-bias independence of the results achieved with the nonlocal damage formulation are studied in Chapter 7, by means of structural applications involving different quasi-brittle materials as plain concrete, reinforced concrete and masonry elements.

4.1 Formulation

4.1.1 Choice of the variable to be averaged

In accordance with (Jirásek, 1998a), the quantities which can be selected as nonlocal have to satisfy some basic requirements. First of all, the averaging has to affect only the nonlinear response, while preserving the local character in the initial elastic phase. Moreover, a reasonable material behaviour has to be obtained in simple loading situations, not only at the onset of the strain localization but during the whole degradation process. Under uniaxial tension, for instance, the adequacy of a formulation is ensured when a localized strain profile and a vanishing stress state are reproduced at complete failure.

On the base of these criteria, the generic constitutive laws of the eligible nonlocal approaches are summarized in Eqs. (4.1), (4.2) and (4.3) (see (Jirásek, 1998a; Bažant and Jirásek, 2002)), where the quantity on which the averaging operator is applied is labeled with an overbar:

$$\boldsymbol{\sigma} = \boldsymbol{D}\Big(\boldsymbol{\varOmega}\big(\bar{\boldsymbol{T}}(\varepsilon_e)\big)\Big):\varepsilon_e \tag{4.1}$$

$$\boldsymbol{\sigma} = \Big(\boldsymbol{C_0} + \bar{\boldsymbol{C}}_d(\varepsilon_e)\Big)^{-1}:\varepsilon_e \tag{4.2}$$

$$\boldsymbol{\sigma} = \boldsymbol{D}(\bar{\varepsilon}_e):\varepsilon_e \tag{4.3}$$

In all cases, the averaging acts only after the appearance of the nonlinear behaviour; since the reversible strain ε_e, by which the stiffness operator $\boldsymbol{D}$ is multiplied, is always present in its local version, a local linear elastic response is initially ensured.

The nonlocal variable in Eq. (4.1) is the tensor $\boldsymbol{T}$ of the equivalent stress quantities τ_{ij}, according to which the damage tensor $\boldsymbol{\varOmega}$ is computed. In the damage model proposed in Chapter 2, the equivalent stress variables necessary to compute d^+ and d^- are τ^+ (Eq. (2.45)) and τ^- (Eq. (2.46)). This is an extension to a generalized constitutive law of the nonlocal isotropic damage models proposed by (Pijaudier-Cabot and Bažant, 1987) and (Saouridis and Mazars, 1992), based on the averaging of the equivalent energy release rate and of the equivalent strain, respectively.

The nonlocal version expressed in Eq. (4.2) concerns the averaging of the inelastic material compliance $\boldsymbol{C}_d$, which is a generalization of the averaging of the specific fracturing strain mentioned in (Pijaudier-Cabot and Bažant, 1987).

Finally, in Eq. (4.3), the nonlocal counterpart of the reversible strain tensor ε_e is adopted only in the definition of the stiffness degradation, while the strain in the stress-strain relation is maintained local, as described for instance in (Bažant and Lin, 1988).

An interesting aspect to be outlined is that the averaging of the damage variable $\boldsymbol{\Omega}$, suggested in (Bažant and Pijaudier-Cabot, 1988), is not included in the class of eligible regularized approaches because it fails in exhibiting full tensile stress relaxation at complete failure.

On the base of these considerations, the nonlocal approach chosen in order to develop a regularized version of the energy-equivalent d^+/d^- model is the one based on the averaging of the elastic strain tensor. Such a strategy is adequate for this specific damage formulation, because it allows to perform the assessment of the damage criteria in tension and compression ($g\pm = \tau\pm\ -r\pm\ \leq 0$,), which depend on the positive and negative split of the elastic stress tensor (see Eqs. (2.45) and (2.46)), on the base of the averaged strain $\bar{\varepsilon}_e$. Conversely, an averaging applied to $\tau\pm$, in line with the nonlocal version described in Eq. (4.1), would be weaker since the distinction between tensile and compressive regimes, inherent in the computation of the equivalent quantities, would be carried out on the basis of the local strains. Moreover, the elastic strain tensor as variable to be averaged allows to apply the multidirectional procedure proposed in Chapter 3 with reference to the principal directions of the regularized strain, which would be otherwise impossible limiting the averaging to the scalar equivalent quantities.

However, the averaging of the type expressed in Eq. (4.3) has to be contextualized, in order to fit with the constitutive operator presented in Eq. (2.24) and derived under the assumption of energy-equivalence. The direct application of Eq. (4.3) to $\boldsymbol{D_E}$ leads to:

$$\bar{\boldsymbol{D}}_{\boldsymbol{E}} = \boldsymbol{D}_{\boldsymbol{E}}\left(\bar{\boldsymbol{\varepsilon}}_{\boldsymbol{e}}, d^+\left(r^+\left(\bar{\boldsymbol{\varepsilon}}_{\boldsymbol{e}}\right)\right), d^-\left(r^-\left(\bar{\boldsymbol{\varepsilon}}_{\boldsymbol{e}}\right)\right)\right) = \bar{\boldsymbol{A}}^*\left(\bar{\boldsymbol{\varepsilon}}_{\boldsymbol{e}}, \bar{d}^+, \bar{d}^-\right) : \boldsymbol{D_0} : \bar{\boldsymbol{A}}^*\left(\bar{\boldsymbol{\varepsilon}}_{\boldsymbol{e}}, \bar{d}^+, \bar{d}^-\right) \quad (4.4)$$

where the regularized mapping operator $\bar{\boldsymbol{A}}^*$ is:

$$\bar{\boldsymbol{A}}^* = \bar{\boldsymbol{A}}^*\left(\bar{\boldsymbol{\varepsilon}}_{\boldsymbol{e}}, d^+\left(r^+\left(\bar{\boldsymbol{\varepsilon}}_{\boldsymbol{e}}\right)\right), d^-\left(r^-\left(\bar{\boldsymbol{\varepsilon}}_{\boldsymbol{e}}\right)\right)\right) = \sqrt{1-\bar{d}^+}\,\boldsymbol{Q}(\bar{\boldsymbol{\varepsilon}}_{\boldsymbol{e}}) + \sqrt{1-\bar{d}^-}\left[\boldsymbol{I} - \boldsymbol{Q}(\bar{\boldsymbol{\varepsilon}}_{\boldsymbol{e}})\right] \quad (4.5)$$

and the following equalities have been exploited:

$$\bar{r}^\pm = r^\pm\left(\bar{\boldsymbol{\varepsilon}}_{\boldsymbol{e}}\right) \qquad\qquad\qquad (4.6)$$

$$\bar{d}^{\pm} = d^{\pm}\left(r^{\pm}\left(\bar{\varepsilon}_e\right)\right) \qquad (4.7)$$

Actually, the definition of the secant stiffness presented in Eq. (4.4) has to be avoided because it violates the rotating nature of the local orthotropic damage model formulated in Chapter 2. As a matter of fact, except for the condition of homogeneous strains, the nonlocal regularized strain tensor $\bar{\varepsilon}_e$ is different from the local strain ε_e and this implies, for $\bar{D}_E \neq D_0$, the lack of coincidence between the axes of orthotropy of the damaged material and the principal directions of the elastic strain. Consequently, the coincidence between principal directions of strain and stress is no more guaranteed. The necessity of maintaining unaltered the rotating aspect of the model, which is beneficial in terms of stress locking reduction, obliges to propose a slightly different format of the constitutive regularized operator D_E, as:

$$\bar{D}_E = D_E\left(\varepsilon_e, d^+\left(r^+\left(\bar{\varepsilon}_e\right)\right), d^-\left(r^-\left(\bar{\varepsilon}_e\right)\right)\right) = \bar{A}^*\left(\varepsilon_e, \bar{d}^+, \bar{d}^-\right) : D_0 : \bar{A}^*\left(\varepsilon_e, \bar{d}^+, \bar{d}^-\right) \quad (4.8)$$

In $\bar{A}^*$, only the scalar damage variables are computed starting from the nonlocal counterpart of the elastic strain tensor, while the projection operator Q depends on the local elastic strain:

$$\bar{A}^* = \bar{A}^*\left(\varepsilon_e, d^+\left(r^+\left(\bar{\varepsilon}_e\right)\right), d^-\left(r^-\left(\bar{\varepsilon}_e\right)\right)\right) = \sqrt{1-\bar{d}^+}\,Q(\varepsilon_e) + \sqrt{1-\bar{d}^-}\left[I - Q(\varepsilon_e)\right] \quad (4.9)$$

Hence, exploiting Eqs. (4.8) and (4.9), the regularized d^+/d^- damage model maintains the same constitutive properties of the local formulation.

These observations can be generalized to the whole class of orthotropic damage models with rotating material principal directions. Different conclusions can be drawn for the class of orthotropic damage models with fixed axes of material orthotropy, for which a nonlocal procedure of the type shown in Eq. (4.3) holds, as demonstrated by the anisotropic nonlocal damage formulation for composites presented in (Kennedy and Nahan, 1996).

On the one hand, the choice of resorting to the elastic strain average distinguishes the present formulation from the majority of nonlocal damage models existing in the literature and, especially, from other d^+/d^- damage models recently developed to study concrete (He et al., 2015), reinforced concrete (Xenos and Grassl, 2016) and masonry structures (Toti et al., 2015), all of them characterized by the averaging of the tensile and compressive equivalent quantities. A comparison

between the two different regularized approaches is shown in Chapter 7, with reference to a reinforced concrete beam subjected to a four-point bending test. On the other hand, a nonlocal d^+/d^- damage formulation which can be considered similar to the present one is the model proposed in (Comi, 2001); in this formulation, the decomposition between tension and compression is performed taking into account the invariants of the averaged strain tensor. Differently from Comi's approach, where two internal lengths are assumed for tension and compression, in the present model only one internal length is considered, with the aim of limiting the number of input parameters.

Finally, it has to be remarked that the permanent strain ε_p is not regarded as a variable to be averaged, so that the local reversible strain ε_e is equal to the difference between the total strain ε and the permanent strain ε_p, both in their local version.

Therefore, the expression of the regularized counterpart of the local strain tensor ε_e, defined in a domain V, is:

$$\bar{\varepsilon}_e\left(x\right) = \frac{\displaystyle\int_V \alpha_0\left(\left|x - \xi\right|\right) \cdot \varepsilon_e\left(\xi\right) \cdot d\xi}{\displaystyle\int_V \alpha_0\left(\left|x - \xi\right|\right) \cdot d\xi} \tag{4.10}$$

where α_0 is the weight function, chosen, as in the majority of nonlocal models, as the Gauss distribution function, centred at x and simulating the interaction between point x and point ξ. Its definition is strictly related to the aforementioned internal length of the regularized continuum l_{RG} (see Figure 4.1):

$$\alpha_0\left(\left|x - \xi\right|\right) = \exp\left(-\frac{\left(\left|x - \xi\right|\right)^2}{2l_{RG}^2}\right) \tag{4.11}$$

The nonlocal operator in Eq. (4.10) is normalized by the expression at its denominator to keep an homogeneous distribution of the local variable unaltered. The Gauss weight function in Eq. (4.9) has an unbounded support, so its interaction radius, i.e. the largest distance of point ξ that influences the regularized variable at x, is infinite. In practice, as shown in Chapter 5, in finite element computations, a finite value of the interaction radius is considered, equal to $2l_{RG}$, in order to compute the nonlocal integral (4.10) over a finite volume V, dependent on x.
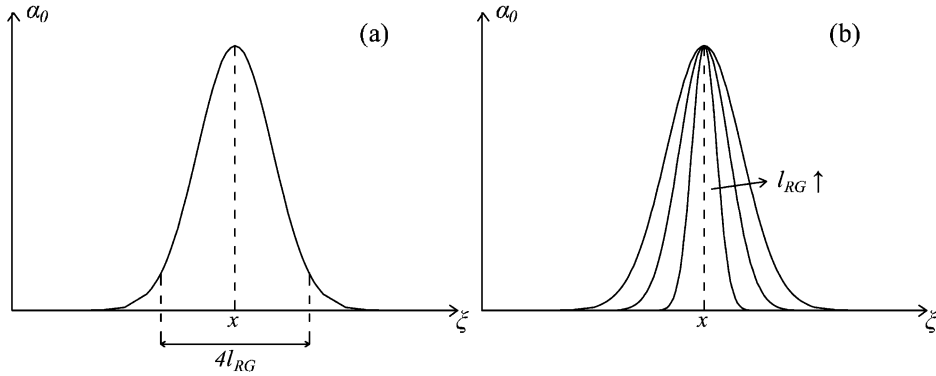
Figure 4.1: Averaging function α_0: (a) identification of l_{RG} and (b) variation of l_{RG}.

4.1.2 Thermo-dynamic framework

The free energy potential of the regularized damage model is defined with reference to the constitutive operator $\bar{D}_E$ presented in Eq. (4.8):

$$\psi\left(\varepsilon_e, d^+\left(r^+\left(\bar{\varepsilon}_e\right)\right), d^-\left(r^-\left(\bar{\varepsilon}_e\right)\right)\right) = \bar{\psi} = \frac{1}{2}\varepsilon_e : \bar{D}_E : \varepsilon_e \qquad (4.12)$$

As visible from Eq. (4.12), $\bar{\psi}$ depends only on the local strain tensor and on the damage variables $\bar{d}^+$ and $\bar{d}^-$, defined starting from the regularized strain tensor (4.10). No additional terms related to the regularization procedure are here present with respect to Eq. (2.30); hence, the standard framework of thermo-dynamics can be applied.

For what concerns the first principle of thermo-dynamics, its satisfaction can be stated by referring to (Carol and Willam, 1996) and (Wu and Xu, 2013), where it is affirmed that, in presence of scalar damage variables, the conservation of energy in the unloading-reloading regime, for a fixed state of degradation, is guaranteed.

Regarding the second principle of thermo-dynamics, the non-negativeness of the dissipated energy can be ensured by verifying the Clausius-Duheim inequality, which is the following:

$$\dot{\gamma} = -\dot{\bar{\psi}} + \boldsymbol{\sigma} : \dot{\boldsymbol{\varepsilon}} \geq 0 \qquad (4.13)$$

Replacing the total derivative of the free energy potential (4.12) with its partial derivatives with respect to the local strain and the internal variables, the inequality (4.13) becomes:

$$\dot{\gamma} = \left(\boldsymbol{\sigma} - \frac{\partial \overline{\psi}}{\partial \boldsymbol{\varepsilon}} \right) : \dot{\boldsymbol{\varepsilon}} - \frac{\partial \overline{\psi}}{\partial \overline{d}^+} \cdot \dot{\overline{d}}^+ - \frac{\partial \overline{\psi}}{\partial \overline{d}^-} \cdot \dot{\overline{d}}^- - \frac{\partial \overline{\psi}}{\partial \boldsymbol{\varepsilon}_p} \cdot \dot{\boldsymbol{\varepsilon}}_p \geq 0 \qquad (4.14)$$

On the one hand, the fulfillment of inequality (4.14) leads to the establishment of the constitutive law:

$$\boldsymbol{\sigma} = \frac{\partial \overline{\psi}}{\partial \boldsymbol{\varepsilon}} = \overline{\boldsymbol{D}}_E : \boldsymbol{\varepsilon}_e \qquad (4.15)$$

while on the other hand, it obliges the non-negativeness of each of the three dissipative quantities present in the following expression:

$$-\frac{\partial \overline{\psi}}{\partial \overline{d}^+} \cdot \dot{\overline{d}}^+ - \frac{\partial \overline{\psi}}{\partial \overline{d}^-} \cdot \dot{\overline{d}}^- - \frac{\partial \overline{\psi}}{\partial \boldsymbol{\varepsilon}_p} \cdot \dot{\boldsymbol{\varepsilon}}_p \geq 0 \qquad (4.16)$$

Due to the local nature of the permanent deformations, the proof of the non-negativeness of the dissipated energy related to this quantity coincides with the one provided in Section 2.4. The same reasoning holds for the derivatives of the free energy potential with respect to $\overline{d}^+$ and $\overline{d}^-$, whose non-negativeness can be proven considering the procedure described in Section 2.2.2. Finally, the only variables affected by the regularization are the rate of $\overline{d}^+$ and $\overline{d}^-$, which directly depend on the rate of the regularized damage thresholds:

$$\dot{\overline{d}}^\pm = \frac{\partial \overline{d}^\pm}{\partial \overline{r}^\pm} \cdot \dot{\overline{r}}^\pm \geq 0 \qquad (4.17)$$

The regularized damage variables are non-decreasing functions since the regularized damage thresholds, as their local counterparts, have to satisfy the Kuhn-Tucker and persistency conditions (see Section 2.5). Hence, the second principle of thermo-dynamics for the regularized d^+/d^- damage model is fully satisfied.

As just mentioned, the evolution of the regularized damage is ruled by the Kuhn-Tucker and persistency conditions, which allow distinguishing between the situations of loading, unloading and re-loading:

$$\dot{\overline{r}}^\pm \geq 0 \qquad \overline{g}^\pm = \overline{\tau}^\pm - \overline{r}^\pm \leq 0 \qquad \dot{\overline{r}}^\pm \cdot \overline{g}^\pm = 0 \qquad (4.18)$$

$$\dot{\overline{r}}^\pm \cdot \dot{\overline{g}}^\pm = 0 \qquad (4.19)$$

According to Eqs. (4.18) and (4.19), in the loading case $\dot{\bar{r}}^{\pm} > 0$ and $\bar{g}^{\pm} = 0$; in the unloading or in the initial undamaged situation, $\dot{\bar{r}}^{\pm} = 0$ and $\bar{g}^{\pm} < 0$. The definition for the non-decreasing regularized damage threshold can be deduced by the persistency condition (4.19):

$$\bar{r}^{\pm} = \max\left(r_0^{\pm} ; \max_{[0,t]}\left(\bar{\tau}^{\pm}\right) \right) \tag{4.20}$$

where the initial value r_0 is the same as in the local model (see Eq. (2.50)) while $\bar{\tau}^{\pm}$ represent the equivalent quantities computed replacing in Eqs. (2.45) and (2.46) the elastic local stress (2.25) with the elastic regularized one $\bar{\sigma}_e$:

$$\bar{\sigma}_e = \sigma_e\left(\bar{\varepsilon}_e\right) = D_0 : \bar{\varepsilon}_e \tag{4.21}$$

4.2 Calibration of the parameters of the regularized model

Hereafter, the superscript $^{\pm}$ used for distinguishing a quantity between tension and compression is intentionally left out for the sake of brevity.

In order to provide a correct representation of the energy dissipated during the degradation process, the calibration of the material parameters has to be performed. In (Bažant and Oh, 1983), it is affirmed that three quantities are sufficient to describe the material fracture properties, and these quantities are the uniaxial tensile strength f_t, the fracture energy G^+_f and the dissipation length l_{dis}, which represents an effective width corresponding to the hypothesis of uniform strain within the fracture process zone.

In order to obtain the correct energy dissipation, independently of the discretization, Bažant and Oh proposed the so-called crack band model, which is based on the principle that the width of the fracture process zone l_{dis} can be replaced by a discretization length h (related to the size and orientation of the finite element) in the computation of the softening modulus, provided that the correct fracture energy G^+_f is however caught. Hence, the crack band model can be defined as a "local" regularization approach, since the mesh-objectivity is ensured by means of a rescaling of the post-localization part of the local softening law, and not by means of a nonlocal spatial averaging over neighbour finite elements. It has to be noted that, in this way, the regularization of the problem is only partial because the mesh-

bias dependence is not eliminated. Moreover, the crack band model renounces to properly describe the width of the fracture process zone: since the localization occurs in one element, its size depends inevitably on the discretization.

In the case of nonlocal damage models, a reliable identification procedure is more complex because two sets of parameters affect the structural response: not only the ones defining the softening law at a local (element-wise) level but also the regularized internal length l_{RG}, which describes the spatial interaction of material points by controlling the spread of the averaging functi'on (see Eq. (4.11)). An intrinsic connection exists between l_{RG} and the local softening law since the width of the fracture process zone l_{dis}, strictly related to l_{RG}, rules the fracture properties of the material, hence also its softening (local) modulus, in accordance with (Bažant and Oh, 1983).

The relationship between l_{dis} and l_{RG} represents the focus of a regularizedv nonlocal calibration strategy. In (Bažant and Pijaudier-Cabot, 1989), the coincidence between l_{RG} and l_{dis} is imposed a priori and their value, obtained experimentally by measuring the energy dissipation in concrete specimens in which damage remains diffused and others in which damage localizes, results equal to 2.7 the maximum aggregate size d_{max}. The main limitations of such a relationship lie in the fact that it holds only for the nonlocal approach there adopted (based on the averaging of the damage variable) and it has not been verified for materials with other mechanical properties or with different aggregate sizes.

In (Ferrara and di Prisco, 2001), a linear dependence between l_{dis} and l_{RG} is found by assuming the local constitutive law independent of l_{RG}. Fixing the specific dissipated energy g_f, for each value of l_{RG}, a corresponding fracture energy G_f is computed by performing a numerical structural analysis upon complete failure. The value of l_{dis} associated to l_{RG} is then determined as G_f / g_f. Two main inconsistencies can be identified in such a procedure: firstly, the dependence of the local constitutive law on the dissipation length l_{dis} is neglected; secondly, the fracture energy G_f is not treated as a mechanical parameter, since it varies with the nonlocal length l_{dis}.

Contrariwise, the calibration strategy adopted in the present work for the determination of the parameters of the regualrized damage model is based on the idea of ensuring the evaluation of the fracture energy G_f independently of the choice of the internal length l_{RG}. Although such a procedure has been followed in the works of (Nguyen and Houlsby, 2007), its analogies with the crack band model proposed by (Bažant and Oh, 1983) have never been outlined. In fact, the majority of the nonlocal formulations presented in the literature is focused on highlighting the

differences between the nonlocal model and the crack band model; hereafter, a different interpretation is proposed, addressed to consider both the approaches governed by only one ruling parameter, which is the fracture energy G_f. In view of this consideration, in the regularized damage model here proposed, as in the crack band model, the fracture energy G_f does not show any size dependence. Therefore, the possibility of calibrating the internal length by fitting the size effect on the nominal fracture energy of specimens (Jirásek et *al.*, 2004) is here not contemplated. Instead, as stated in (Bažant and Jirásek, 2002), if the fracture process zone is sufficiently smaller than the whole structure, the consideration of the fracture energy as an intrinsic material property can be considered valid.

In the following subsections, firstly the calibration strategy adopted is described and its choice justified with respect to other existing calibration approaches. Then, the problem of a bar uni-axially loaded in tension is exploited with the aim of showing how the approach works and how it makes the regularized model comparable with the crack band one by (Bažant and Oh, 1983).

4.2.1 Calibration strategy

In a crack band model, damage localizes in a band of one element-width; therefore, the dissipated energy per unit area G_f is the area enclosed under the element stress-strain curve g_f, multiplied by the element size h. The local softening modulus H_d, derived in Section 2.5 for different types of damage evolution laws, can be defined by replacing the generic length l used in Eqs. (2.82), (2.84b), (2.90) and (2.100) with the element size h, whose computation, depending on the size and orientation of the discretization, can be performed referring to (Oliver, 1989).

In regularized models, two main difficulties appear. Firstly, due to the introduction of the internal length l_{RG}, the width of the zone in which the dissipation takes place does not limit to one element; it is broader and not a priori determinable. Secondly, the specific dissipated energy g_f, whose definition is provided in Eq. (4.22) for the specific case of uniaxial tensile loading and null permanent deformations, is not uniform within the dissipation zone.

$$g_f\left(\boldsymbol{x}\right) = \int_0^\infty \boldsymbol{\sigma} : \dot{\boldsymbol{\varepsilon}} \cdot dt = \int_0^\infty \left(1 - d^+\left(r^+\left(\bar{\varepsilon}\left(x\right)\right)\right)\right) \cdot E \cdot \varepsilon \cdot \dot{\varepsilon} \cdot dt \qquad (4.22)$$

Although Eq. (4.22) refers to a particular load case, it allows to do some considerations which hold general validity: from its analysis, it is clear that the specific dissipated energy evaluated at a point x is affected by the strain values of

all the points whose distance from x is lower than the interaction radius. Hence, it varies with x and depends not only on the type of damage evolution law but also on the specific nonlocal damage model adopted, i.e. on the quantity chosen as nonlocal (Eq. (4.10)) and on the averaging function α_0 (Eq. (4.11)).

In order to deal with these difficulties, the procedure hereafter proposed aims to identify l_{dis} as the width of a uniformly damaged crack band in a local continuum which dissipates the same amount of energy of the same band present in the regularized continuum. To guarantee this energetic equivalence, by exploiting the correspondence between the cohesive crack model and the crack band model, the local specific dissipated energy g_f has to depend on l_{dis} according to the relation:

$$g_f = \frac{G_f}{l_{dis}\left(l_{RG}\right)} \tag{4.23}$$

Eq. (4.23) is equivalent to compute the local softening modulus of the nonlocal damage model by replacing the generic length l with l_{dis}. In Eq. (4.23), the dependence of the dissipation length l_{dis} on the internal length l_{RG} is highlighted, in order to stress how the local constitutive behaviour is affected by the internal length l_{RG}.

The analytical evaluation of l_{dis} starting from Eq. (4.23) is generally unfeasible, because its value depends on the internal length in a nonlinear way, on the other parameters, elastic and inelastic, defining the local constitutive law, on the type of softening law adopted (2.69) and on the nonlocal approach considered (nonlocal averaging function α_0 and quantity chosen as nonlocal). In (Zaho et al., 2005) the specific case of a linear softening law is taken into account to derive the analytical nonlinear relationship between l_{dis} and l_{RG}.

In (Jirásek, 1998b), the idea of providing an analytical solution for l_{dis} is abandoned in order to extend the applicability of the calibration strategy to a wider range of softening laws and to a wider range of nonlocal approaches. On the contrary, the use of predefined trends relating the ductility of the local softening law η and the ratio l_{dis}/l_{RG} are proposed to define l_{dis} in an iterative manner. The iterative procedure is required because η depends on l_{dis}, according to the following expression:

$$\eta = \frac{G_f/l_{dis}}{f^2/2 \cdot E} \tag{4.24}$$

However, the graphs presented in (Jirásek, 1998b) do not cover the case of high local ductility and include only a limited number of combinations of softening laws, nonlocal weight functions and nonlocal variables. Specifically, the averaging of the elastic strain (4.10), in conjunction with the use of the Gauss function for α_0 (4.11), as well as the adoption of softening laws different from the exponential and the linear ones, as the Gaussian damage function proposed in Eq. (2.80) are not foreseen; therefore, these graphs can not be adopted for the calibration of the present regularized damage model.

Hence, a different calibration strategy is here preferred, the one proposed in (Nguyen and Houlsby, 2007), which consists in identifying the nonlinear relation between l_{dis} and l_{RG}, for the material parameters of interest, by performing some structural analyses upon complete failure of a uniaxially loaded bar (see Figure 4.2). In order to trigger the strain localization, a defect is considered in the central part of the bar.

Moreover, to apply this procedure to the d^+/d^- damage model here formulated, the bar is considered under both uniaxial tension (displacement u as plotted in Figure 4.2) and uniaxial compression (displacement u with opposite sign with respect to the one plotted in Figure 4.2). In this way, starting from a unique value of the internal length l_{RG}, two values of l_{dis} are obtained, one for tension l^+_{dis} and one for compression l^-_{dis}, respectively.
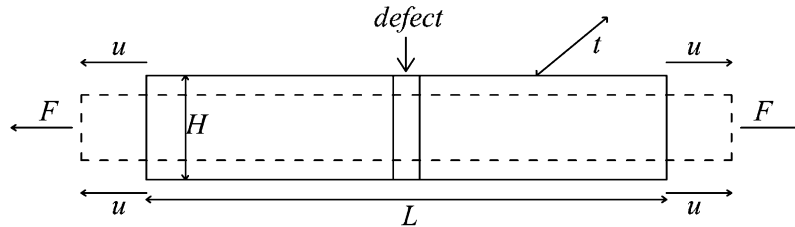
Figure 4.2: Bar under uniaxial loading, considered for the calibration of the nonlocal parameters.

Referring indistinctly to tension or compression, the main steps, which characterize this approach, are summarized in Table 4.1. The procedure starts from the known material constants E and v, the uniaxial strength f, the fracture energy G_f, the parameter ξ defining the intensity of ε_p according to Eq. (2.61) and the internal length l_{RG}.

Table 4.1: Calibration strategy adopted in the regularized damage model.

(i) Assume $k_{dis}^{(1)}$ such that $l_{dis}^{(1)} = k_{dis}^{(1)} l_{RG}$.

(ii) Compute the specific dissipated energy $g_f^{(1)}$, the local ductility parameter $\eta^{(1)}$ and the local softening modulus $H_d^{(1)}$, using $l_{dis}^{(1)}$, according to Eq. (4.23), Eq. (4.24) and one of Eqs. (2.82), (2.84b), (2.90) and (2.100), respectively.

(iii) Perform the numerical analyses of a bar uni-axially loaded with imposed displacement u at both ends (see Figure 4.2), adopting $g_f^{(1)}$ (or, equivalently, $H_d^{(1)}$ or $\eta^{(1)}$) as local constitutive parameter.

(iv) Compute the fracture energy $G_f^{(2)}$, by dividing the area subtended by the force F - displacement u resulting curve for the ligament area $t \times H$ (see Figure 4.2).

(v) Compute $k_{dis}^{(2)}$ as $G_f^{(2)}/ (g_f^{(1)} \cdot l_{RG})$, such that $l_{dis}^{(2)} = k_{dis}^{(2)} l_{RG}$.

(vi) Repeat n times the steps from (i) to (v), starting from a different value of $k_{dis}^{(1)}$, in order to obtain a different value of $k_{dis}^{(2)}$.

(vii) Plot two curves in a graph representing in abscissae the local ductility parameter η and in ordinates the k_{dis} parameter defining l_{dis}: one curve is given by the n couples of ($\eta^{(1)}, k_{dis}^{(1)}$), the other by the n couples of ($\eta^{(1)}, k_{dis}^{(2)}$).

(viii) Evaluate the intersection of the two curves found in the step (vii), which represents the dissipation length l_{dis} able to dissipate the correct fracture energy G_f.

The calibration strategy here presented is very versatile. because it can be applied to any set of material parameters and to any kind of constitutive law (isotropic, orthotropic, with or without irreversible strains).

4.2.2 Application of the calibration strategy: nonlocal damage approach compared with the crack band model

In this section, the steps described in Table 4.1 are followed to calibrate the regularized damage model for a specific set of mechanical parameters, which are collected in Table 4.2. The calibration strategy is performed only under tension, i.e. to find l^+_{dis}. The procedure to identify l^-_{dis} is analogous and it has been omitted.

Table 4.2: Set of material parameters adopted in the calibration.

E	ν	f^+	f^-	G_f^+	G_f^-	ξ	l_{RG}
[MPa]	[-]	[MPa]	[MPa]	[N/mm]	[N/mm]	[-]	[mm]
38000	0.21	2.8	-42.3	0.037	30.00	0.00	6.00

The problem considered for carrying the structural analysis under complete failure is the bar subjected to an imposed elongation at both ends, as shown in Figure 4.2, with the following geometric sizes: $L = 101$ mm, $H = 10$ mm, $t = 1$ mm. The defect is modelled considering a section reduction equal to 10% in the central part of the bar. A mesh of 101 bilinear quadrilateral finite elements is considered.

The two curves obtained according to the steps of Table 4.2 are plotted in Figure 4.3.a. The intersection occurs in correspondence with the value $k_{dis} = 3.73$, which defines the dissipation length $l_{dis} = 3.73 \cdot l_{RG} = 22.4$ mm able to ensure the correct fracture energy G_f^+, as visible from the force F – displacement u curve displayed in Figure 4.3.b.
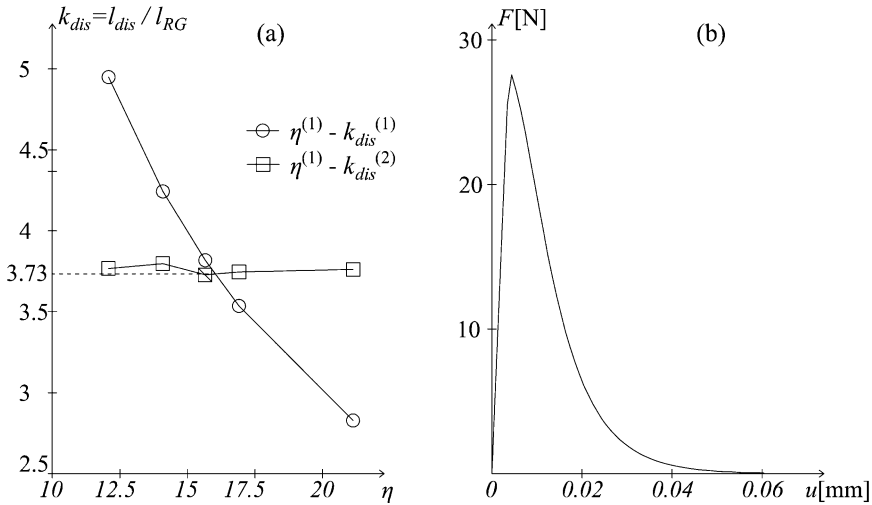
Figure 4.3: (a) Calibration procedure for material parameters in Table 4.2; (b) *F-u* curve obtained with the calibrated dissipation length.

In order to assess the objectivity of the calibration procedure, a check omitted in (Nguyen and Houlsby, 2007), the entity and the kind of the defect in the central element are varied (Figure 4.4.) together with the mesh refinement (Figure 4.5), maintaining fixed the dissipation length obtained from the calibration procedure shown in Figure 4.3.a.
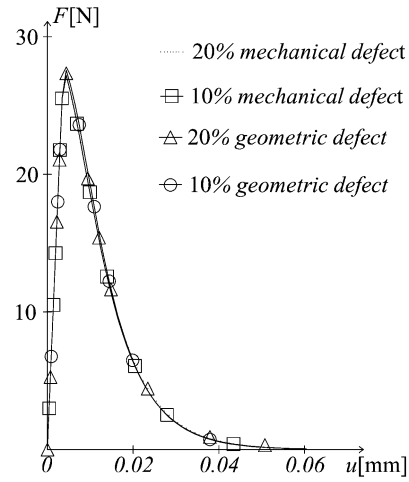
Figure 4.4: Response of the bar under tension for different defects.
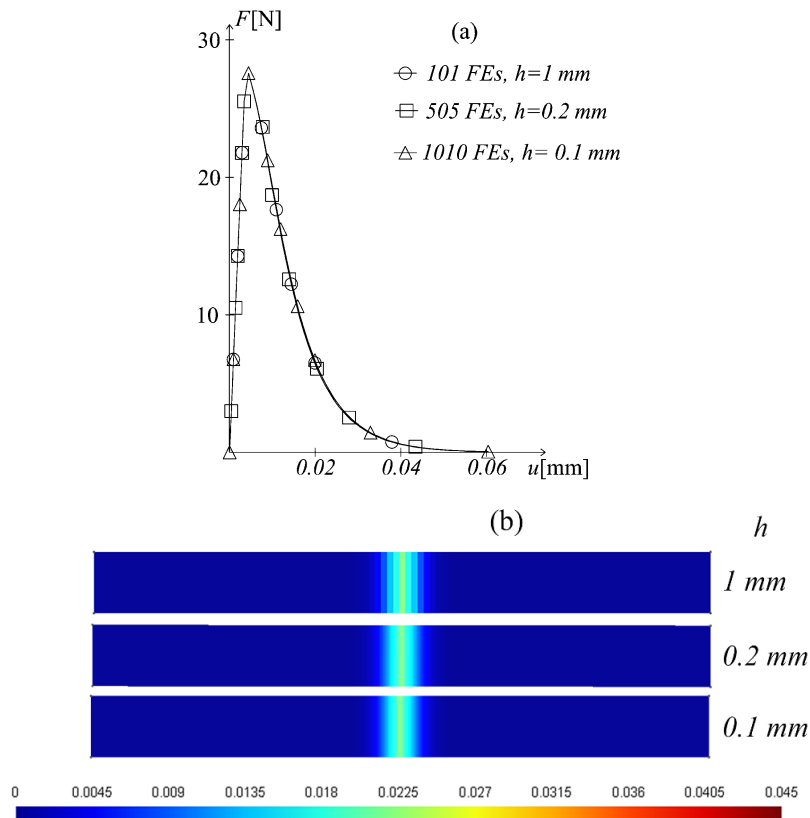
Figure 4.5: Response of the bar under uniaxial tension for different mesh refinements: (a) *F - u* curves; (b) maximum principal strain localization.

The almost full coincidence between the different curves in Figure 4.4 and Figure 4.5.a allows to conclude that neither the choice of the defect nor the

discretization affect the results of the calibration procedure, performed by means of the bar under uniaxial loading conditions.

Moreover, the effect of ε_p is considered, referring to the new definition proposed in Eq. (2.61), replacing the value $\xi = 0$ with $\xi = 0.3$. As commented in Section 2.5, irreversible strains are modelled within a coupled dissipative framework, meaning that their inclusion affects damage evolution (see Eq. (2.70)) in such a way to maintain unaltered the specific energy dissipated with respect to the case of null permanent deformations. For this reason, the consideration of ε_p does not modify the calibration procedure shown in Figure 4.3.a for the case of $\xi = 0$. In fact, as expected, the calibrated dissipation length and the corresponding force F – displacement u curve for $\xi = 0.3$, shown in Figure 4.6, are identical to the ones presented in Figure 4.3.

To analyse the dependence of the results on the parameter l_{RG}, the calibration shown in Figure 4.3.a for $l_{RG} = 6$ mm is repeated for different values of the internal length, in particular for $l_{RG} = 3$ mm and $l_{RG} = 9$ mm. The values of the relative dissipation length k_{dis} obtained are 4.09 and 3.80, respectively. In Figure 4.7, the results of the uniaxial problem adopted for the calibration by varying l_{RG} are exhibited, in terms of F – u curves (Figure 4.7.a) and maximum principal strain localization (Figure 4.7.b).
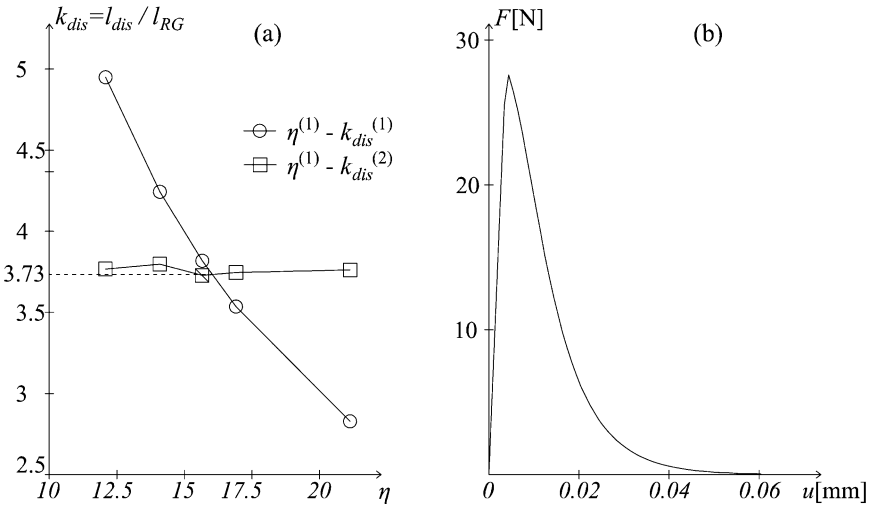
Figure 4.6: (a) Calibration procedure for $\xi = 0.3$; (b) F - u curve obtained with the calibrated dissipation length.
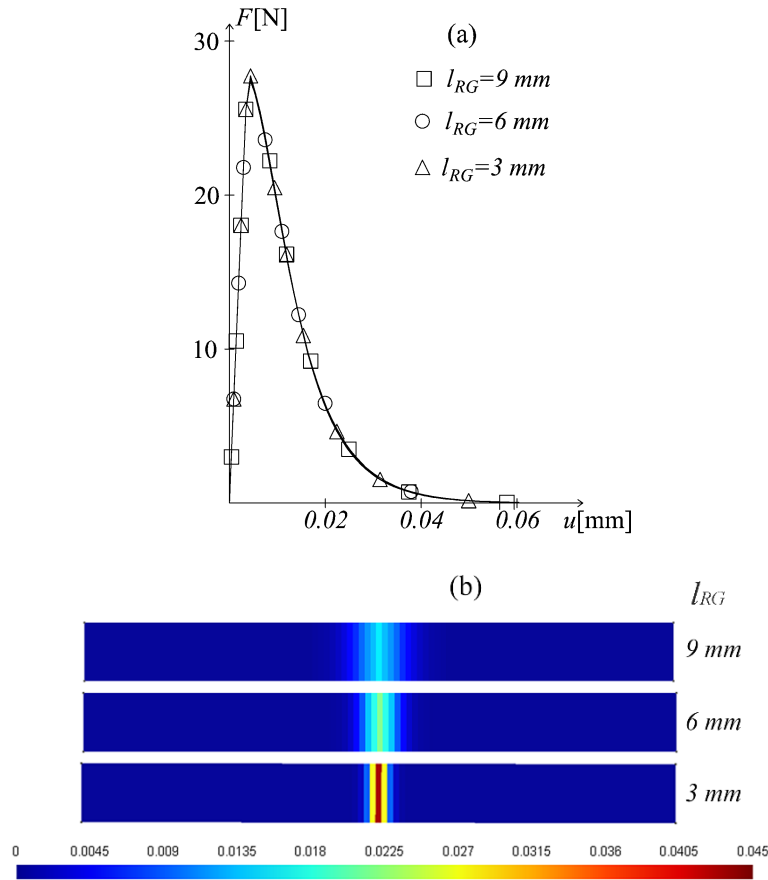
Figure 4.7: Response of the bar under uniaxial tension for different internal lengths: (a) F - u curves; (b) maximum principal strain localization.

It is worth remarking that the independence of the structural response from the internal length (Figure 4.7.a) is obtained thanks to the calibration procedure adopted, which ensures the representation of the fracture energy G_f^+, by properly identifying the value of the dissipation length l_{dis}, related to l_{RG}. On the contrary, the width of the localization band (Figure 4.7.b) is affected by the nonlocal parameter, and increases with it.

Finally, the problem of the bar uniaxially loaded in tension, previously studied with the regularized approach, is solved with the local crack band model, considering three different mesh refinements: 35, 101 and 203 finite elements. The results, in terms of global response curves and strain localization, are displayed in Figure 4.8.a and Figure 4.8.b, respectively.
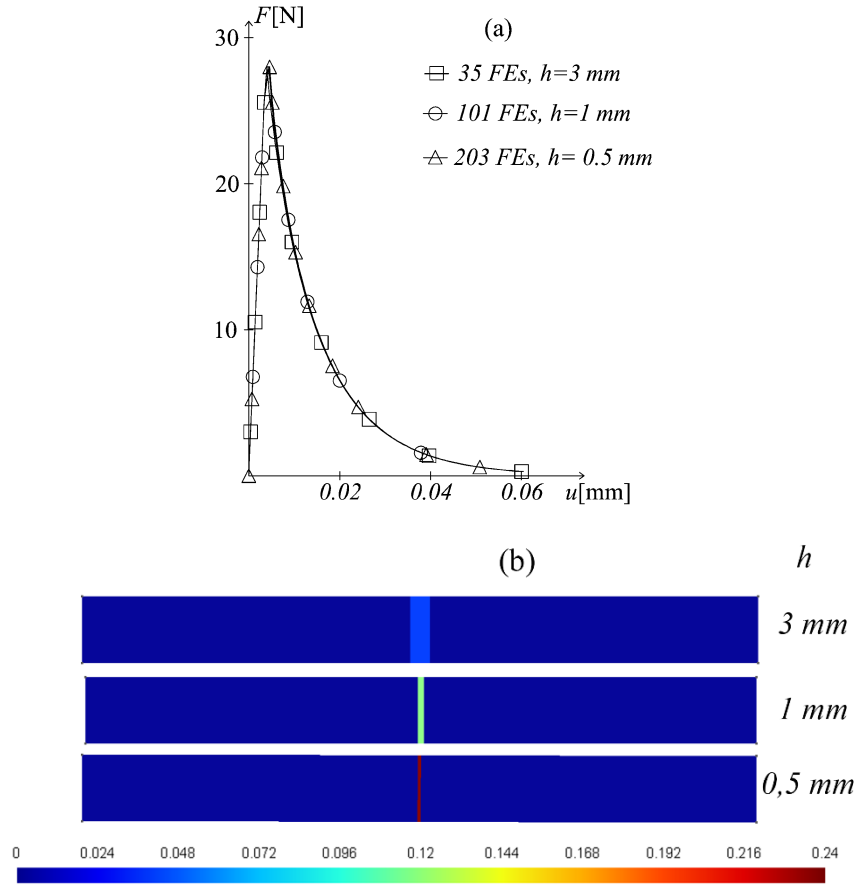
Figure 4.8: Response of the bar under uniaxial tension with a local approach for different mesh refinements: (a) F - u curves; (b) maximum principal strain localization.

With the local approach, on the one hand, the mesh-size independence of the solution in terms of dissipated energy (see Figure 4.8.a) is guaranteed, because of the adoption of a softening modulus adjusted according to the size h of the finite element (Bažant and Oh, 1983). On the other hand, the width of the localization band (Figure 4.8.b) depends drastically on the mesh refinement, coinciding with h.

The majority of the nonlocal formulations, such as, for instance, the recent work by (Xenos, and Grassl, 2016), is focused on the differences between a nonlocal approach and a local one in case of different mesh refinements: specifically, the capability of the nonlocal approach to maintain unaltered the localization band width (Figure 4.5.b.) is usually opposed to the corresponding incapability of the local one (Figure 4.8.b). Here, the main interest is different and is addressed to stress the analogies, and not the divergences, between the regularized model here proposed and the crack band model by Bažant and Oh. As a matter of fact, by comparing Figure 4.7 with Figure 4.8, a parallel between the internal length l_{RG} and

the mesh size *h* can be found: both these terms do not affect the *F-h* curves but their variation influences clearly the localization bandwidth.

Broadening the discussion, it is possible to affirm that the regularized damage model here presented does not require the identification of an internal length on the base of physical reasons. In fact, the procedure shown in Table 4.1 ensures the correct representation of the fracture energy G_f, independently of the value of the internal length, as proven in Figure 4.7.a. Hence, it holds the same versatility of the crack band approach, which needs only the standard material properties (elastic constants, fracture energies and strengths) for the identification of all the model components. Contrariwise, as discussed in (Bažant and Jirásek, 2002), the main cause of nonlocality is usually associated to the material heterogeneity and, consequently, the nonlocal length has to be representative of such material heterogeneity. This fact obliges to find a relation between the internal length and the heterogeneity maximum size. If for concrete a large number of studies have been performed on this topic, for instance in (Bažant and Pijaudier-Cabot, 1989), and a value of approximately 3 times the aggregate size has been found to be the characteristic one, for other materials, as masonry, likewise data are not available. Moreover, in line with these reasoning, homogeneous materials can not be studied with a nonlocal approach, due to the impossibility of finding a valid definition of the nonlocal length.

Together with the advantages, the regularized model here presented has in common with the local approach one of its drawbacks. In fact, if, on the one hand, an arbitrary choice of the internal length allows to correctly describe the dissipated energy, on the other hand, as visible from Figure 4.7.b, it does not allow a detailed description of the width of the fracture process zone.

Although not very common, the interpretation of the internal length as a regularization parameter more than a physical constant can be found in the phase field model proposed in (Wu, 2017). There, exploiting mode I and mixed mode problems, it is proven that the variation of the internal length negligibly affects the global overall response, except for the localization bandwidth.

Despite the analogies found between the regularization damage model and the crack band model, the motivating reason for which the former is here proposed as positive evolution of the latter is its widely recognized better performance in terms of mesh-bias objectivity of the results.

Chapter 5

Numerical implementation of the damage model

The algorithmic implementation of the damage model developed in Chapter 2, Chapter 3 and Chapter 4 is described in the present chapter, with the intent of showing that the new energy-equivalent d^+/d^- formulation, combined with the inclusion of permanent deformations, with a multidirectional treatment of damage and with a regularized approach, follows an efficient fully strain-driven formalism.

The contents are organized as follows. First of all, the algebraic system of equations which defines the global equilibrium in a displacement-based finite element code is recalled. Then, the numerical algorithms of the constitutive law are provided. For the sake of clarity, the problems characterized by the simultaneous presence of permanent deformations and damage and by the use of a multidirectional damage procedure are addressed separately. Specifically, both an explicit and an implicit computation of the permanent deformations is considered. Finally, the implementation details necessary to include in the code the regularized procedure are described and commented.

Part of the topics proposed in the present chapter is already published in (Cervera et *al*., 2018).

5.1 Algebraic implementation

The damage formulation is implemented in a displacement-based finite element code written in a FORTRAN environment. In order to face the material non-linearity, the numerical algorithm works in an incremental-iterative way.

Within a generic load increment, going from the step $n-1$ to the step n, the equilibrium global equations at each iteration i are solved using the Picard method, based on the adoption of the global secant stiffness matrix S. The algebraic system to be solved assumes the following form:

$$S\left({}^{i-1}_{n}u\right)\delta\, {}^{i}_{n}u = -R\left({}^{i-1}_{n}u\right) \tag{5.1}$$

where $\delta\, {}^{i}_{n}u$ is the iterative displacement vector correction adopted to compute the iterative displacement vector ${}^{i}_{n}u$

$$ {}^{i}_{n}u = {}^{i-1}_{n}u + \delta\, {}^{i}_{n}u \tag{5.2}$$

and the residual force vector R is expressed in terms of the internal P and external F force vectors:

$$R\left({}^{i-1}_{n}u\right) = P\left({}^{i-1}_{n}u\right) - {}_{n}F = S\left({}^{i-1}_{n}u\right){}^{i-1}_{n}u - {}_{n}F \tag{5.3}$$

The choice of a Picard method has two main reasons. On the one hand, it is addressed to avoid the computation of the consistent tangent stiffness matrix necessary for the application of the Newton Raphson method. In fact, in the case of the constitutive d^+/d^- damage model here presented, this matrix is non-symmetric and requires the evaluation of the derivative of the projection operator (2.15), which is not straightforward, as demonstrated in (Faria et *al*., 2000) for the original d^+/d^- damage formulation.

On the other hand, it allows taking advantage, from a computational point of view, of the symmetric constitutive stiffness operator D_E (2.24). In fact, the global stiffness matrix S is obtained by assembling the local secant operator D_{sec}, deriving from the following equality:

$$D_{sec} : \varepsilon = D_E : \left(\varepsilon - \varepsilon_p\right) \tag{5.4}$$

Although D_{sec} is not uniquely defined, it can be easily expressed as:

$$D_{sec} = D_E - \frac{\left(D_E : \varepsilon_p\right) \otimes \left(D_E : \varepsilon_p\right)}{\varepsilon : \left(D_E : \varepsilon_p\right)} \qquad (5.5)$$

As visible from Eq. (5.5), a non symmetric local secant matrix is obtained if the constitutive local operator is not symmetric. Thanks to the recourse to the energy-equivalence assumption, a symmetric D_{sec} is ensured by the constitutive symmetric operator D_E (2.24) and this guarantees a symmetric algebraic system to be solved (Eq. (5.1)).

In all the structural analyses shown in Chapter 6, Chapter 7 and Chapter 8, the convergence in a time step n is attained when both the ratio between the norm of the iterative residual forces R and the external forces F (see Eq. (5.3)) and the ratio between the norm of the iterative displacement increments $\delta\,^i_n u$ and the total displacements $^i_n u$ (see Eq. (5.2)) are lower than 1%.

5.2 Numerical algorithm of the constitutive law

5.2.1 Standard scalar damage model with permanent deformations

The objective of the numerical algorithms hereafter proposed is to provide the solution at time n, in terms of stresses ($^n\sigma$), strains ($^n\varepsilon_p$, $^n\varepsilon_e$) and damage variables ($^n d\pm$, $^n r\pm$), starting from the converged known quantitites at time $n-1$.

In purely elasto-degrading formulations, i.e. when irreversible deformations are not considered, the algorithm is straightforward, since the elastic strain tensor ε_e coincides with the total strain tensor ε, which is a known quantity at the beginning of each iteration i in a standard displacement-based finite element environment. In presence of elasto-plastic damage models, such a coincidence does not hold anymore and efficient computational algorithms are required to avoid a further iterative procedure for defining the internal variables within each global equilibrium iteration i.

A first possibility consists in performing the updating of the permanent strain tensor explicitly, using a forward Euler algorithm. This means that $^{n+1}\varepsilon_p$ is computed only once, at the end of the load step n-th, after the attainment of the convergence. This allows to evaluate, within each iteration, the elastic strain tensor ε_e directly from the iterative displacements (5.2) and to define, on the basis of it, the damage variables d^+ and d^-, the projection operator Q (2.15), the secant stiffness D_E (2.24) and, finally, the nominal stress tensor σ (2.33).

A second possibility is to use an implicit backward Euler scheme and consists in evaluating the permanent strain tensor $^{n,\ i}\varepsilon_p$ at each iteration i of the *n-th* step exactly as it is done for all the other quantities (elastic strain, damage thresholds, damage variables, stress).

An explicit computation of the permanent strain tensor increases the robustness of the numerical procedure, but it is accurate only if sufficiently small time steps are adopted. On the other side, an implicit approach is more accurate but it can suffer from convergence difficulties.

While the permanent strain evolution law (2.57) can be evaluated explicitely or implicitely, the permanent strain increment defined in (2.61), due to its intrinsic dependence on the quantity $\dot{\varepsilon}_d^*$ (2.60), fits better for an implicit computation. However, it would be possible to assess it explicitely, simply replacing the quantity $\dot{\varepsilon}_d^*$, evaluated in the hypothesis of null permanent deformations, with the actual quantity $\dot{\varepsilon}_d$. For these reasons, in the present section, the numerical algorithm including the explicit computation of ε_p refers to the permanent strain evolution law (2.57) while the one contemplating the implicit computation of ε_p is developed considering the definition (2.61).

The numerical algorithm of the $d^+/\ d^-$ damage model with the explicit computation of the irreversible deformations is synthetized in Table 5.1.

In implicit algorithms for elasto-plastic damage models, the recourse to the operator split method, described in (Ju ,1989; Simó and Huges, 1998), is frequently adopted (Lee and Fenves, 2001; Wu et *al*., 2006; Taqieddin and Voyiadjis, 2009). This approach is not adequate for the constitutive law here proposed because the decoupling between the elasto-plastic behaviour and damage, proper of the operator split method, does not hold for the present formulation, which is founded on the assumption of a unique failure criterion to completely describe the inelastic phenomena. Hence, the numerical algorithm of the constitutive law is performed through the adoption of a prediction-correction strategy, able to maintain the efficiency of a full strain-driven algorithm even in presence of implicitly computed irreversible deformations. This strategy is characterized by a damage predictor phase and a plastic-damage corrector one and results naturally from the definition itself of the permanent strain evolution law (2.61), as clarified also by Figure 2.6.

Table 5.1: Numerical algorithm of the constitutive law for the d^+/d^- damage model with an explicit computation of the permanent strains (2.57).

<u>Load increment n:</u>

Known quantities:

$^{n-1}\varepsilon, \, ^{n-1}\sigma, \, ^{n-1}\varepsilon_p, \, ^{n-1}d^{\pm}, \, ^{n-1}r^{\pm}$

<u>Iteration i:</u>

(i) Compute the nominal elastic strain tensor $^{n,i}\varepsilon_e$ from the known total iterative strain $^{n,i}\varepsilon$: $^{n,i}\varepsilon_e = ^{n,i}\varepsilon - ^{n-1}\varepsilon_p$.

(ii) Compute the projection operators $^{n,i}Q$ and $I - ^{n,i}Q$ by means of the spectral decomposition of the nominal strain tensor $^{n,i}\varepsilon_e$ (Eq. (2.15)).

(iii) Compute the elastic stress tensor $^{n,i}\sigma_e$ (Eq. (2.25)).

(iv) Compute the equivalent stress quantities $^{n,i}\tau^{\pm}$ (Eqs. (2.45) and (2.46)).

(v) If $^{n,i}\tau^{\pm} > ^{n-1}r^{\pm}$: update damage thresholds $^{n,i}r^{\pm} = ^{n,i}\tau^{\pm}$ and update $^{n,i}d^{\pm}$ by Eq. (2.69).

If $^{n,i}\tau^{\pm} < ^{n-1}r^{\pm}$: no updating is required, $^{n,i}r^{\pm} = ^{n-1}r^{\pm}$ and $^{n,i}d^{\pm} = ^{n-1}d^{\pm}$.

(vi) Compute the operator $^{n,i}A^*$(Eq. (2.18)):

$$^{n,i}A^* = \sqrt{1 - ^{n,i}d^+} \cdot ^{n,i}Q + \sqrt{1 - ^{n,i}d^-} \cdot \left(I - ^{n,i}Q \right).$$

(vii) Compute the nominal stress $^{n,i}\sigma$ (Eq. (2.33)): $^{n,i}\sigma = ^{n,i}A^* : D_0 : ^{n,i}A^* : ^{n,i}\varepsilon_e$.

(viii) Check convergence at a global level:
NO convergence: go to the iteration $i+1$ and start again from (i).
YES convergence:

Update: $^n\varepsilon = ^{n,i}\varepsilon, \, ^n\sigma = ^{n,i}\sigma, \, ^nd^{\pm} = ^{n,i}d^{\pm}, \, ^nr^{\pm} = ^{n,i}r^{\pm}$.

- Update the permanent strain tensor (Eq. (2.57)) and the elastic strain tensor:

$$\Delta^n\varepsilon_p = \left[b^+ \cdot H\left(^nd^+ - ^{n-1}d^+ \right) + b^- \cdot H\left(^nd^- - ^{n-1}d^- \right) \right] \frac{\left\langle ^{n,i}\sigma_e : \left(^n\varepsilon - ^{n-1}\varepsilon \right) \right\rangle}{^{n,i}\sigma_e : ^{n,i}\varepsilon_e} \cdot ^{n,i}\varepsilon_e$$

$$^n\varepsilon_p = ^{n-1}\varepsilon_p + \Delta^n\varepsilon_p ; \quad ^n\varepsilon_e = ^n\varepsilon - ^n\varepsilon_p .$$

- Go to the next load increment $n+1$.

In the first phase, a purely elasto-degrading material behaviour is assumed. This means that the total iterative strain increment $^{n,i}\Delta\varepsilon$, which is a known quantity at the beginning of each iteration, is considered completely reversible, while the irreversible deformations are fixed to the last converged value $^{n-1}\varepsilon_p$. All the quantities (stress, strains, internal variables) associated to this predictive state are identified by their corresponding symbols with the apex *, in analogy with the quantities provided in Eq. (2.60).

Then, a plastic-damage corrector phase is necessary, in order to return back the predictive stresses and the internal variables to the damage surface, due to the development of permanent deformations together with the increase of damage. In this stage, the dependence of the permanent strain increment (2.61) on the reversible strain ε_e and on the stress σ imposes a further consideration to be done. Taking inspiration from the procedure described in (Faria et *al*, 1998) for the numerical computation of the effective stress tensor and adjusting it to the present damage formulation and to the permanent strain evolution law (2.61), the following relations can be exploited in order to adopt an efficient numerical algorithm.

$$\varepsilon_e = \varepsilon_e^* - \left[\xi^+ H\left(\Delta d^{+*}\right) + \xi^- H\left(\Delta d^{-*}\right) \right] \cdot \frac{\left\langle \sigma : \Delta\varepsilon_d^* \right\rangle}{\sigma : \varepsilon_e} \varepsilon_e \tag{5.6}$$

Inverting Eq. (5.6) in order to have an expression for the predictive reversible strain ε_e^* and exploiting the coaxiality (Eq. (5.7)) between the stress σ and the elastic strain ε_e (Section 2.2.1), according to which

$$\boldsymbol{1}_\sigma = \boldsymbol{1}_\varepsilon \qquad\qquad \sigma : \varepsilon_e = \|\sigma\| \boldsymbol{1}_\sigma : \|\varepsilon_e\| \boldsymbol{1}_\varepsilon = \|\sigma\| \cdot \|\varepsilon_e\| \tag{5.7}$$

it is possible to write:

$$\varepsilon_e^* = \frac{\|\sigma\|\|\varepsilon_e\| + \left[\xi^+ H\left(\Delta d^{+*}\right) + \xi^- H\left(\Delta d^{-*}\right) \right] \cdot \left\langle \|\sigma\| \boldsymbol{1}_\sigma : \Delta\varepsilon_d^* \right\rangle}{\|\sigma\|} \frac{\varepsilon_e}{\|\varepsilon_e\|} \tag{5.8}$$

Eq. (5.8) reveals the coaxiality between the elastic strain tensor and the predictive elastic strain ε_e^*, whose definition can be provided in the following way:

$$\varepsilon_e^* = \left\|\varepsilon_e^*\right\| \boldsymbol{1}_{\varepsilon*} \qquad\qquad \boldsymbol{1}_{\varepsilon*} = \boldsymbol{1}_\varepsilon$$

$$\left\|\varepsilon_e^*\right\| = \|\varepsilon_e\| + \left[\xi^+ H\left(\Delta d^{+*}\right) + \xi^- H\left(\Delta d^{-*}\right) \right] \cdot \left\langle \boldsymbol{1}_\sigma : \Delta\varepsilon_d^* \right\rangle \tag{5.9}$$

Form Eq.(5.9), the elastic strain tensor can be expressed as a function of ε_e^*:

$$\varepsilon_e = \left(1 - \frac{\left[\xi^+ H\left(\Delta d^{+*}\right) + \xi^- H\left(\Delta d^{-*}\right) \right] \cdot \left\langle \boldsymbol{1}_\sigma : \Delta\varepsilon_d^* \right\rangle}{\left\|\varepsilon_e^*\right\|} \right) \left\|\varepsilon_e^*\right\| \boldsymbol{1}_{\varepsilon*} \tag{5.10}$$

In the end, by considering the coaxiality expressed in Eq. (5.7), valid in terms of predictive stress/elastic predictive strain tensors, the expression of the elastic strain, completely defined in terms of predictive quantities, is:

$$\varepsilon_e = \left(1 - \frac{\left[\xi^+ H\left(\Delta d^{+*}\right) + \xi^- H\left(\Delta d^{-*}\right)\right] \cdot \left\langle \sigma^* : \Delta\varepsilon_d^* \right\rangle}{\left\|\varepsilon_e^*\right\| \cdot \left\|\sigma^*\right\|}\right) \varepsilon_e^* \tag{5.11}$$

The plastic damage corrector phase for the integration of the d^+/d^- constitutive law starts from the expression (5.11) for the elastic strain. The complete numerical algorithm, thought for taking into account the implicit computation of the irreversible deformations (2.61), is summarized in Table 5.2 and Table 5.3, by distinguishing between the damage predictor and the plastic-damage corrector phases.

Table 5.2: Numerical algorithm of the constitutive law for the d^+/d^- damage model with an implicit computation of the permanent strains (2.61): damage predictor phase.

<u>Load increment n:</u>

Known quantities:

$^{n-1}\varepsilon, \ ^{n-1}\sigma, \ ^{n-1}\varepsilon_p, \ ^{n-1}d^{\pm}, \ ^{n-1}r^{\pm}$

<u>Iteration i, Damage predictor phase:</u>

(i)   Compute the predictive elastic strain tensor $^{n,i}\varepsilon_e^*$ in the assumptions of $^{n,i}\Delta\varepsilon_e^* = \ ^{n,i}\Delta\varepsilon, \ ^{n,i}\Delta\varepsilon_p^* = 0$ and $^{n,i}\varepsilon_p^* = \ ^{n-1}\varepsilon_p$: $^{n,i}\varepsilon_e^* = \ ^{n,i}\varepsilon - \ ^{n-1}\varepsilon_p$.

(ii)   Compute the projection operators $^{n,i}Q^*$ and $I - \ ^{n,i}Q^*$ by means of the spectral decomposition of the nominal strain tensor $^{n,i}\varepsilon_e^*$ (Eq. (2.15)).

(iii)   Compute the elastic stress tensor $^{n,i}\sigma_e^* = D_0 : \ ^{n,i}\varepsilon_e^*$ (Eq. (2.25)).

(iv)   Compute the equivalent stress quantities $^{n,i}\tau^{\pm*}$ (Eqs. (2.45) and (2.46)).

(v)   If $^{n,i}\tau^{\pm*} > \ ^{n-1}r^{\pm}$: update damage thresholds $^{n,i}r^{\pm*} = \ ^{n,i}\tau^{\pm*}$ and update $^{n,i}d^{\pm*}$ by Eq. (2.69).

        If $^{n,i}\tau^{\pm*} < \ ^{n-1}r^{\pm}$: no updating is required, $^{n,i}r^{\pm*} = \ ^{n-1}r^{\pm}$ and $^{n,i}d^{\pm*} = \ ^{n-1}d^{\pm}$.

(vi)   Compute the operator $^{n,i}A^*$ (Eq. (2.18)):

        $^{n,i}A^* = \sqrt{1 - \ ^{n,i}d^{+*}} \cdot \ ^{n,i}Q^* + \sqrt{1 - \ ^{n,i}d^{-*}} \cdot \left(I - \ ^{n,i}Q^*\right)$.

(vii)   Compute the nominal stress $^{n,i}\sigma^*$ (Eq. (2.33)): $^{n,i}\sigma^* = \ ^{n,i}A^* : D_0 : \ ^{n,i}A^* : \ ^{n,i}\varepsilon_e^*$.

(viii) Compute the inelastic strain increment according to the strain increment decomposition (2.55): $^{n,i}\Delta\varepsilon_d^* = \ ^{n,i}\Delta\varepsilon - C_0 : (^{n,i}\sigma^* - \ ^{n-1}\sigma)$.

Table 5.3: Numerical algorithm of the constitutive law for the d^+/d^- damage model with an implicit computation of the permanent strains (2.61): plastic-damage corrector phase.

<u>Load increment n:</u>

<u>Iteration i, plastic damage corrector phase:</u>
Known quantities:

$^{n-1}\boldsymbol{\varepsilon}, \, ^{n-1}\boldsymbol{\sigma}, \, ^{n-1}\boldsymbol{\varepsilon_p}, \, ^{n-1}d^{\pm}, \, ^{n-1}r^{\pm}, \, ^{n,i}\boldsymbol{\varepsilon_e}^*, \, ^{n,i}\boldsymbol{\sigma}^*, \, ^{n,i}\Delta\boldsymbol{\varepsilon_d}^*, \, ^{n,i}\Delta d^{\pm *}$.

Plastic correction

(ix)   Compute the elastic strain tensor $^{n,i}\boldsymbol{\varepsilon_e}$ (Eq. (5.11)):

$$^{n,i}\boldsymbol{\varepsilon_e} = \left(1 - \frac{\left[\xi^+ H\left(^{n,i}\Delta d^{+*} \right) + \xi^- H\left(^{n,i}\Delta d^{-*} \right) \right] \cdot \left\langle ^{n,i}\boldsymbol{\sigma}^* : {}^{n,i}\Delta\boldsymbol{\varepsilon_d}^* \right\rangle}{\left\| ^{n,i}\boldsymbol{\varepsilon_e}^* \right\| \cdot \left\| ^{n,i}\boldsymbol{\sigma}^* \right\|} \right) {}^{n,i}\boldsymbol{\varepsilon_e}^*$$

(x)   Compute the permanent strain tensor according to the total strain decomposition (2.51): $^{n,i}\boldsymbol{\varepsilon_p} = {}^{n,i}\boldsymbol{\varepsilon} - {}^{n,i}\boldsymbol{\varepsilon_e}$.

Damage correction

(xi)   Compute the projection operators $^{n,i}\boldsymbol{Q}$ and $\boldsymbol{I} - {}^{n,i}\boldsymbol{Q}$ by means of the spectral decomposition of the nominal strain tensor $^{n,i}\boldsymbol{\varepsilon_e}$ (Eq. (2.15)).

(xii)   Compute the elastic stress tensor $^{n,i}\boldsymbol{\sigma_e}$ (Eq. (2.25)).

(xiii)   Compute the equivalent stress quantities $^{n,i}\tau^{\pm}$ (Eqs. (2.45) and (2.46)).

(xiv)   If $^{n,i}\tau^{\pm} > {}^{n-1}r^{\pm}$: update damage thresholds $^{n,i}r^{\pm} = {}^{n,i}\tau^{\pm}$ and update $^{n,i}d^{\pm}$ by Eq. (2.69).

If $^{n,i}\tau^{\pm} < {}^{n-1}r^{\pm}$: no updating is required, $^{n,i}r^{\pm} = {}^{n-1}r^{\pm}$ and

$^{n,i}d^{\pm} = {}^{n-1}d^{\pm}$.

(xv)   Compute the operator $^{n,i}\boldsymbol{A}^*$ (Eq. (2.18)):

$$^{n,i}\boldsymbol{A}^* = \sqrt{1 - {}^{n,i}d^+} \cdot {}^{n,i}\boldsymbol{Q} + \sqrt{1 - {}^{n,i}d^-} \cdot \left(\boldsymbol{I} - {}^{n,i}\boldsymbol{Q} \right) .$$

(xvi)   Compute the nominal stress $^{n,i}\boldsymbol{\sigma}$ (Eq. (2.33)): $^{n,i}\boldsymbol{\sigma} = {}^{n,i}\boldsymbol{A}^* : \boldsymbol{D_0} : {}^{n,i}\boldsymbol{A}^* : {}^{n,i}\boldsymbol{\varepsilon_e}$.

(xvii)   Check convergence at a global level:
NO convergence: go to the iteration $i+1$ and start again from (i) of Table 5.1.
YES convergence:

- Update: $^{n}\boldsymbol{\varepsilon} = {}^{n,i}\boldsymbol{\varepsilon}, \, ^{n}\boldsymbol{\sigma} = {}^{n,i}\boldsymbol{\sigma}, \, ^{n}d^{\pm} = {}^{n,i}d^{\pm}, \, ^{n}r^{\pm} = {}^{n,i}r^{\pm}$ and go to the next increment load $n+1$.

5.2.2 Multidirectional damage model

In the present section, the numerical algorithm of the d^+/d^- multidirectional damage model is described, with reference to plane problems, combining it with an explicit updating of the permanent strain tensor (2.57), analogously to the scheme presented in Table 5.1. It is synthetized in Table 5.4.

Three subroutines are adopted in order to make clearer the working principles of the multidirectional procedure. They are:

- *Damage multidirectional updating (ε_e, $d_{1,2}^{\pm}$, $r_{1,2}^{\pm}$, $\tau^{\pm}$; $d^{\pm}$, $\dot{d}^{\pm}$, $r^{\pm}$):* it provides the active damage value d^+ (d^-), its rate $\dot{d}^+$ ($\dot{d}^-$) and the active damage threshold r^+ (r^-) on the basis of the current damage equivalent stress quantity τ^+ (τ^-) which is compared with the damage threshold r_1^+ or r_2^+ (r_1^- or r_2^-), saved in the region where the principal maximum (minimum) strain (ε_e) direction falls (input parameters ε_e, $d_{1,2}^{\pm}$, $r_{1,2}^{\pm}$, $\tau^{\pm}$; output parameters $d^{\pm}$, $\dot{d}^{\pm}$ and $r^{\pm}$);

- *Damage multidirectional saving ($d^{\pm}$, $r^{\pm}$, ε_e; $d_{1,2}^{\pm}$, $r_{1,2}^{\pm}$):* the converged d^+ (d^-) damage value is saved as d_1^+ or d_2^+ (d_1^- or d_2^-) in a region, depending on the maximum (minimum) strain (ε_e) direction which has generated it (input parameters $d^{\pm}$, $r^{\pm}$, ε_e; output parameters $d_{1,2}^{\pm}$, $r_{1,2}^{\pm}$);

- *Damage regions updating:* in loading conditions, for load Type (ii), it changes the bisectors and the amplitudes of the damage regions, with reference to (3.4).

Analyzing Table 5.4 and comparing it with the numerical algorithm in the case of a standard scalar damage formulation (see Table 5.1), it is easy to identify the differences in two main stages. The first is the updating of the tensile (compressive) damage within the iteration, which is performed with reference to the current maximum (minimum) direction of ε_e.

The second is the saving of the damage variables after the attainment of the global equilibrium convergence, which maintains these information about damage directionality.

Finally, in presence of Load Type (ii), there is the necessity of monitoring the rotation of the principal directions, and, consequently, to update the damage regions, which have an evolving nature.

Table 5.4: Numerical algorithm of the multidirectional $d+/d-$ damage model with an explicit computation of the permanent strains (2.57).

<u>Load increment n:</u>

Known quantities:

$^{n-1}\varepsilon$, $^{n-1}\sigma$, $^{n-1}\varepsilon_p$, $^{n-1}d_{1,2}{}^{\pm}$, $^{n-1}r_{1,2}{}^{\pm}$; only for load Type (ii): $^{n-1}r_\theta{}^{\pm}$.

<u>Iteration i:</u>

(i)   Compute the nominal elastic strain tensor $^{n,i}\varepsilon_e$: $^{n,i}\varepsilon_e = {}^{n,i}\varepsilon - {}^{n-1}\varepsilon_p$.

(ii)   Compute the projection operators $^{n,i}Q$ and $I - {}^{n,i}Q$ for $^{n,i}\varepsilon_e$ (Eq. (2.15)).

(iii)   Compute the elastic stress tensor $^{n,i}\sigma_e$ (Eq. (2.25)).

(iv)   Compute the equivalent stress quantities $^{n,i}\tau{}^{\pm}$ (Eqs. (2.45) and (2.46)).

(v)   Only for load Type (ii): compute the equivalent deviation quantity $^{n,i}\tau_\theta{}^{\pm}$ (Eq. (3.2)) on the base of $^{n,i}\varepsilon_e$;

   if $^{n,i}\tau_\theta{}^{\pm} < {}^{n-1}r_\theta{}^{\pm}$: $^{n,i}r_\theta{}^{\pm} = {}^{n,i}\tau_\theta{}^{\pm}$ and call "*Damage regions updating*";

   if $^{n,i}\tau_\theta{}^{\pm} > {}^{n-1}r_\theta{}^{\pm}$: $^{n,i}r_\theta{}^{\pm} = {}^{n-1}r_\theta{}^{\pm}$.

(vi)   Call "*Damage multidirectional updating($^{n,i}\varepsilon_e$, $^{n-1}d_{1,2}{}^{\pm}$, $^{n-1}r_{1,2}{}^{\pm}$,*

   $^{n,i}\tau{}^{\pm}$; $^{n,i}d{}^{\pm}$, $^{n,i}\dot{d}{}^{\pm}$, $^{n,i}r{}^{\pm}$)"

(vii)   Compute the operator $^{n,i}A^*$ (Eq. (2.18)):

   $$^{n,i}A^* = \sqrt{1 - {}^{n,i}d^+}\,{}^{n,i}Q + \sqrt{1 - {}^{n,i}d^-}\left(I - {}^{n,i}Q\right).$$

(viii) Compute the nominal stress $^{n,i}\sigma$ (Eq. (2.33)): $^{n,i}\sigma = {}^{n,i}A^* : D_0 : {}^{n,i}A^* : {}^{n,i}\varepsilon_e$.

(ix)   Check convergence at a global level:
   NO convergence: go to the iteration $i+1$ and start again from (i).
   YES convergence:

- Update: $^n\varepsilon = {}^{n,i}\varepsilon$, $^n\sigma = {}^{n,i}\sigma$; only for load Type (ii): $^n r_\theta{}^{\pm} = {}^{n,i}r_\theta{}^{\pm}$.

- Update permanent strain tensor (Eq. (2.57)) and elastic strain tensor:

$$\Delta^n\varepsilon_p = \left[b^+ \cdot H\left(^n d^+ - {}^{n-1}d^+\right) + b^- \cdot H\left(^n d^- - {}^{n-1}d^-\right)\right]\frac{\left\langle {}^{n,i}\sigma_e : \left(^n\varepsilon - {}^{n-1}\varepsilon\right)\right\rangle}{{}^{n,i}\sigma_e : {}^{n,i}\varepsilon_e} \cdot {}^{n,i}\varepsilon_e$$

$$^n\varepsilon_p = {}^{n-1}\varepsilon_p + \Delta^n\varepsilon_p; \quad ^n\varepsilon_e = {}^n\varepsilon - {}^n\varepsilon_p.$$

- For load Type (i): call "*Damage multidirectional saving ($^{n,i}d{}^{\pm}$, $^{n,i}r{}^{\pm}$,*

   $^n\varepsilon_e$; $^n d_{1,2}{}^{\pm}$, $^n r_{1,2}{}^{\pm}$)".

- For load Type (ii): if $^n r_\theta{}^{\pm} < \cos(\theta_{min})$: call "*Damage multidirectional saving*

   ($^{n,i}d{}^{\pm}$, $^{n,i}r{}^{\pm}$, $^n\varepsilon_e$; $^n d_{1,2}{}^{\pm}$, $^n r_{1,2}{}^{\pm}$)";

   if $^n r_\theta{}^{\pm} = \cos(\theta_{min})$: $^n d_{1,2}{}^+ = {}^{n,i}d^+$; $^n d_{1,2}{}^- = {}^{n,i}d^-$; $^n r_{1,2}{}^+ = {}^{n,i}r^+$; $^n r_{1,2}{}^- = {}^{n,i}r^-$.

- Go to the next increment load $n+1$.

5.3 Implementation details of the regularized formulation

5.3.1 Symmetry and sparsity of the secant stiffness matrix

The adoption of the Picard method described in Section 5.1 with respect to the Newton Raphson for the solution of the algebraic system of equilibrium equations is particularly advantageous in nonlocal regularized damage analyses, although this fact is scarsely recognized. One of the few examples related to the adoption of a secant method combined with nonlocality dates back to the work by Bažant and Lin (Bažant and Lin, 1988).

As noticed in (Jirásek and Patzák, 2002), the nonlocal tangent stiffness matrix is always non symmetric and this fact is intrinsically related to the interactions between close finite elements imposed by the nonlocal approach. Only in (Comi and Perego, 2001b) there is the proposal of a symmetric tangent stiffness matrix to be used in nonlocal analyses, but it is obtained through a computationally expensive procedure, by performing a double averaging both on the damage energy release rate and then on the damage variables. Contrariwise, the secant stiffness matrix S (see Eq. (5.1)) ruling the Picard method is symmetric both in a local approach and in a nonlocal one, the only difference being that in a regularized approach the secant constitutive operator D_{sec} expressed in Eq. (5.5) has to be replaced by its regularized counterpart:

$$\bar{D}_{sec} = \bar{D}_E - \frac{\left(\bar{D}_E : \varepsilon_p\right) \otimes \left(\bar{D}_E : \varepsilon_p\right)}{\varepsilon : \left(\bar{D}_E : \varepsilon_p\right)} \qquad (5.12)$$

where $\bar{D}_E$ is the regularized constitutive operator defined in Eq. (4.8).

Moreover, the use of a secant stiffness matrix eliminates a drawback proper of nonlocality, which is the increase in the bandwidth of the sparse stiffness matrix (Jirásek and Patzák, 2002). In fact, the distribution of non-zero entries in the matrix varies in nonlocal analyses with respect to local ones because of the inclusion of the tangent stiffness component, which takes into account the nonlocal interaction among close finite elements.

Hence, the adoption of the Picard method for the numerical implementation of the regularized damage model described in Chapter 4 allows to save computational resources thanks to the use of a symmetric stiffness matrix which maintains the same degree of sparsity held in a local analysis.

5.3.2 Algorithmic extension for the regularized model

The numerical algorithm, which allows computing the constitutive law in a regularized nonlocal damage model, does not undergo substantial changes from the one adopted in a local formulation and shown, in different versions, in Section 5.2. As a matter of fact, the regularization procedure does not affect the algorithmic efficiency seen in Table 5.1, Table 5.2, Table 5.3 and Table 5.4 and similarly permits an evaluation of the stress tensor by means of a full-strain driven procedure.

The only additional step required by the regularized approach consists in computing the averaging of the elastic strain tensor by means of Eq. (4.10), in order to obtain its nonlocal counterpart. The integral present in the definition of the regularized strain (4.10) of element i is computed numerically by Gaussian quadrature including in the summation only the Gauss points belonging to the set Ω_i of interacting elements. The following discrete version of expression (4.10) is considered, referring to the generic component ε_{ekl} of the elastic strain tensor:

$$\bar{\varepsilon}_{e_{kl}}\left(\boldsymbol{x}_{Ci}\right) = \frac{\sum_{j=1}^{N_i} w_j \alpha_0\left(\left|\boldsymbol{x}_{Ci} - \boldsymbol{x}_j\right|\right) \cdot \varepsilon_{e_{kl}}\left(\boldsymbol{x}_j\right)}{\sum_{j=1}^{N_i} w_j \alpha_0\left(\left|\boldsymbol{x}_{Ci} - \boldsymbol{x}_j\right|\right)} \tag{5.13}$$

where w_j are the integration weights, $\boldsymbol{x}_{Ci}$ and $\boldsymbol{x}_j$ the spatial coordinates of the centroid of element i and of the Gauss point j, respectively, and N_i the number of Gauss points included in Ω_i. As visible from Eq. (5.13), the damage variables (and all the related quantities) employ a reduced integration scheme and are evaluated at the centroid of the finite element with spatial coordinates $\boldsymbol{x}_C$. For each element i, the neighbouring set of interacting elements Ω_i is determined by means of a purely geometric criterion: all elements whose centroid has a distance lower or equal to two times the internal length l_{RG} (see Eq. (4.11)) with respect to the centroid of the element i belong to this set. This works better when the internal length is large compared to the dimension of the finite elements. The adopted procedure is illustrated in Figure 5.1.
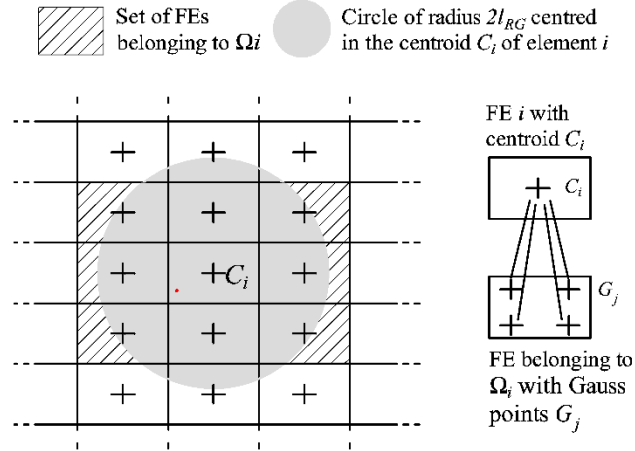
Figure 5.1: Evaluation of the interaction nonlocal domanin Ω_i highlighting the interactions taken into account in the computation of the nonlocal integral quantity.

The interaction information is computed only once, in the initialization procedure before the beginning of the incremental iterative procedure. Specifically, for each element i, the set of interacting elements Ω_i is saved. This allows to keep low the additional computational costs required by the regularized model with respect to a local one. The evaluation of the regularized quantity is performed at each iteration, before the evaluation of the equivalent stress variables. In order to avoid storage overload, the data concerning the weight function are not stored in the initial step; consequently, they have to be computed every time, starting from the distance between the centroid of element i x_{Ci} and of the Gauss point j x_j.

The complete numerical algorithm for the regularized damage model, in presence of the implicit computation of the permanent strain tensor (2.61), is summarized in Table 5.5 and Table 5.6, by distinguishing between the damage predictor phase and the plastic-damage corrector one.

Table 5.5: Numerical algorithm of the constitutive law for the regularized d^+/d^- damage model with an implicit computation of the permanent strains (2.61): damage predictor phase.

<u>Load increment n:</u>

Known quantities:

$^{n-1}\boldsymbol{\varepsilon}$, $^{n-1}\overline{\boldsymbol{\sigma}}$, $^{n-1}\boldsymbol{\varepsilon_p}$, $^{n-1}\overline{d}^{\pm}$, $^{n-1}\overline{r}^{\pm}$

<u>Iteration i, Damage predictor phase:</u>

(i) Compute the predictive elastic strain tensor $^{n,\,i}\boldsymbol{\varepsilon}_e^{\,*}$ in the assumptions of $^{n,\,i}\Delta\boldsymbol{\varepsilon}_e^{\,*} = {}^{n,\,i}\Delta\boldsymbol{\varepsilon}$, $^{n,\,i}\Delta\boldsymbol{\varepsilon}_p^{\,*} = 0$ and $^{n,\,i}\boldsymbol{\varepsilon}_p^{\,*} = {}^{n-1}\boldsymbol{\varepsilon_p}$: $^{n,\,i}\boldsymbol{\varepsilon}_e^{\,*} = {}^{n,\,i}\boldsymbol{\varepsilon} - {}^{n-1}\boldsymbol{\varepsilon_p}$.

(ii) Compute the projection operators $^{n,\,i}\boldsymbol{Q}^*$ and $\boldsymbol{I} - {}^{n,\,i}\boldsymbol{Q}^*$ by means of the spectral decomposition of the nominal strain tensor $^{n,\,i}\boldsymbol{\varepsilon}_e^{\,*}$ (Eq. (2.15)).

(iii) Compute the regularized averaging of $^{n,\,i}\boldsymbol{\varepsilon}_e^{\,*}$ by means of Eq. (5.13), $^{n,\,i}\overline{\boldsymbol{\varepsilon}}_e^{\,*}$.

(iv) Compute the elastic stress tensor $^{n,\,i}\overline{\boldsymbol{\sigma}}_e^{\,*} = \boldsymbol{D_0} : {}^{n,\,i}\overline{\boldsymbol{\varepsilon}}_e^{\,*}$. (Eq. (4.21)).

(v) Compute the regularized equivalent stress quantities $^{n,\,i}\overline{\tau}^{\pm*}$ (Eqs. (2.45) and (2.46)).

(vi) If $^{n,\,i}\overline{\tau}^{\pm*} > {}^{n-1}\overline{r}^{\pm}$: update damage thresholds $^{n,i}\overline{r}^{\pm*} = {}^{n,\,i}\overline{\tau}^{\pm*}$ and update $^{n,\,i}\overline{d}^{\pm*}$ by Eq. (2.69).

  If $^{n,\,i}\overline{\tau}^{\pm*} < {}^{n-1}\overline{r}^{\pm}$: no updating is required, $^{n,\,i}\overline{r}^{\pm*} = {}^{n-1}\overline{r}^{\pm}$ and $^{n,\,i}\overline{d}^{\pm*} = {}^{n-1}\overline{d}^{\pm}$.

(vii) Compute the operator $^{n,i}\overline{\boldsymbol{A}}^*$ (Eq. (4.9)):

$$^{n,i}\overline{\boldsymbol{A}}^* = \sqrt{1 - {}^{n,i}\overline{d}^{+*}}\,{}^{n,i}\boldsymbol{Q}^* + \sqrt{1 - {}^{n,i}\overline{d}^{-*}}\left(\boldsymbol{I} - {}^{n,i}\boldsymbol{Q}^*\right).$$

(viii) Compute the nominal stress (Eq. (2.33)): $^{n,i}\overline{\boldsymbol{\sigma}}^* = {}^{n,i}\overline{\boldsymbol{A}}^* : \boldsymbol{D_0} : {}^{n,i}\overline{\boldsymbol{A}}^* : {}^{n,i}\boldsymbol{\varepsilon}_e^{\,*}$.

(ix) Compute the inelastic strain increment according to the strain increment decomposition (2.55): $^{n,\,i}\Delta\boldsymbol{\varepsilon}_d^{\,*} = {}^{n,\,i}\Delta\boldsymbol{\varepsilon} - \boldsymbol{C_0}:({}^{n,\,i}\overline{\boldsymbol{\sigma}}^* - {}^{n-1}\overline{\boldsymbol{\sigma}})$.

Table 5.6: Numerical algorithm of the constitutive law for the regularized d^+/d^- damage model with an implicit computation of the permanent strains (2.61): plastic-damage corrector phase.

<u>Load increment n:</u>

<u>Iteration i, plastic damage corrector phase:</u>
Known quantities:

$^{n-1}\varepsilon,\ ^{n-1}\overline{\sigma},\ ^{n-1}\varepsilon_p,\ ^{n-1}\overline{d}^{\pm},\ ^{n-1}\overline{r}^{\pm},\ ^{n,i}\varepsilon_e^*,\ ^{n,i}\overline{\sigma}^*,\ ^{n,i}\Delta\varepsilon_d^*,\ ^{n,i}\Delta\overline{d}^{\pm*}.$

(x)   Compute the elastic strain tensor $^{n,i}\varepsilon_e$ (Eq. (5.11)):

$$^{n,i}\varepsilon_e = \left(1 - \frac{\left[\xi^+ H\left(^{n,i}\Delta\overline{d}^{+*}\right) + \xi^- H\left(^{n,i}\Delta\overline{d}^{-*}\right)\right] \cdot \left\langle ^{n,i}\overline{\sigma}^* : ^{n,i}\Delta\varepsilon_d^*\right\rangle}{\left\|^{n,i}\varepsilon_e^*\right\| \cdot \left\|^{n,i}\overline{\sigma}^*\right\|}\right)\ ^{n,i}\varepsilon_e^*$$

(xi)   Compute the permanent strain tensor according to the total strain decomposition (2.51): $^{n,i}\varepsilon_p = {}^{n,i}\varepsilon - {}^{n,i}\varepsilon_e.$

(xii)   Compute the projection operators $^{n,i}Q$ and $I - {}^{n,i}Q$ by means of the spectral decomposition of the nominal strain tensor $^{n,i}\varepsilon_e$ (Eq. (2.15)).

(xiii) Compute the regularized averaging of $^{n,i}\varepsilon_e$ by means of Eq. (5.13), $^{n,i}\overline{\varepsilon}_e$.

(xiv)   Compute the elastic stress tensor $^{n,i}\overline{\sigma}_e = D_0 : {}^{n,i}\overline{\varepsilon}_e$. (Eq. (4.21)).

(xv)   Compute the regularized equivalent stress quantities $^{n,i}\overline{\tau}^{\pm}$ (Eqs. (2.45) and (2.46)).

(xvi)   If $^{n,i}\overline{\tau}^{\pm} > {}^{n-1}\overline{r}^{\pm}$: update $^{n,i}\overline{r}^{\pm} = {}^{n,i}\overline{\tau}^{\pm}$ and update $^{n,i}\overline{d}^{\pm}$ by Eq. (2.69).

        If $^{n,i}\overline{\tau}^{\pm} < {}^{n-1}\overline{r}^{\pm}$: no updating is required, $^{n,i}\overline{r}^{\pm} = {}^{n-1}\overline{r}^{\pm}$ and $^{n,i}\overline{d}^{\pm} = {}^{n-1}\overline{d}^{\pm}$.

(xvii) Compute the operator $^{n,i}\overline{A}^*$ (Eq. (4.9)):
        $$^{n,i}\overline{A}^* = \sqrt{1 - {}^{n,i}\overline{d}^+}\ {}^{n,i}Q + \sqrt{1 - {}^{n,i}\overline{d}^-}\left(I - {}^{n,i}Q\right).$$

(xviii) Compute the nominal stress (Eq. (2.33)): $^{n,i}\overline{\sigma} = {}^{n,i}\overline{A}^* : D_0 : {}^{n,i}\overline{A}^* : {}^{n,i}\varepsilon_e$.

(xix)   Check convergence at a global level:
        NO convergence: go to the iteration $i+1$ and start again from (i) of Table 5.5.
        YES convergence:

- Update: $^{n}\varepsilon = {}^{n,i}\varepsilon$, $^{ni}\overline{\sigma} = {}^{n,i}\overline{\sigma}$, $^{n}\overline{d}^{\pm} = {}^{n,i}\overline{d}^{\pm}$, $^{n}\overline{r}^{\pm} = {}^{n,i}\overline{r}^{\pm}$ and go to the next increment load $n+1$.

Chapter 6

Validation of the damage model under monotonic and cyclic load conditions

In this chapter, the energy-equivalent damage model described in Chapter 2 and the multidirectional procedure specifically thought for cyclic loadings (Chapter 3) are validated by means of comparisons between experimental and numerical results, considering 2D plane stress problems. Parts of the numerical results hereafter presented are already published in (Cervera et *al*., 2018).

In Section 6.1, the capability of the new d^+/d^- damage model to describe the asymmetrical behaviour of quasi-brittle materials under tension and compression is proven, considering concrete samples subjected to uniaxial and biaxial tension, uniaxial and biaxial compression and biaxial shear. Not only monotonic loading conditions are considered but also cyclic conditions and conditions of loading and unloading. In this way, the performance of the different new ingredients characterizing the proposed damage formulation are investigated: the new constitutive operator (2.24), the unified dissipative approach according to which damage and permanent strains are treated, the new Gaussian hardening/softening law in compression (Section 2.5) and the new definition for the permanent strain tensor (2.61). The numerical algorithm adopted for studying these problems

includes the implicit computation of the irreversible deformations, detailed in Table 5.2 and Table 5.3.

In Section 6.2, three examples involving unreinforced concrete elements are solved in order to investigate the adequacy of the new d^+/d^- damage model at a structural level, specifically the effects produced by the adoption of the constitutive secant stiffness operator, derived within an energy-equivalence framework. For this purpose, only monotonically increasing loadings are analysed.

Conversely, in Section 6.3, the potentialities of the multidirectional damage procedure described in Chapter 3 are shown with reference to a masonry wall and a reinforced concrete wall, both subjected to cyclic shear conditions. Finally, the efficiency of the smooth transition proposed in Section 3.3 for crack closure and reopening is discussed in a quantitative way. For all these structural applications, the numerical algorithm preferred uses the explicit calculation of the permenant strains, because of its higher robustness. Specifically, the numerical schemes described in Table 5.1 and Table 5.4 are taken into accoun in case of monotonic and cyclic loading conditions, respectively.

All the analyses presented in this chapter are performed by resorting to a local approach, in order to focus the attention on the constitutive aspects of the formulation rather than on the aspects related to the regularization procedure. Therefore, to ensure mesh-size objective results, in the follow up the local damage formulation is combined with the crack band theory (Bažant and Oh, 1983). This consists in computing the local softening moduli in tension and compression (Section 2.5) starting from the finite element size h: for equilateral triangles $h^2 = 4/\sqrt{3}\, A_e$ while for quadrilateral elements $h^2 = A_e$, with A_e area of the finite element. The application of the regularized damage model is extensively discussed in Chapter 7.

6.1 Monotonic and cyclic validation examples at a local level

6.1.1 Uniaxial tension test on concrete with loading and unloading stages (Gopalaratnam and Shah, 1985)

The present example validates the ability of the model to describe the softening behaviour, the stiffness degradation and the irreversible deformations of concrete under uniaxial tension. The dissipative behaviour is modelled by means of the

exponential softening law (2.79) for describing the evolution of d^+, and by the new definition (2.61) for representing the permanent strain tensor increment. An effective specimen size is adopted to represent the concrete sample, equal to 100 mm × 100 mm, with thickness 1 mm. The material constants considered in the numerical analysis are summarized in Table 6.1 and the comparison between experimental and numerical results is shown in Figure 6.1.

Table 6.1: Material parameters for concrete under uniaxial cyclic tension.

E	ν	f^+	G_f^+	ξ^+
[MPa]	[-]	[MPa]	[N/mm]	[-]
34500	0.2	3.5	0.105	0.51
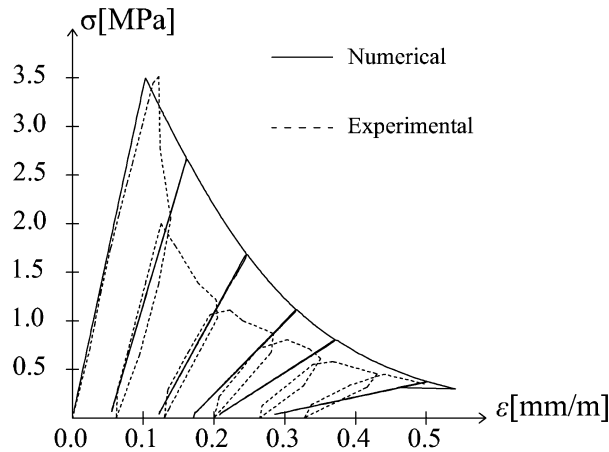
Figure 6.1: Concrete under uniaxial tension with unloading: comparison between numerical and experimental (Gopalaratnam and Shah, 1985) results.

Although a slight underestimation of the permanent deformations and of the softening behaviour is visible in Figure 6.1, the correspondence between numerical predictions and experiment is satisfactory, especially in terms of unloading stiffness in the first cycles.

6.1.2 Uniaxial compression test on concrete with loading and unloading stages (Sinha et *al.*, 1964)

The performance of the model under uniaxial compression is studied adopting the new softening Gaussian function (2.80), in conjunction with the new definition of the permanent strain tensor (2.61). The concrete sample has a length equal to

305 mm and a resisting section equal to 135 mm × 135 mm. The compressive
material properties used in the numerical analysis are summarized in Table 6.2,
while the comparison between numerical and experimental results is presented in
Figure 6.2.

Table 6.2: Material parameters for concrete under cyclic compression.

E	ν	f^-	G_f^-	ξ^-
[MPa]	[-]	[MPa]	[N/mm]	[-]
29500	0.2	-31.5	38.0	0.45
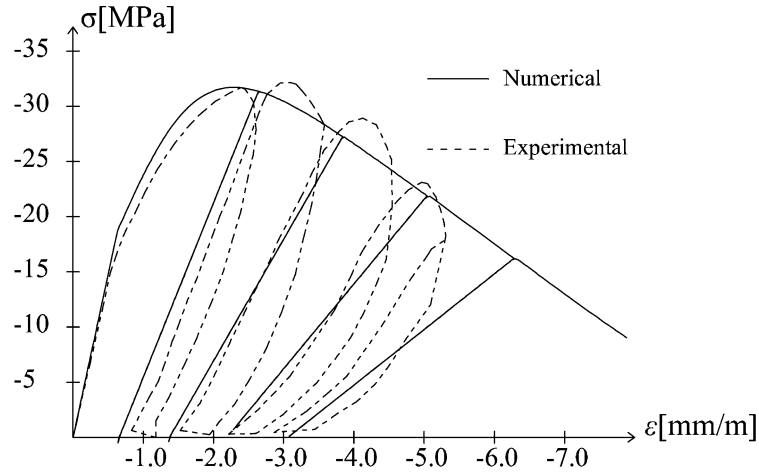
Figure 6.2: Concrete under uniaxial compression with unloading: comparison between
numerical and experimental (Sinha et *al.*, 1964) results.

As visible in Figure 6.2, the overall response is properly described by the
damage model, in terms of strength reduction, stiffness degradation and progressive
accumulation of permanent deformations. This constitutes a proof of the adequacy
of the Gaussian softening function to describe the behaviour of concrete (and quasi-
brittle materials in general) under uniaxial compressive regime. Specifically, the
hypothesis of fixing the end of the linearity in correspondence with a stress value
equal to f^-·exp(−0.5) (see Section 2.5.2 and Eq. (2.93)) fits adequately with the
experimental trend, as well as the assumption of defining the width of the Gaussian
bell on the basis of the fracture energy.

6.1.3 Uniaxial cyclic tension-compression test on concrete (Ramtani, 1990)

In this section, the crack-closure effects typical of concrete, visible in a uniaxial cyclic loading history characterized by two loading-unloading stages in tension and a further reloading in compression, are reproduced with the d^+/d^- damage model.

Due to the adequate fit obtained under uniaxial tension (Section 6.1.1) and uniaxial compression (Section 6.1.2), the softening function adopted in tension is the exponential one while in compression the Gaussian softening law is preferred.

In accordance with (He et *al.*, 2015), an effective concrete specimen is considered, 1 mm thick and with dimensions 80 mm × 80 mm. The material parameters are collected in Table 6.3 and the numerical results, compared with the experimental ones, are shown in Figure 6.3.a. Moreover, in Figure 6.3.b, a zoom on the tensile response is provided.

Table 6.3: Material parameters for concrete under uniaxial alternate cyclic conditions.

E [MPa]	ν [-]	f^+ [MPa]	f^- [MPa]	G_f^+ [N/mm]	G_f^- [N/mm]	$\xi\pm$ [-]
16400	0.2	1.2	-18	0.02	7.50	0.4
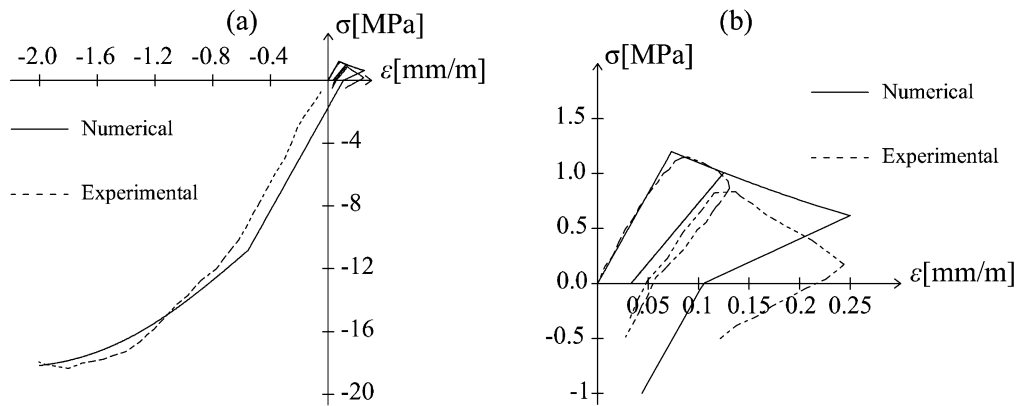
Figure 6.3: Concrete under uniaxial cyclic conditions: comparison between numerical and experimental (Ramtani, 1990) results in (a) compression and (b) tension.

The experimental behaviour of the material under alternate cyclic conditions is fairly simulated by the damage model; specifically, the crack closure is represented thanks to the spectral decomposition of the elastic strain tensor ε_e, combined with the use of two damage variables, one for tension and one for compression.

6.1.4 2D tests on concrete in biaxial tension, combined tension and compression and biaxial compression (Kupfer et *al.*, 1969)

The material behaviour under biaxial stress-strain conditions is validated by referring to the experimental tests described in (Kupfer et *al.*, 1969) on several concrete samples, subjected to different stress combinations, in the regimes of biaxial tension, combined tension-compression and biaxial compression.

The softening functions adopted in tension and in compression are the exponential and the Gaussian one, respectively. The specimens have dimensions 200 mm × 200 mm × 50 mm. The set of experiments herein simulated is the one related to a concrete with compressive strength equal to 32.8 MPa. All the input material properties considered in the numerical analyses are synthetized in Table 6.4. With respect to the previous examples, two additional parameters are here specified, which are the ratio between the biaxial and the axial compressive strengths, useful in biaxial compression, and the parameter k, defining the amplitude of the compressive damage surfaces in the 2nd and 4th quadrants (see Figure 2.4).

Table 6.4: Material parameters for concrete under biaxial stress.

E	ν	f^+	f^-	G_f^+	G_f^-	f_b^-/f^-	k	$\xi\pm$
[MPa]	[-]	[MPa]	[MPa]	[N/mm]	[N/mm]	[-]	[-]	[-]
32000	0.2	2.66	-32.8	0.105	26.00	1.16	0.75	0.22

The normalized longitudinal stress – longitudinal strain curves obtained in biaxial compression, combined tension-compression and biaxial compression for different stress ratios are shown in Figure 6.4, Figure 6.5 and Figure 6.6. The longitudinal direction indicates the direction in which the maximum stress σ_1 is applied. According to the decomposition on the elastic strain tensor, dispalyed in Figure 2.1.b, the cases of biaxial compression and biaxial tension are treated with an isotropic damage model, since the ratio between the transversal and the longitudinal imposed stresses is higher than the Poisson's ratio ν. The cases of

uniaxia tension, uniaxial compression and combined tension-compression imply instead the adoption of an orthotropic damage model.
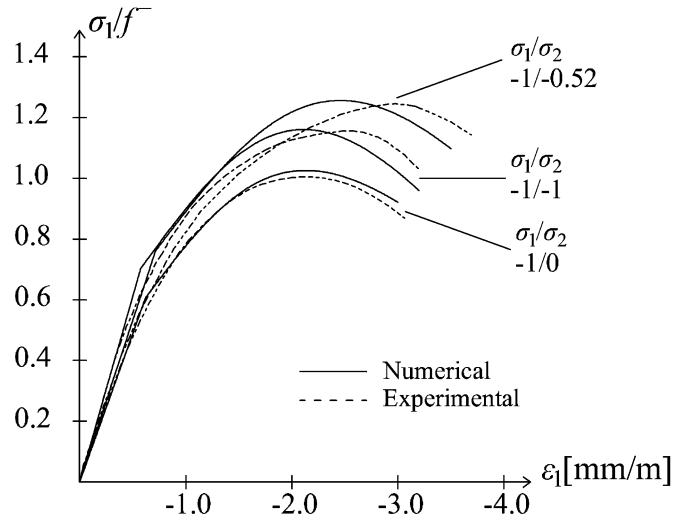
Figure 6.4: Stress-strain relationships of concrete under biaxial compression, with stress normalized with respect to compressive strength: comparison between numerical and experimental (Kupfer et *al.*, 1969) results.
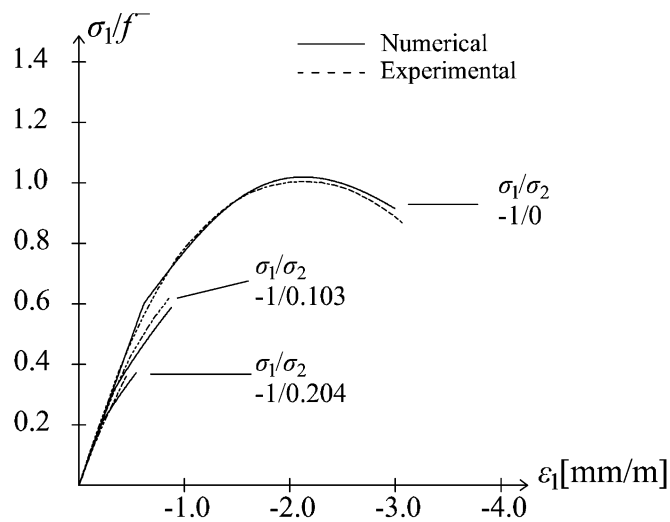
Figure 6.5: Stress-strain relationships of concrete under combined tension-compression, with stress normalized with respect to compressive strength: comparison between numerical and experimental (Kupfer et *al.*, 1969) results.
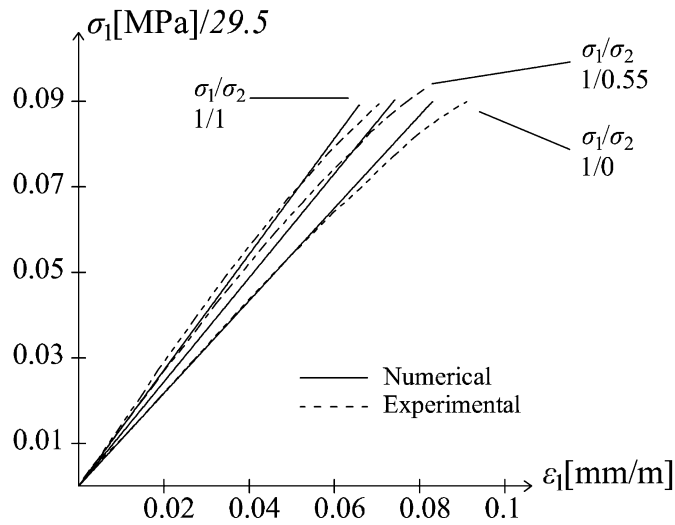
Figure 6.6: Stress-strain relationships of concrete under biaxial tension, with stress normalized with respect to 29.5 MPa: comparison between numerical and experimental (Kupfer et *al.*, 1969) results.

The satisfactory fit among experimental and numerical results, especially in terms of peak loads, confirms the adequacy of the damage formulation for the analyses of concrete structures under generic biaxial conditions.

6.2 Monotonic loads: validation of the energy-equivalent d^+/d^- damage model

Three different structural applications are studied with the new energy-equivalent d^+/d^- damage model: a wedge-splitting test performed on a concrete specimen in the experimental program described in (Trunk, 2000), a three-point bending test shown in (Kormeling and Reinhardt, 1983) and a mixed-mode three-point bending test documented in (Gálvez et *al.*, 1998), both on single-edged-notched concrete beams.

The geometry, the boundary and the loading conditions for the just mentioned examples are illustrated in Figure 6.7, Figure 6.8 and Figure 6.9, respectively. In all the problems, the increasing forces P are applied by imposing increasing displacements of the application points.
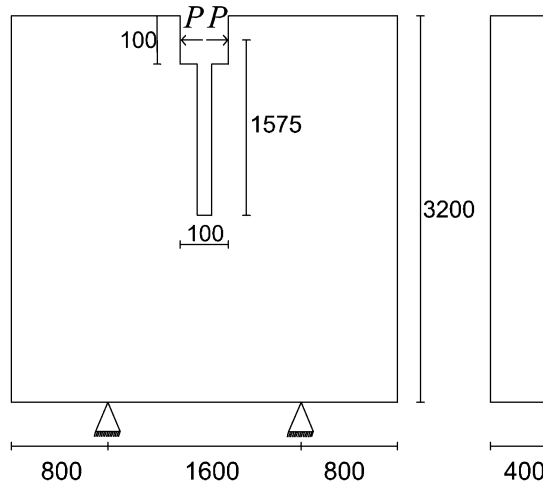
Figure 6.7: Wedge-splitting test set-up (dimensions in mm).
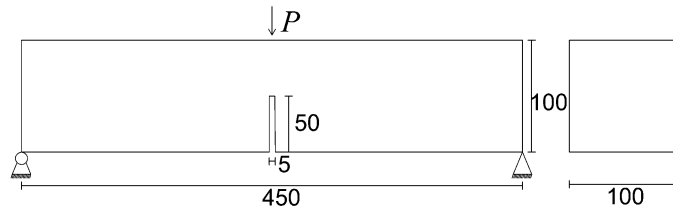
Figure 6.8: Three-point bending test set-up.(dimensions in mm).
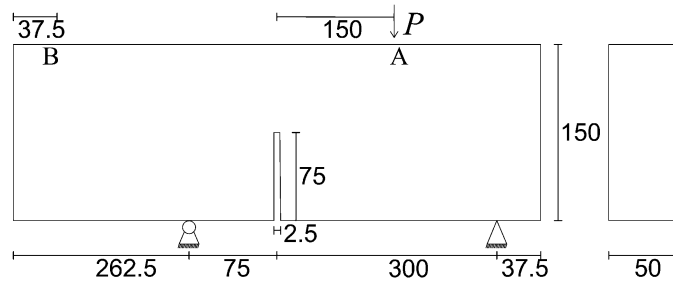
Figure 6.9: Mixed mode three-point bending test (dimensions in mm).

All the numerical analyses are performed considering an exponential damage evolution law in tension (Eq. (2.76) with $r_0^+ = f^+ = f_p^+$, i.e. $\gamma_e^+ = \gamma_p^+$) and a parabolic hardening-exponential softening trend in compression (Eq. (2.76) with $r_0^- < f^- < f_p^-$, $\gamma_e^- = 0.33$ and $\gamma_p^- = 1.33$). The permanent strains are taken into account by means of Eq. (2.57).

The mechanical properties assumed for concrete in each case are summarized in Table 6.5, Table 6.6 and Table 6.7.

Table 6.5: Concrete parameters for the wedge-splitting test.

E	ν	f^+	f^-	G_f^+	G_f^-	f_b^-/f^-	$b+$	$b-$	k
[MPa]	[-]	[MPa]	[MPa]	[N/mm]	[N/mm]	[-]	[-]	[-]	[-]
28300	0.2	1.59	-25	0.35	35	1.16	0.05	0.30	0.8

Table 6.6: Concrete parameters for the three-point bending test.

E	ν	f^+	f^-	G_f^+	G_f^-	f_b^-/f^-	$b+$	$b-$	k
[MPa]	[-]	[MPa]	[MPa]	[N/mm]	[N/mm]	[-]	[-]	[-]	[-]
20000	0.2	2.40	-24	0.133	30	1.16	0.05	0.30	0.8

Table 6.7: Concrete parameters for the mixed mode three-point bending test.

E	ν	f^+	f^-	G_f^+	G_f^-	f_b^-/f^-	$b+$	$b-$	k
[MPa]	[-]	[MPa]	[MPa]	[N/mm]	[N/mm]	[-]	[-]	[-]	[-]
38000	0.2	3.00	-54	0.069	38	1.16	0.05	0.30	0.8

The mesh has been generated taking care of refining the discretization where the propagation of the crack is expected; for the wedge-splitting test, a mesh of 3353 quadrilateral elements is adopted with a representative length in the proximity of the cracking zone equal to 17.5 mm. In the three-point bending and in the three-point mixed-mode bending tests, the concrete beams are discretized with 2752 and 13336 elements, respectively: in the regions around the notch, triangular elements with an average size of 2.5 mm are used while the other zones are discretized with larger quadrilateral meshes.

The adequacy of the proposed orthotropic d^+/d^- damage model in capturing the nonlinear behaviour is proven by comparing the numerical and the experimental results in terms of deformed configurations, damage distribution, applied load P – crack mouth opening displacement $CMOD$ and/or applied load P – displacement of relevant points.

Regarding the wedge-splitting test, as expected due to the problem symmetry, the localization of the tensile damage occurs in correspondence of the notched zone

(see Figure 6.10.a and Figure 6.10.b) and is vertical, in accordance with the vertical crack path found experimentally.
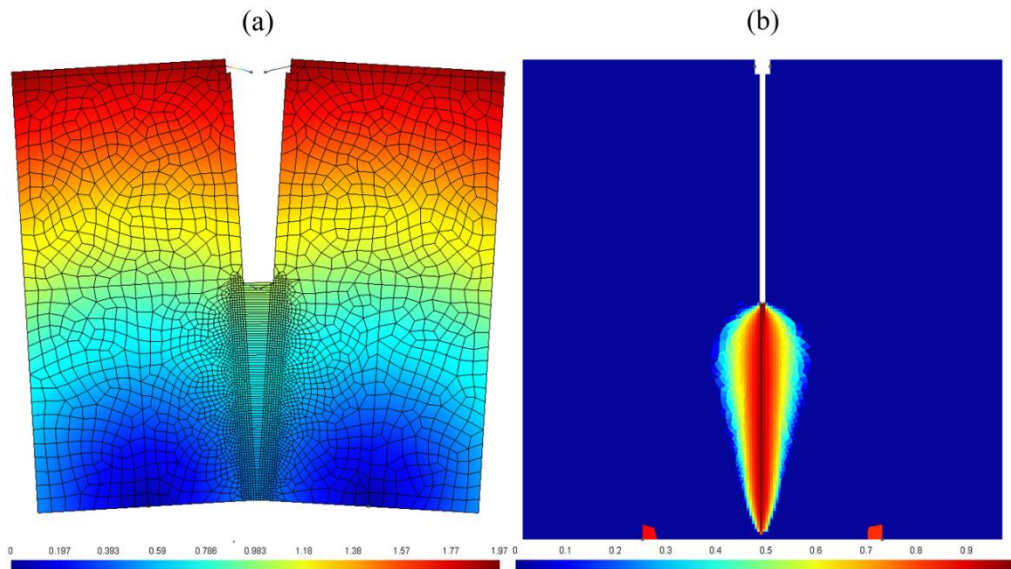
Figure 6.10: Wedge-splitting test: (a) deformed configuration (× 100) (in mm) and (b) tensile damage distribution.

The numerical *P* - *CMOD* curve is compared in Figure 6.11 with the experimental one: both the peak-load and the post-peak behaviour are satisfactorily described with the proposed model.
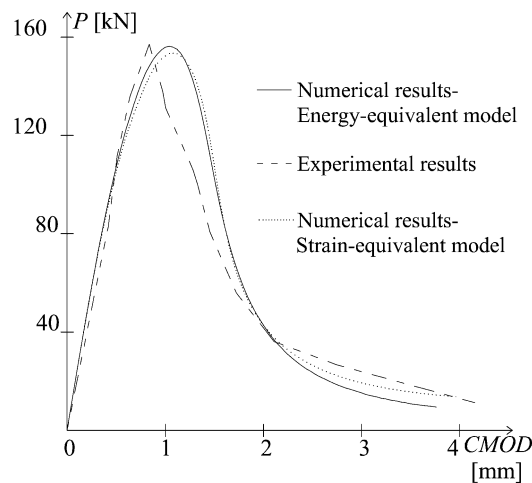
Figure 6.11: Load *P – CMOD* curve for the wedge-splitting test: comparison between numerical and experimental results.

The accordance of the results obtained numerically with the experimental ones is evident also for the three point bending test, as confirmed by the deformed configuration of the beam and by the d^+ distribution (Figure 6.12.a and Figure 6.12.b), which show the localization of the maximum deformations in correspondence of the mid-span, above the notch. The agreement between experimental and numerical results is evident also in Figure 6.13, where the load P – mid-point displacement δ curve obtained with the proposed damage model falls in between the maximum and minimum experimental envelopes.
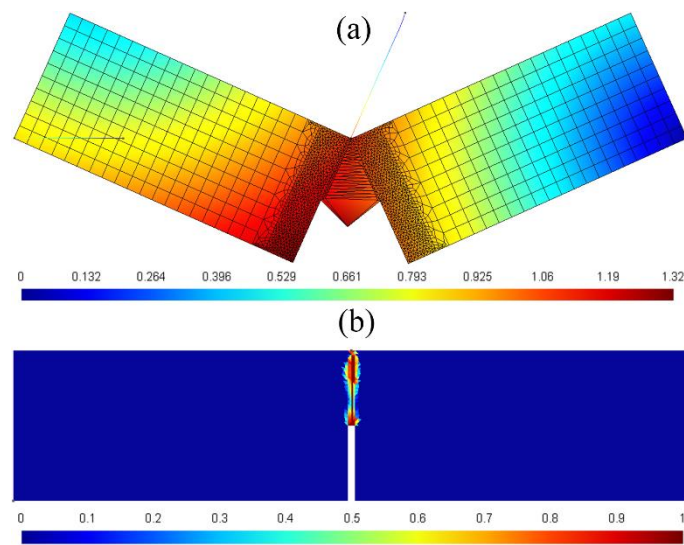
Figure 6.12: Three point bending beam: (a) deformed configuration (× 100, in mm) and (b) tensile damage distribution map.
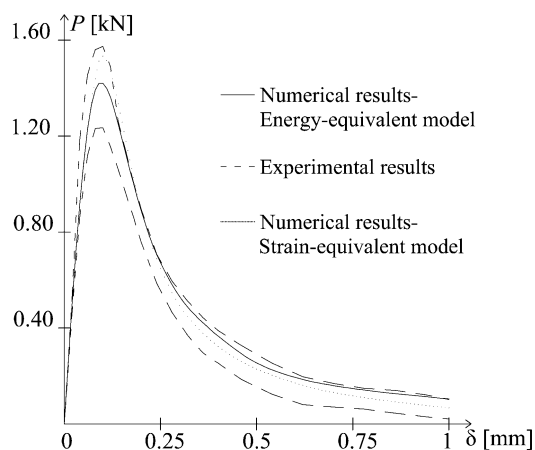
Figure 6.13: Load P – δ curve for the three-point bending test: comparison between numerical and experimental results.

Finally, as regards the three-point mixed-mode bending test, the deformed configuration (Figure 6.14.a) and the distribution of the tensile damage (Figure 6.14.b) are in perfect agreement with the crack trajectory found in the experiment, which has an inclined direction of propagation, as accurately documented in (Gálvez et *al.*, 1998). The structural curves obtained with the proposed orthotropic model, in terms of applied load P – $CMOD$ (Figure 6.15.a) and applied load P – displacement of point B (Figure 6.15.b), fit satisfactorily with the experimental results, except for a slight overestimation of the dissipated energy in the post peak regime.
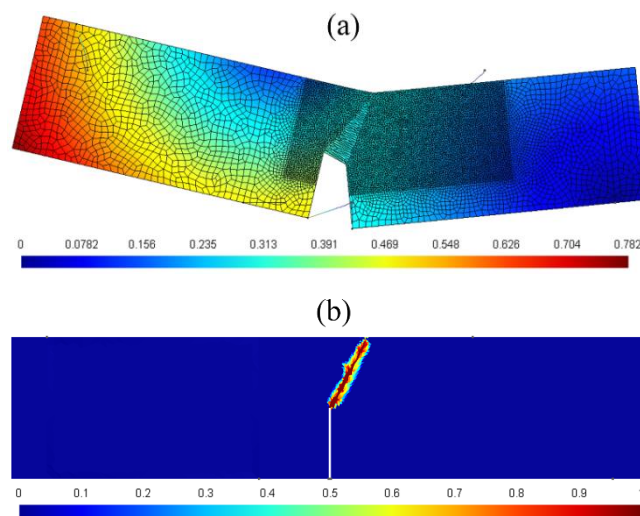
Figure 6.14: Three-point mixed-mode bending test: (a) deformed configuration ($\times$ 100, in mm) and (b) tensile damage distribution map.
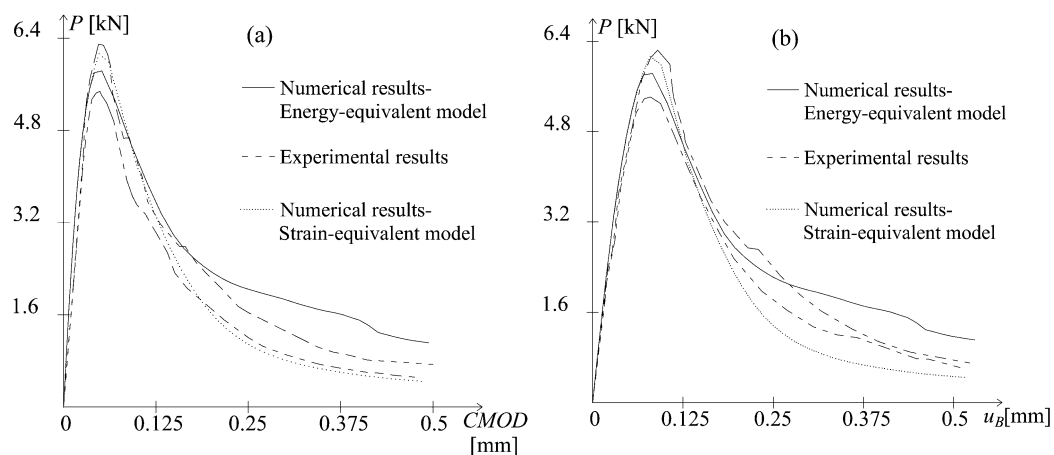
Figure 6.15: (a) Load P – $CMOD$ curve and (b) load P – u_B curve for the three-point mixed-mode bending test: comparison between numerical and experimental results.

All the problems just described are solved also with the constitutive law presented in (Faria et *al*., 1998), derived in the framework of strain-equivalence, but resorting to the same permanent strain rate (2.57), damage criterion (Eqs. (2.45) and (2.46)) and damage evolution laws (Eq. (2.79) in tension and Eq. (2.76) in compression) here considered. The corresponding numerical curves are plotted in Figure 6.11, Figure 6.13 and Figure 6.15, together with the experimental ones and the ones obtained with the new d^+/d^- damage model described in Section 2.2. The objective is to discuss the effects of the energy-equivalence assumption, here adopted for the derivation of the constitutive operator (2.24), compared with the strain-equivalence hypothesis, whose constitutive equation is expressed in Eq. (2.6).

On the one hand, it is possible to note how the differences between the two different formulations are substantially slight in the structural response, being both of them able to reproduce satisfactorily the laboratory results. Hence, although the choice of energy-equivalence ensures a gain in thermodynamic consistency with respect to the strain-equivalence one, as observed in Section 2.2, both the formulations are adequate in describing the strain-softening response typical of quasi-brittle materials.

However, the adoption of the constitutive symmetric operator $\boldsymbol{D}_E$ (Eq. (2.24)) is convenient in computational terms because it allows solving the algebraic system of equations referring to a symmetric secant stiffness matrix, as explained in Section 5.1. Looking at the CPU time necessary to complete the numerical analyses, collected in Table 6.8, this fact is confirmed. The maximum beneficial effect consists in a saved time equal to 51%, which results from the adoption of the new energy-equivalent damage model with respect to the original one. It is worth remarking that such an high saving of computational resources has to be ascribed not only to the assemblage and inversion of a symmetric stiffness matrix with respect to a non-symmetric one but also to the fact that, with the use of a symmetric matrix, the convergence is found in a lower number of iterations.

Table 6.8: Comparison in terms of CPU's time between the new energy-equivalent damage formulation and the original strain-equivalent one (Faria et al., 1998).

Problem	Number of FEs	CPU time Energy equivalence	CPU time Strain equivalence	Saved CPU time
Wedge-splitting	3359	1042.95 s	1223.85 s	14.7%
Three-point bending	2971	8813.53 s	17996.26 s	51.0%
Mixed-mode bending	13635	5452.77 s	10393.5 s	47.5%

6.3 Cyclic shear loads: validation of the multidirectional d^+/d^- damage model

6.3.1 Masonry shear panel under cyclic conditions

The first problem analyzed with the model presented in Chapter 2 enriched with the multidirectional procedure described in Chapter 3 is an unreinforced brick masonry wall under in-plane quasi-static shear loading conditions. The reference solution is represented by the results of laboratory tests provided in (Anthoine et al., 1994) and (Magenes and Calvi, 1997), dealing with a laboratory campaign addressed to investigate the seismic behaviour of masonry existing buildings. The loading conditions of the analyzed problem are representative of the ones sustained by vertical structural elements during a seismic event, i.e. permanent vertical loads and double bending moments.

According to the experimental set-up (Anthoine et al., 1994), the wall, with an height H-width ratio equal to 1.35, width B 1000 mm and thickness 250 mm, is first subjected to a vertical compressive force of 150 kN ($p = 0.6$ N/mm^2) and then to cyclic horizontal displacements u_h of increasing amplitudes applied on the top boundary. The base of the panel is completely constrained and the vertical displacements of its top side are prevented, forcing the bottom and top panel sections to remain parallel. Both the geometry and the loading conditions adopted in the numerical analyses are summarized in Figure 6.16.
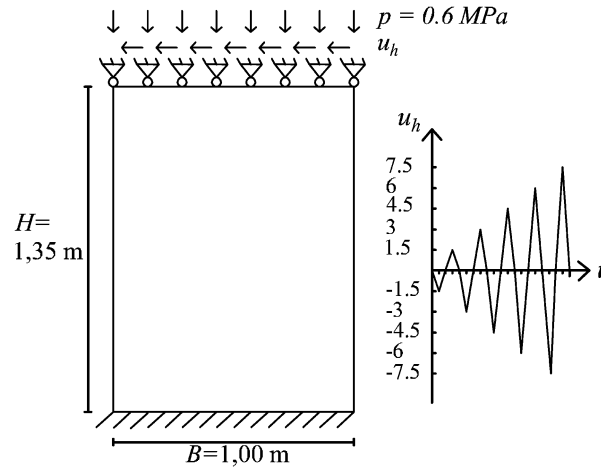
Figure 6.16: Geometry, boundary and loading conditions for the masonry shear wall.

All the numerical analyses are performed considering an exponential damage evolution law in tension (Eq. (2.76) with $r_0^+ = f^+ = f_p^+$, i.e. $\gamma_e^+ = \gamma_p^+$) and a parabolic hardening-exponential softening trend in compression (Eq. (2.76) with $r_0^- < f^- < f_p^-$, $\gamma_e^- = 0.5$ and $\gamma_p^- = 1.5$). The permanent strains are taken into account by means of Eq. (2.57). Regarding the mechanical parameters, except for the Young's modulus and the compressive uniaxial strengths f^-, inferable from (Anthoine et al., 1994), the majority of the other values have been chosen in accordance with the experimental data expressed in (Berto et al., 2002; Magenes and Calvi, 1992) for brick masonry panels with mechanical features comparable with the ones of the analyzed wall and belonging to the same research program. The input values for the constitutive parameters adopted in the numerical simulations are collected in Table 6.9.

Table 6.9: Masonry parameters for the wall under in-plane cyclic shear.

E	ν	f^+	f^-	G_f^+	G_f^-	f_b^-/f^-	$b+$	$b-$	k
[MPa]	[-]	[MPa]	[MPa]	[N/mm]	[N/mm]	[-]	[-]	[-]	[-]
1500	0.15	0.26	-6.2	0.25	28	1.15	0.1	0.30	0.8

Due to the presence of a non-negligible constant vertical force in addition to the cyclic actions, the problem is solved by resorting to the multidirectional procedure specifically devised for Load Type (ii) (Section 3.1.2), i.e. taking into account the evolution of the damage regions related to the continuous rotation of the principal directions. The two additional deviation parameters required by the

multidirectional damage procedure, θ_{min} (Eq. (3.3)) and θ_t (Eq. (3.6)), are assumed equal to $\pi/8$ and $\pi/36$, respectively.

The response of the panel obtained in the laboratory test is plotted in Figure 6.17.a, in terms of the horizontal shear force F_h recorded at the top side versus the imposed horizontal displacement u_h. The F_h - u_h curves deriving from the application of the multidirectional damage model, considering three quadrilateral mesh configurations with different refinement, are shown in Figure 6.17.b, Figure 6.17.c and Figure 6.17.d. For comparison purposes, each numerical curve is plotted together with the envelope of the experimental one.
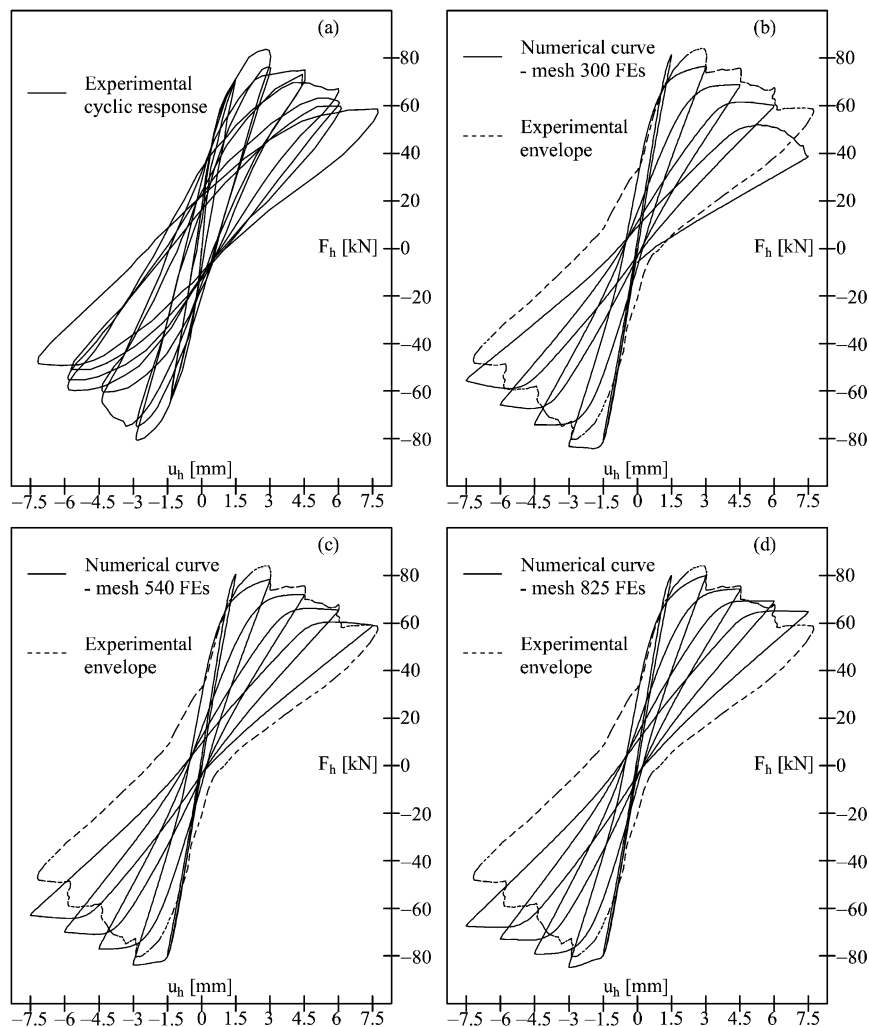
Figure 6.17: Masonry wall under in-plane cyclic shear: (a) experimental results; (b), (c) and (d) numerical results obtained with the multidirectional procedure for different mesh refinements.

The experimental response (Figure 6.17.a) is typical of a brittle failure mechanism dominated by shear, where the peak load, equal to 84 kN in correspondence of a drift of 0.20 %, corresponds to the formation of diagonal cracks in the center of the panel; the pre-cracking behaviour is characterized by a modest hysteresis behaviour while, after the attainment of the maximum carrying capacity, rapid strength and stiffness degradation and high energy dissipation are visible. The cyclic conditions are responsible for a trapezoidal cracking pattern which presents two sets of intersecting cracks in the mid-height of the panel, as well as horizontal flexural ones in correspondence of the corners.

Analyzing the numerical curves (Figure 6.17.b, Figure 6.17.c, Figure 6.17.d), firstly it is evident how the dependence of the results on the discretization, ensured by the adoption of the mesh-adjusted softening moduli in tension and compression, is very small and can be considered negligible. Secondly, it can be noticed that the numerical results reproduce satisfactorily the overall structural response of the shear panel: both the peak load, achieved at a drift of 0.22 % ($u_h = -3$ mm) and equal to 84,8 kN (curve in Figure 6.17.d), and the post-peak softening trend are well approximated. Moreover, the effect of the multidirectional procedure is visible in the similarity of the response in terms of ultimate load, ultimate displacement and softening behaviour between positive and negative displacements. This is simulated thanks to the stiffness recovery capabilities of the multidirectional model in correspondence of loading reversal; in fact, going from negative to positive displacements, an increase in stiffness is visible in the numerical response, particularly evident in the unloading stage after the attainment of the maximum carrying capacity (cycle 2, amplitude 3 mm): here, the closure of a set of diagonal cracks just opened translates in almost the total recovery of the initial stiffness, since the generation of the diagonal cracks in the orthogonal direction is not occurred yet. In the subsequent cycles, this phenomenon, although present, is less evident because the closure of a set of cracks coincides with the re-activation of the other set of cracks previously originated.

To make clearer how this stiffness regain is simulated, the contour plots of the active tensile damage value d^+ corresponding to different stages of cycle 2 are shown in Figure 6.18. In Figure 6.18.a, Figure 6.18.b and Figure 6.18.c, the contour plots refer to the situations of maximum loading ($u_{hmax} = -3$ mm), loading reversal ($u_{hmax} = +0.12$ mm) and maximum reloading ($u_{hminx} = +3$ mm).
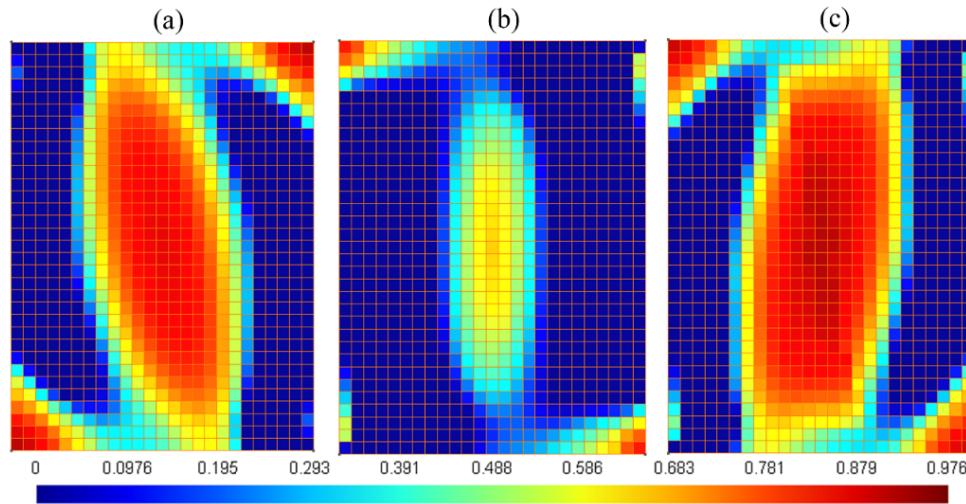
Figure 6.18: Active d^+ contour plots in cycle 2: (a) u_h=−3mm, (b) u_h=+0.12mm and (c) u_h=+3mm.

In Figure 6.18.a, the high values of damage at the center of the panel and at the two corners identify the formation of the shear and flexural cracks, respectively, induced by a horizontal displacement towards the right. Just after loading reversal, in Figure 6.18.b, the closure of the previously generated cracks is represented by making inactive the damage values displayed in Figure 6.18.a: in fact, due to the rotation of the principal directions, the transition from a damage region to the other one has occurred and the active damage values coincide with the maximum ones attained during the reloading in cycle 1. Starting from this damage configuration, due to the increase of the horizontal displacement towards the left, the active damage distribution in Figure 6.18.c is obtained, almost symmetric with respect to the one in Figure 6.18.a.

A further confirmation that the collapse mechanism captured by the numerical analysis is governed by shear is given in Figure 6.19 and Figure 6.20, where the maximum tensile strains ε_{max} are displayed in cycle 2 and in cycle 5, respectively, at the end of loading and at the end of the reloading stages. The contour plots in Figure 6.19 confirm the formation of the dominant cracking mechanism in the center of the panel. In Figure 6.20, the results refer to the end of the analysis, when the crack propagation towards the corners has occurred, causing the maximum strain values to leave the central part. Although the adoption of a smeared approach does not allow identifying with accuracy the strain localization, the numerical solutions shown in Figure 6.19 and Figure 6.20 are in good agreement with the cracking pattern observed in laboratory and documented in (Anthoine et al., 1994).
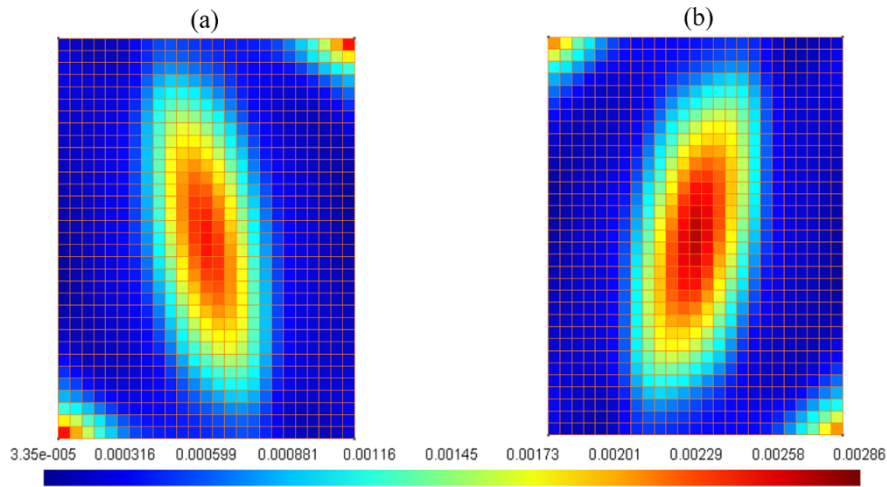
Figure 6.19: Maximum tensile strain contour plots in cycle 2: (a) $u_h = -3$ mm and (b) $u_h = +3$ mm.
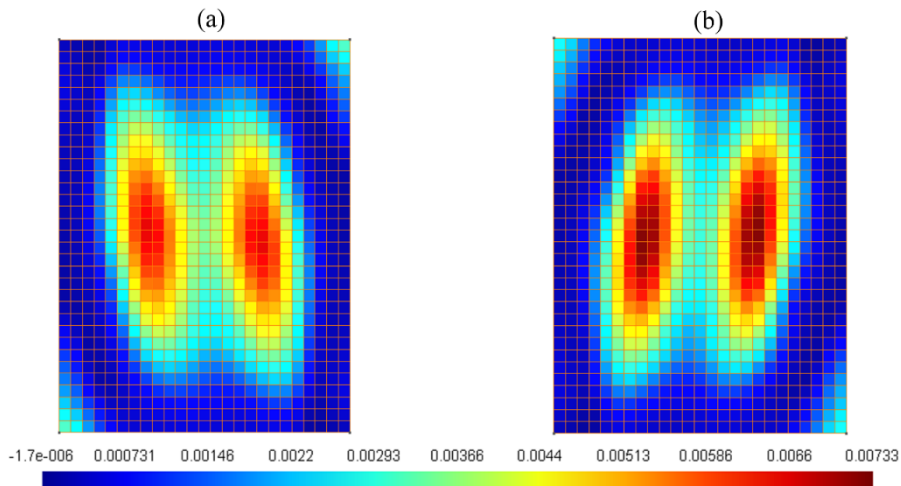
Figure 6.20: Maximum tensile strain contour plots in cycle 5: (a) $u_h = -7.5$ mm and (b) $u_h = +7.5$ mm.

For comparison purposes, the F_h - u_h curve obtained by the adoption of the damage model without a multidirectional treatment of damage is shown in Figure 6.21.a. Even though the peak load and the envelope of the experimental curve are basically captured, the lack of unilateral effects reflects in a relevant underestimation of the dissipated energy. This can be noticed both in the unrealistic shape of the hysteretic cycles and in the evolution of permanent deformations, which accumulate mainly in the positive loading stages, and not in the reloading ones (in accordance with the observations provided in Section 3.4). Differently, in the response obtained with the multidirectional damage model (see Figure 6.17.d),

although the permanent strains are somewhat underestimated, their evolution is qualitatively correct, as permanent deformations are generated both in the loading and in the reloading stages.

In order to provide a quantitative proof of the beneficial role of the multidirectional damage approach in terms of representation of the dissipative behaviour, the equivalent viscous damping coefficients are computed for each load cycle, referring to the numerical response with and without enhanced MCR capabilities, Figure 6.17.d and Figure 6.21.a, respectively. The equivalent viscous damping is evaluated as the ratio between the energy dissipated in a cycle W_d and the elastic energy W_e at the maximum displacement u_{hmax}:

$$\xi_{eq} = \frac{W_d}{2\pi\left(W_e^+ + W_e^-\right)} \tag{6.1}$$

In Figure 6.21.b, these quantities are plotted as a function of the drift (u_{hmax}/H) and compared with the ones derived from the experimental response (data provided in (Magenes and Calvi, 1997)).
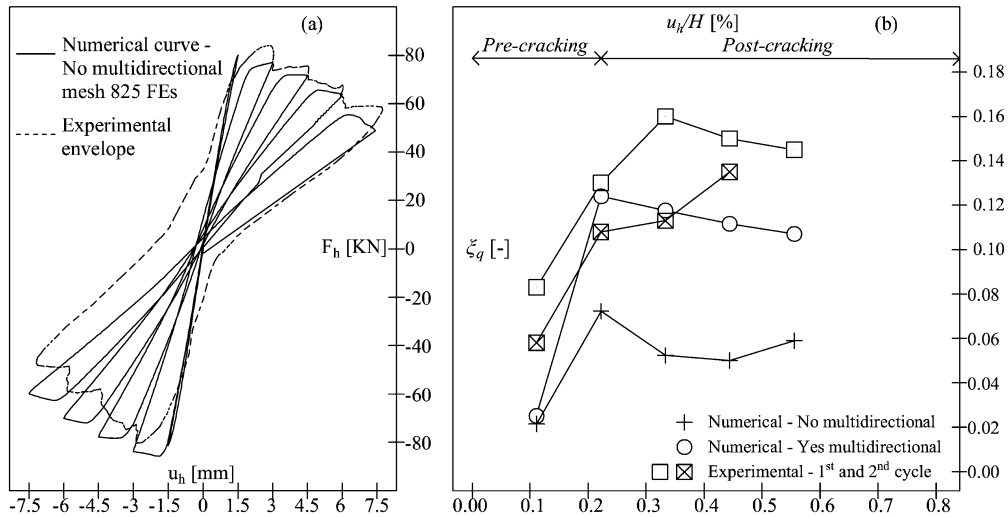
Figure 6.21: Masonry shear wall under in-plane cyclic shear: (a) numerical results without the multidirectional procedure; (b) comparison in term of viscous damping coefficients between the numerical response obtained with and without the multidirectional procedure.

On the one hand, Figure 6.21.b shows the adequacy of the multidirectional model in treating the cyclic shear failure: after cracking, the numerical trend of the

equivalent viscous damping is close to the experimental one, meaning that the growth of the dissipated energy due to increasing damage and increasing displacement demand is well reproduced. The slightly lower values obtained in the analyses can be attributed to the slight underestimation of the permanent strains. On the other hand, Figure 6.21.b confirms the incapability of a pure scalar damage formulation in describing the real dissipative behaviour under shear cyclic conditions, because independent degradation processes along different directions can not be represented.

As mentioned above, a slight underestimation of the permanent deformations is visible in the numerical response from Figure 6.17.d. This deserves some further consideration on the adequacy of the simplified definition (2.57) here adopted for the irreversible strain tensor ε_p and the importance of this model component in cyclic loading conditions. To do this, two additional analyses are carried out, varying the values of the material parameters b^+ and b^- with respect to the ones indicated in Table 6.9. Specifically, both the case of high permanent deformations ($b^+ = 0.17$ and $b^- = 0.45$) and null permanent deformations ($b^+ = 0$ and $b^- = 0$) are considered. The resulting F_h - u_h curves, obtained using the finer mesh, are plotted in Figure 6.22. Moreover, these solutions are also re-elaborated in terms of damping coefficients-drift trends in Figure 6.23, in order to directly evaluate the variation of energy dissipation associated to the variation of ε_p.
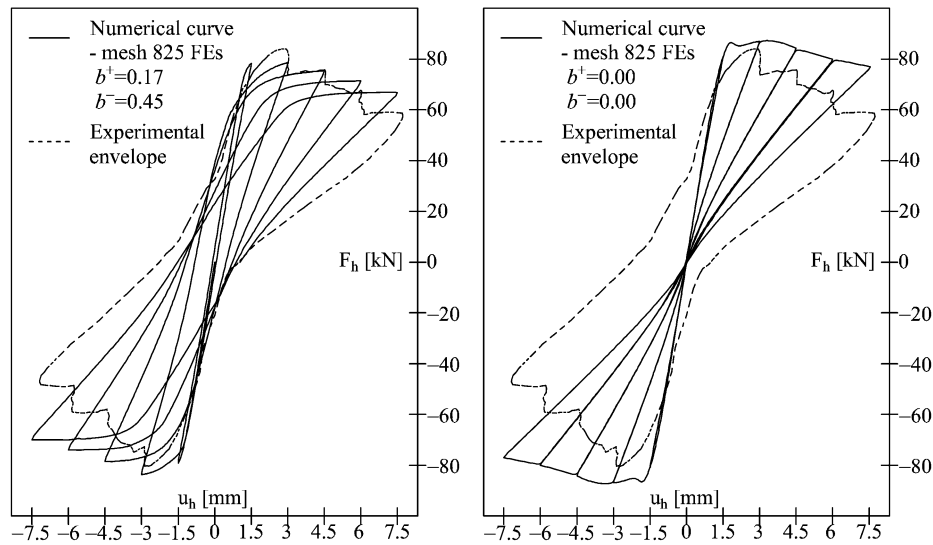
Figure 6.22: Masonry shear wall under in-plane cyclic shear: F_h - u_h curves in case of (a) high permanent deformations and (b) absent permanent deformations.
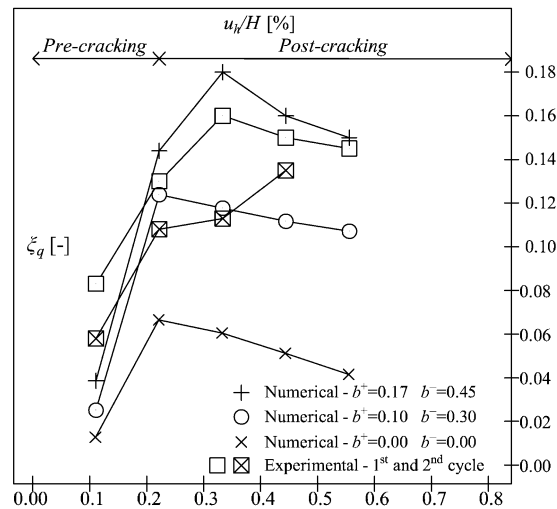
Figure 6.23: Masonry shear wall under in-plane cyclic shear: numerical responses with different levels of permanent deformations compared in terms of viscous damping coefficients.

Some relevant aspects emerge from the analysis of these figures. Firstly, although the inclusion of permanent deformations in the damage model is perfomed in a simplified manner, it results adequate for describing the experimental evidence, both in terms of residual deformations at complete unloading (Figure 6.22.a) and in terms of energy dissipation capacity (Figure 6.23). Secondly, a less pronounced softening response is obtained when the permanent deformations are not included (Figure 6.22.b); this is not surprising because, according to the coupled definition of the softening modulus proposed in Section 2.5 (Eq. (2.84b)), a reduction of the permanent deformations implies a reduction of the softening modulus, hence a slower evolution of damage. Moreover, the unrealistically low values of ξ_{eq} obtained with null ε_p (Figure 6.23) are very similar to the ones derived without the multidirectional procedure, in case of $b^+= 0.1$ and $b^-= 0.3$ (Figure 6.21.b). It is concluded that the modelling of permanent deformations is important as the modelling of microcrack closure-reopening effects for a correct representation of the behaviour of quasi-britttle structures under cyclic loading.

6.3.2 Reinforced concrete wall under cyclic shear

The second problem studied with the multidirectional procedure described in Chapter 3 is a reinforced concrete wall subjected to horizontal cyclic shear forces, tested within the French national research project CEOS.fr (Rospars and Chauvel, 2014). The specimen analyzed is the one identified in the experimental campaign

with the acronym SHW2 and represents a 1/3 reduced-scale model of reinforced concrete thick shear walls employed in industrial buildings to resist seismic loadings.

In the numerical analysis, the experimental set-up, detailed in (Rospars and Chauvel, 2014; Bisch et *al*., 2014), is reproduced as shown in Figure 6.24: the reinforced concrete specimen (Zone 1, Zone 2), of overall dimensions 4.2 m × 1.05 m × 0.15 m, is connected on the top and on the bottom to highly reinforced thick horizontal beams (Zone 3 and Zone 4), which allow redistributing the shear loading on the panel. The horizontal action, in the laboratory test assigned by means of hydraulic actuators placed on each side of the top beam, 100 mm over the wall, is provided in terms of horizontal imposed displacements u_h alternated on the Surfaces 1 and 2. Moreover, the constraint represented by the steel frame in which the whole test body is installed is modelled by preventing horizontal displacements on Surfaces 3 and 4 and vertical displacements on Surfaces 5 and 6. Rebars ϕ 10, spaced 100 mm in both vertical and horizontal directions on both faces of the wall (Zone 1) are considered while vertical rebars ϕ 25 and ϕ 32 are added in the left and right sides of the wall (Zone 2), in order to control the opening of cracks due to bending.
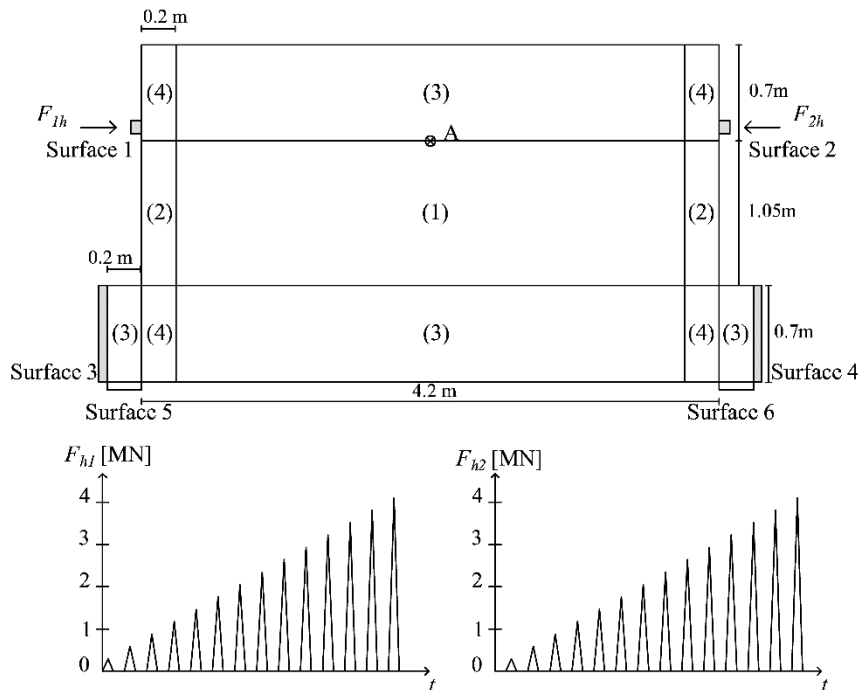
Figure 6.24: Geometry, boundary and loading conditions for the reinforced concrete shear wall.

In the highly reinforced zones, specifically the top and bottom beams (Zone 3, Zone 4) and the left and right parts of the wall (Zone 2), it is assumed that the concrete behaviour is elastic. Hence, the damage formulation developed in Chapter 2 and Chapter 3 is applied only to Zone 1, considering the definition for permanent strains (2.57), an exponential softening law in tension (Eq. (2.76) with $r_0^+ = f^+ = f_p^+$, i.e. $\gamma_e^+ = \gamma_p^+$) and a parabolic-exponential damage evolution law in compression (Eq. (2.76) with $r_0^- < f^- < f_p^-$, $\gamma_e^- = 0.4$ and $\gamma_p^- = 1.6$). The mechanical parameters adopted for concrete, class C40, are collected in Table 6.10. They are chosen in accordance to (Rospars and Chauvel, 2014; Vassaux et al., 2015) and, in absence of data availability, calibrated in order to optimize the fitting between numerical and experimental results.

Table 6.10: Concrete parameters for the problem of the R.C. wall under cyclic shear.

E	ν	f^+	f^-	G_f^+	G_f^-	f_b^-/f^-	$b+$	$b-$	k
[MPa]	[-]	[MPa]	[MPa]	[N/mm]	[N/mm]	[-]	[-]	[-]	[-]
22000	0.2	3.9	-42	0.7	45	1.16	0.1	0.35	0.8

The reinforcement is modeled as follows, exploiting the fact that it is oriented along the Cartesian directions x and y. Assuming the hypothesis of perfect adherence between concrete and rebars, the axial forces sustained by steel in the horizontal and vertical direction, P_{sx} and P_{sy}, are computed starting from the deformations ε_x and ε_y in the concrete, taking into account the percentage of horizontal and vertical reinforcement ρ_x and ρ_y. The uniaxial constitutive law chosen to represent the cyclic behaviour of the reinforcement is the one proposed in (Menegotto and Pinto, 1973) and illustrated in Figure 6.25. The expression for the steel stress σ_s is explicited in (Faria et al., 2004).
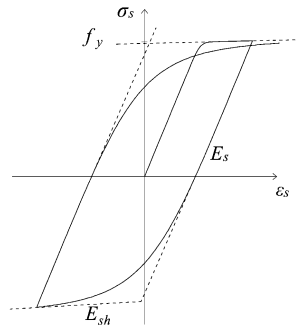
Figure 6.25: Constitutive law of the reinforcement under uniaxial cyclic history.

The parameters adopted in the analyses for the characterization of the reinforcement are synthetized in Table 6.11, where E_s is the Young's elastic modulus, E_{sh} is the hardening modulus, f_y is the yielding stress and a_1, a_2 and a_3 are three constants chosen to fit the Baushinger effect observed experimentally.

Table 6.11: Reinforcement constitutive parameters for the problem of the R.C. wall under cyclic shear.

E_s	E_{sh}	f_y	a_1	a_2	a_3
[MPa]	[MPa]	[MPa]	[-]	[-]	[-]
210000	2100	420	18.5	0.15	20

The percentages of steel reinforcement considered in the different Zones highlighted in Figure 6.24 are summarized in Table 6.12, together with the thickness of each Zone.

Table 6.12: Percentage of the reinforcement and thickness for each Zone of the R.C. shear wall body test.

Zone	ρ_x	ρ_y	Thickness
	[-]	[-]	[mm]
Zone 1	0.011	0.011	150
Zone 2	0.025	0.243	150
Zone 3	0.043	0.005	450
Zone 4	0.048	0.155	450

Due to the absence of vertical loads, except for the self-weight which is negligible compared to the horizontal cyclic action, the multidirectional approach is applied referring to load Type (i), considering non-evolving damage regions during the loading history (Section 3.1.1). Therefore, the only additional parameter required by the multidirectional procedure is θ_t (Eq. (3.6)), assumed equal to $\pi/36$.

In Figure 6.26, the experimental results in terms of global horizontal force F_h – horizontal displacement u_{hA} of point A on the top side of the specimen (see Figure 6.24) are plotted (Bisch et al., 2014). In Figure 6.27, four different numerical predictions are shown: Figure 6.27.a and Figure 6.27.b exhibit the force-

displacement curves obtained by means of the multidirectional procedure, considering two different quadrilateral mesh refinements; Figure 6.27.c represents the numerical response derived by applying the standard scalar damage formulation, without a multidirectional treatment of damage; finally, in Figure 6.27.d the results are obtained with the multidirectional procedure and increasing the intensity of the permanent deformations with respect to the values presented in Table 6.10 ($b^+= 0.18$ and $b^-= 0.45$).
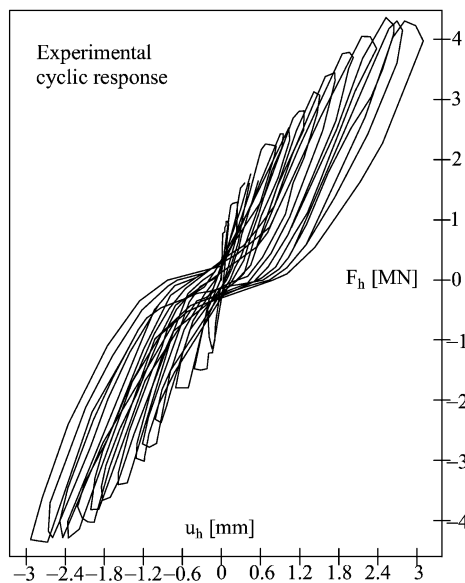
Figure 6.26: R.C. wall under in-plane cyclic shear: experimental results.

First of all, comparing Figure 6.27.a and Figure 6.27.b, a very low dependence of the results on the discretization can be appreciated. Secondly, good representativeness of the experimental curve is noticed. Specifically, the progressive evolution of degradation with the development of cracking is captured, as well as the lateral resistance of the structure (4.07 MN against 4.3 MN). Even in terms of displacement capacity, the numerical and observed results are in good agreement: the slightly greater deformability visible in Figure 6.26 for high load cycles is attributable to the assumption of elastic behaviour for the Zones 2, 3 and 4 displayed in Figure 6.24.
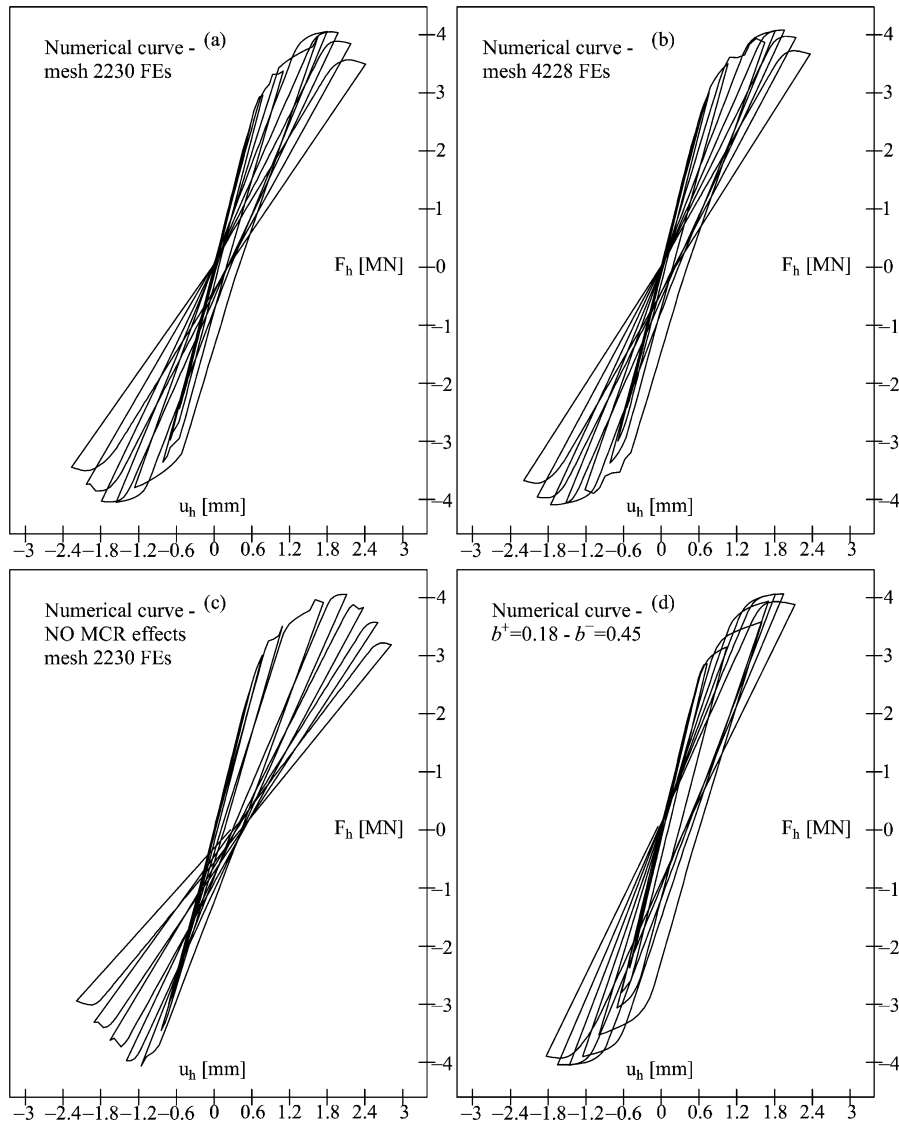
Figure 6.27: R.C. wall under in-plane cyclic shear: (a) and (b) numerical results obtained with the multidirectional procedure for two different mesh refinments; (c) numerical results without the multidirectional procedure; (d) numerical results obtained with the multidirectional procedure and with an higher level of permanent deformations.

In addition, comparing Figure 6.27.b and Figure 6.27.d, it is worth noting that the level of permanent deformations experimentally observed is better modelled by increasing the parameters b^+ and b^-. This represents a further confirmation of the adequacy of Eq. (2.57) for describing the evolution of ε_p.

For what concern the effects of the alternating loadings, the global response obtained with the adoption of the multidirectional procedure (Figure 6.27.a, Figure

6.27.b and Figure 6.27.d) is essentially symmetric. This proves an appropriate consideration of the microcracks closure-reopening phenomena. In fact, the same peak loads and the same dissipative trends can be obtained in the loading and reloading stages only by means of appropriate stiffness recovery capabilities upon loading reversal. These features are absent in the response obtained without the multidirectional procedure (Figure 6.27.c), in which the full conservation of damage from the loading to the reloading stages is evident and is due to the impossibility of distinguishing between two sets of defects with different orientations. In addition, as discussed in Section 3.4, the lack of unilateral capabilities have consequences even on the evolution of permanent strains, which unrealistically accumulate only for positive thrusts.

The only notable discrepancy between numerical and observed results lies in the pinched shape of the hysteresis cycles, which is evident in Figure 6.26 and is not appreciable in Figure 6.27.a, Figure 6.27.b and Figure 6.27.d. Pinching is associated to the bond slip between concrete and rebars (Vecchio, 1999), neglected in the analysis due to the hypothesis of perfect adherence. Removing such an assumption would add significant complexity to the model and it is not in line with the objective of the present example of application, which is to show the enhanced unilateral capabilities of concrete ensured by the application of the multidirectional procedure.

In order to demonstrate how the multidirectional approach allows reproducing the stiffness recovery, the contour plots of the active tensile damage at the end of the loading ($u_{hA} = 1.55$ mm) and at the end of the reloading ($u_{hA} = -1.35$ mm) in the fourth cycle of the curve plotted in Figure 6.27.b are displayed in Figure 6.28.a and Figure 6.28.b, respectively. The approach is based on the deactivation of some values of damage (the one referred to the closed cracks) and on the reactivation of other values (the one referred to the open ones).

(a)   (b)

0   0.0936   0.187   0.281   0.374   0.468   0.562   0.655   0.749   0.842   0.936
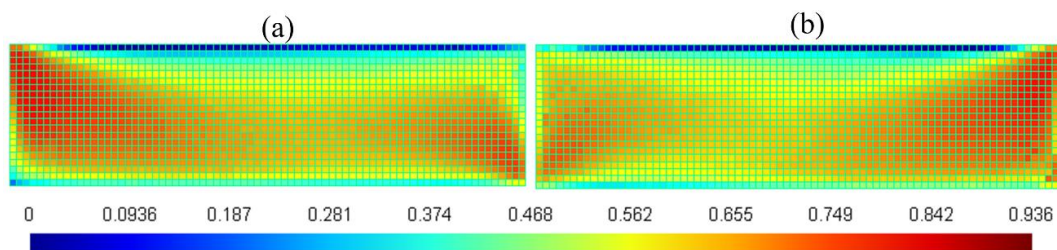
Figure 6.28: Contour plots of the active tensile damage value d^+ for the R.C. wall under in-plane cyclic shear: (a) $u_{hA} = 1.55$ mm and (b) $u_{hA} = -1.35$ mm.

Finally, the symmetry found in the active damage contour plots (Figure 6.28) between the two sets of alternating active cracks reflects in a symmetric distribution of the longitudinal strains ε_{xx}, between the situation $u_{hA} = 2.35$ mm and $u_{hA} = -2.2$ mm, as shown in Figure 6.29.a and Figure 6.29.b respectively. These contour plots reproduce satisfactorily the two symmetric sets of cracks observed in the laboratory test (Rospars and Chauvel, 2014) and confirm the adequacy of the proposed mechanical model in dealing with cyclic shear actions.
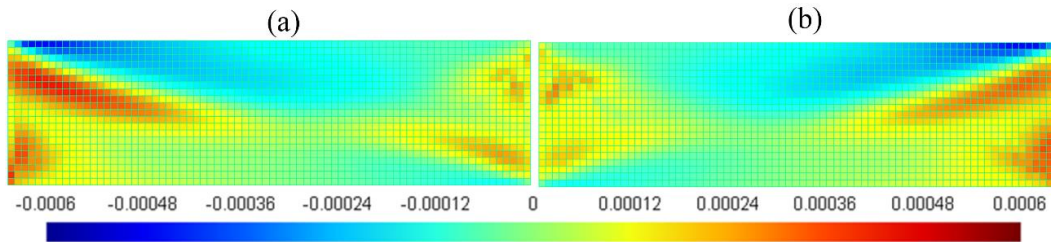
Figure 6.29: Contour plots of the longitudinal strains ε_{xx} for the R.C. wall under in-plane cyclic shear: (a) $u_{hA} = 2.35$ mm and (b) $u_{hA} = -2.2$ mm.

6.3.3 Numerical robustness of the multidirectional damage procedure

In Section 3.3, a smooth transition between different damage regions is proposed with the aim of alleviating the convergence difficulties expected when cracks close and reopen. Here, the effects of this procedure on the numerical performance of the multidirection damage approach are investigated and quantified with reference to the problem of the masonry shear panel studied in Section 6.3.1. This is carried out by varying the value of the parameter θ_t which identifies the amplitude of the transition region (see Eq. (3.6) and Figure 3.4) for each level of permanent deformations considered in the numerical analyses (Figure 6.23). The variable used to quantify the numerical performance is the number of iterations necessary to achieve convergence in a load step.

The convergence data discussed in the following regards the unloading-reloading stages after the achievement of the maximum load (cycle 2, amplitude 3 mm). As previously discussed, this is in fact the situation in which stiffness recovery is more emphasised and hence convergence difficulties are expected to be greater. Specifically, the load increments around crack-closure, which require the highest number of iterations to converge, are thirteen. For these thirteen load steps, the number of necessary iterations is indicated in Figure 6.30.a, Figure 6.30.b and Figure 6.30.c, which refer to the case of high permanent deformations ($b^+ = 0.17$

and $b^- = 0.45$), intermediate permanent deformations ($b^+ = 0.1$ and $b^- = 0.3$) and null permanent deformations ($b^+ = 0.0$ and $b^- = 0.0$), respectively.

In each graph, different values of θ_t are taken into account: from $\theta_t = \pi/180$ (1°) to $\theta_t = \pi/36$ (5°). Higher is θ_t, smoother is the modelling of the crak closure.
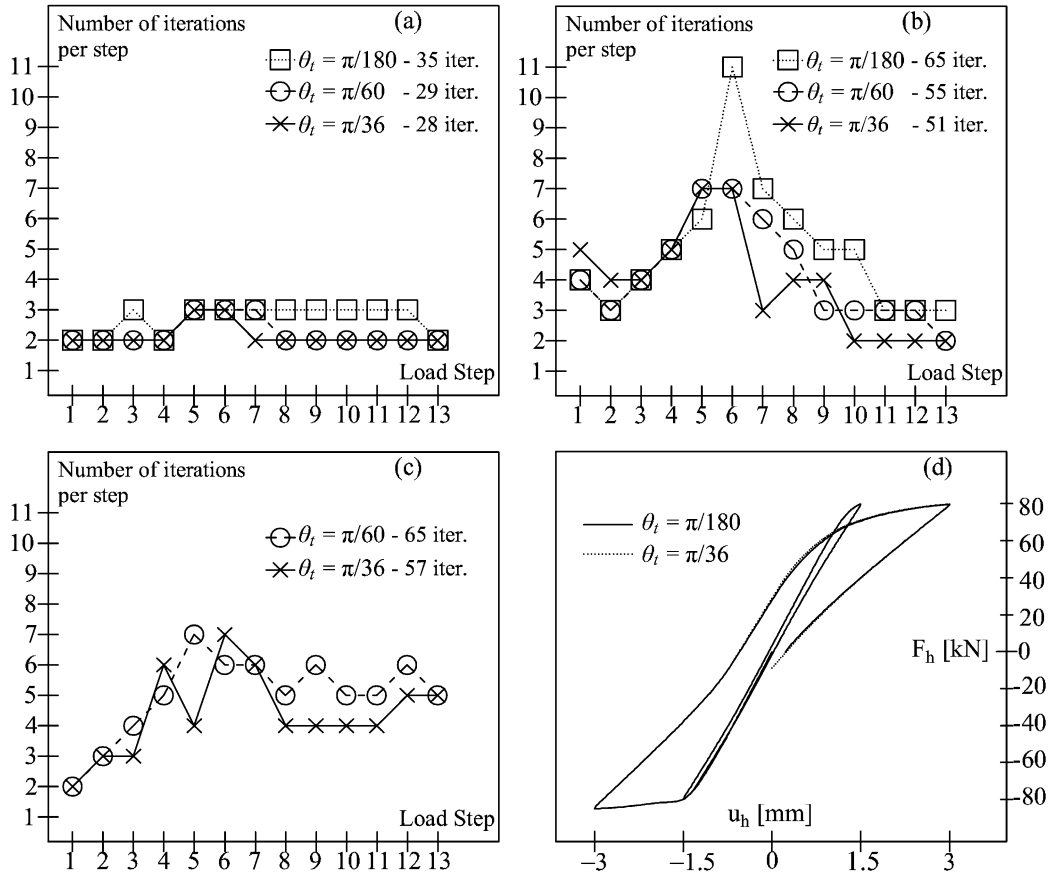
Figure 6.30: Numerical convergence in correspondence with crack closure for varying θ_t: (a) high permanent deformations, (b) intermediate permanent deformations, (c) zero permanent deformations and (d) effects of θ_t on the structural response.

Moreover, Figure 6.30.d shows the structural responses obtained with different values of θ_t, in case of $b^+ = 0.1$ and $b^- = 0.3$.

Analysing Figure 6.30, it is possible to observe that passing from $\theta_t = \pi/180$ to $\theta_t = \pi/36$ there is a non-negligible reduction of the total number of iterations, which is of 22% in the case of high ε_p and 24% in the case of intermediate ε_p. However, the beneficial effect of the smoothing procedure is more significant in the case of zero permanent deformations, where the inclusion of a sufficiently wide transition

region ($\theta_t = \pi/36$) allows to obtain convergence in 57 iterations, while, with the adoption of $\theta_t = \pi/180$, lack of covergence has been encountered. For this reason the curve associated to $\theta_t = \pi/180$ is not present in Figure 6.30.c. This consideration is in agreement with another trend inferable from Figure 6.30: permanent deformations improve the numerical performance as they mitigate the abrupt stiffness changes in correspondence of crack closure. Finally, Figure 6.30.d shows that the structural response is unaffected by the transition parameter θ_t, confirming that its role is only the one of improving the robusteness of the multidirectional damage procedure.

Chapter 7

Validation of the regularized strain tensor damage model

In the present chapter, different structural problems are solved with the regularized d^+/d^- damage model presented in Chapter 4. The versatility of such a formulation is proven by studying a masonry arch and reinforced and unreinforced concrete elements. Besides the validation of the numerical results with experimental or analytical data, each example highlights one or more features of the regularized formulation: the mesh-size and mesh-bias independence of the results, the influence of the nonlocal internal length l_{RG}, the effect of the choice of the nonlocal variable to be averaged, the possibility to reproduce structural size effects. The numerical algorithm adopted for studying these problems is the one detailed in Table 5.5 and Table 5.6.

7.1 Masonry arch subjected to a vertical point load

The first problem solved with the regularized damage model is a masonry arch subjected to a vertical cyclic point-load located at one quarter of the span.

On the one hand, the example is addressed to show the applicability of the proposed damage model to a common typology of masonry structures under gravity loads. In these loading conditions, a damage criterion in compression can be omitted because crushing is far from being attained. Therefore, with respect to the general formulation, the further assumption of $d^- = 0$ is here considered. Although

the choice of a linear elastic behaviour in compression does not reproduce accurately the reality, it is undertaken also in (Heyman, 1995) for applying limit analysis to masonry structures and in (Cuomo and Ventura, 2000), for describing the masonry mechanical behaviour in combination with a no-tension material model.

On the other hand, the problem discusses the negligible dependence of the regularized solution on the mesh-size. As mentioned at the end of Section 4.1.1, the averaging is applied to the elastic strain tensor ε_e whilst the permanent strain tensor ε_p is always considered in its local version. Therefore, the capability of the regularized approach to ensure objective results with respect to the discretization has to be investigated in presence of irreversible deformations. For this reason, such an example, characterized by loading and reloading stages, is taken into account for validating the mesh-size independence of the regularized formulation.

The reference solution is represented by the results of a static cyclic laboratory test illustrated in (Ramos et al., 2010) and (Ramos, 2007). A comparison between these experimental results and the numerical solution obtained by means of a unilateral nonlocal damage model is also developed in (Toti et al., 2014).

The arch, made of brick masonry, has a semicircular shape with a radius of 0.77 m, a span of 1.5 m and a cross section equal to 0.05 m (thickness) × 0.45 m (depth). The geometry and loading conditions are considered with reference to a plane stress problem. Both vertical and horizontal displacements are restrained at the arch springers, simulating as infinitely stiff the concrete abutments present in the experimental configuration. The applied point load at the quarter span is modelled by means of a prescribed displacement history in order to capture the post-peak structural response. The material properties are reported in Table 7.1.

Although damage in compression is not taken into account, the value of the compressive strength is provided because the damage surface in tension depends on the ratio between the tensile and compressive uniaxial strengths, as shown in Figure 2.4.a and in the expression of the positive equivalent stress quantity (2.45).

Table 7.1: Material parameters for the analysis of the masonry arch.

E [MPa]	ν [-]	f^+ [MPa]	f^- [MPa]	G_f^+ [N/mm]	ξ^+ [-]	l_{RG} [mm]	γ_m [kN/m^3]
4000	0.2	0.11	-3	0.0085	0.5	21	16

The elastic material properties as well as the masonry specific weight are chosen according to (Ramos, 2007) and (Toti et al., 2014): $E = 4000$ MPa, $v = 0.2$ and $\gamma_m = 16$ kN/m^3. In (Toti et al., 2014), these parameters are calibrated by means of an inverse procedure, taking into account the modal structural properties derived by the dynamic tests carried out on the arch in (Ramos et al., 2010). The parameters governing the damage propagation and the development of irreversible deformations are assumed in order to obtain a response curve as close as possible to the experimental one: $f_t = 0.11$ MPa, $G_f^+ = 0.0085$ N/mm and $\xi^+ = 0.5$. The use of the parameter ξ^+ indicates that the new definition of the permanent deformations, expressed in Eq. (2.61), is here considered. Finally, according to the calibration procedure commented in Section 4.2, a relative dissipation length k_{dis} equal to 2, is associated to the internal length $l_{RG} = 21$ mm.

As done in the laboratory test, the numerical analysis is performed under a cyclic load history, in order to validate the capability of the proposed constitutive law to catch the experimental response in terms not only of carrying capacity and strain localization but also stiffness degradation and permanent deformations. The numerical cyclic structural response is shown in Figure 7.1 in a diagram whose axes are the vertical applied displacement u and measured reaction force F as abscissae and ordinates, respectively. The numerical solution for a structured triangular mesh of 1563 finite elements is plotted together with the experimental envelope. The unloading braches obtained in the cyclic experimental test are omitted and only the loading stages are shown.
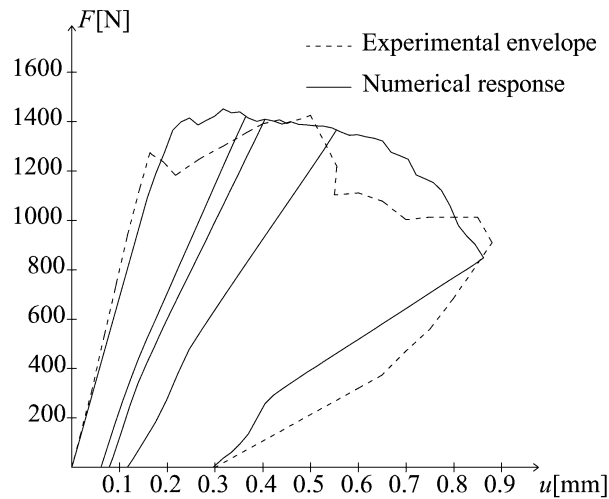
Figure 7.1: Concentrated force F - vertical displacement u curve for the arch: comparison between experimental and numerical results with a mesh of 1563 FEs.

The numerical results are satisfactory: the decrease of the initial stiffness at the elastic limit, the ascending stage up to the peak load as well as the softening regime are well captured by the model. In particular, the approximation of the peak load is excellent, with a negligible difference between the numerical (1424.7 N) and the measured (1424.9 N) values.

In terms of failure mechanism, the opening of the four experimentally observed cracks is well reproduced. The crack sequence, not registered in the laboratory test, can be positively compared with some preliminary numerical results provided in (Ramos, 2007). In Figure 7.2, the tensile damage distribution shows how strain localization appears first just below the concentrated load at the intrados (Figure 7.2.a), then at the intrados of the right support (Figure 7.2.b), then again at a symmetrical position with respect to the first crack but at the extrados (Figure 7.2.c) and lastly at the extrados of the left support (Figure 7.2.d; here damage concentration is only slightly displayed).

The map of the maximum principal permanent strains at the end of the analysis, plotted in Figure 7.3, constitutes a further evidence of the fact that the expected resistant mechanism based on four hinges is numerically well reproduced.
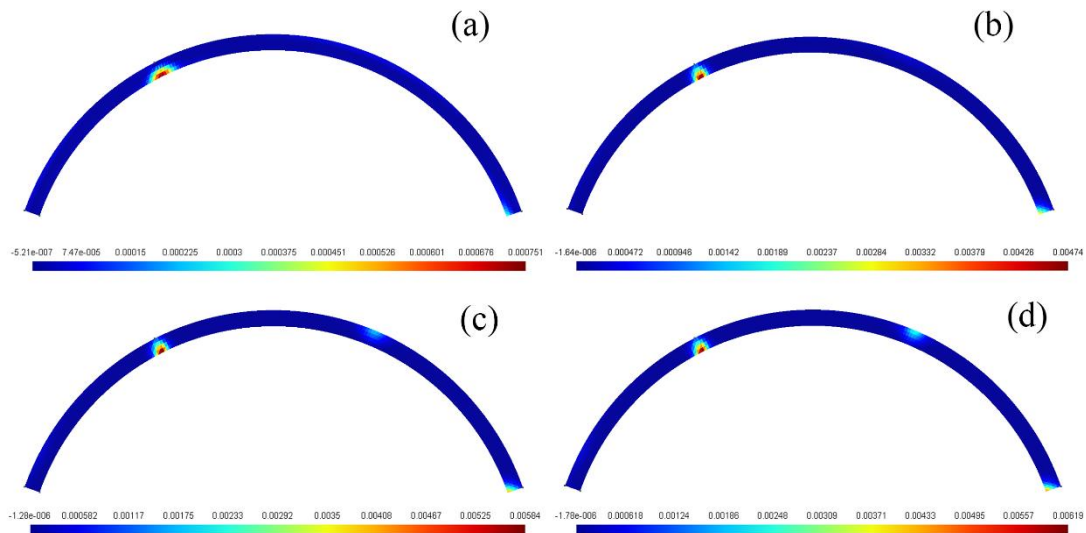
Figure 7.2: Numerical crack localization and opening crack sequence: first crack at a vertical displacement of 0.3 mm (a), second crack at 0.51 mm (b), third at 0.79 mm(c), fourth at 0.86 mm.

-7.9e-008   0.000408   0.000816   0.00122   0.00163   0.00204   0.00245   0.00286   0.00326   0.00367   0.00408
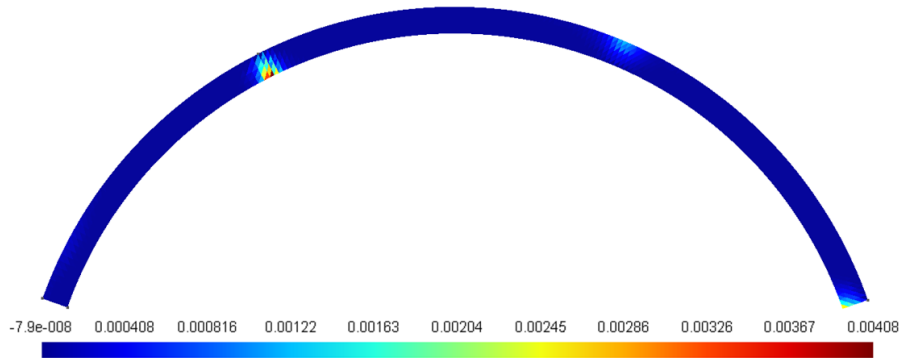
Figure 7.3: Contour plots of maximum principal permanent strains at the end of the analysis.

A detailed comparison between the numerical F - u trends in the loading and unloading stages and the four cycles observed in the laboratory test is provided in Figure 7.4 in order to verify the adequacy of the new definition of permanent strains introduced in Eq. (2.61). From the analysis of Figure 7.4, it can be inferred that relating the evolution of permanent deformations to the partial irreversibility of the microcrack opening through Eq. (2.61) finds experimental confirmation: except for the first load cycle, in all the other cases a fair correspondence is found in terms of residual deformations at complete unloading.
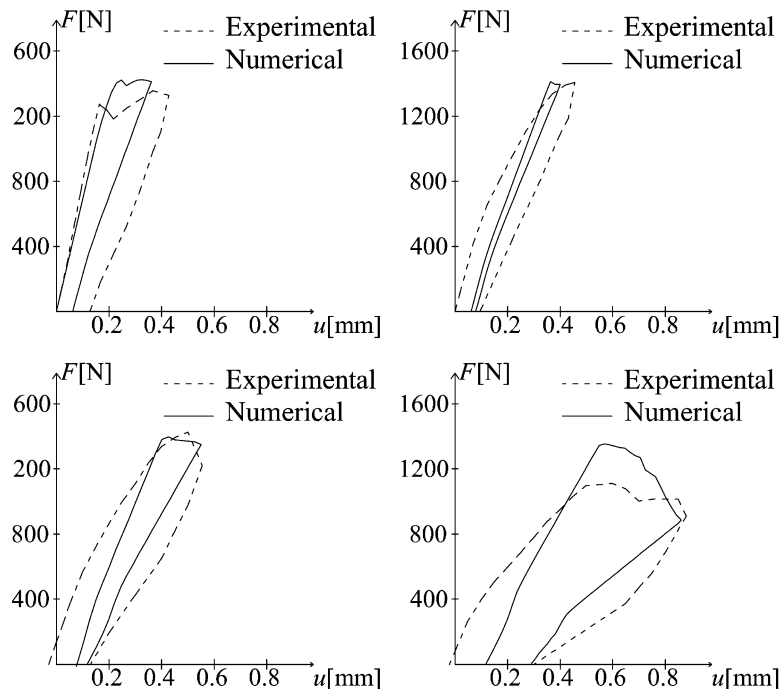
Figure 7.4: Comparison between numerical and experimental cyclic response.

This allows to conclude that the new simplified definition of the permanent deformations (2.61) is effective, as well as the one proposed by (Faria et al., 1998) and reconsidered in the form (2.57), but has a stronger mechanical basis, which is the plastic microcracking.

A further confirmation of the adequacy of the constitutive law is provided by its capability of representing faithfully the stiffness degradation during the loading history. This is shown in Figure 7.5, where the evolution of the numerical relative secant unloading stiffness is compared with the corresponding experimental value.

Finally, the example of the masonry arch subjected to a point load is exploited to investigate the positive consequences of a regularized approach in terms of dependence of the solutions on the mesh refinement. Three different degree of mesh refinements are considered, all of them characterized by the use of triangular structured finite elements: the coarse mesh has 1072 finite elements, the intermediate 1536 finite elements while the finer 2112 finite elements. The global response curves for the different discretizations are collected in Figure 7.6.

The mesh objectivity study proves the capability of the regularized damage model to provide solutions negligibly affected by the discretization. In particular, higher is the refinement, lower are the differences visible in the response curve, as confirmed by the almost perfect superimposition between the F - u curves obtained with the intermediate and the fine mesh.
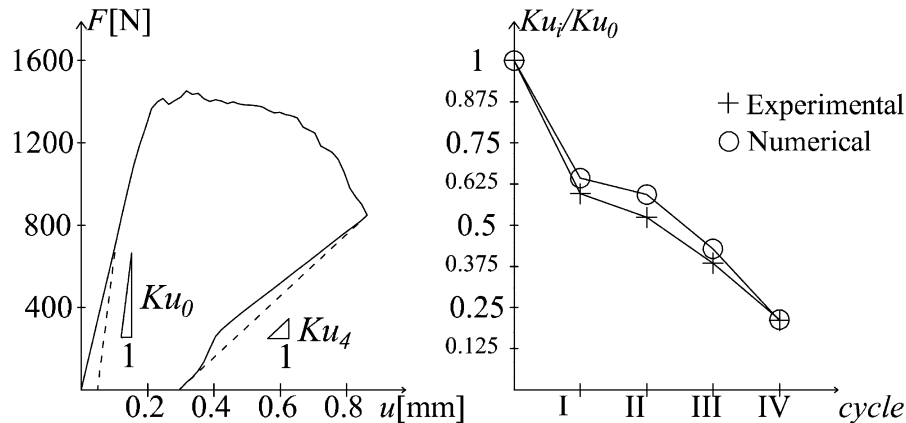
Figure 7.5: (a) Identification of unloading secant stiffness and (b) comparison between numerical and experimental unloading relative stiffness values.
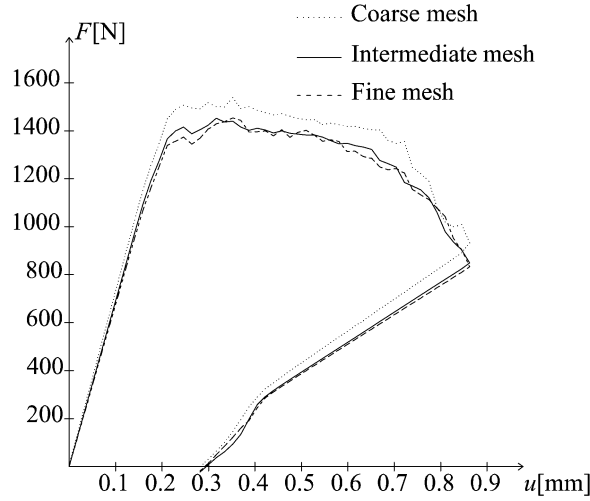
Figure 7.6: Dependence on the mesh refinement of the results obtained with the regularized damage model for the problem of the arch subjected to a vertical point wise load.

It is worth noting that not only the load values are not influenced by the choice of the mesh refinement, but also the irreversible strains. This allows concluding that the averaging of only the elastic strain tensor ε_e, performed in accordance with the calibration procedure explained in Section 4.2, is sufficient to ensure the mesh-objectivity of the results; consequently, the permanent strains, introduced by means of a unified dissipative framework, can be treated as local variables.

7.2 Perforated slab under uniaxial tension

The present section highlights the capability of the regularized approach described in Chapter 4 to provide strain localization results independent of the mesh alignment, comparing it with the performance of the corresponding local approach.

The reference solution considered to verify the adequacy of the regularized model is represented by the analytical results obtained with the strain localization analysis proposed in (Wu and Cervera, 2017). In this paper, the strain localization analysis is applied to some classical isotropic damage models, among which there is the "$1 - d$" damage model described in (Simó and Ju, 1987). For such damage formulation, a closed form solution for the discontinuity orientations is provided in (Wu and Cervera, 2017), strongly dependent on the Poisson ratio v.

Therefore, to validate the mesh-bias objectivity of the regularized strain tensor approach, firstly the Simo and Ju isotropic damage model is considered, in order to use known analytical results as comparison. Then, the strain localization analysis

proposed in (Wu and Cervera, 2017) is extended to the new constitutive operator presented in its regularized version in Eq. (4.8) (for the case of $d^- = 0$). This allows to study the effect of the orthotropy on the discontinuity inclination as well as to verify the reliability of the regularized procedure in conjunction with the new constitutive orthotropic stiffness operator (4.8).

The problem chosen to develop this topic is a singly perforated slab loaded in uniaxial tension by means of imposed vertical displacements at top and bottom ends. The slab, with dimensions 20 m × 40 m × 1 m, holds a slanted perforation of diameter 1 m, introduced in order to avoid symmetric solutions. The imposed vertical displacement u_v at both ends is equal to 0.1 m. This is the same example of application adopted in (Wu and Cervera, 2017) to validate numerically the proposed strain localization analysis. However, there the mesh-bias independence of the results is ensured by the adoption of the mixed strain/displacement finite element method (Cervera et al., 2011). The material properties used in the numerical analyses are summarized in Table 7.2.

Table 7.2: Material parameters for the analysis of the perforated slab.

E [MPa]	v [-]	f^+ [MPa]	G_f^+ [N/mm]	ξ [-]
10	0.0 – 0.15 – 0.3	0.01	0.5	0.0

The absence of the material properties related to compression in Table 7.2 is justified by the fact that the damage criteria adopted in the follow-up in the isotropic and orthotropic cases are not dependent on them, in accordance with the formulation proposed by (Simó and Ju, 1987).

Three values for the Poisson ratio v are considered since the discontinuity angle is affected by v, as demonstrated in (Wu and Cervera, 2017). In fact, the strategy to validate the mesh-bias objectivity of the model is different from the one usually adopted, consisting in changing the mesh alignment and monitoring the variation of the numerical solution. Here, the mesh is maintained fixed and the capability of the regularized approach to catch the analytical solution is assessed by varying the Poisson ratio. Actually, to test further the regularized approach, two different triangular meshes are adopted, both with an average size of 0.3 m in correspondence with the perforation: an unstructured mesh is adopted in case of $v = 0$ (Figure 7.7.a) and a structured one in case of $v \neq 0$ (Figure 7.7.b), since horizontal and inclined discontinuities are expected from the analytical results, respectively.
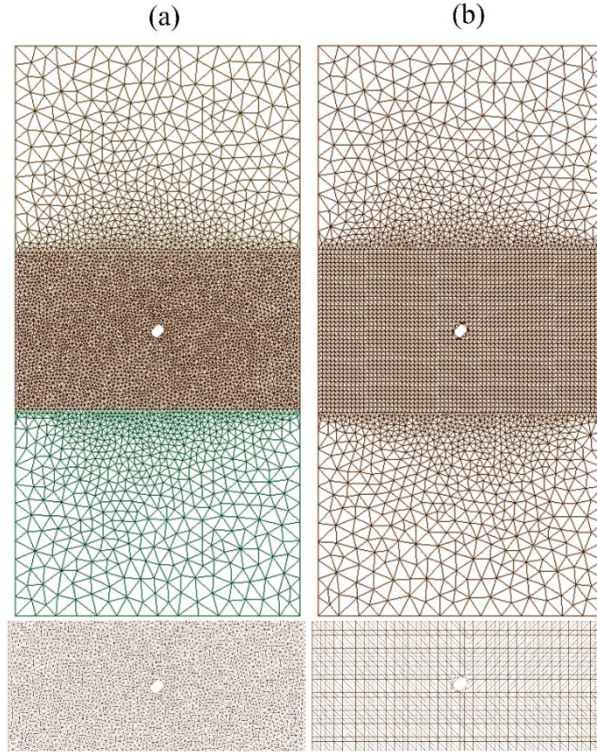
Figure 7.7: (a) Triangular unstructured mesh adopted for $\nu = 0$ with 9694 finite elements and (b) triangular structured mesh adopted for $\nu \neq 0$ with 7684 finite elements.

7.2.1 Isotropic model

The isotropic model considered is the strain-based one proposed in (Simó and Ju, 1987), whose salient aspects (constitutive law and damage criterion) are summarized in Eqs. (7.1), (7.2) and (7.3).

$$\boldsymbol{\sigma} = (1-d)\bar{\boldsymbol{\sigma}} = (1-d)\boldsymbol{D_0} : \boldsymbol{\varepsilon_e} \tag{7.1}$$

$$g = \tau - r \leq 0 \tag{7.2}$$

$$\tau = \sqrt{\boldsymbol{\varepsilon} : \boldsymbol{D_0} : \boldsymbol{\varepsilon}} \qquad r = \max\left(r_0; \max_{[0,t]}(\tau)\right) \tag{7.3}$$

In Eqs. (7.1), (7.2) and (7.3), τ and r represent the equivalent and the damage threshold quantities; in particular, r_0 is equal to $f^+/\sqrt{E}$. An exponential softening law of the type expressed in Eq. (2.79) is adopted to define d starting from r.

In the local analyses, in accordance with the crack band theory, the softening modulus H_d is adjusted according to the size h of the discretization (h replaces the generic length l present in Eq. (2.84b)). In the regularized analyses, the internal length l_{RG} is assumed equal to 0.215 m (i.e, the interaction radius is 0.43 m) and the relative dissipation lengths k_{dis}, which vary slightly with the Poisson's ratio, computed according to the calibration procedure described in Section 4.2, are: $k_{dis} = 2.11$ for $v = 0.0$, $k_{dis} = 2.09$ for $v = 0.15$ and $k_{dis} = 2.06$ for $v = 0.3$.

The vertical force F- vertical displacement u_v curves obtained with the regularized approach, for the three different values of the Poisson's ratio, are shown in Figure 7.8, together with a comparison between the global response obtained with the local and with the regularized approach for the representative case of $v = 0.3$.
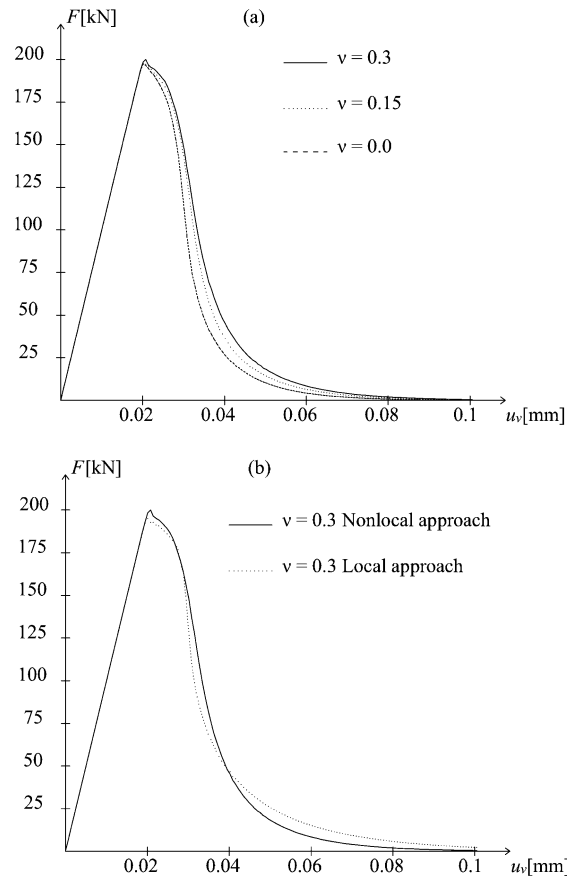
Figure 7.8: (a) Force F - vertical displacement u_v curves with the regularized isotropic damage model for different values of v; (b) local and regularized approaches for $v = 0.3$.

As shown in Figure 7.8, the structural response is slightly affected by the Poisson ratio. The comparison between the curve obtained with the local and with the

nonlocal approach highlights the fact that, thanks to the calibration procedure, the two models are able to dissipate the same amount of energy, being the damage evolution ruled by the common fracture energy G_f^+.

In addition, the vertical displacements at the end of the analysis obtained with the local approach and with the r one are plotted for the different values of the Poisson's ratio in Figure 7.9 and Figure 7.10, respectively. These figures clearly show how v strongly affects the discontinuity orientation and how significantly different results are achieved with a local approach and with a regularized one.

The analytical localization angle in case of plane stress problems, derived in (Wu and Cervera, 2017) for the Simó and Ju isotropic damage model, is:

$$\cos 2\theta_{cr} = \frac{1-v}{1+v} \cdot \frac{\sigma_1 + \sigma_2}{\sigma_1 - \sigma_2} \tag{7.4}$$

where θ_{cr} is the angle (clockwise verse) between the principal direction associated to σ_1 and the normal to the discontinuity. Due to the uniaxial loading conditions ($\sigma_1 \neq 0$, $\sigma_2 = 0$), the localization angle for the perforated slab under study becomes:

$$\cos 2\theta_{cr} = \frac{1-v}{1+v} \tag{7.5}$$
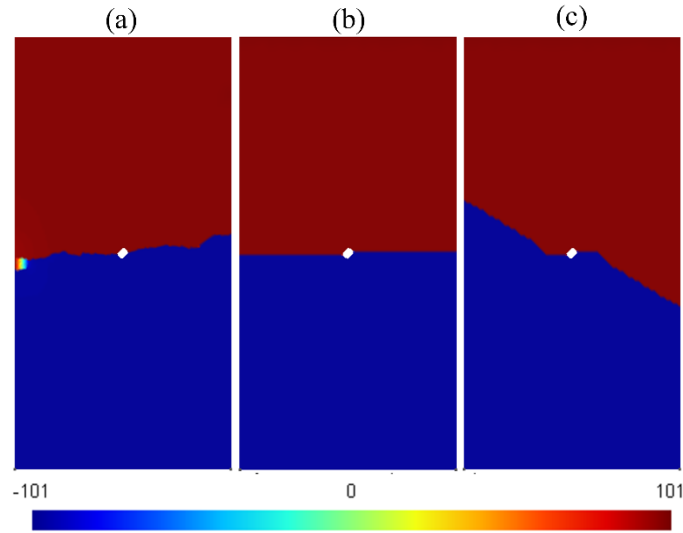
Figure 7.9: Contour plots of the vertical displacements (mm) with the isotropic local damage model for (a) $v = 0$, (b) $v = 0.15$ and (c) $v = 0.3$.
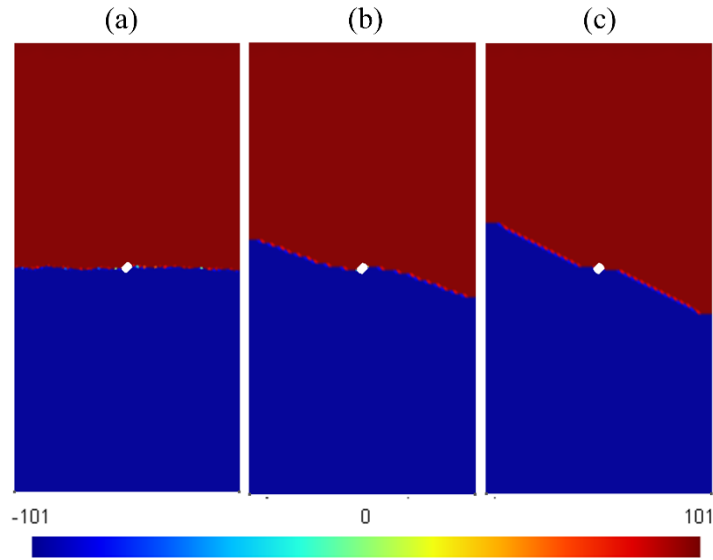
Figure 7.10: Contour plots of the vertical displacements (mm) with the isotropic regularized damage model for (a) $v = 0$, (b) $v = 0.15$ and (c) $v = 0.3$.

The comparison between the analytical results, the local (Figure 7.9) and regularized (Figure 7.10) localization angles is provided in Table 7.3.

Table 7.3: Comparison between analytical, local and regualrized discontinuity angles for the perforated slab under uniaxial tension studied with an isotropic damage model.

Poisson's ratio	Analytical	Numerical-local	Numerical-Regularized
$v = 0.0$	0.00°	10.60°	0.00°
$v = 0.15$	21.17°	0.00°	21.80°
$v = 0.3$	28.71°	34.31°	28.9°

On the one hand, the agreement between the discontinuity orientations obtained with the regualrized approach and the analytical values is remarkable, proving the independence of the proposed model from the mesh alignment. On the other hand, the local results are strongly affected by the mesh-bias. For $v = 0.0$ the horizontal crack is not represented due to use of the unstructured mesh (Figure 7.7.a), while for $v = 0.15$ and $v = 0.3$ the discontinuities tend to follow the two preferential directions induced by the structured mesh (Figure 7.7.b), which are the horizontal direction and the one inclined of 45°, respectively.

7.2.2 Orthotropic model

The Simó and Ju isotropic damage model exhibits a dependence of the strain localization on the lateral deformation behaviour which is inconsistent with the hypotheses at the base of the smeared and discrete crack models and that can be ascribed to its constitutive secant stiffness (see Eq. (7.1)).

In the present section, the adoption of the new energy-equivalent d^+/d^- constitutive operator $\boldsymbol{D_E}$ (see Eq. (4.8)) is investigated to discuss the effect of the orthotropy on the strain localization orientations. For the sake of clarity, the assumption of $d^- = 0$ is done. Moreover, in order to make the results comparable to the ones obtained in the previous section, the strain-driven damage criterion adopted in (Simó and Ju, 1987) and expressed in Eqs. (7.2) and (7.3) is considered, together with a damage evolution law of the exponential type. Only regularized analyses are performed with the orthotropic model, adopting the same internal length and the same dissipation lengths previously introduced for the isotropic formulation.

The structural responses obtained with the regularized orthotropic damage model, for the three different values of the Poisson ratio, are displayed in Figure 7.11. Although some slight differences between the curves plotted in Figure 7.11 are visible, they are smaller than the ones characterizing Figure 7.8.a, meaning that the effect of v is mitigated by the damage-induced orthotropy. The same consideration arises from the analysis of the vertical displacements, shown in Figure 7.12.
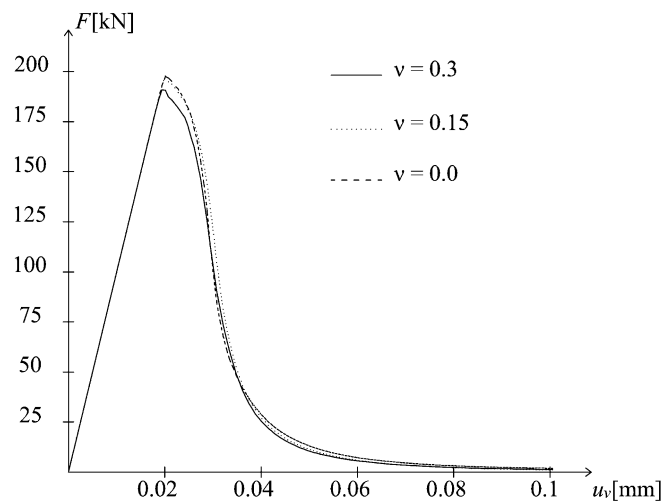
Figure 7.11: Vertical force F - vertical displacement u_v curves obtained with the regularized orthotropic damage model for different v.
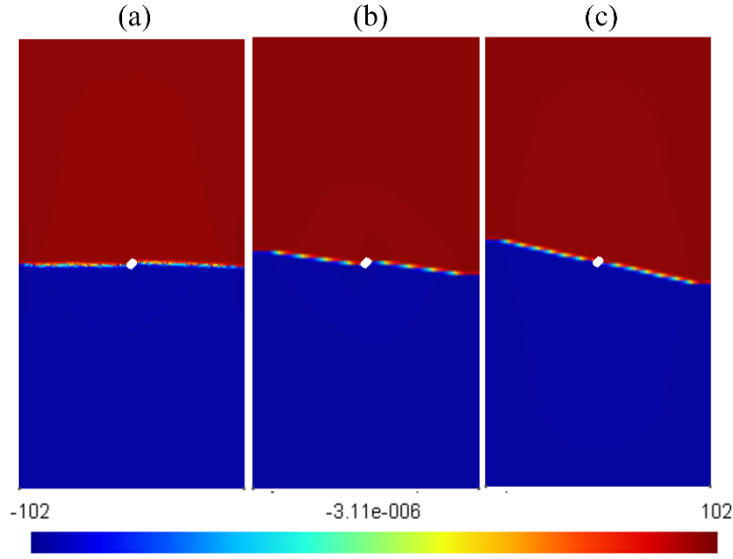
Figure 7.12: Contour plots of the vertical displacements (mm) with the orthotropic regularized damage model for (a) ν = 0, (b) ν = 0.15 and (c) ν = 0.3.

In order to compare the discontinuity angles found numerically with some analytical values, a strain localization analysis is carried out, following the procedure described in (Wu and Cervera, 2017) for plane stress problems. Such a procedure identifies the discontinuity angle θ_{cr} by setting appropriate kinematic constraints on the characteristic second order tensor Λ, which has the following definition:

$$\Lambda = \frac{\varepsilon_d}{\omega} = \frac{C_d : \sigma}{\omega} \tag{7.6}$$

In Eq. (7.6), ω is the alternative scalar damage variable $d^+/(1-d^+)$ while C_d is the damage compliance. Referring to the specific loading conditions of the perforated slab, the principal reference system of stresses coincides with the Cartesian reference system. The damage compliance C_d, derived by the inverse of the constitutive stiffness D_E, the stress σ and the characteristic tensor Λ in the principal reference system of the stress tensor are defined according to the Voigt notation in Eqs. (7.7), (7.8) and (7.9).

$$C_d = \omega \cdot \begin{bmatrix} \dfrac{1}{E} & -\dfrac{v \cdot \sqrt{1-d^+} \cdot \left(1 - \sqrt{1-d^+}\right)}{E} \\[3ex] -\dfrac{v \cdot \sqrt{1-d^+} \cdot \left(1 - \sqrt{1-d^+}\right)}{E} & 0 \end{bmatrix} \tag{7.7}$$

$$\sigma = \begin{bmatrix} \sigma_1 \\ 0 \end{bmatrix} \tag{7.8}$$

$$\Lambda = \begin{bmatrix} \dfrac{\sigma_1}{E} \\[3ex] -v \cdot \sqrt{1-d^+} \cdot \left(1 - \sqrt{1-d^+}\right) \cdot \dfrac{\sigma_1}{E} \end{bmatrix} \tag{7.9}$$

The kinematic condition to be set in order to identify the discontinuity angle θ_{cr} (clockwise verse) between the first principal direction (associated to the principal stress value σ_1) and the normal to the discontinuity is expressed in the following:

$$\cos 2\theta_{cr} = \frac{\Lambda_1 + \Lambda_2}{\Lambda_1 - \Lambda_2} \tag{7.10}$$

By replacing in Eq. (7.10) the principal components of the characteristic tensor defined in Eq. (7.9), the discontinuity inclination obtained with the orthotropic damage ruled by the constitutive operator D_E results:

$$\cos 2\theta_{cr} = \frac{1 - v\left(\sqrt{1-d^+} - 1 + d^+\right)}{1 + v\left(\sqrt{1-d^+} - 1 + d^+\right)} \tag{7.11}$$

Eq. (7.11) is fully comparable to Eq. (7.5): they have the same formalism but in the former the undamaged Poisson ratio is reduced by the positive damage quantity $\left(\sqrt{1-d^+} - 1 + d^+\right)$.

The dependence of θ_{cr} on d^+ in Eq. (7.11) implies that the orientation of the discontinuity depends on the damage value for which the strain localization occurs. Since the strain localization occurs for $d^+ < 1$ in case of exponential softening, a complete independence of the localization angles from the Poisson ratio is not

achieved with the present orthotropic model. However, the fact that the nominal Poisson ratio does not remain constant throughout the damage process is responsible for a reduction of the inclination of the discontinuity with respect to the horizontal direction. Such a consideration is in agreement with the numerical results obtained with the regularized orthotropic damage model, plotted in Figure 7.12: a certain dependence on the Poisson ratio is still visible but it is smaller than for the isotropic damage formulation (see Figure 7.10).

The comparison between the numerical localization angles and the analytical ones, computed from Eq. (7.11) assuming that the complete crack propagation happens for a damage value equal to 0.95, is provided in Table 7.4. From these data, the objectivity of the regularized approach with respect to the mesh-bias, even in conjunction with the orthotropic constitutive stiffness operator D_E, is validated.

Table 7.4: Comparison between analytical and regularized discontinuity angles for the perforated slab under uniaxial tension studied with an orthotropic damage model.

Poisson ratio	Analytical	Numerical-Regularized
$v = 0.00$	0.00°	0.00°
$v = 0.15$	9.19°	8.98°
$v = 0.30$	12.9°	13.3°

Finally, the evolution of the tensile damage obtained with the regularized orthotropic damage formulation in case of $v = 0.3$ is plotted in Figure 7.13, in order to show the reliability of the hypothesis of $d^+ = 0.95$ as value for which the strain localization completely occurs.
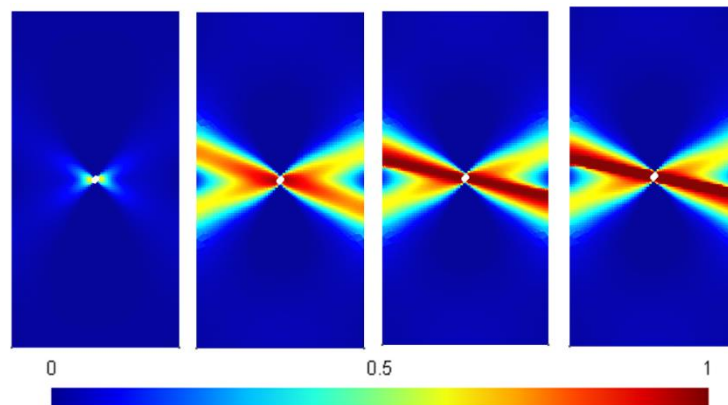
Figure 7.13: Evolution of tensile damage with the regularized orthotropic damage model, for the case of v=0.3.

7.3 Longitudinally-reinforced concrete beam under four point bending test

The example of application analysed in the present section is a longitudinally-reinforced concrete beam subjected to a four point bending test, experimentally tested in (Leonhardt and Walther, 1962) and numerically reproduced in (Xenos and Grassl, 2016). The geometry, the loading and the boundary conditions of the plane stress problem are illustrated in Figure 7.14.a. To avoid stress concentrations, steel plates are placed in correspondence with the loading points and the supports. The loading conditions are modelled assigning a prescribed vertical displacement to the central points of the loading surfaces; consequently, the point force P is evaluated as reaction at the support.

Due to the absence of transversal reinforcement, the observed failure, displayed in Figure 7.14, is governed by shear and consists in a set of cracks which, getting away from the mid-span, abandon the verticality and incline towards the supports. The study of this structural problem, characterized by multiple cracks and by an arch-resistant mechanism, with the proposed d^+/d^- regularized damage model is interesting because here the damage criterion in compression plays a fundamental role as well as the one in tension.
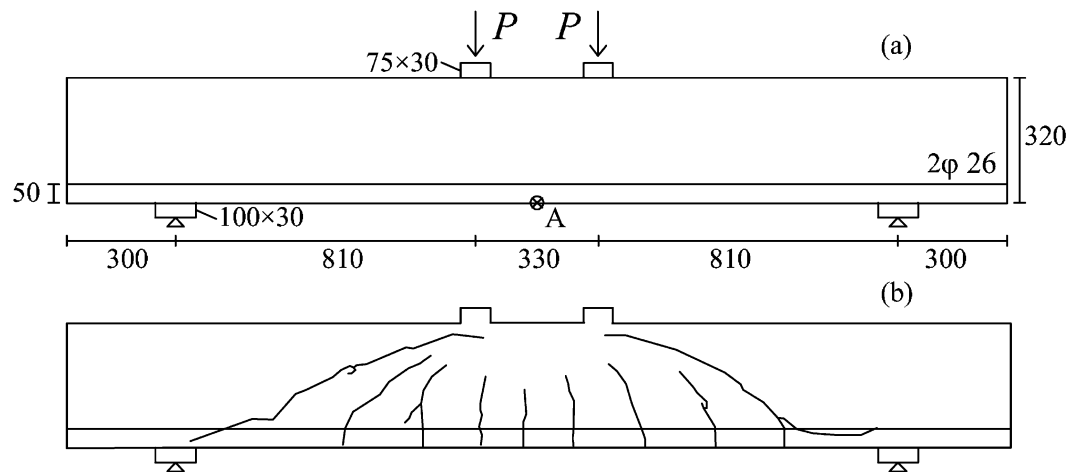
Figure 7.14: Geometry [mm], loading and boundary conditions of the four point bending test and (b) experimental cracking pattern documented in (Leonhardt and Walther, 1962).

Moreover, the example discusses in a quantitative way two fundamental aspects of the regularized damage model, extensively commented, in a qualitative way, in Section 4.1 and Section 4.2. On the one hand, the choice of the elastic strain tensor as variable to be averaged is compared to another, more common choice, based on the averaging of the equivalent quantity $\tau\pm$, other than to the local crack band approach. The comparison among the regularized strain tensor approach, the regularized approach based on the averaging of $\tau\pm$, hereafter named "regularized scalar approach", and the crack band model is developed in terms of mesh-objectivity and numerical performance. On the other hand, the influence of the internal length l_{RG} on the structural response is investigated. Interesting considerations are expected regarding this topic because of the multiple localization zones characterizing the example.

The material parameters considered in the numerical analyses for concrete are collected in Table 7.5. The majority of them, and in particular the elastic constants, the uniaxial strengths and G_f^+, are chosen in perfect agreement with the values provided in (Xenos and Grassl, 2016). They allow to identify the damage surfaces in tension and compression (note that $k = 0.8$ is chosen in the definition of τ^- (2.46)), the damage evolution laws (an exponential softening (2.79) is adopted in tension and a "Gaussian" hardening-softening (2.80) in compression) and the entity of the permanent deformations, according to Eq. (2.61).

Table 7.5: Material parameters for concrete.

E [MPa]	ν [-]	f^+ [MPa]	f^- [MPa]	G_f^+ [N/mm]	G_f^- [N/mm]	$\xi\pm$ [-]	f_b^-/f^- [-]
30500	0.2	2.18	-28.5	0.133	10.00	0.1	1.16

Five different values of the internal length l_{RG} are considered in the numerical simulations. Their values, together with the corresponding relative dissipation lengths in tension and compression, evaluated by means of the calibration procedure described in Section 4.2, are synthetized in Table 7.6.

Table 7.6: Internal lengths adopted in the numerical simulations of the reinforced concrete beam under four point bending test.

l_{RG}	Interaction radius	k^+_{dis}	k^-_{dis}
[mm]	[mm]	[-]	[-]
5.7	11.4	4.09	8.09
7.8	15.6	4.14	6.22
11.3	22.6	4.16	4.40
14.1	28.2	4.18	3.78
17.0	34	4.04	3.37

In addition, the hypothesis of linear elastic behaviour is considered for the steel of the reinforcement and of the loading plates, whose material constants are specified in Table 7.7. Specifically, the longitudinal reinforcement's behaviour is modelled as uniaxial (hence, the Poisson ratio shown in Table 7.7 is actually neglected), under the assumption of perfect adherence between concrete and steel. Exploiting the orientation of the rebars along the Cartesian direction x, the axial forces sustained by the reinforcement are evaluated by the total deformation ε_x in the concrete, taking into account the percentage of horizontal reinforcement ρ_x, equal to 1.75%.

Table 7.7: Material parameters for the steel plates and the steel reinforcement.

E	ν
[MPa]	[-]
198000	0.3

Finally, the triangular unstructured meshes adopted in the simulations (Figure 7.15) have an average size, from the coarser to the finer, equal to: 20 mm (5462 FEs), 15 mm (10052 FEs), 12 mm (15168 FEs) and 7 mm (54065 FEs).
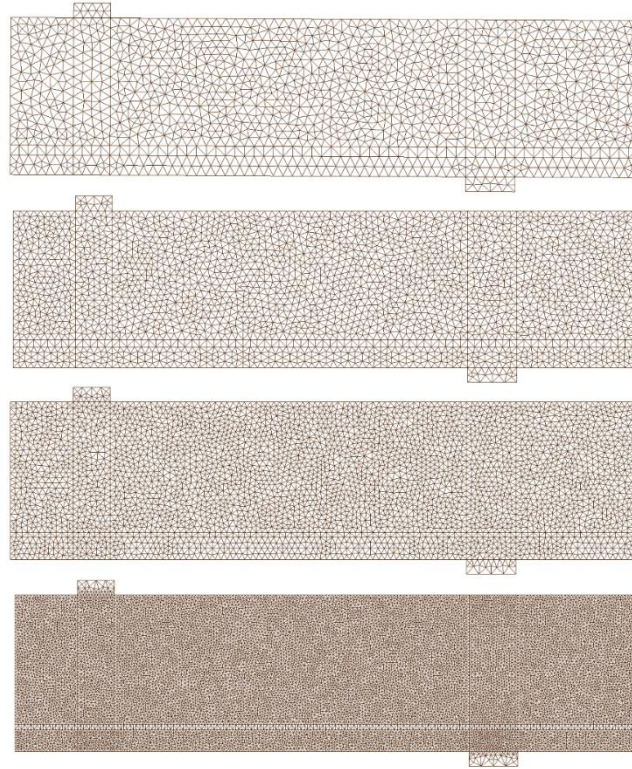
Figure 7.15: Discretization refinements (half beam) from the coarsest to the finest.

7.3.1 Comparison among regularized strain tensor, regularized scalar and crack band models

The first aspect analyzed for comparative purposes regards the mesh-objectivity exhibited by the different approaches. In order to limit the computational effort, only the discretizations with average size 20 mm (coarse mesh), 15 mm (intermediate mesh) and 12 mm (fine mesh) are here taken into account. The force P - mid span (point A in Figure 7.14.a) deflection v curves resulting from the adoption of the regularized strain tensor approach, regularized scalar approach and crack band model are plotted in Figure 7.16, accompanied by the experimental response. All the regularized results are obtained with the adoption of the same internal length, equal to l_{RG}= 7.8 mm (see Table 7.6).

(a)

(b)
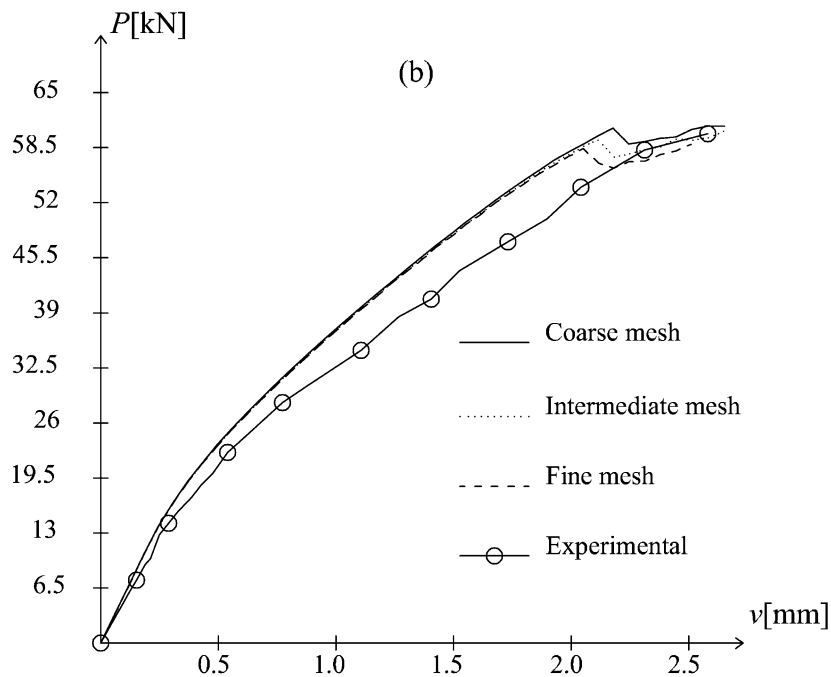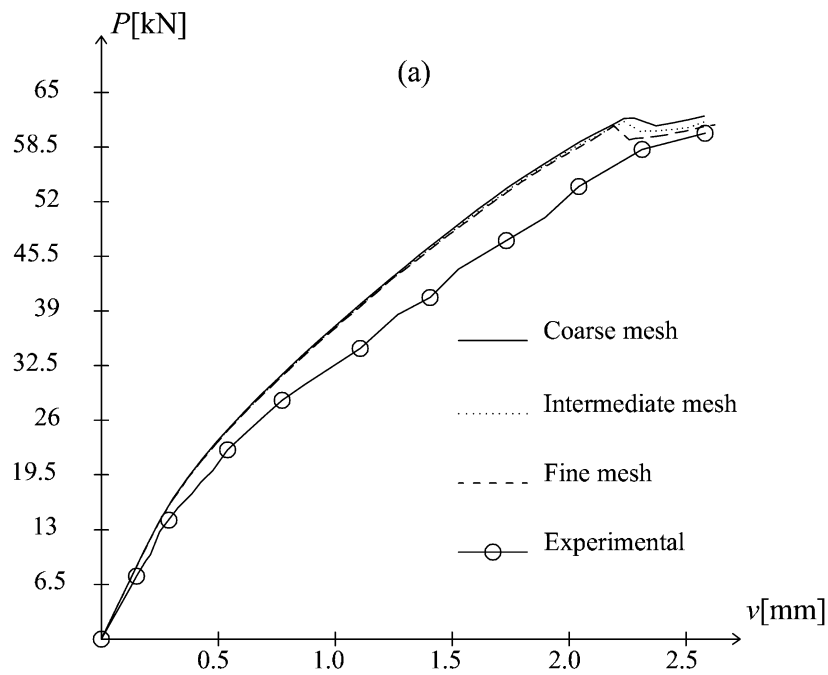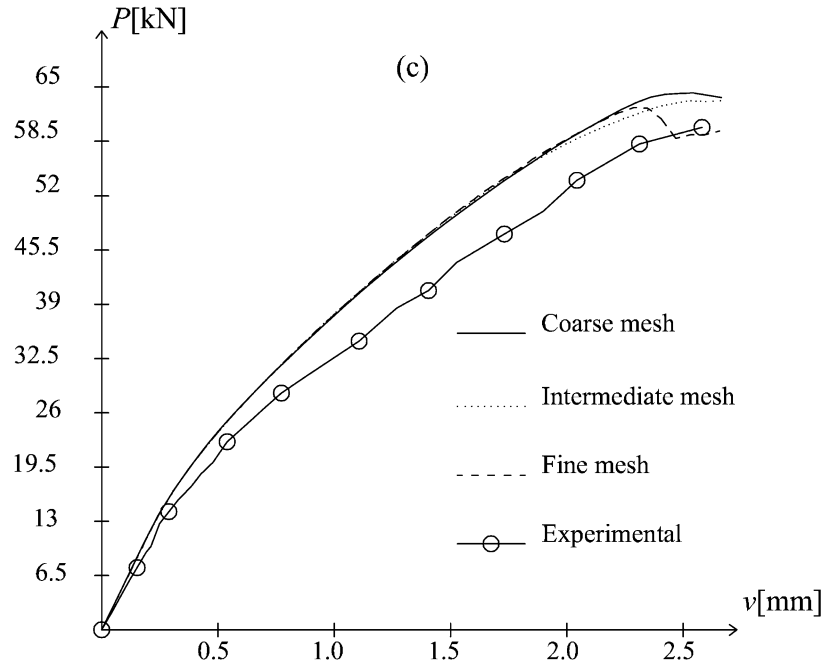
Figure 7.16: Mesh-size objectivity studies: (a) regularized elastic strain tensor approach, (b) regularized scalar approach and (c) crack band (local) approach.

The first consideration with emerges from the analysis of the results is that the experimental structural response is satisfactorily described by the regularized formulations as well as by the local one. The correspondence between numerical and experimental values is evident in terms of load carrying capacity and this is a confirmation of the adequacy of the damage surfaces considered for d^+ and d^-. It is worth noting that, by neglecting the damage in compression, an overestimation of the observed shear carrying capacity would be obtained. In terms of stiffness degradation, the numerical curves show a slightly lower deformability than the response observed in the laboratory; this can be ascribed to the simplifying assumptions of linear-elasticity and perfect adherence considered for the reinforcement.

To study the dependence of the results plotted in Figure 7.16 on the discretization in a quantitative manner, the peak load differences are evaluated, for each approach, and shown, in percentage, in Table 7.8.

Table 7.8: Percentage differences [%] among peak loads obtained with different approaches.

Compared meshes	Regularized strain tensor approach	Regularized scalar approach	Crack band approach
Coarse - Intermediate	0.66	2.34	1.50
Intermediate - Fine	0.86	1.66	1.35
Coarse - Fine	1.52	4.00	2.85

Among the approaches, the lowest variation with respect to the mesh refinement is provided by the regularized procedure applied to the elastic strain tensor ε_e. Further confirmation of this comes from comparing, for each formulation, the maximum total strain contour plots resulting by the adoption of different meshes. The strain localization maps, displayed in Figure 7.17, Figure 7.18 and Figure 7.19 refer to the end of the analysis, once the shear resistance is attained.
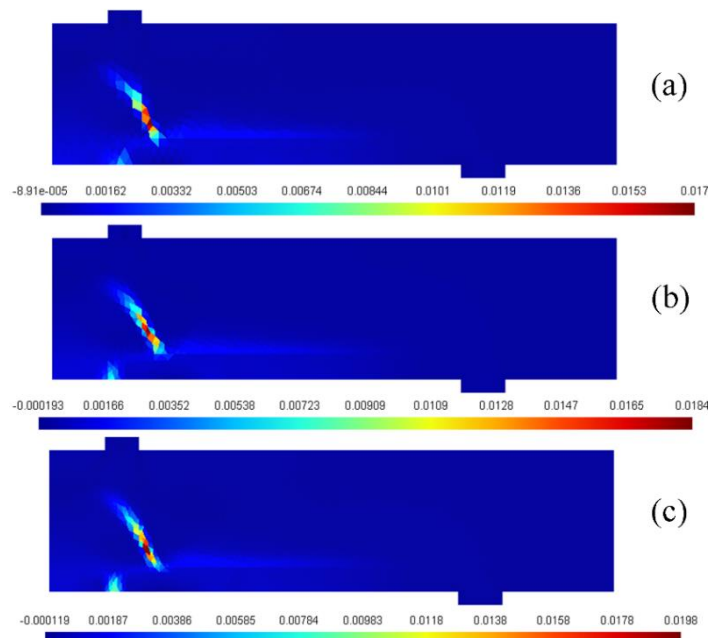
Figure 7.17: Maximum principal strain localization obtained with the regularized elastic strain tensor approach: (a) coarse mesh, (b) intermediate mesh and (c) fine mesh.
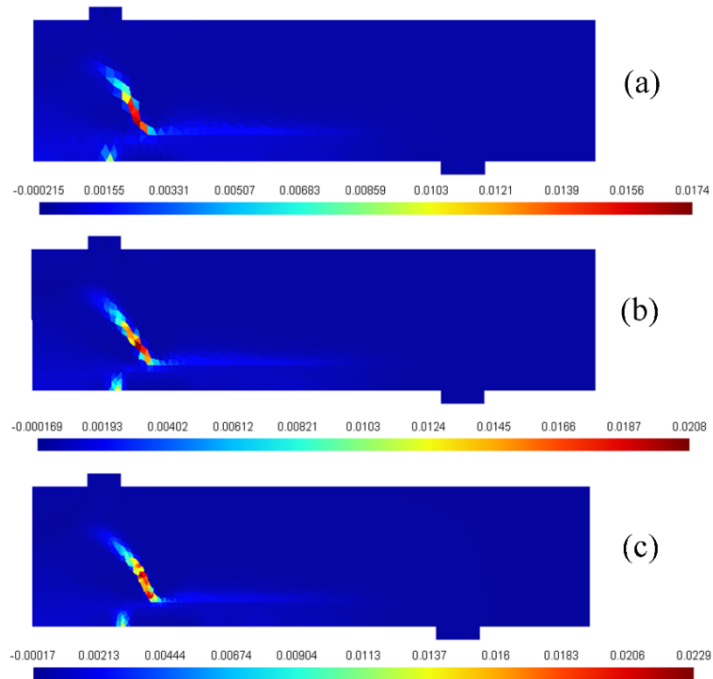
Figure 7.18: Maximum principal strain localization obtained with the regularized scalar approach: (a) coarse mesh, (b) intermediate mesh and (c) fine mesh.
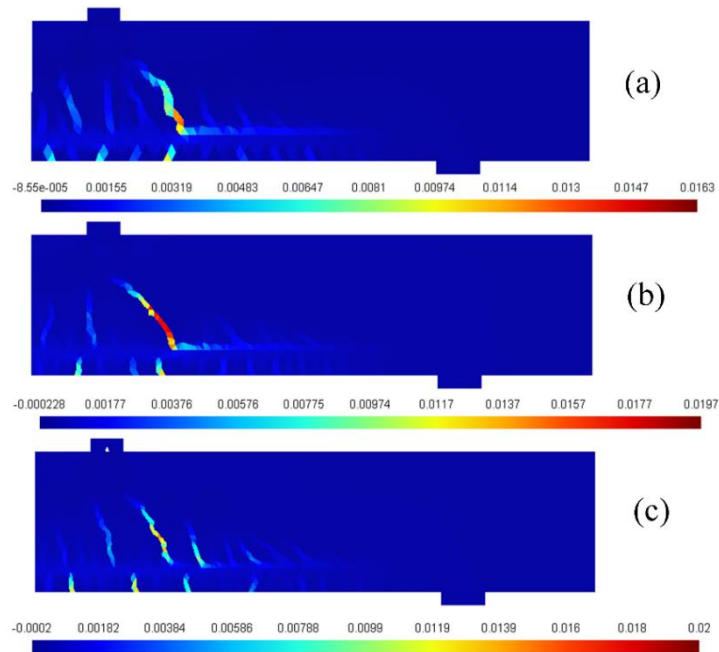
Figure 7.19: Maximum principal strain localization obtained with the crack band approach: (a) coarse mesh, (b) intermediate mesh and (c) fine mesh.

Some considerations are drawn by these figures. First of all, the well-known mesh-bias dependence of the local approach is proven, together with the mesh-bias independence of the nonlocal formulations. As a matter of fact, the orientation of the cracks, their number, their position and their width strongly differ passing from the coarser to the finer mesh in Figure 7.19 whilst similar solutions are obtained both in Figure 7.17 and Figure 7.18.

Moreover, differences between the two regularized formulations are not very evident, but present: although the localization orientation at rupture is almost identical, the maximum strain values plotted in Figure 7.17 and Figure 7.18 show that their variation with the mesh refinement is less significant with the nonlocal strain tensor approach than with the nonlocal scalar one.

On the basis of all these observations, it is concluded that, in terms of mesh independence,the regularized model ensures an higher reliability than a local one; more specifically, within the regularized formulations, the averaging of the elastic strain tensor is preferable, even if not crucial, with respect to the averaging of the scalar equivalent stress quantities.

Finally, the local and the two regularized approaches are compared in terms of numerical performance, i.e. number of iterations necessary to find the convergence of the residuals on the global level. The displacement is applied at the two application points in 40 load steps. The data concerning the total number of iterations performed adopting the three different procedures and an average number of iterations for each load step are collected in Table 7.9, with reference to solutions obtained with the intermediate mesh.

Table 7.9: Comparison among the three different approaches in terms of numerical performance.

	Regularized strain tensor approach	Regularized scalar approach	Crack band approach
Total number of iterations	192	234	287
Average number of iterations for each load step	4.8	5.85	7.18

Despite the higher number of iterations, the local approach is the fastest one in terms of computational time, since it does not require any averaging to be computed among neighbour elements. However, the data suggest that a regularized approach is able to achieve convergence to equilibrium in a lower number of iterations, due to the higher smoothness introduced with the averaging. Specifically, comparing the regularized "tensor" approach and the regularized "scalar" one, an improved convergence rate is obtained with the former with respect to the latter. Consequently, the reduced number of iterations necessary to achieve convergence compensates the increased numerical effort deriving from the averaging of a tensor quantity.

7.3.2 Dependence of the regularized solutions on the internal length l_{RG}

In Section 4.2 it is explained that the use of the particular calibration procedure ensures the independence of the response from the internal length for the problem of a bar loaded in uniaxial tension (see Figure 4.7.a). The objective of the present section is to investigate the influence of the parameter l_{RG} on the structural behaviour of the reinforced concrete beam under four point bending and to assess if the results obtained in uniaxial conditions can be extended to more complex stress-strain states.

It is worth noting that, in the nonlocal framework, such a sensitivity analysis is usually considered secondary with respect to the mesh dependency study, usually conducted to prove mesh-bias objectivity. This is for instance the case of the work presented in (Xenos and Grassl, 2016), where the same structural application is treated but only a marginal part is devoted to assess the influence of the internal length on the results.

The dependence of the regularized formulation on the length l_{RG} is studied adopting the intermediate triangular unstructured discretization (see Figure 7.15), whose average size h is equal to 15 mm. The numerical simulations are performed considering all the values of the internal length collected in Table 7.6, except $l_{RG} = 5.7$ mm, because an interaction radius smaller than the average size of the finite elements corresponds to this internal length, and consequently, the nonlocal interaction between elements is not guaranteed uniformly in the whole structure. The force P - mid span deflection v curves resulting from the adoption of the regularized strain tensor damage model with different nonlocal lengths are displayed in Figure 7.20.
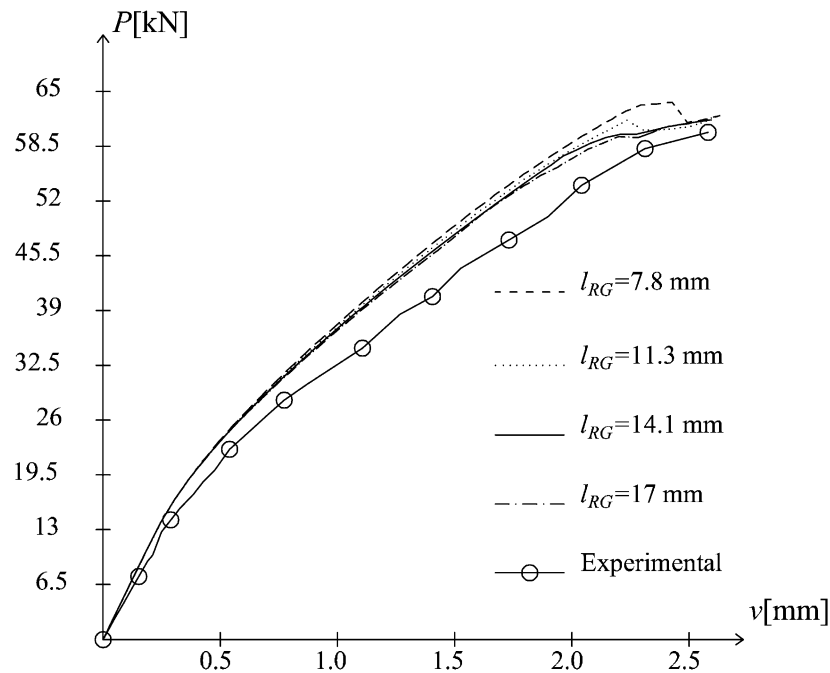
Figure 7.20: Structural responses of the reinforced concrete beam under four point bending test with the adoption of the regularized strain tensor formulation, for different l_{RG}.

The curves plotted in Figure 7.20 show that the dependence of the regularized formulation on the choice of the internal length is substantially low. As a matter of fact, the structural responses corresponding to l_{RG}= 14.1 mm and l_{RG}= 17 mm are almost coincident and differ only slightly (2.6% in terms of peak loads) from the one obtained with l_{RG}= 11.3 mm. A more significant variation, in any case small (3.4% in terms of peak loads), can be observed between the solutions with l_{RG}= 11.3 mm and l_{RG}= 7.8 mm.

These data confirm that the dependence of the regularized strain tensor formulation on the internal length, in terms of response curves, is small, fully comparable with the dependence exhibited by the same model on the mesh refinement (see Figure 7.16.a), and negligible when high values of l_{RG} with respect to the discretization are considered. For this specific mesh refinement (average size 15 mm), an internal length equal to 11.3 mm, characterized by a nonlocal interaction radius equal to 22.6 mm, seems to be sufficient.

Despite these considerations, it is proper to observe that the perfect coincidence of the results obtained with different internal lengths for the uniaxial case (Figure 4.7) is not reproduced for this structural application (Figure 7.20). This is due to the fact that the calibration, addressed to obtain the relative dissipative lengths k^+_{dis} and

k^-_{dis} collected in Table 7.6, is performed considering a particular stress-strain state, which does not coincide with the one experienced in the beam. Similar comments on this topic are discussed in (Nguyen and Houlsby, 2007).

To extend this sensitivity analysis, the maximum principal strain contour plots obtained with the different values of l_{RG}, just before the attainment of the maximum carrying capacity, are displayed in Figure 7.21. It is worth noting that the effect of the internal length is not negligible in the maximum strain distributions. Specifically, a higher length l_{RG} implies a higher width of the strain localization zones, as well as the concentration of close localization zones in a unique failure area. This second aspect, in particular, is proper of damaged structures characterized by multiple failure zones.

The results collected about the influence of the internal length parameter on the solution (Figure 7.20 and Figure 7.21) lead to find analogies between the role played by the mesh size in the crack band approach and the role played by l_{RG} in the regularized formulation. Firstly, as the crack band approach is able to ensure the correct description of the dissipated energy independently of the mesh size, similarly the regularized damage model does the same independently of the internal length, thanks to the adoption of the calibration procedure described in Section 4.2 (Figure 7.20). Secondly, analogously to the mesh size in the crack band approach (Figure 7.19), l_{RG} influences not only the width of the localization band but also the number of resulting failure zones. All these observations allow to interpret the length l_{RG} as a regularization parameter, as it is the mesh size in the crack band approach. Moreover, in problems characterized by multiple failure zones, it emerges that the internal length has to be kept sufficiently low to capture the interspace between cracks, as the mesh refinement has to be chosen sufficiently high in the crack band approach, in order to achieve the same goal.

In order to visualize with the regularized approach the single cracks present in the laboratory tests (Figure 7.14), a lower value of l_{RG} with respect to the ones adopted in Figure 7.21, accompanied by a higher mesh refinement, is used in the follow up. In order to visualize with the regularized approach the single cracks present in the laboratory tests (Figure 7.14), a lower value of l_{RG} with respect to the ones adopted in Figure 7.21, accompanied by a higher mesh refinement, is used in the follow up. Specifically, the lowest value of l_{RG} in Table 7.6 is adopted (l_{RG}= 5.7 mm) in conjunction with the finest mesh present in Figure 7.15, to show how the numerical nonlocal strain localization approaches qualitatively the experimental cracking pattern (Figure 7.22).
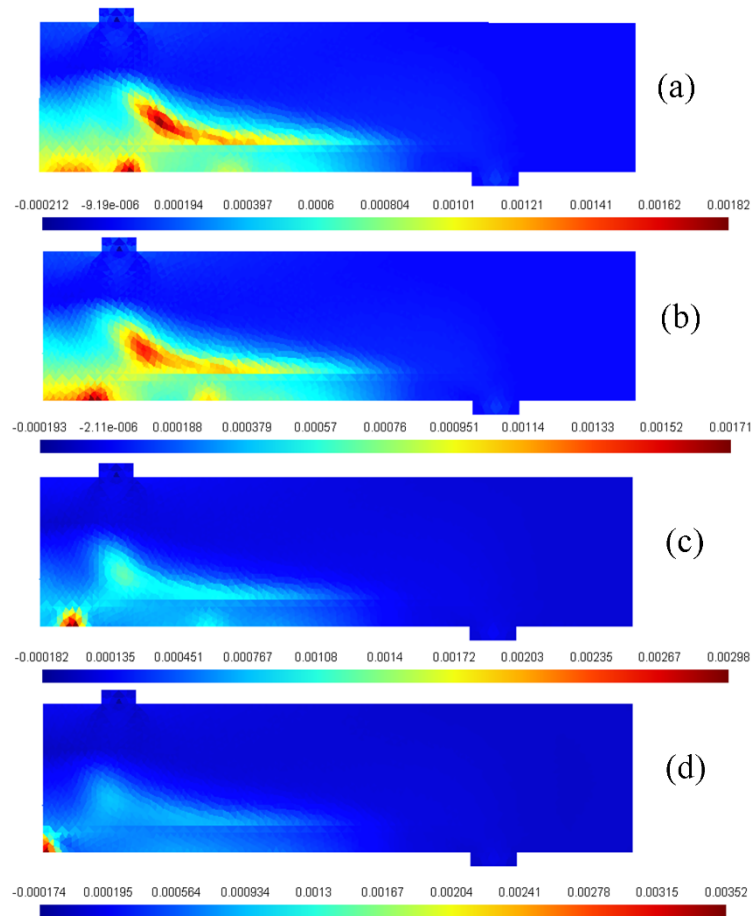
Figure 7.21: Maximum principal strain contour plots before the attainment of the peak load in case of: (a) l_{RG}= 7.8 mm, (b) l_{RG} = 11.3 mm, (c) l_{RG} = 14.1 mm and (a) l_{RG}= 17 mm.
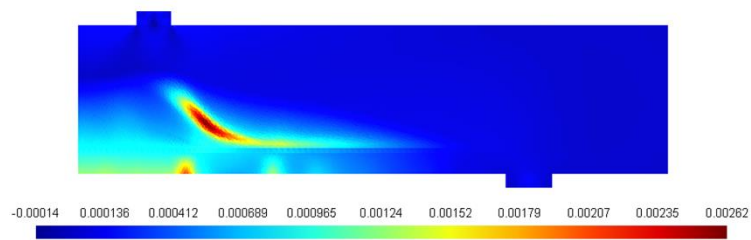
Figure 7.22: Maximum principal strain contour plots before the attainment of the peak load in case of l_{RG}= 5.7 mm and average mesh size equal to 7 mm.

Finally, to confirm the reliability of the regularized damage model to represent the failure arch-mechanism, the contour plots of the minimum principal stresses at the end of the analysis is provided in Figure 7.23.
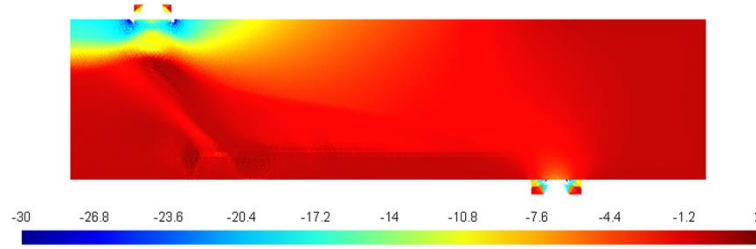
Figure 7.23: Minimum principal stress contour plot at the end of the analysis in case of l_{RG}= 5.7 mm and average mesh size equal to 7 mm.

7.4 Size effect for notched and unnotched plain concrete beams under three-point bending test

An important aspect of damage models for quasi-brittle materials is that they should be able to represent the structural size effect, i.e. the dependence of the nominal strength on the structural size.

Size effect derives from the fact that the elastic stored energy is proportional to the total volume while the energy dissipation by fracture is proportional to the fracture surface. Defining a brittleness index br as the ratio between the stored energy and the dissipated energy:

$$br = \frac{\left(\dfrac{1}{2}\dfrac{f^2}{E}\right)\cdot S^3}{G_f \cdot S^2} = \frac{S}{\left(\dfrac{2\cdot E\cdot G_f}{f^2}\right)} = \frac{S}{l_{mat}} \tag{7.12}$$

it is possible to note how, as the generic structural size S increases with respect to the material fracture length l_{mat}, brittleness increases too.

Hence, as commented in (Bažant and Planas, 1998), the behaviour of geometrically similar specimen is not geometrically similar, because the fracture surface maintains constant whilst the structural size changes and this implies different energy redistributions from the remaining part of the structure to the fracture process zone.

Numerically, such effect can be reproduced thanks to the use of a procedure which dissipates G_f through a surface. Therefore, nonlocal formulations, as well as enhanced gradient models, phase field models and also crack band models (Cervera and Chiumenti, 2009) are able to represent the size effect.

In the present section, the capability of the proposed regularized damage model to describe the size effect is explored. The experimental data taken as reference solution are the ones presented in (Grégoire et *al.*, 2013), where the results of three point bending tests on notched and unnotched concrete beams, made of the same material, are collected. The specimens are characterized by a span *L*-to-depth *D* ratio equal to 2.5, a constant width *b* of 50 mm, various depths and various notch-to-depth ratios (see Figure 7.24).

3.5D	3.5D	3.5D
Half notched	Fifth notched	Unnotched

D =400 mm h=200 mm	D =400 mm h=320 mm	D =400 mm h=400 mm
D =200 mm h=100 mm	D =200 mm h=160 mm	D =200 mm h=200 mm
D =100 mm h=50 mm	D =100 mm h=80 mm	D =100 mm h=100 mm
D =50 mm h=25 mm	D =50 mm h=40 mm	D =50 mm h=50 mm
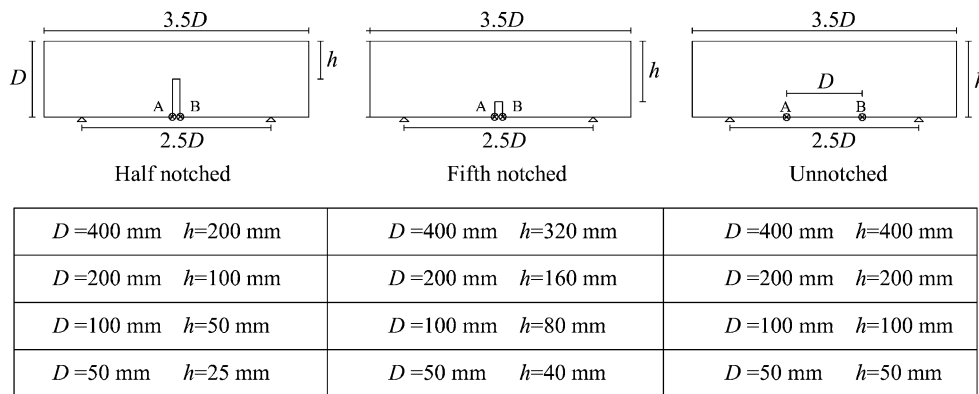
Figure 7.24: Different geometries and different sizes considered in the three point bending tests on concrete beams documented in (Grégoire et *al*., 2013).

For each geometry, four depths *D* are considered: 400 mm, 200 mm, 100 mm and 50 mm. Moreover, the three geometries are designated as: half notched (notch-to-depth ratio equal to 0.5), fifth notched (notch-to-depth ratio equal to 0.2) and unnotched (notch-to-depth ratio equal to 0).

The numerical description of the structural size effects for various geometries is an ambitious objective, as commented in (Grégoire et *al*., 2013). As a matter of fact, the capability of nonlocal models to capture the size effect on beams with a single specific geometry is quite common, as shown for instance in (Bažant and Lin, 1988) and (Jirásek et *al*., 2004), but the extension to other geometries, with the adoption of the same set of input parameters, is not obvious. For instance, in (Krayani et *al*., 2009), the impossibility of adopting the same model parameters for fitting data regarding notched and unnotched beams with a nonlocal damage model is pointed out. Moreover, in (Grégoire et *al*., 2013), some numerical simulations with the damage model presented originally in (Pijaudier-Cabot and Bažant, 1987) show the same difficulties, compared with the experimental results. In fact, the procedure there followed, described in detail in (Le Bellégo et *al*., 2003), consists in calibrating the nonlocal length and the material parameters governing the local

tensile softening behaviour in order to obtain a good fit with the results associated to three different sizes (50 mm, 100 mm and 200 mm) of the same geometry (fifth notched beams). The numerical results show that the calibrated material parameters are able to describe accurately the structural response for those specific sizes and for that specific geometry but they are not likewise good in describing the results for the largest specimen (400 mm) with that geometry and for the other geometries. In particular, the correspondence is poor in the case of the unnotched specimens.

The regularized damage model proposed in Chapter 4 is used for studying the structural response of the concrete beams under three point bending tests shown in Figure 7.24. For the sake of simplicity, permanent deformations are neglected in the present example. The parameters adopted in the numerical analyses, for all the sizes and all the geometries, are collected in Table 7.10.

Table 7.10: Parameters adopted in the analyses of notched and unnotched concrete beams.

E [MPa]	ν [-]	f^+ [MPa]	f^- [MPa]	G_f^+ [N/mm]	G_f^- [N/mm]	$\xi\pm$ [-]	l_{RG} [mm]
38000	0.21	2.8	-42.3	0.037	30.00	0.00	6.00

The elastic properties, as well as the compressive strength's values, are chosen in accordance with the measured ones, documented in (Grégoire et al., 2013). For what regards the tensile material parameters, a lower value is here adopted with respect to the one specified in (Grégoire et al., 2013) and measured by means of a splitting test. This is in line with the fact that the direct tensile strength, which is the one considered in the damage criterion (see Figure 2.4 and Eq. (2.45)), is usually lower than the splitting tensile strength of, at least, 10% - 15%. The fracture energy in tension G_f^+ is similar to the value computed in (Grégoire et al., 2013) from a load-deflection curve, according to RILEM recommendations (around 0.045 N/mm). G_f^- is assumed as a typical value for concrete because of its null influence in the present structural application.

Finally, the internal length of the regularized model is chosen in order to guarantee a sufficiently high ratio between the interaction radius ($2 \cdot l_{RG}$= 12 mm) and the triangular mesh average size, maintained fixed in the fracture process zone for all the geometries and equal to 1.5 mm. Thanks to the application of the calibration procedure, starting from this value of l_{RG}, a tensile dissipation length equal to 22.4 mm is obtained, which is reasonable if compared to the experimental

value of approximately 3 times the maximum aggregate size proposed in (Bažant and Oh, 1983) and (Bažant and Pijaudier-Cabot, 1989). Hence, with the use of this dissipation length in place of the generic length l in the softening modulus (2.84b), the local softening law is calibrated in order to describe the correct fracture energy.

The numerical predictions, together with the experimental envelopes, are plotted in terms of force F - crack mouth opening displacements $CMOD$ curves in Figure 7.25, Figure 7.26 and Figure 7.27 for the half notched, fifth notched and unnotched beams, respectively. The CMOD is evaluated as the relative displacement between points A and B at the intrados of the beams (see Figure 7.24).
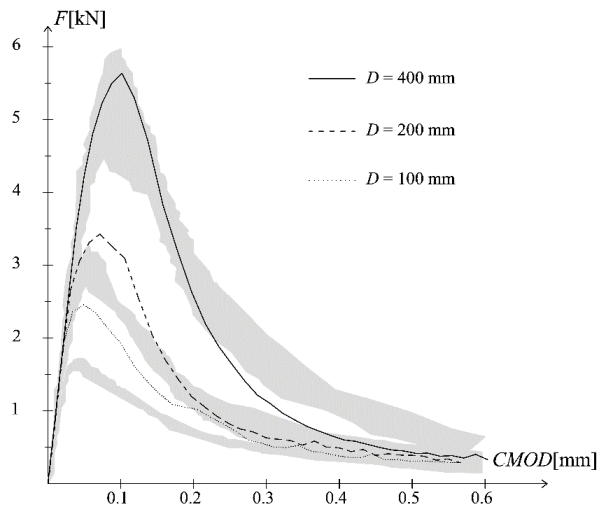
Figure 7.25: Size effect results for the half notched beams with the nonlocal model.
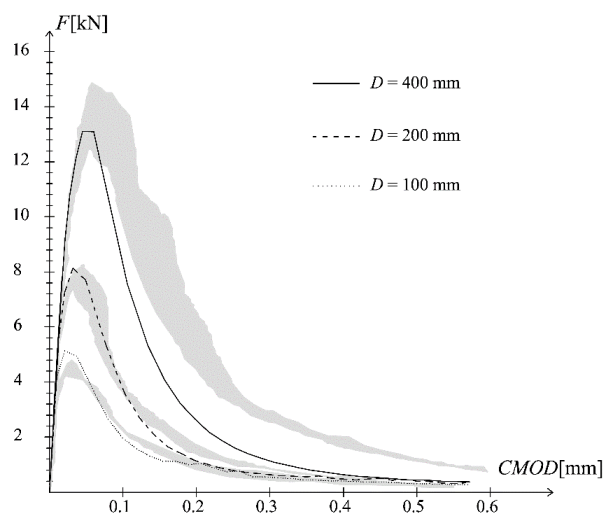
Figure 7.26: Size effect results for the fifth notched beams with the nonlocal model.
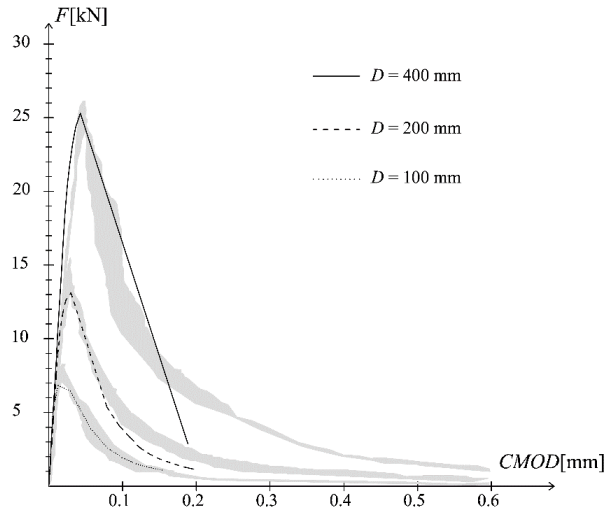
Figure 7.27: Size effect results for the unnotched beams with the nonlocal model.

Good agreement between experimental and numerical results can be observed for all the geometries, especially in terms of peak loads.

For each geometry, the trend of the numerical nominal strength as a function of the structural size is shown in Figure 7.28, compared with the experimental values (maximum and minimum) documented in (Grégoire et *al*., 2013). The nominal strength is computed in its simplest form for three point bending tests (Bažant and Planas, 1998):

$$\sigma_N = \frac{3}{2} \frac{FL}{bh^2} \qquad (7.13)$$

where L is the distance between the supports, b is the width of the beam and h is the ligament height.

In terms of softening behaviour, a more emphasized decrease in load is visible in the post peak numerical regimes. However, the higher deviation with respect to the experimental softening is visible in the unnotched beams (Figure 7.27), especially in the largest one, and can be ascribed to numerical issues, deriving from the imposed increasing displacements conflicting with the snap-back in the experimental data. The difficulties in achieving convergence, shown by the fact that all the curves stop at a *CMOD* approximately equal to 0.2 mm, have to be probably related to these problems.

Finally, it is important to note that the only significant discrepancy between experimental and numerical peak loads regards the smallest half notched beam

(Figure 7.25). This is not surprising because this is the beam, among the ones numerically verified, which has the smallest ligament, equal to 50 mm. The overestimation of the peak load obtained numerically can be explained considering that the assumption of constant fracture energy G_f holds, provided that the structural size is large enough with respect to the process zone size (Bažant and Jirásek, 2002). For a ligament 50 mm long, the nonlocal damage formulation proposed does not provide reliable results and for this reason, the set of beams with a depth equal to 50 mm (Figure 7.24) is not studied numerically.
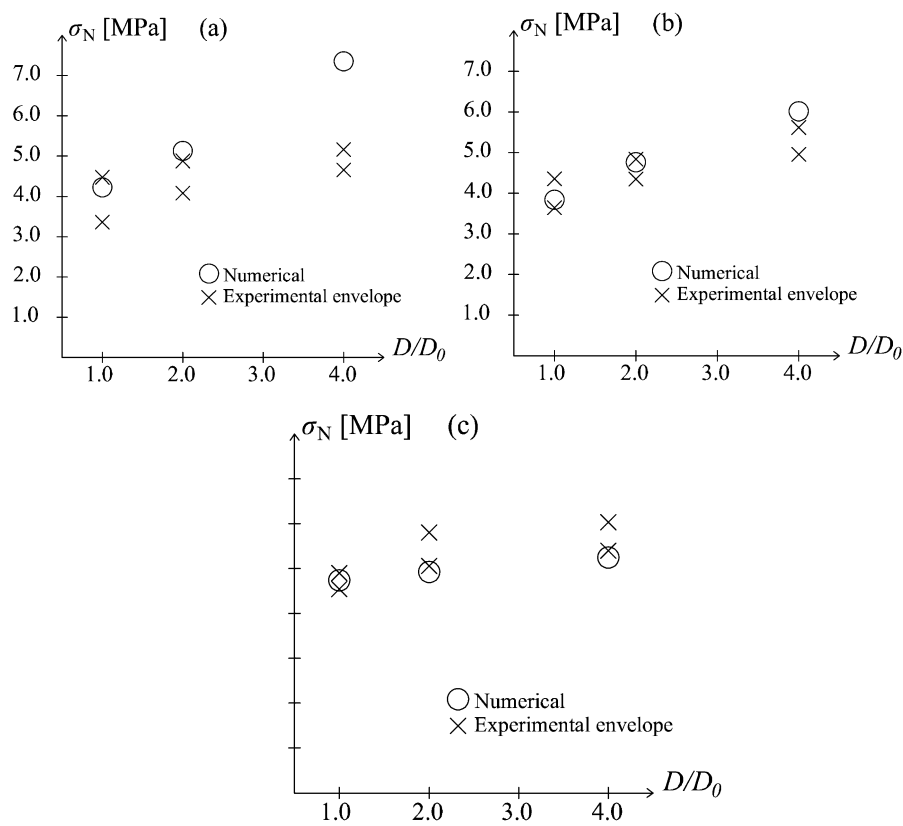
Figure 7.28: Comparison between experimental and numerical size effect laws: (a) half notched beams, (b) fifth notched beams and (c) unnotched beams (D_0= 400 mm).

Chapter 8

Large-scale application: masonry multi-span arch bridge

8.1 Introduction to the structural analysis of masonry arch bridges

Masonry arch bridges represent one of the most diffused construction typologies for railway and road networks in Europe. The majority of these structures were built in the nineteenth century, as a consequence of the birth and expansion of the railway system, and had a further impulse after the II World War. Multi-span bridges were usually preferred to single-span arches because of their easier construction, especially when long distances had to be covered.

As noticed in (Melbourne et $al.$, 1997), the structural behaviour of a multi-span arch bridge, similarly to the one of a multi-bay portal frame with fixed base, foresees a degree of redundancy equal to $3 \cdot m$, where m is the number of the spans. In order to have a complete failure hinged mechanism, $3m + 1$ hinges are required while, in case of partial collapse which involves only a number of spans $n < m$, the necessary hinges are $3n + 1$. Finally, four hinges generate the failure of a single span. The formation of a complete, partial or single-span mechanism depends on several factors, which include not only the arches themselves but also the other resisting elements, such as piers and spandrel walls if present, and their interaction.

In this regard, in (Harvey and Smith, 1991), the role of the flexibility of the piers is underlined. In fact, Harvey and Smith observe that, in intact conditions, the loaded span of a multi-span arch bridge behaves as an active arch which tends to move apart its abutments; contemporarily, the close unloaded span resists this movement as a passive arch. In case of collapse of one span, the interruption of this resisting system occurs and the piers have to counterbalance the actions exerted by the remaining structure.

On the one hand, piers are defined stocky when they are able to behave as abutments, i.e., they are able, in case of collapse of an arch span, to sustain the others preventing the rest of the structure to go down. The case of the medieval bridge in Boroughbridge, which failed under the passage of a train of about 160 tons in 1945 can be classified within the category of stocky pier collapse.

On the other hand, piers are identified as slender when they are involved in the mechanism, causing the collapse of more arches, because of their incapability to equilibrate the thrusts of the remaining parts. This behaviour was observed in 1989 at Balnacraig in Deeside, where the removal of an arch span in a disused railway bridge caused the progressive collapse of the whole viaduct.

However, as remarked in (Melbourne et *al.*, 1997), it is not possible to predict the kind of mechanism on the base of those geometrical features which are usually adopted to define the slenderness of vertical structural elements. As a matter of fact, the height-width ratio does not provide complete information because even other factors, as the type of interaction between piers and arches, the geometrical features of arches and the presence or not of collaborating spandrel walls intervene drastically.

In the past decades, several assessment procedures have been proposed for the study of masonry arch bridges, which can be classified into two wide sets of structural analysis techniques.

On the one hand, limit analysis is applied to masonry constructions with its basis on the formulation originally provided by Heyman (Heyman, 1969; Heyman, 1985). The adoption of the static (lower bound) theorem of plasticity for assessing the behaviour of masonry multi-span arch bridges is present, for instance, in (Harvey and Smooth, 1991; Cavicchi and Gambarotta, 2007). The kinematic (upper bound) theorem is instead used in (Gilbert and Melbourne, 1994; Huges, 1995). From these contributions, it is inferable that inevitably the identification of the thurstline in the static approach, as well as the definition of a sufficient number of hinges in the kinematic one, become more complex in case of multi-span bridges

than in single-span ones (Brencich and De Francesco, 2004a; Brencich and De Francesco, 2004b). Moreover, if the assumption of null tensile strength is conservative, the other one at the base of the limit analysis, related to the infinite compressive strength of masonry, can lead to overestimate the load-carrying capacity, especially in case of degraded materials and severe loading conditions.

In addition, even if a failure criterion and a maximum ductility are set to describe the nonlinear compressive behaviour of masonry, as done in (Crisfield and Packham, 1988), some other intrinsic limitations of the formulation can not be eliminated. They regard the possibility of having only information about the load-carrying capacity of the structure whilst disregarding displacement and strain quantities. This implies that the structural displacement capacity can not be assessed, and this is a restriction especially in case of time-varying loadings, as earthquakes. It is worth noting that the lack of information about the kinematic quantities is a drawback especially in the study of multi-span arch bridges, since it does not allow considering the influence of the pier flexibility, above discussed, on the structural response.

On the other hand, there is the possibility of studying arch bridges by means of finite element method based approaches, in conjunction with nonlinear constitutive laws appropriate for masonry. The main advantage of an incremental finite element analysis, with respect to a limit analysis, lies in the fact that the former provides more information than the latter: not only the load-carrying capacity can be evaluated, but also the displacement capacity at failure and the stress-strain states of all the significant parts of the structure during the incremental loading history.

Differently from other typologies of masonry structures, masonry arch bridges can be studied also with one-dimensional models. A lot of one-dimensional models exist, because of their computational advantages. Among the first models developed for studying arch bridges with the finite element method, there is the contribution by Crisfield and Wills (Crisfield and Wills, 1985), which consists in a no tension material model implemented in uni-dimensional and bi-dimensional finite elements. Another approach, presented in (Choo et *al.*, 1991), uses uni-dimensional elements to represent the arch rings, whose thickness is progressively modified in order to take into account cracking and crushing phenomena.

More recent are the works by Molins and Roca (Molins and Roca, 1998) and by Brencich and De Francesco (Brencich and De Francesco, 2004a; Brencich and De Francesco, 2004b). In the former, a numerical model for the study of curved and spatial structures by means of uni-dimensional elements is proposed, assuming an elastic-perfectly brittle behaviour in tension and an elasto-plastic constitutive

response in compression and shear. In the latter, the behaviour of single and multi-span bridges is studied considering no tensile resistance and an elasto-plastic behaviour with limited strength and limited ductility in compression. Finally, De Felice addresses the evaluation of the load carrying capacity of multi-span masonry arch bridges by means of a model based on the adoption of nonlinear beam elements with fibre cross section (De Felice, 2009).

Despite the adequacy of the results obtained with these simplified uni-dimensional formulations, 2D and 3D models allow to perform more complete analyses. First of all, they permit to deal with the geometry complexity characterizing this kind of structures, which are usually curved and with varying cross sections. Moreover, they allow modelling the interaction between the arch barrel and the infill and the presence of cooperating spandrel walls, whose influence is not negligible as stressed in the experimental programme described in (Melbourne et al., 1997).

Among the first interesting contributions of two-dimensional finite elements for the study of masonry arch bridges, there is the work in (Gong et al., 1993), where a no tension material model for masonry is combined with a discrete crack modelling. In this approach, cracks can be generated only at the boundaries of the finite elements, both in radial and tangential direction (separation between adjacent rings). Besides the problems related to the use of a simple no-tension material model for describing cracking, such a model suffers from the limitations proper of micro-modelling approaches when applied to describe large structures. In fact, it requires a very high computational effort and a non-automatic mesh generation, due to the necessity of reproducing with the discretization the masonry pattern.

A more effective 2D procedure is proposed in (Loo and Yang, 1991), where, in the context of a macro-modelling approach for masonry, cracking and crushing phenomena are both considered, assuming a softening behaviour in tension and an elastic-perfectly plastic behaviour in compression. However, the formulation is validated considering only single-span arches.

More recently, Boothbly et al. (Boothbly et al., 1998) and Fanning and Boothby (Fanning and Boothby, 2001) performed 2D and 3D numerical analyses for studying the service load conditions of masonry arch bridges using a commercially available finite element package. Among the few examples of application of non-commercial finite element codes for the analysis of masonry arch bridges, it is worth remembering the work by Milani and Lourenço (Milani and Lourenço, 2012), where it is observed that a full 3D analysis has a clear advantage with respect to a 2D one only when skewed geometry and 3D loading conditions have to be

investigated. The approach adopted consists in assuming an infinitely rigid behaviour for the eight-node brick elements and in localizing elastic and inelastic deformations in interface quadrilateral elements.

The overview of existing assessment methods just described can be a reference for the study of masonry arch bridges not only subjected to vertical (permanent and vehicular) loads but also to horizontal (seismic) actions, in the framework of nonlinear static approaches.

In view of the above discussion, it can be affirmed that the adoption of a non-linear mechanical model with softening in tension and compression for the 2D finite element analysis of masonry multi-span arch bridges have been rarely adopted in literature. In fact, the assumptions of no-tension material and elasto-plastic behaviour in compression are generally preferred and this results in the fact that the application of damage mechanics to study the non-linear behaviour of such structures has not been sufficiently explored. Therefore, the following sections of this chapter are addressed to investigate the adequacy of the regularized d^+/d^- damage model to assess the structural behaviour of multi-span masonry arch bridges. In order to prove the reliability of the proposed formulation, the objectivity of the response with respect to the discretization is also verified. Such a study is generally skipped in the analysis of large structures but it is fundamental to evaluate the actual predictive capabilities of the numerical model. Finally, to gain further insight on the potentialities of the proposed approach, the results obtained with the d^+/d^- damage model are compared with the ones deriving from limit analysis.

8.2 Numerical study of a large-scale three-span bridge model under vertical loads

8.2.1 Experimental programme and modelling assumptions

The structural problem studied in the follow up is a 1:5 scale model of a three-span arch bridge, tested under concentrated vertical loads in laboratory within the experimental programme described in (Melbourne et *al*., 1995; Melbourne et *al*., 1997). The same problem has been previously assessed, by means of 1D finite element formulations, by Brencich and De Francesco (Brencich and De Francesco, 2004b) and De Felice (De Felice, 2009).

The geometry of the structure is plotted in Figure 8.1. Each span is 3 m long and is characterized by a span-rise ratio equal to 4. The thickness of the single ring

is equal to 0.215 m. All the elements composing the bridge, i.e. the piers, the abutments, the arch barrels, the spandrel walls, present typical geometries for multi-span brickwork arch bridges.

As visible from the central section of the central span displayed in Figure 8.1.b, the spandrel walls are not collaborating with the arches, despite they lie on the same piers and abutments. The resisting width of the arch barrels is in fact equal to 2.88 m. In fact, the bridge considered in the following numerical analysis, schematically named "bridge 2" in (Melbourne et al., 1997), differs from the other two bridges experimentally studied because of its detached spandrel walls.
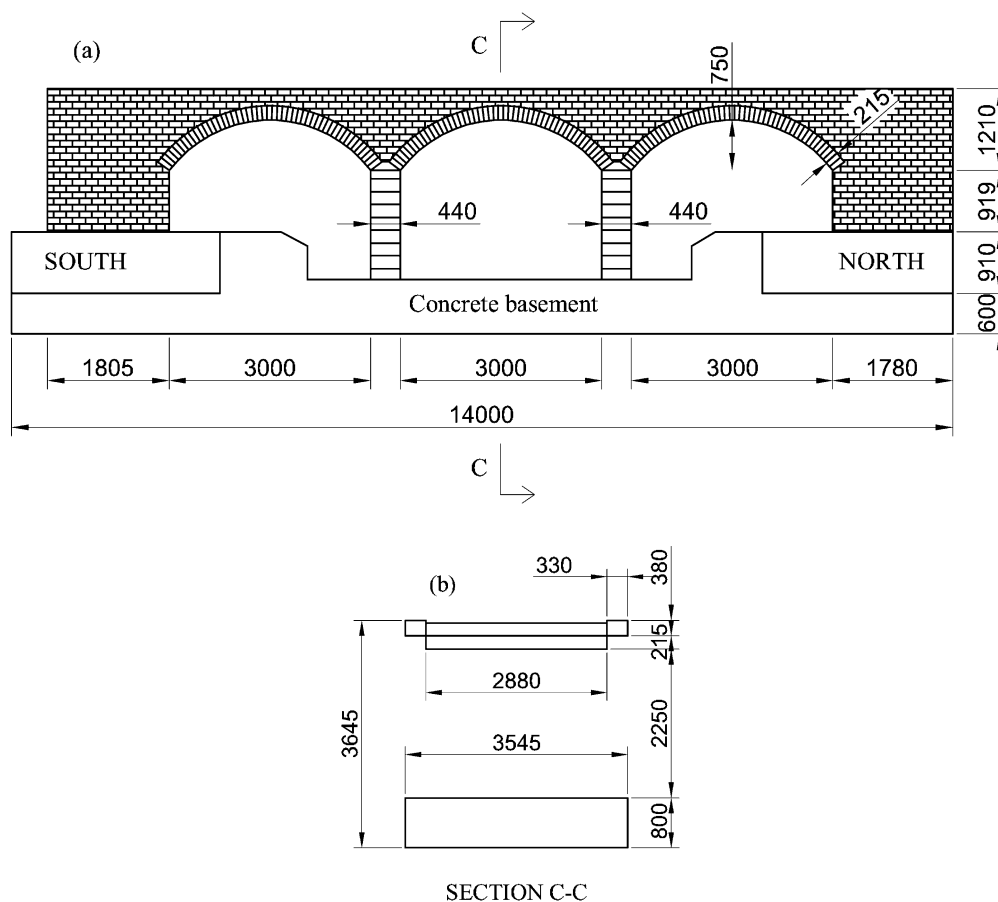
Figure 8.1: Geometry [mm] of the large-scale model of the multi-span masonry arch bridge described in (Melbourne et al., 1995; Melbourne et al., 1997): (a) longitudinal profile and (b) central section of the central span.

The masonry used to build the large-scale model of the bridge is composed of solid, class *A* clay "engineering" bricks and cement-lime-sand (1:2:9) mortar. In Table 8.1, the material properties available in (Melbourne et al., 1995; Melbourne

et *al*., 1997) for the brickwork are collected, together with the data for the backfill placed in the spandrel void.

Table 8.1: Parameters of masonry and backfill material for the problem of the multi-span masonry arch bridge as indicated in (Melbourne et *al*., 1995; Melbourne et *al*., 1995).

Masonry			Backfill		
E	f	γ_m	c	*Angle of friction*	γ_{bdry}
[MPa]	[MPa]	[kN/m^3]	[MPa]	[°]	[N/mm]
17000	-26.8	22.4	0	60.5	24.0

It is worth noting how the mechanical performance of the brickwork is really high, having a compressive strength value which is usually proper of concrete and not of masonry. No information about the tensile strength and the tensile fracture energy of the material is provided in (Melbourne et *al*., 1995; Melbourne et *al*., 1997).

The problem is studied in plane stress conditions. The loading and boundary conditions used in the numerical analyses are synthetized in Figure 8.2. As visible from this figure, the backfill and the spandrel walls are not included in the numerical model, nor the concrete basement which supports piers and abutments.

Due to the fact that the spandrel walls are not attached to the arch vaults, they do not collaborate in the resisting mechanism. Therefore, their stiffness, together with the stiffness of the backfill, is neglected. The stabilizing effect of their weight is however taken into account, by applying, in the first load step of the analyses, a distributed load at the extrados of the barrels and of the abutments together with the dead load of the structural elements (arches, piers and abutments).

In order to avoid superposition wih the concentrated load, in Figure 8.2 this distributed load is not plotted at the extrados of the central span, but it is obviously included in the numerical analysis. A specific weigth equal to 23 kN/m^3 is considered for the backfill while the specific weight for the masonry of the structural elements is equal to 22.4 kN/m^3.
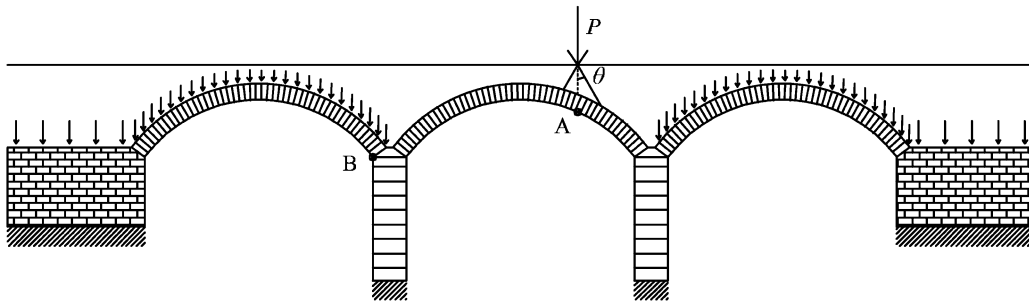
Figure 8.2: Boundary and loading conditions in the numerical analyses of the three-span masonry arch bridge.

A dispersion angle θ is used to identify the loaded surface at the extrados of the central arch, starting from the concentrated force applied at the quarter span on the top of the bridge. On this curved surface, the action is applied uniformly in terms of imposed vertical displacements. For what regards the concrete basement, it is considered infinitely stiff: hence, piers and abutments clamped at the base are assumed.

By performing the numerical analysis, it is found that the angle of load dispersion θ defined in Figure 8.2 has a non-negligible influence on the structural overall strength: higher is θ, wider is the surface of load application at the extrados and higher is the load carrying capacity, given that all the other input parameters are fixed. In addition, it is also noted that the material quantities which affect most the estimated load-carrying capacity of the bridge are the tensile strength and the tensile fracture energy, which are not available in (Melbourne et *al.*, 1995; Melbourne et *al.*, 1997). This consideration is in agreement with the observations done in (Loo, 1995), where indications on the reliable values to assign to f^+ and to the ultimate strain in a local linear softening curve are provided.

In order to show the dependence of the results on θ, the structural behaviour of the arch bridge is studied considering a very low value of load dispersion ($\theta = 5°$) and a standard value of load dispersion ($\theta = 25°$). Only by adopting two different sets of material properties, with different uniaxial tensile strengths, it is possible to reproduce the maximum peak load observed in laboratory for both the values of θ. These two groups of input parameters are summarized in Table 8.2.

Table 8.2: Two sets of input parameters used for the numerical analysis of the multi-span masonry arch bridge.

Set	θ [°]	E [MPa]	ν [-]	f^+ [MPa]	f^- [MPa]	G_f^+ [N/mm]	G_f^- [N/mm]	l_{RG} [mm]	k [-]
I	5	17000	0.2	0.21	-26.8	0.58	30.00	35.00	0.0
II	25	17000	0.2	0.14	-26.8	0.58	30.00	35.00	0.0

From Table 8.2, it is inferable that, higher is θ, lower is the chosen tensile strength in order to have an appropriate fit with the experimental results, while the rather high value for the tensile fracture energy is maintained equal. Starting from the value of the nonlocal length, by means of the calibration procedure detailed in Section 4.2, the dissipation lengths in tension and compression can be defined and are: $l_{dis}^+ = 147$ mm for $f^+= 0.21$ MPa and $l_{dis}^+ = 148$ mm for $f^+= 0.14$ MPa, $l_{dis}^- = 100$ mm. The local softening behaviour of the material is represented according to these values; by comparing it with the recommended softening trends proposed in (Loo, 1995), lower values of tensile strengths and a slightly higher specific dissipated energy g_f^+ are here adopted. The absence of the parameters ξ^+ and ξ^- in Table 8.2 is justified by the simplifying assumption here done to consider the permanent deformations absent.

Finally, the damage evolution laws adopted in the numerical analyses foresee an exponential softening behaviour in tension (softening modulus in Eq. (2.84b)) and a Gaussian damage evolution law in compression (softening modulus in Eq. (2.100)).

8.2.2 Numerical results

On the base of the boundary and loading conditions described in Figure 8.2, the structural analyses of the three-span masonry arch bridge are performed considering as input parameters of the nonlocal d^+/d^- damage model the values collected in Table 8.2.

The unstructured triangular mesh used is composed of 19360 finite elements, with an average size of 24 mm which is sufficiently smaller than the interaction radius $2 \cdot l_{RG} = 70$ mm.

The numerical responses are shown in Figure 8.3 in terms of applied concentrated force – radial displacement of point A (see Figure 8.2) curves, where the comparison with the experimental trend is also provided. Figure 8.3.a refers to the solution obtained adopting the set I of input parameters whilst Figure 8.3.b refers to the one obtained with the set II (see Table 8.2).

Thanks to the proper calibration of the tensile strength associated to the dispersion angle θ, the load-carrying capacity of the structure is well captured in both cases. In fact, in Figure 8.3.a, the peak load is equal to 316.5 kN while in Figure 8.3.b it is equal to 317.5 kN, against an experimentally measured failure load of 320 kN. In the post-peak regime, the numerical trend derived with the value of $\theta = 25°$ appears to be more faithful to the the experimental trend than the one obtained with $\theta = 5°$, which is, actually, an excessively low dispersion angle. Both the numerical curves show a slightly lower deformability than the experimental one, which can be mainly ascribed to the assumption of excluding from the structural model the backfill and its interaction with the arches.
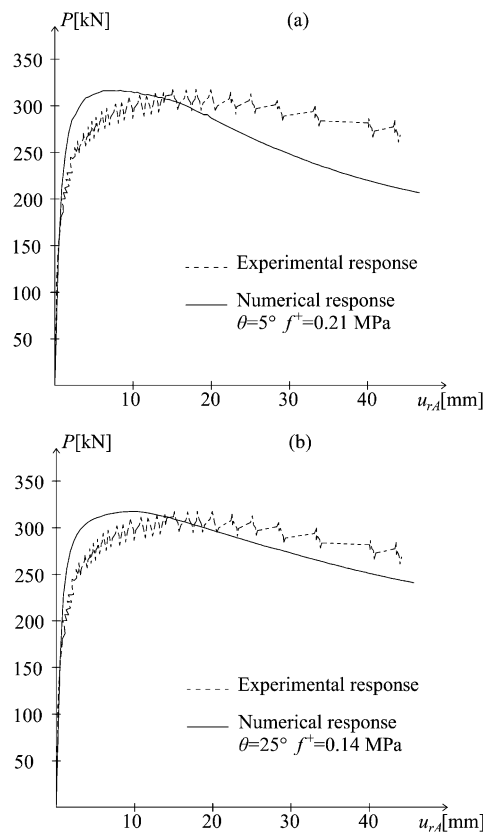
Figure 8.3: Comparison between numerical and experimental concentrated load-radial displacement of point A curves: (a) set of input paramters I and (b) set of input parameters II (see Table 8.2).

In order to check the mesh-independence of the proposed nonlocal damage approach, the same analyses are repeated adopting a less refined discretization. By modifying the number of finite elements both in the radial and tangential directions of the arches, a mesh with an almost halved number of finite elements, equal to 10419, is used. Even with this mesh, the average size of the finite elements (34 mm) is sufficiently smaller than the nonlocal interaction radius (70 mm). The mesh objectivity study is shown in Figure 8.4, where both the sets of input parameters collected in Table 8.2 are considered.

From Figure 8.4, it can be seen that the variations induced by the adoption of a different mesh are only minimal, and negligible in engineering terms. In fact, in both cases they are less than 3%. This proves that the regularized damage formulation provides solutions almost unaffected by the discretization even in large-scale applications.
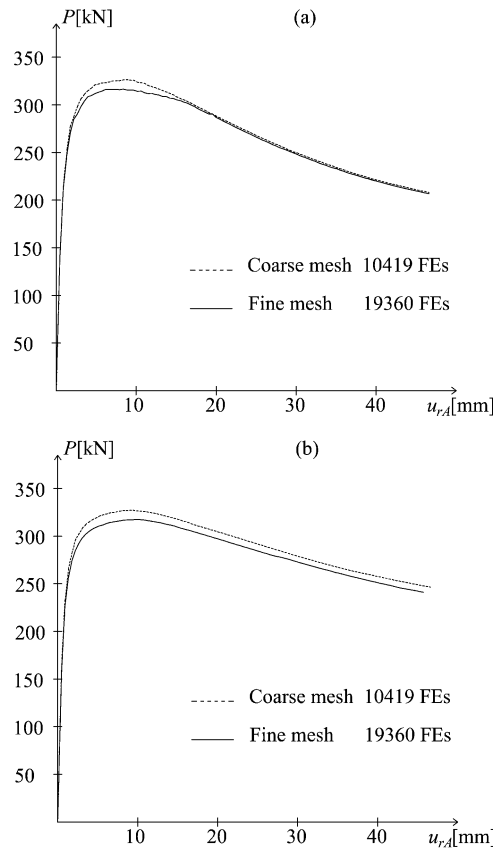
Figure 8.4: Mesh objectivity study considering a fine (19360 FEs) and a coarse (10419 FEs) discretization: (a) set of input parameters I and (b) set of input parameters II (see Table 8.2).

Hereafter, the analysis performed with the higher, and more realistic, angle of dispersion is detailed to show how the damage formulation is able not only to describe the load-carrying capacity of the bridge and its post-peak regime but also its failure mechanism.

In the laboratory, a collapse involving two spans, the central and the south ones, is observed, generated by the formation of seven hinges. Hence, according to the classification provided in Section 8.1, the south pier is flexibile and is not able to counterbalance the thrusts coming from the south span, once the central one has collapsed.

The numerical results are in perfect agreement with the experimental behaviour: in fact, the spans involved in the failure mechanisms are the central and the south one and seven hinges can be identified, three for each span plus one at the base of the south "flexible" pier. This is confirmed by the deformed configuration and the contour plots of the maximum principal strains obtained at the end of the analysis, displayed in Figure 8.5 and Figure 8.6, respectively.

Specifically, the distribution of maximum principal strains is exhibited both with the fine and with the coarse mesh, in order to show the independence from the discretization, even in terms of strain localization.

A further proof of the accuracy of the numerical results is represented by the concentrated load - top south pier radial displacement (point B in Figure 8.2) curve, shown in Figure 8.7.
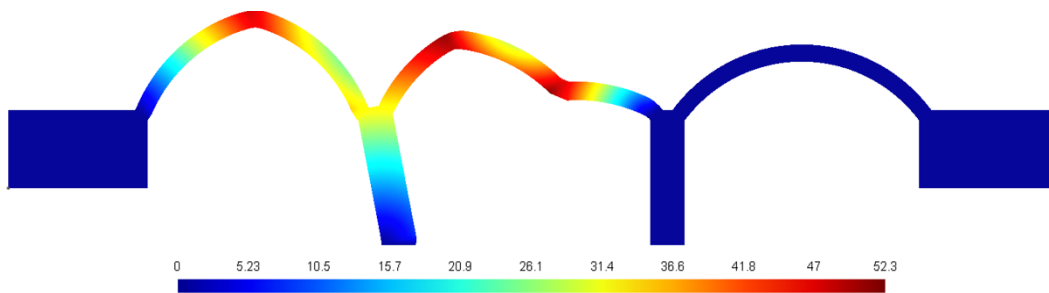
Figure 8.5: Deformed configuration (× 10) of the three-span masonry arch bridge at the end of the analysis.

(a)

(b)
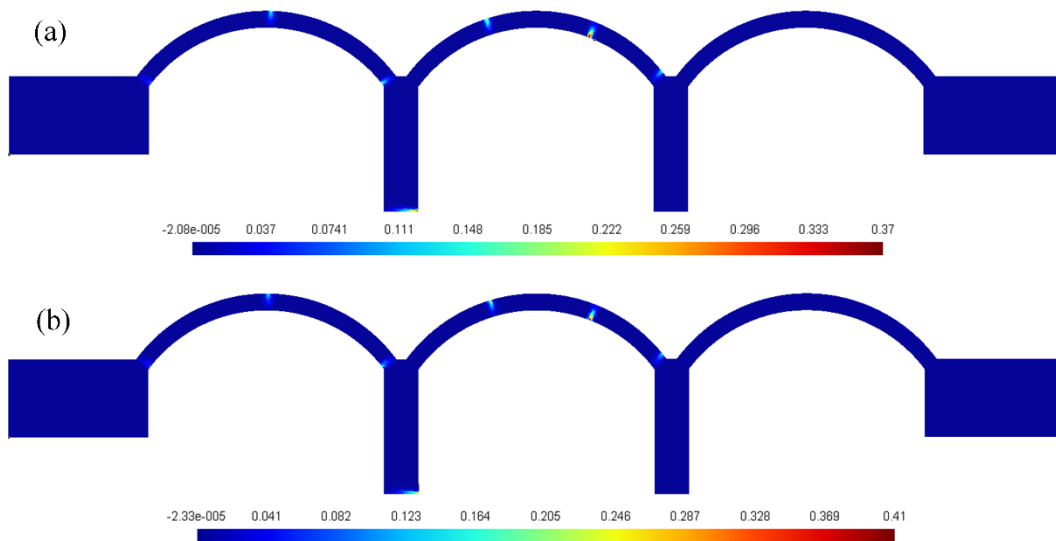
Figure 8.6: Contour plots of the maximum principal strains of the three-span masonry arch bridge at the end of the analysis: (a) fine mesh and (b) coarse mesh.
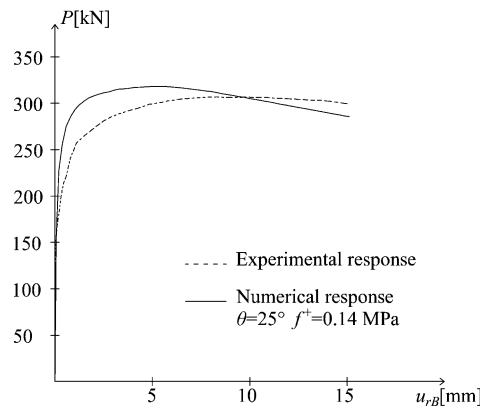
Figure 8.7: Comparison between numerical and experimental concentrated load-radial displacement of point B curves.

The position of the hinges, identifiable from the position of the predicted cracks in Figure 8.6, coincides with the experimental observation. The loads for which the cracks are generated in the laboratory and in the numerical analyses are summarized in Table 8.3. In the same table, information about the placement of the cracks are reported, in order to compare the experimental and the numerical sequence. In the numerical solution, the formation of a crack is associated to a value of tensile damage equal or higher to 0.95. The experimental load values are recorded in (Melbourne et al., 1995; Melbourne et al., 1997).

Table 8.3: Comparison between experimental and numerical loads [kN] of crack generation.

Results	1	2	3	4	5	6	7	Failure
Exp.	130	230	250	265	270	270	270	320
	under load	base of south pier	south span; north	loaded span; north	loaded span; south	south span; crown	south span; south	-
Num.	129.9	181.2	236.0	245.3	253.4	266.3	290.6	317.5
	under load	loaded span; north	south span; north	base of south pier	loaded span; south	south span; south	south span; crown	-

As visible from Table 8.3, there is adequate agreement between the experimental and the numerical predicted loads of crack generation; this agreement is remarkable if only the loads in correspondence with the formation of the first hinge and the failure are considered. Also the formation of the hinges is satisfactory, with the only discrepancy lieing in the fact that the south pier and the south span are involved in the collapse mechanism later than in the experimental test.

Finally, it has to be noted that no compressive damage is present at the end of the analysis, meaning that the masonry crushing is not reached in any point of the structure. This is reasonable due to the very high strength exhibited by the material in the compressive tests (see Table 8.1).

8.2.3 Comparison with limit analysis

The three-scale masonry arch bridge under concentrated vertical load described in (Melbourne et *al*., 1995; Melbourne et *al*., 1997) is studied with the commercial software RING 1.5 (LimitState, 2014). This is a software specifically developed to study the collapse state of masonry arch bridges, based on the adoption of computational limit analyses methods.

To do this, the geometry and the loading conditions described in Figure 8.1 and Figure 8.2 are imported in RING 1.5. The material input parameters required by the software and adopted in the non-linear finite element analyses are the compressive strength, the specific weights for masonry and for the backfill. As additional

information, the software needs the definition of the radial and tangential coefficient of frictions for masonry (assumed as the default values) and of the load dispersion type (uniform or Boussinesq) for backfill. In accordance with the modelling assumptions done in Section 8.21, the horizontal backfill pressure is disregarded and the load dispersion is assumed uniform, although the value of the dispersion angle can not be defined by the user but is automatically computed by the software.

The solution of the limit analysis appears to be excessively conservative for this specific problem; in fact, a load-carrying capacity equal to 192 kN is obtained. This value, together with the collapse mechanism, is plotted in Figure 8.8, where a screen-shot of the software results is reported.

The high discrepancy between the results provided by RING 1.5 and the experimental ones has to be ascribed to the hypothesis of no tension material at the base of the limit analysis. In fact, the brickwork composing the scale bridge model has non negligible tensile strengths and high values of fracture energies, coherently with the high compressive performance of the material tested in laboratory (Melbourne et *al.*, 1995; Melbourne et *al.*, 1997)
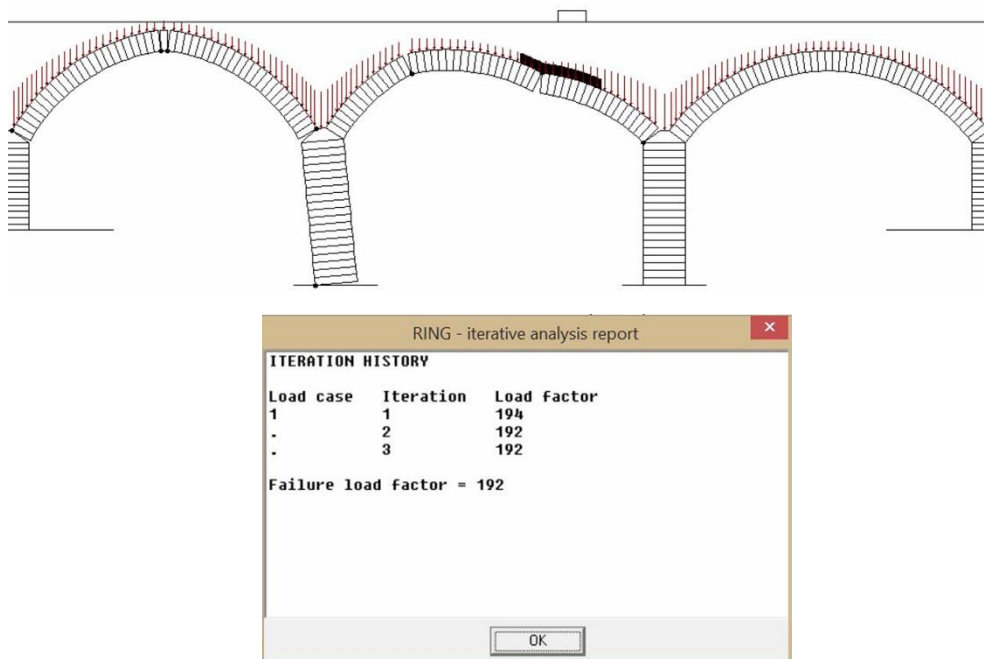
Figure 8.8: Collapse solution for the multi-span masonry arch bridge provided by the limit analysis software RING 1.5.

To prove this, the FE analyses performed in Section 8.22 are repeated by diminuishing G_f^+ and f^+ with respect to the values indicated in Table 8.2 (material set II). By simulating a material which is close to the condition of null tensile resistance and null dissipated energy in tension, the load-carrying capacity evaluated with the damage formulation is a good estimation of the ultimate load derived by limit analysis (see Figure 8.9). The former is higher than the latter because a certain tensile strength and a certain fracture energy are considered.

It is important to note that, even including in RING 1.5 the presence of a passive uniform horizontal backfill pressure (50 kN/m^2), whose contribution is observed in laboratory, the maximum strength of the structure remains far below the experimental failure load (231 kN against 320 kN).

Finally, the absence of crushing numerically detected with the d^+/d^- damage model is confirmed with the use of RING 1.5. In fact, the ultimate capacity of the bridge varies from 192 kN to 194 kN, considering the actual compressive strength of the material or assuming it as infinite, respectively.

It is worth specifying that the over-conservative feature of the limit analysis observed in this specific case can not be generalized. In fact, in the evaluation of existing bridges, in which the materials have been subjected to degradation processes, the assumption of no tensile resistance is not so far from the actual behaviour as here instead found (Figure 8.9).
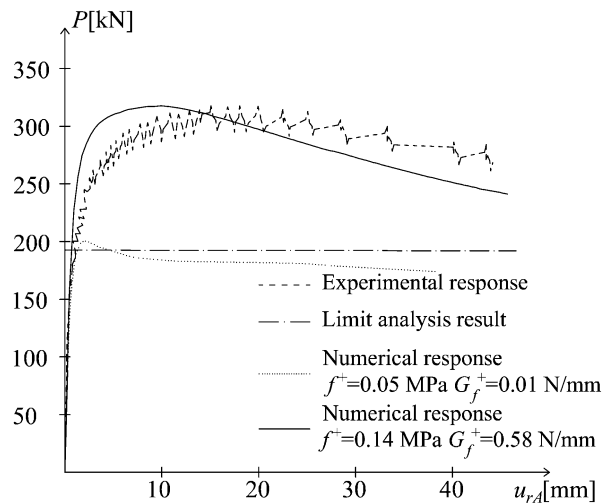
Figure 8.9: Tendency of the damage formulation to recover the ultimate load provided by RING 1.5 for small values of G_f^+ and f^+.

Chapter 9

Conclusions

9.1 Summarizing considerations

In the present thesis, a new d^+/d^- damage model apt for the nonlinear analysis of masonry, unreinforced and reinforced concrete structures under monotonic and cyclic loading conditions is proposed. The formulation, implemented in a displacement-based finite element environment, aims to be a reliable structural assessment tool which could provide accurate results at an affordable computational cost.

In these concluding remarks, the different stages described in the previous chapters, i.e. formulation, implementation in a finite element code and validation, are retraced to put in evidence the salient aspects of the damage model and its capabilitites to describe the response of structures made of concrete- and masonry-like materials.

To take into account the several distinctive mechanical features proper of these materials, the following aspects characterize the new d^+/d^- damage formulation at a constitutive level:

- the pronounced non-symmetrical behaviour under tension and compression, due to different strengths and different fracture energies, is simulated by the adoption of two independent scalar damage variables, d^+ and d^-, which describe the softening and the degradation of the elastic stiffness under tensile and compressive regimes, respectively. Similarly, two damage surfaces, one for tension and one for compression, inspired from the failure criterion proposed

for concrete in (Lubliner et *al*., 1989), are considered to assess, separately, the evolution of d^+ (Figure 2.4.a) and d^- (Figure 2.4.b).

- The damage-induced orthotropy is represented thanks to the spectral decomposition of the elastic strain tensor (see Figure 2.1). Specifically, the strain equivalence assumption between nominal and effective configurations, considered in the original model, is abandoned in favor of an energy-equivalence framework, with the consequent derivation of a new constitutive operator (Eq. (2.24)), which is positive definite and symmetric. In thermodynamic terms, its adoption allows proving the consistency of the constitutive law with respect to the Schwartz theorem about the equality of the mixed partial derivatives of the potential (2.30) and the 1st and 2nd principles of thermo-dynamics (Section 2.2.2). In addition, from a mechanical point of view, it permits simulating a reduction of Poisson's ratio throughout the damage process, rather than considering it unrealistically constant (Section 2.2.3). Analogously to the original formulation, the new one can be classified within the orthotropic rotating models due to the coincidence between the material axes of orthotropy and the principal reference systems of the stress and the elastic strain tensors.

- The development of permanent deformations ε_p is taken into account in a simplified as well as effective way, without introducing concepts proper of a plasticity theory. This is achieved considering the evolution of ε_p only when there is progression of damage and occuring in the direction of the elastic strain tensor. Two different definitions of the permanent strain rate tensor, based on this simplification, are proposed: the first (Eq. (2.57)) is a revisitation of the expression for ε_p proposed in (Faria et *al*., 1998) while the second (Eq. (2.61)) finds its mechanical basis on the plastic micro-cracking.

- The evolution of all the internal variables (d^+, d^- and ε_p) is treated within a unified dissipative approach since G_f^+ and G_f^-, the material constants ruling the energy dissipation under tension and under compression, are not pure fracture parameters but they are actually composed of both damage and plastic dissipative contents. This leads to a modification of the softening modulus usually adopted for exponential damage evolution laws, with the aim of taking into account the simultaneous presence of both the dissipation mechanisms (Section 2.5). Moreover, a new damage evolution law, exhibiting a Gaussian trend (Section 2.5.2), is proposed, suitable to describe the hardening-softening response of quasi-brittle materials under compression.

- To deal with microcrack closure-reopening effects, crucial under cyclic loading, a multidirectional damage approach is adopted, especially effective in case of orthogonal, or however intersecting, sets of cracks, typical of cyclic shear conditions. The procedure consists in enriching at a constitutive level the orthotropic rotating scalar damage model with some features proper of fixed crack models, in order to maintain memory about the degradation directionality. This is done, in plane problems, by performing a partition into two damage regions for d^+ and two damage regions for d^-, with the intent of monitoring and saving during the loading history two damage values in tension and two damage values in compression (Section 3.1). The opening and the closure of cracks can be simulated by activating or deactivating, respectively, a damage value on the base of the current principal directions of ε_e. Moreover, the distinction between two different cyclic conditions, i.e., cyclic loadings considered alone (Type Load (i)) or preceded by not-cyclic permanent loads (Type Load (ii)), and the proposal of an ad-hoc procedure for each of them, add versatility to the formulation. In fact, after loading reversal, a complete stiffness recovery, partial stiffness recovery and no stiffness recovery can be modelled, as shown with reference to the problem of the panel subjected to in-plane cyclic shear without or with a precompression (Section 3.4).

In order to circumvent the convergence difficulties in correspondence with crack closure and reopening and the dependence of the results on the discretization, the formulation is enriched according to the following points:

- the modelling of unilateral effects incorporates a smoothing procedure in the transition from an unloading stiffness to a reloading one, in order to improve the robustness and performance of the multidirectional approach in the numerical analyses (Section 3.3).

- A regularized nonlocal integral approach is adopted to ensure the mesh-objectivity of the results. Specifically, the variable chosen to be averaged is not a scalar, as done in the majority of nonlocal damage models, but is the elastic strain tensor ε_e. The regularized counterpart of ε_e is used to define the evolution of the internal variables whilst, in the constitutive law (2.33), the local elastic strain tensor is maintained. The local strain is also the quantity with reference to which the spectral decomposition is performed, in order to keep the coincidence between the axes of orthotropy of the damage material and the principal directions of elastic strains and stresses unaltered even in the nonlocal formulation.

- The calibration strategy chosen to define the parameters affecting the softening behaviour, inspired by the work presented in (Nguyen and Houlsby, 2007), consists in the modification of the local softening law on the basis of the internal length l_{RG}, with the intent of ensuring the evaluation of the correct fracture energy G_f, independently of l_{RG}. Such a calibration strategy is preferable because it makes the fracture energy the only ruling material parameter while releasing the obtained solution from the choice of the internal length, whose assessment is one of the most debated aspects of regularized damage models.

The new d^+/d^- formulation here summarized has been efficiently implemented, thanks to its full strain driven formalism, in a displacement-based finite element code which works incrementally and iteratively. To solve the algebraic system of equations, the Picard (secant) method has been preferred to the Newton Raphson one, since the use of the new symmetric constitutive operator ensures the adoption of a symmetric global secant stiffness matrix.

Several structural applications are presented as validation of the predictive capabilitites of the new damage model. From these numerical analyses and their comparison with experimental (or analytical) solutions, the following considerations can be drawn:

- the response of concrete samples under cyclic uniaxial tension, cyclic uniaxial compression and biaxial stresses, studied at a local level, can be satisfactorily reproduced by the model, proving the adequacy of the constitutive operator, of the damage criteria and of the evolution laws for the internal variables (see Section 6.1).
- At a structural level, the performance of the new mechanical model, and specifically, the effect of the new energy-equivalent constitutive operator (2.24), compared with the strain-equivalent original one (2.8), is analyzed with reference to unreinforced concrete notched elements subjected to pure tension, pure bending and mixed-mode bending (Section 6.2). Despite the gain in thermo-dynamic consistency ensured by the former, no significant differences are appreciable in the structural responses obtained with the two formulations, being both of them able to fit adequately the experimental results. However, the adoption of the constitutive symmetric operator $\boldsymbol{D_E}$ is convenient in computational terms. In fact, saving in CPU time ranging from 14.7 % to 51 % are found adopting the new symmetric contitutive operator with respect to the non-symmetric original one (see Table 6.8).
- The microcrack closure-reopening capabilities are ensured in cyclic shear conditions, as demonstrated in the problems of a masonry and a reinforced

concrete wall subjected to in-plane cyclic shear (Section 6.3). In both the examples, the experimental evidence is satisfactorily reproduced in terms of lateral resistance and also hysteretic behaviour and symmetry in the response between loading and reloading. This is obtained thanks to the multidirectional procedure, which gives the possibility of differentiating the damage processes on the basis of the orientation of the principal strain directions, taking into account, realistically, the energy dissipated in the formation of both the sets of orthogonal cracks typical of these loading conditions. To quanitify the beneficial effects of the new approach on the simulated hysteretic behaviour, the results coming from the multidirectional procedure and a standard scalar damage formulation are compared with the experimental ones in terms of viscous damping coefficients, for the case of the masonry shear panel. While with the former the energy dissipation capacity of the wall is fairly reproduced, with the latter it is strongly underestimated (Figure 6.21).

- Both the definitions for the permanent deformations here formulated, although simplified, are able to adequately fit the experimental results, as visible in the problem of the masonry arch subjected to loading and unloading stages (Section 7.1) and in the problems of the masonry and reinforced concrete walls under cyclic in-plane shear (Section 6.3). In the latter case, its effect on the structural response is investigated (Figure 6.23) by varying the intensity of the permanent strain tensor with the conclusion that an adequate modelling of permanent deformations is essential, as an adequate modelling of unilateral effects, for the correct representation of the hysteretic behaviour of these structures under cyclic loadings.

- The problem of the masonry wall subjected to in-plane cyclic shear is also exploited to quantify the improved numerical robustness guaranteed by the adoption of the smoothing procedure in correspondence with closure and reopening of cracks (Section 3.3). Data related to the convergence histories, evaluated for different intensities of the permanent strain tensor and for different amplitudes θ_t of the transition region, are collected. They suggest two main observations. On the one hand, the higher is θ_t, the smoother is the modelling of the crak closure and the faster is the convergence; actually, for null permanent deformations, it is found that with $\theta_t = \pi/36$ the convergence in correspondence with the crack-closure is achieved with 57 iterations while, with $\theta_t = \pi/180$, it is not found. On the other hand, the smoothing procedure is more effective when irreversible strains are not considered, because they tend to naturally mitigate the abrupt stiffness changes in presence of unilateral effects.

- The adoption of the regularized approach is able to guarantee objectivity of the results with respect to the size and the alignment of the discretization. The mesh-size independence is proven both in the case of the masonry arch subjected to a vertical point load and of a reinforced concrete beam under four-point bending test, solving the problems with different discretization refinements. Specifically, in the former case, the averaging applied to the elasic strain tensor ε_e only, is however capable of describing the objectivity of the residual deformations at complete unloading, although the irreversible strain tensor is considered as a local variable (Figure 7.6). In addition, the independence of the results on the mesh bias is demonstrated in Section 7.2, with reference to the case of a perforated slab under uniaxial tension. For this problem, the analytical inclination of the discontinuity is known by a strain localization analysis and it strongly depends on the Poisson ratio v. By varying v, the solutions coming from the regularized approach are able to reproduce the analytical ones (Figure 7.10), differently from the ones obtained with the local approach, which are influenced by the mesh alignment (Figure 7.9).

- For this specific constitutive law, within the regularized formulations, the averaging of the elastic strain tensor is preferable with respect to the averaging of the scalar equivalent stresses. This is shown in the example of application regarding the reinforced concrete beam under four point bending test (Section 7.3.1), where a slightly higher level of mesh-objectivity is observed (Table 7.8), together with an improved convergence speed (Table 7.9), adopting the regularized strain tensor approach instead of the regularized "scalar" one.

- The dependence of the regularized solutions on the internal length in terms of force-displacement curves is almost null in uniaxial loading conditions (Figure 4.7.b) and substantially slight in general stress-strain states (Figure 7.20), thanks to the calibration strategy adopted to define the energy dissipation. In terms of strain localization, the internal length influences the localization bandwidth in problems characterized by a single failure zone (Figure 4.7.b) and the number and width of the damaged areas in problems characterized by multiple failure zones (Figure 7.21). All these considerations can be interpreted finding a significant analogy between the regularized approach and the local crack band approach proposed in (Bažant and Oh, 1983), with a parallelism intervening between the role played by the internal length l_{RG} and the mesh size.

- The proposed regularized strain-tensor approach, in combination with the adopted calibration strategy, appears to be able to describe the structural size effect for different geometries, with the same set of input parameters (Section 7.4). In fact, experimental results coming from three-point bending

tests on notched and unnotched beams, with different scales, are fairly reproduced in the numerical analyses, especially in terms of peak loads. Other nonlocal formulations applied to the same set of specimens are not likewise good in catpturing the structural size effect on different geometries, i.e., on different notch-to-depth ratios.

- The application of the regularized d^+/d^- damage model to the study of a three-span masonry arch bridge subjected to a vertical point-wise load is satisfactory and encourages the adoption of finite element nonlinear analysis based on damage mechanics for the study of masonry arch bridges with a single or more spans. In fact, the results obtained with the proposed model are able to estimate the load-carrying capacity of the structure, its post-peak response and the failure mechanism which involves the collapse of two of the three spans, due to the piers' flexibility. In addition, the reliability of the numerical results is proven by performing a mesh objectivity study. The material constants which affect most the structural response are the ones related to the tensile behaviour of masonry, i.e. the uniaxial strength f^+ and the fracture energy G_f^+, hence the accuracy of the results depends on the reliable characterization of the material parameters. It is however shown that, for the specific problem analyzed, by performing a limit analysis with the commercial software RING 1.5, an excessive underestimation of the structural resistance is found, suggesting that the assumption of a null tensile strength and a null fracture energy is not always a valid option.

9.2 Main contributions

The main contributions of the present thesis to the field of the structural analysis of masonry and concrete structures by means of damage mechanics-based finite element codes are summarized in the following points:

- the proof that a new version of the original d^+/d^- damage model (Faria et *al*., 1998) is necessary and derives from the difficulties found in defining a consistent consitutive operator (positive-definite and endowed with major and minor symmetries) under the assumption of strain equivalence between the effective and the nominal configurations.
- The adoption of tensor mapping procedures existing in literature to describe an orthotropic material starting from an isotropic one (Pelà et *al*., 2014) to represent the orthotropy induced by the degradation process in an initially isotropic material. Indeed, the use of the energy-equivalence assumption to derive the new constitutive operator is equivalent to consider a mapping tensor

which relates the effective, isotropic, configuration of the undamaged material between microcracks, to the nominal, orthotropic, configuration of the damaged material (see Figure 2.2). The d^+/d^- damage model deriving from this assumption is thermo-dynamically consistent and is governed by a constitutive operator which is positive definite and endowed with both major and minor symmetries.

- The cognition that the d^+/d^- damage models in the existing literature are not able to describe the unilateral effects in generic cyclic conditions, but only in alternating full tensile - full compressive regimes. This represents a strong limitation because the modelling of microcrack closure-reopening is not possible, for instance, in shear cyclic conditions, which are the ones typically induced during an earthquake in resisting vertical panels.

- The formulation of a multidirectional damage approach, which allows to preserve memory regarding degradation directionality while maintaining unaltered the dependence of the stress tensor from only the scalars d^+ and d^-. This procedure is based on the incorporation of aspects proper of fixed crack models in a constitutive law which has, instead, a rotating nature, due to the split of the elastic strain tensor into its positive and negative counterparts. Therefore, the application of the multidirectional damage approach is versatile and all those orthotropic damage models based on the use of scalar damage variables and on the spectral decomposition of a second order tensor can take advantage from it.

- The consideration of the microcrack closure-reopening effects also from a numerical point of view, with the proposal of a smoothing procedure to alleviate convergence difficulties in correspondence with loading reversal. This topic has not received by the existing literature the same degree of attention of other numerical issues, as the ones related to the spurious mesh dependence in simulating cracking and strain-softening.

- The application of the multidirectional approach to the study of masonry and reinforced concrete walls under in-plane cyclic shear, with the successful description of the structural response, in terms of lateral resistance but also hysteretic behaviour and symmetry between loading and reloading. The experimental energy dissipation capacity of the structure, related to the formation of intersecting sets of cracks, is well reproduced by the proposed model, thanks to the correct representation of unilateral effects and to the development of permanent deformations.

- The identification of the elastic strain tensor as the variable to be regularized, in order to optimize the mesh-objectivity of the formulation while maintaining the

coincidence between the axes of material orthotropy and the principal directions of elastic strains and stresses, typical of the local constitutive model.

- The notion that the nonlocal integral damage model has not to be opposed drastically to the crack band approach proposed in (Bažant and Oh, 1983). Indeed, by considering the internal length as a pure regularization parameter, it is possible to establish a parallelism between its role in nonlocal damage models and the mesh size's role in crack band approaches. Both these parameters affect the local softening law in such a way that, independently of their value, the correct fracture energy is represented at a structural level. In terms of strain localization, both of them influence the width (and even the number in case of multiple failure zones) of the damage areas. The essential advantage of a nonlocal model with respect to a crack band one mainly lies in its mesh-bias objectivity.

- The attention dedicated to the dependence of the regularized formulations on the choice of the internal length. Such a sensitivity analysis is often neglected in the existing literature, usually addressed to show only the independence of the nonlocal results from the discretization.

- The adoption of the Picard (secant) method to solve the algebraic system of equations, which leads to a symmetric global stiffness matrix in the local as well as in the regularized version of the damage formulation, with the consequent saving of computation resources.

- The application of the regularized d^+/d^- damage model for the structural assessment of a multi-span masonry arch bridge. Both the load carrying capacity and the global failure mechanisms are well caught by the proposed formulation. Numerical issues, usually neglected in large-scale applications, are also addressed proving the reliability of the nonlocal damage approach, due to its capacity to provide mesh-independent results.

9.3 Topics for further research

Being the field of the structural assessment of masonry, reinforced and unreinforced concrete structures by means of damage mechanics-based formulations very wide, the possibilities to extend the present work are several.

- To widen the typologies of structures and the loading configurations to be studied, the application of the d^+/d^- damage formulation to 3D problems has to be performed. It is worth noting that the formulation of the damage model, as well as the formulation of its regularized version, do not need additional ingredients to be applied to three-dimensional cases. Therefore, only their

validation is required. Regarding the 3D extension of the multidirectional approach, it does not appear conceptually difficult, as described in Chapter 3, but it requires a certain implementation effort, due to the necessity of partitioning the space into solid regions.

- At a constitutive level, to explore the possibilities of modelling different types of damage-induced orthotropy, other forms for the tensor A^*, which defines the dependence of the constitutive operator on the scalar variables and on the operator Q performing the spectral decomposition of the elastic strain tensor (2.23) can be analyzed. For instance, Q can be fixed at a certain degradation level, interrumpting the rotation of the directions of material orthotropy, in order to switch from a rotating crack model to a fixed one. This has beneficial effects in terms of stiffness recovery capabilitites under cyclic loadings, making the multidirectional procedure unnecessary, but it requires to face another essential issue, typical of fixed crack models, which is the stress locking. An alternative to describe an higher degree of damage-induced orthotropy is to monitor three distinct tensile damage variables and three distinct compressive damage variables, each one associated to a principal direction. The main complication arising from such a procedure regards the definition of the equivalent stress variables, which have to be representative of a directional stress-strain state.

- To increase the accuracy of the results at the expense of an higher number of necessary material parameters, a plastic theory can be considered for the evaluation of the irreversible deformations and creep effects can be modelled as another source of material degradation.

- The application of the d^+/d^- damage model to the study of masonry arch bridges by means of 2D finite elements can be deepened, introducing suitably the resisting contribution of the spandrel walls and the fill-arch interaction.

- A natural continuation of this work can be also the extension to seismic analysis, which deals with the formulation in a finite element framework of the dynamic balance equation and the refinement of the constitutive laws in order to take into account the fatigue behaviour and the strain-rate sensitivity of the material properties. The proper modelling of the unilateral effects, achieved with the multidirectional damage procedure conceived in the present thesis, is obviously essential in this kind of analysis.

- The capability of the multidirectional damage approach to provide a reliable response under cyclic actions can be exploited to extract, for some recurrent typologies of structures, the characteristic value of some input parameters of less-refined seismic analysis techniques. For instance, thanks to the possibility of describing with accuracy the hysteretic behaviour, the proposed damage

model, enriched with the multidirectional procedure, can be adopted in the definition of the viscous damping coefficient in dynamic linear analyses.

References

Addessi, D., Marfia, S., Sacco, E. (2002). A plastic nonlocal damage models. *Computer Methods in Applied Mechanics and Engineering* 191, 1291-1310.

Addessi, D., Marfia, S., Sacco, E., Toti, J. (2014). Modeling Approaches for Masonry Structures. *The Open Civil Engineering Journal* 8, 288-300.

Aifantis, E.C. (1984). On the microstructural origin of certain inelastic models. *Journal of Engineering Materials and Technology ASME* 106, 326–330.

Anthoine, A., Magonette, G. (1994). Shear-compression testing and analysis of brick masonry walls. *Proceedings 10th European Conference on Earthquake Engineering Vienna*, 1657-1662.

Areias, P.M.A., Belytschko, T. (2005). Analysis of threedimensional crack initiation and propagation using the extended finite element method. *International Journal for Numerical Methods in Engineering* 63(5), 760-788.

Armero, F., Oller, S., (2000). A general framework for continuum damage models. i: Infinitesimal plastic damage models in stress space. *International Journal of Solids and Structures* 37, 7409–7464.

Barbat, G.B, Cervera, M., Chiumeni, M. (2018). Appraisment of planar, bending and twisting cracks in 3D with isotropic and orthotropic damage models. *International Journal of Fracture* DOI 10.1007/s10704-018-0261-3.

Bažant, Z.P. (1983a). Microplane model for fracture of heterogeneous materials. ASCE Annual Convention Houston, Texas.

Bažant, Z.P. (1983b). Comment on orthotropic models for concrete and geometarials. *Journal of Engineering Mechanics* ASCE 109(3), 849-865.

Bažant, Z.P. (1996). Analysis of work-of-fracture method for measuring fracture energy of concrete. *Journal of Engineering Mechanics* 122(2), 138-144.

Bažant, Z.P. Cedolin, L. (1983). Finite element modeling of crack band propagation. *Journal of Structural Engineering* 109(1), 69–92.

Bažant, Z. P., Jirásek, M. (2002). Nonlocal integral Formulations of Plasticity and Damage: Survey of Progress. *Journal of Engineering Mechanics* 128(1), 1119-1149.

Bažant, Z. P., Lin, F. B. (1988). Nonlocal smeared cracking model for concrete fracture. *Journal of Engineering Mechanics ASCE* 114, 2493-2510.

Bažant, Z.P., Oh, B.H. (1983). Crack band theory for fracture of concrete. *Materials and Structures* 16, 155-177.

Bažant, Z.P., Pfeiffer, P.A. (1986). Shear fracture tests of concrete. *Materials andStructures* 19(2),111–121.

Bažant, Z.P., Pijaudier-Cabot, G. (1988). Nonlocal continuum damage, localization instability and convergence. *Journal of Applied Mechanics ASME* 55, 287-293.

Bažant, Z.P., Pijaudier-Cabot, G. (1989). Measurement of characteristic length of nonlocal continuum. *Journal of Engineering Mechanics* 115(4), 755-767.

Bažant, Z.P., Planas, J. (1998). Fracture and Size Effect in Concrete and other Quasibrittle materials. *CRC Press.*

Belytschko, T., Black, T. (1999). Elastic crack growth in finite elements with minimal remeshing. *Computer Methods in Applied Mechanics and Engineering* 45 (5), 601–620.

Belytschko, T., Fish, J., Engelmann, B.E. (1988). A finite element with embedded localization zones. *ComputerMethods in Applied Mechanics and Engineering* 70(1), 59–89.

Belytschko, T., Gracie, R., Ventura, G. (2009). A review of extended/generalized finite element methods for material modelling. *Modelling and Simulation in Materials Science and Engineering* 17, 043001.

Berto, L., Saetta, A., Scotta, R., Vitaliani, R. (2002). An orthotropic damage model for masonry structures. *International Journal for Numerical Methods in Engineering* 55, 127-157.

Bisch, Philippe, Erlicher, S., Huguet, M. (2014). Cracking in shear walls: experimental results and analytical predictions. *Proceedings 2ⁿᵈ European Conference on Earthquake Engineering, Istanbul*.

Boothby, T.E., Domalik, D.E., Dalal, V.A. (1998). Service Load Response of Masonry Arch Bridges. *Journal of Structural Engineering* 124(1), 17-23.

Brencich, A., De Francesco, U. (2004a). Assessment of Multispan Masonry Arch Bridges. I: Simplified Approach. *Journal of Bridge Engineering* 9(6), 582-590.

Brencich, A., De Francesco, U. (2004b). Assessment of Multispan Masonry Arch Bridges. II: Examples and Applications. *Journal of Bridge Engineering* 9(6), 591-598.

Caboche, J.L. (1988a). Continuum Damage Mechanics: Part I — General Concepts. *Journal of Applied Mechanics* 55(1), 59–64.

Caboche, J.L. (1988b). Continuum damage mechanics: Part II — Damage growth, crack initiation, and crack growth. *Journal of applied mechanics* 55(1), 65–72.

Caboche, J.L. (1992). Damage induced anisotropy: On the difficulties associated with the active/passive unilateral condition. *Internation Journal of Damage Mechanics* 1, 148–171.

Camacho, G.T., Ortiz, M. (1996). Computational modelling of impact damage in brittle materials. *International Journal of Solids and Structures* 33(20-22), 2899-2938.

Carol, I., Willam, K. (1996). Spurious Energy Dissipation/Generation in Stiffness Recovery Models for Elastic Degradation and Damage. *International Journal of Solids and Structures* 33, 2939–2957.

Cavicchi, A., Gambarotta, L. (2007). Lower bound limit analysis of masonry bridges including arch-fill interaction. *Engineering Structures* 29, 3002-3014.

Carol, I., Rizzi, E.; Willam, K. (2001). On the formulation of anisotropic elastic degradation. I. Theory based on a pseudo-logarithmic damage tensor rate. *International Journal of Solids and Structures 38*, 491–518.

Celano, F., Cimmino, M., Coppola, O., Magliulo, G., Salzano, P. (2016). Report dei danni registrati a seguito del terremoto del Centro Italia del 24 agosto 2016 (Release 1). Available at http://www.reluis.it.

Cervera, M. (2003). Viscoelasticity and Rate Dependent Continuum Damage Models. CIMNE Monograph n° 79, Barcellona, Spain.

Cervera, M. (2008). An orthotropic mesh corrected crack model. Computer Methods in Applied Mechanics and Engineering 197, 1603-1619.

Cervera, M., Barbat, G.B., Chiumenti, M. (2017). Finite element modelling of quasi-brittle cracks in 2D and 3D with enhanced strain accuracy. Computational Mechanics   DOI :http://dx.doi.org/10.1007/s00466-017-1438-8.

Cervera, M., Chiumenti, M. (2006). Smeared crack approach: back to the original track. *International Journal for Numerical and Analytical Methods in Geomechanics* 30(12), 1173–1199.

Cervera, M., Chiumenti, M. (2009). Size effect and localization in J2 plasticity. *International Journal of Solids and Structures* 46(17), 3301–3312.

Cervera, M., Chiumenti, M., Benedetti, L., Codina, R. (2015). Mixed stabilized finite element methods in nonlinear solid mechanics: Part III: compressible and incompressible plasticity. *Computer Methods and Applied Mechanics in Engineering* 285, 752-775.

Cervera, M., Chiumenti, M., Codina, R. (2010a). Mixed stabilized finite element methods in nonlinear solid mechanics: Part I: formulation. *Computer Methods and Applied Mechanics inEngineering* 199 (37-40), 2559-2570.

Cervera, M., Chiumenti, M., Codina, R. (2010b). Mixed stabilized finite element methods in nonlinear solid mechanics: Part II: strain localization. *Computer Methods and Applied Mechanics in Engineering* 199 (37-40), 2571-2589.

Cervera, M., Chiumenti, M., Codina, R. (2011). Mesh objective modeling of cracks using continuous linear strain and displacement interpolations. *International Journal for Numerical Methods in Engineering* 87, 962-987.

Cervera, M., Oliver, J., Faria, R., (1995). Seismic evaluation of concrete dams via continuum damage models. *Earthquake Engineering & Structural Dynamics* 24, 1225-1245.

Cervera, M., Oliver, J., Herrero, E., Oñate, E. (1990). A computational model for progressive cracking in large dams due to the swelling of concrete. *Engineering Fracture Mechanics* 35(1), 573–585.

Cervera, M., Oliver, J., Manzoli, O. (1996). A rate-dependent isotropic damage model for the seismic analysis of concrete dams. *Earthquake Engineering & Structural Dynamics* 25(9), 987-1010.

Cervera, M., Tesei, C. (2017). An energy-equivalent d^+/d^- damage model with enhanced microcrack closure-reopening capabilities for cohesive frictional materials. *Materials* 10(4), 433.

Cervera, M., Tesei, C., Ventura, G. (2018). Cracking of quasi-brittle structures under monotonic and cyclic loadings: a d^+/d^- damage model with stiffness recovery in shear. *International Journal of Solids and Structures* 135, 148-171.

Chang, G.A., Mander, J.B. (1994). Seismic Energy Based Fatigue Damage Analysis of Bridge Columns: Part I – Evaluation of Seismic Capacity. *Technical Report NCEER-94-0006* State University of New York at Buffalo.

Chessa, J., Wang, H.. Belytschko, T. (2003) On the construction of blending elements for local partition of unity enriched finite elements. *International Journal for NumericalMethods in Engineering* 57 (7), 1015‑1038.

Choo, B.S.*,* Coutie, M.G., Gong, N.G. (1991). Finite-elementanalysis of masonry arch bridges using tapered elements. *Proceedings of the Institution of Civil Engineers* (U.K.) 91, 755-770.

Cicekli, U., Voyiadjis, G.Z., Abu Al-Rub, R.K. (2007). A plasticity and anisotropic damage model for plain concrete. International Journal of Plasticity 23, 1874-1900.

Clemente, R., Roca, P., Cervera, M. (2006). Damage model with crack localization-Application to historical buildings. *Proceedings of Structural Analysis of Historical Constructions*, New Dehli 2006.

Coleman, B.D., Gurtin, M.E. (1967). Thermodynamics with internal state variables. *Journal of Chemical Physics* 47, 597–613.

Comi, C. (1999). Computational modelling of gradient-enhanced damage in quasi-brittle materials. *Mechanics of Cohesive-Frictional Materials* 4, 17–36.

Comi, C. (2001). A nonlocal model with tension and compression damage mechanisms. *European Journal of Mechanics – A/Solids* 20, 1-22.

Comi, C., Perego, U. (2001a). Fracture energy based bi-dissipative damage model for concrete. *International Journal of Solids and Structures* 38, 6427-6454.

Comi, C., Perego, U. (2001b). Numerical aspects on nonlocal damage analyses. *Revué Européenne des éléments finis* 10, 227-242.

Contraffato, L., Cuomo, M. (2006). A framework of elastic–plastic damaging model for concrete under multiaxial stress states. *International Journal of Plasticity* 22, 2272–2300.

Cope, R.J., Rao, P.V., Clark, L.A., Norris, P. (1980). Modelling of reinforced concrete behaviour for finite element analysis of bridge slabs. In Talor C. et *al*. (Eds.), Numerical method for nonlinear problems 1. Pineridge Press, Swansea, 457-470.

Cordebois, J.P., Sidoroff, F. (1982). Endommagement anisotrope en elasticité et plasticité. *Journal of theoretical and applied mechanics* Special Volume, 45–60.

Cowin, S.C. (1994). Optimization of the strain energy density in linear anisotropic elasticity. *Journal of Elasticity* 34, 45–68.

Crisfield, M.A., Packham, A.J. (1988). A mechanism program for computing the strength of masonry arch bridges. *Research Report* 124, Dept. of Transport, TRL, Crowthorne.

Crisfield, M. A., Wills, J. (1985). Nonlinear analysis of concrete and masonry structures. *Proceedings of the Europe-U.S. Symposium on Finite Element Methods for Nonlinear Problems,* 639-652.

Cuomo M., Ventura G. (2000). A complementary energy formulation of no tension masonry like solids. *Computer Methods in Applied Mechanics and Engineering* 189, 313-39.

De Borst, R. (2002). Fracture in quasi-brittle materials: A review of continuum damage-based approaches. *Engineering Fracture Mechanics* 69, 95–112.

De Borst, R., Muhlhaus, H.B. (1992). Gradient-dependent plasticity: formulation and algorithmic aspects. *International Journal for Numerical Methods in Engineering* 35, 521–539.

De Borst, R., Nauta, P. (1985). Non-orthogonal cracks in a smeared finite element model. *Engineering Computations* 2, 35-46.

De Borst, R., Verhoosel, C.V. (2016). Gradient damage *vs* phase field approaches for fracture: similarities and differences. *Computer Methods in Applied Mechanics and Engineering* 312, 78–94.

De Felice, G. (2009). Assessment of the load-carrying capacity of multi-span masonry arch bridges using fibre beam elements. *Engineering Structures* 31, 1634-1647.

Dias-da-Costa D., Alfaiate J., Sluys L., Júlio E. (2010). A comparative study on the modelling of discontinuous fracture by means of enriched nodal and element techniques and interface elements. *Internation Journal of Fracture* 161(1), 97–119.

Dvorkin, E.N., Cuitino, A.M. and Gioia, G. (1990). Finite elements with displacement interpolated embedded localization lines insensitive to mesh size and distortions. *International Journal for Numerical Methods in Engineering* 30(3), 541–564, 1990.

Faria, R., Oliver, J. (1993). A Rate Dependent Plastic-Damage Constitutive Model for Large Scale Computations in Concrete Structures. *CIMNE Monograph* 17, CIMNE, Barcelona, Spain.

Faria, R., Oliver, J., Cervera, M. (1998). A strain-based plastic viscous-damage model for massive concrete structures. *International Journal of Solids and Structur*es 35(14), 1533-1558.

Faria, R., Oliver, J., Cervera, M. (2000) *On Isotropic Scalar Damage Models for the Numerical Analysis of Concrete Structures*; Publication CIMNE No. 198; CIMNE: Barcelona, Spain.

Faria, R., Oliver, J., Cervera, M. (2004). Modelling Material Failure in Concrete Structures under Cyclic Actions. *Journal of Structural Engineering* ASCE 130, 1997-2005.

Fanning, P., Boothby, T.E. (2001). Three-dimensional modelling and full-scale testing of stone arch bridges. *Computer and Structures* 79(29–30), 2645–2662

Ferrara, L., di Prisco, M. (2001). Mode I fracture behaviour in concrete: nonlocal damage modeling. *Journal of Engineering Mechanics* 127(7), 678-692.

Fries, T.P. (2008). A corrected XFEM approximation without problems in blending elements. *International Journal for Numerical Methods in Engineering* 75 (5), 503‑532.

Gálvez, J.C., Elices, M, Guinea, G.V., Planas, J. (1998). Mixed mode fracture of concrete under proportional and non proportional loading. *International Journal of Fracture* 94, 267-284.

Gambarotta, L., Lagomarsino, S. (1997). Damage models for the seismic response of brick masonry shear walls. Part I & Part II. Earthquake Engineering & Structural Dynamics 26, 423-462.

Geers, M.G.D., De Borst, R., Brekelmans, W.A.M., Peerlings, R.H.J. (1998). Strain-based transient-gradient damage model for failure analyses. *Computer Methods in Applied Mechanics and Engineering* 160, 133-153.

Gilbert, M., Melbourne, C. (1994). Rigid block analysis of masonry structures. *The Structural Engineer* 72(21), 356-361.

Gong, N.G., Choo, B.S., Coutie, M.G. (1993). Crack and contact problems in masonry arch bridges." *Proc. V ICCCBE,* ASCE, New York, N.Y., 801-808.

Gopalaratnam, V.S., Shah, S.P. (1985). Softening response of plain concrete in direct tension. *ACI Journal Proceedings* 82.

Gracie, R., Wang, H., Belytschko, T. (2008). Blending in the extended finite element method by discontinuous Galerkin and assumed strain methods, *International Journal for Numerical Methods in Engineering* 74(11), 1645-1669, 2008.

Grégoire, D., Rojas-Solano, L.B., Pijaudier-Cabot, G. (2013). Failure and size effect for notched and unnotched concrete beams. *International Journal for Numerical and Analytical Methods in Geomechanics* 37, 1434-1452.

Gupta, A.K., Akbar, H. (1984). Cracking in reinforced concrete analysis. *Journal of Structural Engineering ASCE* 110(8), 1735-1746.

Harvey, W.J., Smith, F.W. (1991). The behaviour and assessment of multispan arches. *The Structural Engineer* 69(24), 411-417.

He, W., Wu, Y.F., Xu, Y., Fu, T.T. (2015). A thermodynamically consistent nonlocal damage model for concrete materials with unilateral effects. *Computer Methods in Applied Mechanics and Engineering* 297, 371-391.

Heyman, J. (1969). The safety of masonry arches. *International Journal of Mechanical Sciences* 11, 363-385.

Heyman J. (1995). The Stone Skeleton. Cambridge University Press.

Hillerborg, A., Modeer, M., Petersson, P.E. (1976). Analysis of crack formation and crack growth in concrete by means of fracture mechanics and finite elements. *Cement and Concrete Research* 6, 773-782.

Hofstetter, G., Meschke, G. (2011). Numerical modelling of concrete cracking. CISM courses and lectures volume 532, SpringerWienNewYork.

Horstemeyer, M.F., Bammann, D.J. (2010). Historical review of internal state variable theory for inelasticity. *International Journal of Plasticity* 26, 1310-1334.

Hughes, T.G. (1995). Analysis and assessment of twin-span masonryarch bridges. *Proceedings of the Institution of Civil Engineers* (U.K.) 110, 373–382.

Jefferson, A.D., Mihai, I.C. (2015). The simulation of crack opening-closing and aggregate interlock behavior in finite element concrete models. *International Journal for Numerical Methods in Engineering* 104, 48-78.

Jirásek, M. (1998a). Nonlocal models for damage and fracture: comparison of approaches. *International Journal of Solids and Structures* 35, 4133-4145.

Jirásek, M. (1998b). Comparison of nonlocal models for damage and fracture. *LSC Internal Report 98/02,* Dept. of Civil Eng., Swiss Federal Institute of Technology (EPFL), Lausanne, Switzerland.

Jirásek, M., Zimmermann, Th. (1998). Rotating crack model with transition to scalar damage. *Journal of Engineering Mechanics ASCE* 124, 277-284.

Jirásek, M. (2001) Embedded crack model. I: Formulation; II: Combination with smeared cracks. International Journal for Numerical Methods in Engineering 50, 1269-1305.

Jirásek, M., Patzák, B. (2002). Consistent tangent stiffness for nonlocal damage models. *Computer and Structures* 80, 1279-1293.

Jirásek, M., Rolshoven, S. (2003). Comparison of integral-type nonlocal plasticity models for strain-softening materials. *International Journal of Engineering Science* 41, 1553-1602.

Jirásek, M., Rolshoven, S., Grassl, P. (2004). Size effect on fracture energy induced by nonlocality. *International Journal for Numerical and Analytical Methods in Geomechanics* 28, 653-670.

Ju, J.W. (1989). On energy-based coupled elastoplastic damage theories: Constitutive modelling and computational aspects. *International Journal of Solids and Structures* 25, 803–883.

Kachanov, L.M. (1958). Time of the rupture process under creep conditions. *Isv. Akad. Nauk. SSR. Otd Tekh. Nauk.* 8, 26–31.

Kennedy, T. C., Nahan, M. F. (1996). A simple nonlocal damage model for predicting failure in a composite shell containing a crack. *Composite Structures* 35, 229-236.

Kormeling, H.A., Reinhardt, H.W. (1983). Determination of the fracture energy of normal concrete and epoxy modified concrete. In: Report 5–83-18, Delft University of Technology.

Krajcinovic, D., Fonseka, G.U. (1981). The continuous damage theory of brittle materials. *Journal of Applied Mechanics* 48, 809–824.

Krayani, A., Pijaudier-Cabot, G., Dufour, F. (2009). Boundary effect on weight function in nonlocal damage model. *Engineering Fracture Mechanics* 76, 2217-2231.

Kuhn, C., Müller, R. (2010). A continuum phase field model for fracture. *Engineering Fracture Mechanics* 77(18), 3625–3634.

Kupfer, H., Hilsdorf, H.K., Rusch, H., 1969. Behavior of concrete under biaxial stresses. *ACI Journal* 66-52, 656–666.

Le Bellégo, C., Dubé, J.F., Pijaudier-Cabot, G., Gérard, B. (2003). Calibration of nonlocal damage model from size effect tests. *European Journal of Mechanics A/Solids* 22, 33-46.

Lee, J., Fenves, G.L. (2001). A return-mapping algorithm for plastic-damage models: 3-D and plane stress formulations. *International Journal for Numerical Methods in Engineering* 50, 487-506.

Lemaitre, J., Chaboche, J.L. (1978). Aspects phènomènologiques de la rupture par endommagement. *Journal of Applied Mechanics* 1978, *2*, 317–365.

Leonhardt, F., Walther, R. (1962). Schubversuche an einfeldrigen Stahlbetonbalken mit und ohne Schubbewehrung zur Ermittlung der Schubtragfähigkeit und der oberen Schubspannungsgrenze. *DAfStb-Deutscher Ausschuss für Stahlbeton.*

LimitState (2014). RING manual version 3.1.b. Sheffield: LimitState.

Lotfi, H.R., Shing, P.B. (1994). Interface model applied to fracture of masonry structures. Journal of Structural Engineering ASCE 120(1), 63-80.

Loo, Y. C. (1995). Collapse load analysis of masonry arch bridges. *Arch bridges,* C. Melbourne, ed., Thomas Telford, London, U.K., 167-174.

Loo, Y. C., Yang, Y. (1991). Cracking and Failure Analysis of Masonry Arch Bridges. *Journal of Structural Engineering* 117(6), 1641-1659.

Lourenço, P.B., Rots, J.G. (1997). A multi-surface interface model for the analysis of masonry structures. Journal of Engineering Mechanics ASCE 123(7), 660-668.

Lourenço, P.B, Rots, J.G., Blaauwendraad J. (1998). Continuum model for masonry: parameter estimation and validation. *Journal of Structural Engineering* 124, 642-652.

Lubliner, J., (1972). On the thermodynamics foundations of nonlinear solid mechanics. *International Journal of Nonlinear Mechanics* 7, 237–254.

Lubliner, J., Oliver, J., Oller, S., Oňate, E. (1989). A plastic-damage model for concrete. *International Journal of Solids and Structures* 25, 299–326.

Mallardo, V., Malvezzi, R., Milani, E., Milani, G. (2008). Seismic vulnerability of historical masonry buildings: a case study in Ferrara. *Engineering Structures* 30, 2223-2241.

Magenes, G., Calvi, G.M. (1992). Cyclic behavior of brick masonry walls. *Proceedings 10th World Conference on Earthquake Engineering Rotterdam*, 3517-3522.

Magenes, G., Calvi, G.M., (1997). In-plane seismic response of brick masonry walls. *Earthquake Engineering & Structural Dynamics* 26, 1091-1112.

Mazars, J., Lemaitre, J. (1985). Application of continuous damage mechanics to strain and fracture behavior of concrete. In *Application of Fracture Mechanics to Cementitious Composites*, Springer, 507–520.

Mazars, J., Pijaudier-Cabot, G. (1989). Continuum damage theory- Application to concrete. *Journal of Engineering Mechanics* 115, 345–365.

Mazars, J., Berthaud, Y., Ramtani, S., 1990. The unilateral behaviour of damaged concrete. *Engineering Fracture Mechanics* 35, 629-635.

Melbourne, C., Gilbert, M., Wagstaff, M. (1995). The behaviour of multi-span masoonry arch bridges. *Arch bridges,* C. Melbourne, ed., Thomas Telford, London, U.K., 489-497.

Melbourne, C., Gilbert, M., Wagstaff, M. (1997). The collapse behaviour of multispan brickwork arch bridges. *The Structural Engineer* 75(17), 297-305.

Menegotto, M., Pinto, P. (1973). Method of analysis for cyclically loaded reinforced concrete plane frames including changes in geometry and non-elastic behavior of elements under combined normal force and bending.

Proceedings IABSE Symposium on Resistance and Ultimate Deformability of Structures Acted on by Well-Defined Repeated Loads, Final Report, Lisbon.

Miehe, C., Welschinger, F., Hofacker, M. (2010). Thermodynamically consistent phase-field models of fracture: Variational principles and multi-field FE implementations. *International Journal for Numerical Methods in Engineering* 83 (10), 1273–1311.

Milani, G., Lourenço, P.B. (2012). 3D non-linear behaviour of masonry arch bridges. *Computer and Structures* 110-111, 133-150.

Möes, N., Dolbow, J., Belytschko, T. (1999). A finite element method for crack growth without remeshing. *International Journal of Numerical Methods in Engineering* 46, 131–150.

Molins, C., Roca, P. (1998). Capacity of Masonry Arches and Spatial Frames. *Journal of Structural Engineering* 124(6), 653-663.

Ngo, D., Scordelis, A.C. (1967). Finite element analysis of reinforced concrete beams. *ACI Journal* 64(3),152–163.

Nguyen, G.D., Houlsby, G.T. (2007). Nonlocal damage modelling of concrete: a procedure for the determination of model parameters. *International Journal for Numerical and Analytical Methods in Geomechanics* 31, 867-891.

Nguyen, G.D., Houlsby, G.T. (2008). A coupled damage-plasticity model for concrete based on thermodynamic principles: Part I: model formulation and parameter identification. *International Journal for Numerical and Analytical Methods in Geomechanics* 32, 353-389.

Nilson, A. H. (1968). Nonlinear analysis of reinforced concrete by the finite element method. 65(9),757–766.

Oliveira, D.V. (2003). Experimental and Numerical analysis of blocky masonry structures under cyclic loading. Ph.D. Thesis. Portugal: University of Minho.

Oliver, J. (1989). A consistent characteristic length for smeared cracking models. *International Journal for Numerical Methods in Enginee*ring 28(2), 461-474.

Oliver, J. (2000). On the discrete constitutive models induced by strong fiscontinuity kinematics and continuum constitutive equations. Int. J. Solids Struct. 37, 7207-7229.

Oliver, J., Cervera, M., Manzoli, O. (1999). Strong discontinuities and continuum plasticity models: the strong discontinuity approach. *International Journal of Plasticity* 15, 319–351.

Ortiz, M. (1985). A constitutive theory for the inelastic behaviour of concrete. *Mechanics of Materials* 4, 67–93.

Ortiz, M., Leroy, Y., Needleman, A. (1987). A finite element method for localized failure analysis. *Computer Methods in Applied Mechanics and Engineering* 61(2), 189‑214.

Pandolfi, A., Krysl, P., Ortiz, M. (1999). Finite element simulation of ring expansion and fragmentation: the capturing of length and time scales through cohesive models of fracture. *International Journal of Fracture* 95(1-4), 279‑297.

Papa, E. (1996). A unilateral damage model for masonry based on a homogenisation procedure. *Mechanics of Cohesive-Frictional Materials* 1, 349-366.

Papa, E., Taliercio, A. (1996). Anisotropic damage model for the multiaxial static and fatigue behaviour of plain concrete. *Engineering Fracture Mechanics* 55, 163–179.

Pasca, M. (2012). Il costruito italiano: tiplogie, problematiche, interventi pre e post sisma. *Tafter Journal Esperienze e Strumenti per Cultura e Territorio*, 1-12.

Pedersen, P. (1989). On optimal orientation of orthotropic materials. *Structural Optimization* 1, 101–106.

Peerlings, R.H.J., De Borst, R., Brekelmans, W.A.M., de Vree, H.P.J. (1996). Gradient-enhanced damage for quasi-brittle materials. *International Journal for Numerical Methods in Engineering*. 39, 3391–3403.

Peerlings, R. H. J., Geers, M.G.D., de Borst, R., Brekelmans, W.A.M. (2001). A critical comparison of nonlocal and gradient-enhanced softening continua. *International Journal of Solids and Structures* 38, 7723-7746.

Pelà, L., Aprile, A., Benedetti, A. (2009). Seismic assessment of masonry arch bridges. *Engineering Structures* 31, 1777-1788.

Pelà, L., Cervera, M., Oller, S., Chiumenti, M. (2014). A localized mapped damage model for orthotropic materials. *Engineering Fracture Mechanics* 124–125, 196–216.

Pelà, L., Cervera, M., Roca, P. (2011). Continuum damage model for orthotropic materials: Application to masonry. *Computer Methods and Applied Mechanics in Engineering* 200 (9-12), 917-930.

Pelà, L., Cervera, M., Roca, P. (2013). An orthotropic damage model for the analysis of masonry structures. *Construction and Building Matererials* 41, 957-967.

Petracca, M., Pelà, L., Rossi, R., Oller, S., Camata, G., Spaccone, E. (2017). Multiscale computational first order homogenization of thick shells for the analysis of out-of-plane loaded masonry walls. *Computer Methods in Applied Mechanics and Engineering* 315, 273–301.

Pijaudier-Cabot, G., Bažant, Z. P. (1987). Nonlocal damage theory. *Journal of Engineering Mechanics* 113 (10), 1512-1533.

Rabczuk, T. (2013).Computational methods for fracture in brittle and quasi-brittle solids: state-of-the-art review and future perspectives. *ISRN Applied Mathematics* DOI http://dx.doi.org/10.1155/2013/849231.

Ramos L.F., De Roeck G., Lourenço P.B., Campos-Costa A. (2010). Damage identification on arched masonry structures using ambient and random impact vibrations. *Engineering Structures* 32,146-62.

Ramos L.F. (2007). Damage identification on masonry structures based on vibration signatures. Ph.D. Thesis. Portugal: University of Minho. Available from: www.civil.uminho.pt/masonry.

Ramtani, S. (1990). Contribution à la modélisation du comportement multiaxial du béton endommagé avec description du caractère unilatéral. University Paris 6.

Rashid, Y. (1968). Ultimate strength analysis of prestressed concrete pressure vessels. *Nuclear Engineering and Design* 7, 334–344.

Reinhardt, H.W. (1984). Fracture mechanics of an elastic softening material like concrete. *HERON* 29, 1–42.

Reinhardt, H.W., Cornelissen, H., (1984). Postpeak cyclic behaviour of concrete in uniaxial tensile and alternating tensile and compressive loading. *Cement and Concrete Research* 14, 263-270.

Reyes, E., Galvez, J.C., Casati, M.J., Cendon, D.A., Sancho, J.M., Planas, J. (2009). An embedded cohesive crack model for finite element analysis of brickwork masonry fracture. Engineering Fracture Mechanics 76, 1933-1944.

Riccardi, F., Kishta, E., Richard, B. (2017). A step-by-step global cracktracking approach in E-FEM simulations of quasi-brittle materials. *Engineering Fracture Mechanics* 170, 44–58.

Riggs, H.R., Powell, G.H. (1986). Rough crack model for analysis of concrete. *Journal of Engineering Mechanics* ASCE 112 (5), 448-464.

Roca, P., Cervera, M., Gariup, G., Pelà, L. (2010) Structural analysis of masonry historical constructions. Classical and advanced approaches. *Archives of Computational Methods in Engineering* 35, 299-325.

Roca, P., Cervera, M., Pelà, L., Clemente, R., Chiumenti, M. (2012). Viscoelasticity and Damage Model for Creep Behaviour of Historical Masonry Structures. *The Open Civil Engineering Journal* 6, 188-199.

Rospars, C., Chauvel, D., (2014). CEOS.fr experimental programme and reference speciement test results. European Journal of Environmental and Civil Engineering 18 (7), 738-753.

Rots, J.G. (1988). Computational modelling of concrete fracture. Ph.D. thesis, Delft University of Technology, Delft, Netherlands.

Rots, J.G. (1991). Numerical simulation of cracking in masonry. HERON 36(2), 49-63.

Rots, J.C., De Borst, R. (1987). Analysis of mixed-mode fracture in concrete. *Journal of Engineering Mechanics* 113(11), 1739–1758.

Rots, J.G., Nauta, P., Kusters, G.M.A., Blaauwendraad, J. (1985). Smeared crack approach and fracture localization in concrete. *HERON* 30, 1–48.

Rots, J.G., Blaauwendraad, J. (1989). Crack models for concrete: discrete or smeared? Fixed, multidirectional or rotating? *HERON* 34(1), 1-59.

Saloustros, S., Cervera, M., Pelà, L. (2017a). Tracking multi-directional intersecting cracks in numerical modelling of masonry shear walls under cyclic loading. *Meccanica* New Trend in Mechanics of Masonry, 1–20.

Saloustros, S., Pelà, L., Cervera, M., Roca, P. (2017b). Finite Element Modelling of Internal and Multiple Localized Cracks. *Computational Mechanics* 59, 299–316.

Saloustros, S., Pelà, L., Cervera, M. (2015). Finite Element Modelling of Internal and Multiple Localized Cracks. *Engineering Fracture Mechanics* 150, 96–114.

Saloustros, S., Pelà, L., Cervera, M., Roca, P. (2017c). An Enhanced Finite Element Macro-Model for the Realistic Simulation of Localized Cracks in Masonry Structures: A Large-Scale Application. *International Journal of Architectural Heritage* DOI: 10.1080/15583058.2017.1323245.

Sancho, J.M., Planas, J., Cendón, D.A., Reyes, E., Gálvez, J.C. (2007). An embedded cohesive crack model for finite element analysis of concrete fracture. *Engineering. Fracture Mechanics* 74 (1–2), 75–86.

Saouridis, C., Mazars, J. (1992). Prediction of the failure and size effect in concrete via a biscale damage approach. *Engineering with computers* 9, 329-334.

Silva, B.., Guedes, J.M., Arêde, A., Costa, A. (2012). Calibration and application of a continuum damage model on the simulation on stone masonry structures: Gondar church as a case study. *Bulletin of Earthquake Engineering* 10, 211–234.

Silva, B.Q., Pappas, A., Guedes, J.M., da Porto, F., Modena, C. (2017). Numerical analysis of the in-plane behaviour of three-leaf stone masonry panels consolidate with grout injection. *Bulletin of Earthquake Engineering* 15, 357–383.

Simó, J.C., Hughes, T.J.R. (1998). Computational Inelasticity. Springer-Verlag, New York.

Simó, J.C., Ju, J.W. (1987). Strain- and stress-based continuum damage models. I: Formulation; II: Computational aspects. *International Journal of Solids and Structures* 23, 821-869.

Sinha, E., Gerstle, K., Tulin, L. (1964). Stress-strain relations for concrete under cyclic loading. *Journal of the American Concrete Institute* 62(2), 195-210.

Slobbe, A., M. Hendriks, M., and J. Rots, J. (2014). Smoothing the propagation of smeared cracks. *Engineering Fracture Mechanics* 132, 147–168.

Suidan, M., Schnobrich, W.C. (1973). Finite element analysis of reinforced concrete. *Journal of the Structural Division ASCE* 99(10), 2109-2122.

Sukumar, N., Möes, N., Moran, B., Belytschko, T. (2000). Extended finite element method for three-dimensional crack modelling, *International Journal of Numerical Methods in Engineering* 48, 1549–1570.

Taqieddin, Z.N., Voyiadjis, G.Z. (2009). Elastic Plastic and Damage Model for Concrete Materials: Part II: Implementation and Application to Concrete and Reinforced Concrete. *International Journal of Structural Changes in Solids* 1(1), 187-209.

Toti, J., Gattulli, V., Sacco, E. (2014). Damage propagation in a masonry arch subjected to slow cyclic and dynamic loadings. *Frattura ed Integrità Strutturale* 29, 166-77

Toti, J., Gattulli, V., Sacco, E. (2015). Nonlocal damage propagation in the dynamics of masonry elements. *Computer and Structures* 152, 215-227.

Trunk, B. (2000). Einfluss der Bauteilgroesse auf die Bruchenergie von Beton. Aedificatio Publishers (in German).

Tveergard, V., Needleman, A. (1995). Effects of nonlocal damage in porous plastic solids. *International Journal of Solids and Structures* 32, 1063-1077.

Vassaux, M., Richard, B., Ragueneau, B., Millard, A. (2015). Regularised crack behaviour effects on continuum modelling of quasi-brittle materials under cyclic loading. *Engineering Fracture Mechanics* 149, 18-36.

Vecchio, F.J. (1999). Towards Cyclic Load Modeling of Reinforced Concrete. *ACI Structural Journal* 96(2), 193-202.

Vecchio, F.J., Collins, M.P. (1986). The modified compression-field theory for reinforced concrete elements subjected to shear. *Journal of the American Concrete Institute* 83 (2), 219-231.

Ventura, G. (2006). On the elimination of quadrature subcells for discontinuous functions in the extended finite-element method. *International Journal for Numerical Methods in Engineering* 66, 761‑795.

Ventura, G., Benvenuti, E. (2015). Equivalent polynomials for quadrature in heaviside function enriched elements. *International Journal for Numerical Methods in Engineering* 102, 688‑710.

Vignollet, J., May, S., De Borst, R., Verhoosel, C.V. (2014). Phase-field models for brittle and cohesive fracture. *Meccanica* 49(11), 2587–2601.

Voyiadjis, G.Z., Taqieddin, Z.N., Kattan, P.I. (2008). Anisotropic damage-plasticity model for concrete. *International Journal of Plasticity* 24, 1946–1965.

Xenos, D., Grassl, P. (2016). Modelling the failure of reinforced concrete with nonlocal and crack band approaches using damage-plastictiy model CDPM2. *Finite elements in Analysis and Design* 117-118, 11-20.

Xue, X., Yang, X. (2014). A damage model for concrete under cyclic actions. *International Journal of Damage Mechanics* 23(2), 155-177.

Wu, J.Y. (2017). A unified phase-field theory for the mechanics of damage and quasi-brittle failure. *Journal of the Mechanics and Physics of Solids* 103, 72–99.

Wu, J.Y., Cervera, M. (2016). Thermodynamically consistent plastic-damage framework for localized failure in quasi-brittle solids: material model and strain localization analysis. *International Journal of Solids and Structures* 88-89, 227-247.

Wu, J.Y., Cervera, M. (2017). Strain localization of elastic-damaging frictional-cohesive materials: analytical results and numerical verification. *Materials* 10, 434.

Wu, J.Y., Li, J. (2008). On the mathematical and thermodynamical descriptions of strain equivalence based anisotropic damage model. *Mechanics of Materials* 2008 40, 377–400.

Wu, J.Y., Li, J., Faria, R. (2006). An energy rate-based plastic-damage model for concrete. *International Journal of Solids and Structures* 43, 583-612.

Wu, J.Y., Xu, S.L. (2013). Reconsideration on the elastic damage/degradation theory for the modelling of microcrack closure-reopening (MCR) effects. *International Journal of Solids and Structures* 50, 795–805.

Wu, J.Y., Cervera, M. (2017). A novel positive/negative projection in energy norm for the damage modelling of quasi-brittle solids. Submitted to *International Journal of Solids and Structures.*

Yazdani, S., Schreyer, H.L. (1990). Combined plasticity and damage mechanics model for plain concrete. *Journal of Engineering Mechanics ASCE* 116, 1435-1450.

Zaho, J., Sheng, D., Zhou, W. (2005). Shear banding analysis of geomaterials by strain gradient enhanced damage model. *International Journal of Solids and Structures* 42 (20), 5335–5355.

Zhang, Y., Lackner, R., Zeiml, M., Mang, H. (2015). Strong discontinuity embedded approach with standard SOS formulation: Element formulation, energy-based crack-tracking strategy, and validations. *Computer Methods in Applied Mechanics and Engineering* 287, 335–366.